# EXAMINING ECOSYSTEM DROUGHT RESPONSES USING REMOTE SENSING AND FLUX TOWER OBSERVATIONS

Wenzhe Jiao

Submitted to the faculty of the University Graduate School
in partial fulfillment of the requirements
for the degree
Doctor of Philosophy
in the Department of Earth Sciences,
Indiana University

September 2022

Accepted by the Graduate Faculty of Indiana University, in partial fulfillment of the requirements for the degree of Doctor of Philosophy.

Doctoral Committee

_____
Lixin Wang, PhD, Chair

_____
Kimberly A Novick, PhD

June 21, 2022

_____
Gabriel Filippelli, PhD

_____
Honglang Wang, PhD

_____
Lin Li, PhD

ACKNOWLEDGEMENT

I have many people to thank for their help, support, and friendship throughout graduate school. They made my Ph.D. journey a fulfilling and exciting one. Without them none of this work would have been possible.

First and foremost, I would like to express my full gratitude to my advisor Dr. Lixin Wang for giving me the opportunity to pursue my studies under his mentorship. He helped me get a smooth start in graduate school at the very beginning, and later on, gave me tremendous freedom to explore new research topics based on my interest. My deepest thanks for all his guidance, opportunities, collaborations, general advice on life during this remarkable journey.

I would also like to thank my committee members: Professor Kimberly Novick, Professor Gabriel Filippelli, Professor Honglang Wang and Professor Lin Li for their support and insightful comments that improved the quality of this dissertation.

The advice and supports from all faculty members, students and administrative staff from the Department of Earth Sciences on IUPUI campus also made my time at IUPUI a wonderful experience. My friends Chao Tian, Ruiguang Pan, Matt Lanning, Bishwodeep Adhikari, Brooke Vander Pas, Yusen Yuan, Kudzai Farai Kaseke, Igor Ogashawara, John Shukle, and Yu Peng inspired me not only on teaching, but also on career development, and research presentation during so many casual conversations.

I would also like to thank my friends Michael Benson, Sander Denham, Kesondra Key, Daniela Cala from Novick Lab at IU Bloomington campus. I spent two wonderful years living in Bloomington. Their friendship gave me strong support.

I am also grateful that I had great collaborators: Prof. Paolo D'Odorico from the University of California, Berkeley; Prof. Matthew F McCabe from King Abdullah University of Science and Technology; Prof. William Kolby Smith from the University of Arizona. Their insightful comments and suggestions improved the quality of my work.

I would also like to thank Lake Thunderbird in Oklahoma. I really enjoyed my hiking and fishing time there for three summers, which gave me so much fun and made me have enough break both physically and mentally after work.

Finally, I sincerely thank all of my family including my parents, my wife Qing, my daughter Colleen, my dog Rebecca (even though Rebecca probably will never understand my acknowledgement to her here), who always give me so many supports to overcome all the difficulties in my life. I love you all and you have helped make me the person I am today.

Wenzhe Jiao

EXAMINING ECOSYSTEM DROUGHT RESPONSES USING REMOTE SENSING AND FLUX TOWER OBSERVATIONS

Water is fundamental for plant growth, and vegetation response to water availability influences water, carbon, and energy exchanges between land and atmosphere. Vegetation plays the most active role in water and carbon cycle of various ecosystems. Therefore, comprehensive evaluation of drought impact on vegetation productivity will play a critical role for better understanding the global water cycle under future climate conditions.

In-situ meteorological measurements and the eddy covariance flux tower network, which provide meteorological data, and estimates of ecosystem productivity and respiration are remarkable tools to assess the impacts of drought on ecosystem carbon and water cycles. In regions with limited in-situ observations, remote sensing can be a very useful tool to monitor ecosystem drought status since it provides continuous observations of relevant variables linked to ecosystem function and the hydrologic cycle. However, the detailed understanding of ecosystem responses to drought is still lacking and it is challenging to quantify the impacts of drought on ecosystem carbon balance and several factors hinder our explicit understanding of the complex drought impacts. This dissertation addressed drought monitoring, ecosystem drought responses, trends of vegetation water constraint based on in-situ metrological observations, flux tower and multi-sensor remote sensing observations. This dissertation first developed a new integrated drought index applicable across diverse climate regions based on in-situ meteorological observations and multi-sensor remote sensing data, and another integrated

drought index applicable across diverse climate regions only based on multi-sensor remote sensing data. The dissertation also evaluated the applicability of new satellite dataset (e.g., solar induced fluorescence, SIF) for responding to meteorological drought. Results show that satellite SIF data could have the potential to reflect meteorological drought, but the application should be limited to dry regions. The work in this dissertation also accessed changes in water constraint on global vegetation productivity, and quantified different drought dimensions on ecosystem productivity and respiration. Results indicate that a significant increase in vegetation water constraint over the last 30 years. The results highlighted the need for a more explicit consideration of the influence of water constraints on regional and global vegetation under a warming climate.

Lixin Wang, PhD, Chair

Kimberly A Novick, PhD

Gabriel Filippelli, PhD

Honglang Wang, PhD

Lin Li, PhD

TABLE OF CONTENTS

LIST OF TABLES

LIST OF FIGURES

LIST OF ABBREVIATIONS

| | |
|---|---|
| AGC: | Aboveground biomass carbon |
| AMS: | American Meteorological Society |
| AOD: | Aerosol optical depth |
| ASCAT: | Advanced Scatterometer |
| AVHRR: | Advanced Very High Resolution Radiometer |
| BRT: | Boosted regression trees |
| CART: | Classification and regression tree |
| CCI: | Climate Change Initiative |
| CDMI: | Combined drought monitoring index |
| COT: | Cloud optical thickness |
| ECOSTRESS: | ECOsystem Spaceborne Thermal Radiometer Experiment on Space Station |
| EDDI: | Evaporative demand drought index |
| ENSO: | El Nino-Southern Oscillation |
| EPMC: | Evolution Process-based Multi-sensor Collaboration |
| ERSATSR: | European Remote Sensing Satellite–Along Track Scanning Radiometer |
| ESA: | European Space Agency |
| ESI: | Evaporative Stress Index |
| FDA: | flexible discriminant analysis |
| FIDI: | Fuzzy Integrated Drought Index |
| FLEX: | FLuorescence EXplorer |
| fPAR: | fraction of absorbed photosynthetic active radiation |
| GEDI | Global Ecosystem Dynamics Investigation |
| GEO: | Geostationary Earth orbit |
| GFED: | Global Fire Emissions Database |
| GNSS: | Global Navigation Satellite System |
| GPCP: | Global Precipitation Climatology Project |
| GPP: | Gross primary productivity |
| GRACE: | Gravity Recovery and Climate Experiment |
| GWR: | Geographically weighted regression |
| HiFIS : | High-fidelity imaging spectroscopy |
| HLS: | Harmonized Landsat and Sentinel-2 |
| HSMDI: | High resolution Soil Moisture Drought Index |
| ICESat-2: | Ice, cloud, and land elevation satellite-2 |
| IDI: | Integrated Drought Index |
| IMS: | Ice Mapping System |
| INFORM: | Invertible forest reflectance model |
| InSAR: | Interferometry of Synthetic Aperture Radar |
| ISDI: | Integrated Surface Drought Index |

| | |
|---|---|
| JAXA: | Japan Aerospace Exploration Agency |
| KECA: | Kernel entropy component analysis |
| LAI: | Leaf area index |
| LEO: | Low Earth orbit |
| LFMC: | Live fuel moisture content |
| LiDAR: | Light detection and ranging |
| LST: | Land surface temperature |
| MAIAC: | Multi-Angle Implementation of Atmospheric Correction |
| MARS: | Multivariate adaptive regression splines |
| MIDI: | Microwave Integrated Drought Index |
| MODIS: | Moderate Resolution Imaging Spectroradiometer |
| MRMS: | Multi-Radar Multi-Sensor |
| NASA: | National Aeronautics and Space Administration |
| NDII: | Normalized Difference Infrared Index |
| NDVI: | Normalized Difference Vegetation Index |
| NDWI: | Normalized Difference Water Index |
| NIR: | Near infrared radiation |
| $NIR_V$: | Near-infrared reflectance of vegetation |
| NISAR: | NASA-ISRO Synthetic Aperture Radar |
| NLDAS-2: | North American Land Data Assimilation System-2 |
| NOAA: | National Oceanic and Atmospheric Administration |
| OMDI: | Optimized Meteorological Drought Index |
| OVDI: | Optimized Vegetation Drought Index |
| PADI: | Process-based Accumulated Drought Index |
| PAR: | Photosynthetically active radiation |
| PCA: | Principal component analysis |
| PCI: | Precipitation Condition Index |
| PDSI: | Palmer drought severity index |
| PERSIANN: | Precipitation Estimation from Remotely Sensed Information using Artificial Neural Networks |
| PHDI: | Palmer Hydrologic Drought Index |
| PLSR: | Partial least squares regression |
| PRI: | Photochemical reflectance index |
| QuickDRI: | Quick Drought Response Index |
| RCI: | Rapid change index |
| RF: | Random forests |
| RTM: | Radiative transfer models |
| SDCI: | Scaled Drought Condition Index |
| SDI: | Synthesized drought index |
| SESR: | Standardized evaporative stress ratio |
| SIF: | Solar-induced chlorophyll fluorescence |

| | |
|---|---|
| SKPCA: | Sparse KPCA |
| SMCI: | Soil Moisture Condition Index |
| SMMR: | Scanning Multi-channel Microwave Radiometer |
| SMRI: | Standardized Snow Melt and Rain Index |
| SPEI: | Standardized Precipitation Evapotranspiration Index |
| SPI: | Standardized Precipitation Index |
| SSM/I: | Special Sensor Microwave Imager |
| SVI: | Standardized Vegetation Index |
| SVM: | Support vector machines |
| SWSI: | Surface Water Supply Index |
| SZI: | Standardized Moisture Anomaly Index |
| Tandem-X: | TerraSAR-X add-on for Digital Elevation Measurement |
| TCI: | Temperature Condition Index |
| TRMM: | Tropical Rainfall Measuring Mission |
| TWS: | Terrestrial water storage |
| USGS: | United States Geological Survey |
| VCI: | Vegetation condition index |
| VegDRI: | Vegetation Drought Response Index |
| VIS/IR: | Visible and infrared radiation |
| VOD: | Vegetation optical depth |
| VPD: | Vapor pressure deficit |

.

# CHAPTER 1: INTRODUCTION

Drought is recognized as the world's most costly and pressing natural hazard that influences water resources, agricultural production and natural ecosystems (Sheffield et al., 2008). It is an intermittent disturbance of the water cycle with significant consequences on the carbon cycle. It causes disturbances in the reservoirs of soil moisture, organic matter, water vapor, soil nutrients, and plant carbon stores, leading to long-term effects in water and carbon cycling (Van der Molen, Dolman, Ciais, Eglin, Gobron, Law, Meir, Peters, Phillips, Reichstein, et al., 2011). Vegetation plays the most active role in water and carbon cycle of various ecosystems (Sitch et al., 2003). When vegetation is affected by drought (e.g., tree mortality or reduced biomass accumulation), it can significantly alter hydrological processes (Brown et al., 2005) and influence the availability of surface and subsurface water resources (Mankin et al., 2019; Vicente-Serrano et al., 2019). Therefore, comprehensive evaluation of drought impact on vegetation productivity will play a critical role for better understanding the global water cycle under future climate conditions.

*In-situ* meteorological measurements and the eddy covariance flux tower network, which provides meteorological data, and estimates of net ecosystem exchange (NEE), gross ecosystem productivity (GPP), and ecosystem respiration (Reco), are remarkable tools to assess the impacts of drought on ecosystem carbon and water cycles. In regions with limited *in situ* observations, remote sensing can be a very useful tool to monitor ecosystem drought status since it provides continuous observations of relevant variables linked to ecosystem function and the hydrologic cycle (AghaKouchak et al., 2015b). However, the detailed understanding of ecosystem responses to drought is still lacking

and it is challenging to quantify the impacts of drought on ecosystem carbon balance and several factors hinder our explicit understanding of the complex drought impacts. For example, current single-sensor remote sensing based drought indices cannot capture the complex drought impact and multi-sensor remote sensing drought indices are in their infancy stage. A suite of remotely-sensed drought indices already exists, each with different emphasis. However, drought has complex environmental impacts and affects different components (e.g., soil, air and vegetation) of ecosystems. In isolation a single drought index may not be sufficient to capture the complex processes and diverse impacts of drought (Hao and Singh, 2015). To this end, integrated drought indices, which are capable of representing drought impacts, are urgently needed. One of the unique elements of remote sensing platforms is their multi-sensor capabilities, which enhance the capacity for characterizing drought from a variety of aspects at regional to global scale. Leveraging multi-sensor remote sensing provides unique benefits for regional to global drought studies, particularly in: 1) revealing the complex drought impact mechanisms on various ecosystem components; 2) providing continuous long-term drought related information at large scales; 3) presenting real-time drought information with high spatiotemporal resolution; 4) providing multiple lines of evidence of drought monitoring to improve modeling robustness; and 5) improving the accuracy of drought monitoring and assessment efforts. However, few of these indices were developed under diverse environmental conditions covering large spatial scales. This geographic constraint could lead to poor performance if certain indices are applied in climate regions that are much different from those in which they were developed (Zhang, Jiao, et al., 2017). Another major issue is that the empirical relationships used to derive the integrated remote-

sensing drought indices are typically viewed as spatially homogeneous (Hao, Zhang, et al., 2015; Zhang and Jia, 2013). For example, it is often assumed that all the sub-areas of a particular study area contribute the same weight for a particular single index, and an empirical linear combination method is used to derive a relationship that is believed to be uniformly applicable across the study area. However, this type of integration may not be applicable to characterize the covariability of drought related indices, since it may miss local details that can be significant if the relationship of the related indices is spatially non-stationary (AghaKouchak, 2015c). Thus, a reliable multi-sensor remote sensing based integrated drought index, which has good performance across diverse environmental conditions, is the key to characterize the spatial and temporal changes of drought impacts on vegetation productivity at a global scale.

With advances in remote sensing capacity and the increasing range of platforms available for analysis, there are growing interests to study the effect of drought on new satellite based remote sensing datasets such as Solar-induced chlorophyll fluorescence (SIF). However, to what extent SIF responds to drought and how the responses vary under different precipitation, temperature and potential evapotranspiration conditions are not clear. Traditionally, Large-scale remotely sensed drought estimation often relies on optical, near-infrared (NIR), thermal and microwave reflectance observations. For example, satellite-based vegetation indices (VIs) have been widely used for detecting the severity and impact of drought globally through assessing the water-stress related vegetation conditions (Asner et al., 2010; Di et al., 1994; Mishra et al., 2010; Myneni et al., 1989; Singh et al., 2003; Tate et al., 2000; Tucker et al., 1987; Van Loon et al., 2016b). Some of the research indicated that VIs are good indicators to monitor drought

(Ji et al., 2003; Kogan, 1997; Liu et al., 1996; Zhang, Jiao, et al., 2017). However, other studies have shown that VIs should be used with caution for drought monitoring, as they fail to capture rapid changes in drought responses since these indices are not directly linked to photosynthetic functioning (Dobrowski et al., 2005; Sun et al., 2015). SIF is considered to have a more close relationship to the functional status of photosynthetic machinery than VIs (Meroni et al., 2009). Satellite-based SIF provides a new method for observing vegetation function from space (Guanter et al., 2007; Guanter et al., 2012; Joiner et al., 2011; Joiner et al., 2013; Yang, Tang, et al., 2015). However, the sensitivity of satellite SIF to the drought-related environmental variables is complicated and SIF anomaly is not responsive to soil water deficit alone. The change of vapor pressure deficit (VPD), LUE, fraction of photosynthetically active radiation (fPAR), and fluorescence yield under drought conditions have also been shown affecting the SIF anomaly (Sun et al., 2015; Yoshida et al., 2015). In addition, SIF dynamics could be affected by some other biotic and abiotic factors such as plant functional types, temperature, and evapotranspiration (Porcar-Castell et al., 2014). Furthermore, even if the meteorological drought indices indicate that there is drought, the vegetation may not necessarily experience water stress and decrease SIF signal. To what extent satellite SIF responds to meteorological drought which are estimated from precipitation, temperature and PET perspectives, and how the responses vary under different climatic conditions remain unclear.

The multiple-dimension property of drought has made the accurate drought impact assessments on ecosystem carbon cycles challenging. Drought has not only simultaneous impacts but also cumulative and lagged impacts on ecosystem carbon

cycles. In addition, different drought intensity, time-scale, and timing may impact ecosystem production and respiration differently. Only considering one or two drought dimensions may not objectively reflect the actual drought impacts. However, it is difficult to comprehensively quantify drought with all dimensions using a single metric (Jiao, Wang and McCabe, 2021; Lloyd-Hughes, 2014; Vicente-Serrano et al., 2019). The concept of drought time scale can incorporate multiple drought dimensions. This is because drought indices with a certain time scale is based on the cumulative water deficit over the preceding months of this time scale (Vicente-Serrano et al., 2010), and drought time-scale is a function of drought duration and frequency (McKee et al., 1993). Therefore, a time series of drought indices with various time scales can reflect drought information including the onset, offset, duration, frequency, magnitude, and intensity of drought events. Yet, the time scale based metrics still cannot reflect other relevant drought information (e.g., drought timing), which is important since plants in different growth stages have different sensitivity to drought (Chaves et al., 2003; D'Orangeville et al., 2018b; McDowell et al., 2008). In addition, while most of the drought studies focused on simultaneous impacts and post drought recoveries, few studies incorporated the effects of water availability prior to the studied month. Recently, climate factors (i.e., precipitation, temperature, and radiation) are found to have lagged on vegetation growth (Wen et al., 2018; Wen et al., 2019; Wu, Zhao, et al., 2015), and drought has been found to have lagged and cumulative impacts on autumn leaf senescence (Peng et al., 2019) based on satellite observations. However, few studies quantified the impacts of prior water availability at the ecosystem scale and not considering the impact of prior water availability can cause significant errors in drought impact estimates. In addition, it

remains unclear how the widely-used drought definitions could reflect plant water stress. Numerous drought indices have been developed to define and quantify drought based on various aspects of observations (e.g., soil moisture, temperature, vapor pressure deficit (VPD), precipitation, and runoff) (Green et al., 2019; Novick et al., 2016; Sulman et al., 2016; Zhang, Jiao, et al., 2017; Zhang, Ficklin, et al., 2019) and using different quantification methods (Ruppert et al., 2015; Slette, Post, et al., 2019). Among all these indices, drought indices defined by meteorological variables, such as Standardized Precipitation Evapotranspiration Index (SPEI), are becoming more widely used in recent years. However, there are debates about the application of the temporal standardization based drought quantifications, and it was argued that the temporal standardization based drought indices do not directly correspond to the plant water stress, especially in humid regions (Slette, Smith, et al., 2019; Zang et al., 2020). The same severity of drought events could affect humid regions very differently from dry regions, because the differences in the plant physiological response to drought can determine the levels of ecosystem resistance and resilience to drought (Chaves et al., 2003; D'Orangeville et al., 2018b; McDowell et al., 2008). Short-term meteorological drought associated with higher temperature and sunny weather may even enhance plant productivity. It thus remains unclear how temporal standardization derived drought indices (e.g., SPEI) could be better used to reflect plant water stress in humid regions. Uncertainties of quantifying different dimensions of drought using drought indices could result in magnified errors of drought impact estimates.

Despite the growing interest in predicting global and regional trends in vegetation productivity in response to a changing climate, changes in vegetation growth limited by

water remain poorly understood. Recent studies have documented vegetation response to water availability in terms of the negative impact of drought on vegetation productivity (Buermann et al., 2018b; Ciais et al., 2005b; Zhao et al., 2010), the timescale of vegetation response to drought(Vicente-Serrano et al., 2013), and vegetation resilience and recovery from severe drought(Anderegg et al., 2015; Anderegg et al., 2018). Yet, it remains unclear whether the impact of water availability on vegetation growth is changing in a warming climate. While various water deficit impacts have been documented, to our knowledge, a comprehensive global assessment of changes in long-term vegetation response to water constraints using the full satellite record is still missing. This knowledge gap prevents an adequate understanding of vegetation response to the expected intensification of drought frequency, severity, and duration (Cook et al., 2015; Dai, 2013; Field et al., 2012; Milly et al., 2016; Trenberth et al., 2013; Xu et al., 2019), and change in water availability (Konapala et al., 2020). In addition, recent studies have suggested that the strength of the terrestrial carbon sink might be shifting from an increasing to a decreasing trend (Humphrey et al., 2018; Peñuelas et al., 2017; Yuan, Zheng, et al., 2019), likely as a result of water constraints.

Based on the uncertainties described above, in this document I will address drought monitoring, drought impacts on ecosystems, trends of vegetation water constraint based on *in-situ* metrological observations, flux tower and multi-sensor remote sensing observations. Specifically, the dissertation has the following main objectives and will be structured as Chapter 2: overview of multi-sensor remote sensing for drought characterization: current status, opportunity and a roadmap for the future. Chapter 3: Developing a newly integrated drought index applicable across diverse climate regions

based on *in-situ* meteorological observations and multi-sensor remote sensing data. Chapter 4: Developing a newly integrated drought index applicable across diverse climate regions only based on multi-sensor remote sensing data. Chapter 5: Evaluating the applicability of satellite solar-induced chlorophyll fluorescence (SIF) to examine meteorological drought. Chapter 6: Accessing changes in water constraint on global vegetation productivity using multi-sensor satellite products. Chapter 7: Quantifying the effects of drought on NEE, GPP and $R_{ECO}$ by considering multiple drought dimensions.

**References**

AghaKouchak, A., 2015c. A multivariate approach for persistence-based drought prediction: Application to the 2010–2011 East Africa drought. *Journal of Hydrology*, 526: 127-135.

AghaKouchak, A. et al., 2015b. Remote sensing of drought: Progress, challenges and opportunities. *Reviews of Geophysics*, 53(2): 452-480.

Anderegg, W.R. et al., 2018. Hydraulic diversity of forests regulates ecosystem resilience during drought. *Nature*, 561(7724): 538.

Anderegg, W.R. et al., 2015. Pervasive drought legacies in forest ecosystems and their implications for carbon cycle models. *Science*, 349(6247): 528-532.

Asner, G.P. and Alencar, A., 2010. Drought impacts on the Amazon forest: the remote sensing perspective. *New phytologist*, 187(3): 569-578.

Brown, A.E., Zhang, L., McMahon, T.A., Western, A.W. and Vertessy, R.A., 2005. A review of paired catchment studies for determining changes in water yield resulting from alterations in vegetation. *Journal of Hydrology*, 310(1-4): 28-61.

Buermann, W. et al., 2018b. Widespread seasonal compensation effects of spring warming on northern plant productivity. *Nature*, 562(7725): 110.

Chaves, M.M., Maroco, J.P. and Pereira, J.S., 2003. Understanding plant responses to drought—from genes to the whole plant. *Functional Plant Biology*, 30(3): 239-264.

Ciais, P. et al., 2005b. Europe-wide reduction in primary productivity caused by the heat and drought in 2003. *Nature*, 437(7058): 529.

Cook, B.I., Ault, T.R. and Smerdon, J.E., 2015. Unprecedented 21st century drought risk in the American Southwest and Central Plains. *Science Advances*, 1(1): e1400082.

D'Orangeville, L. et al., 2018b. Drought timing and local climate determine the sensitivity of eastern temperate forests to drought. *Global Change Biology*.

Dai, A., 2013. Increasing drought under global warming in observations and models. *Nature Climate Change*, 3(1): 52.

Di, L., Rundquist, D.C. and Han, L., 1994. Modelling relationships between NDVI and precipitation during vegetative growth cycles. *International Journal of Remote Sensing*, 15(10): 2121-2136.

Dobrowski, S., Pushnik, J., Zarco-Tejada, P. and Ustin, S., 2005. Simple reflectance indices track heat and water stress-induced changes in steady-state chlorophyll fluorescence at the canopy scale. *Remote Sensing of Environment*, 97(3): 403-414.

Field, C.B., Barros, V., Stocker, T.F. and Dahe, Q., 2012. Managing the risks of extreme events and disasters to advance climate change adaptation: special report of the intergovernmental panel on climate change. Cambridge University Press.

Green, J.K. et al., 2019. Large influence of soil moisture on long-term terrestrial carbon uptake. *Nature*, 565(7740): 476-479.

Guanter, L. et al., 2007. Estimation of solar-induced vegetation fluorescence from space measurements. *Geophysical Research Letters*, 34(8).

Guanter, L. et al., 2012. Retrieval and global assessment of terrestrial chlorophyll fluorescence from GOSAT space measurements. *Remote Sensing of Environment*, 121: 236-251.

Hao, C., Zhang, J. and Yao, F., 2015. Combination of multi-sensor remote sensing data for drought monitoring over Southwest China. *International Journal of Applied Earth Observation and Geoinformation*, 35: 270-283.

Hao, Z. and Singh, V.P., 2015. Drought characterization from a multivariate perspective: A review. *Journal of Hydrology*, 527: 668-678.

Humphrey, V. et al., 2018. Sensitivity of atmospheric $CO_2$ growth rate to observed changes in terrestrial water storage. *Nature*, 560(7720): 628-631.

Ji, L. and Peters, A.J., 2003. Assessing vegetation response to drought in the northern Great Plains using vegetation and drought indices. *Remote Sensing of Environment*, 87(1): 85-98.

Jiao, W., Wang, L. and McCabe, M.F., 2021. Multi-sensor remote sensing for drought characterization: current status, opportunities and a roadmap for the future. *Remote Sensing of Environment*, 256: 112313.

Joiner, J. et al., 2013. Global monitoring of terrestrial chlorophyll fluorescence from moderate spectral resolution near-infrared satellite measurements: methodology,

simulations, and application to GOME-2. *Atmospheric Measurement Techniques*, 6(2): 2803-2823.

Joiner, J., Yoshida, Y., Vasilkov, A. and Middleton, E., 2011. First observations of global and seasonal terrestrial chlorophyll fluorescence from space. *Biogeosciences*, 8(3): 637-651.

Kogan, F.N., 1997. Global drought watch from space. *Bulletin of the American Meteorological Society*, 78(4): 621-636.

Konapala, G., Mishra, A.K., Wada, Y. and Mann, M.E., 2020. Climate change will affect global water availability through compounding changes in seasonal precipitation and evaporation. *Nature Communications*, 11(1): 1-10.

Liu, W. and Kogan, F., 1996. Monitoring regional drought using the vegetation condition index. *International Journal of Remote Sensing*, 17(14): 2761-2782.

Lloyd-Hughes, B., 2014. The impracticality of a universal drought definition. *Theoretical and Applied Climatology*, 117(3-4): 607-611.

Mankin, J.S., Seager, R., Smerdon, J.E., Cook, B.I. and Williams, A.P., 2019. Mid-latitude freshwater availability reduced by projected vegetation responses to climate change. *Nature Geoscience*: 1-6.

McDowell, N. et al., 2008. Mechanisms of plant survival and mortality during drought: why do some plants survive while others succumb to drought? *New Phytologist*, 178(4): 719-739.

McKee, T.B., Doesken, N.J. and Kleist, J., 1993. The relationship of drought frequency and duration to time scales, Proceedings of the 8th Conference on Applied Climatology. American Meteorological Society Boston, MA, pp. 179-183.

Meroni, M. et al., 2009. Remote sensing of solar-induced chlorophyll fluorescence: Review of methods and applications. *Remote Sensing of Environment*, 113(10): 2037-2051.

Milly, P.C. and Dunne, K.A., 2016. Potential evapotranspiration and continental drying. *Nature Climate Change*, 6(10): 946.

Mishra, A.K. and Singh, V.P., 2010. A review of drought concepts. *Journal of Hydrology*, 391(1): 202-216.

Myneni, R.B., Ross, J. and Asrar, G., 1989. A review on the theory of photon transport in leaf canopies. *Agricultural and Forest Meteorology*, 45(1-2): 1-153.

Novick, K.A. et al., 2016. The increasing importance of atmospheric demand for ecosystem water and carbon fluxes. *Nature Climate Change*, 6(11): 1023-1027.

Peng, J., Wu, C., Zhang, X., Wang, X. and Gonsamo, A., 2019. Satellite detection of cumulative and lagged effects of drought on autumn leaf senescence over the Northern Hemisphere. *Global Change Biology*, 25(6): 2174-2188.

Peñuelas, J. et al., 2017. Shifting from a fertilization-dominated to a warming-dominated period. *Nature Ecology & Evolution*, 1(10): 1438-1445.

Porcar-Castell, A. et al., 2014. Linking chlorophyll a fluorescence to photosynthesis for remote sensing applications: mechanisms and challenges. *Journal of Experimental Botany*, 65(15): 4065-4095.

Ruppert, J.C. et al., 2015. Quantifying drylands' drought resistance and recovery: the importance of drought intensity, dominant life history and grazing regime. *Global Change Biology*, 21(3): 1258-1270.

Sheffield, J. and Wood, E.F., 2008. Projected changes in drought occurrence under future global warming from multi-model, multi-scenario, IPCC AR4 simulations. *Climate Dynamics*, 31(1): 79-105.

Singh, R.P., Roy, S. and Kogan, F., 2003. Vegetation and temperature condition indices from NOAA AVHRR data for drought monitoring over India. *International Journal of Remote Sensing*, 24(22): 4393-4402.

Sitch, S. et al., 2003. Evaluation of ecosystem dynamics, plant geography and terrestrial carbon cycling in the LPJ dynamic global vegetation model. *Global Change Biology*, 9(2): 161-185.

Slette, I.J. et al., 2019. How ecologists define drought, and why we should do better. *Global Change Biology*, 25(10): 3193-3200.

Slette, I.J. et al., 2019. Standardized metrics are key for assessing drought severity. *Global Change Biology*.

Sulman, B.N. et al., 2016. High atmospheric demand for water can limit forest carbon uptake and transpiration as severely as dry soil. *Geophysical Research Letters*, 43(18): 9686-9695.

Sun, Y. et al., 2015. Drought onset mechanisms revealed by satellite solar-induced chlorophyll fluorescence: Insights from two contrasting extreme events. *Journal of Geophysical Research: Biogeosciences*, 120(11): 2427-2440.

Tate, E. and Gustard, A., 2000. Drought definition: a hydrological perspective, Drought and drought mitigation in Europe. Springer, pp. 23-48.

Trenberth, K.E. et al., 2013. Global warming and changes in drought. *Nature Climate Change*, 4: 17.

Tucker, C.J. and Choudhury, B.J., 1987. Satellite remote sensing of drought conditions. *Remote Sensing of Environment*, 23(2): 243-251.

Van der Molen, M.K. et al., 2011. Drought and ecosystem carbon cycling. *Agricultural and Forest Meteorology*, 151(7): 765-773.

Van Loon, A.F. et al., 2016b. Drought in a human-modified world: reframing drought definitions, understanding, and analysis approaches. *Hydrology and Earth System Sciences*, 20(9): 3631.

Vicente-Serrano, S.M. et al., 2013. Response of vegetation to drought time-scales across global land biomes. *Proceedings of the National Academy of Sciences*, 110(1): 52-57.

Vicente-Serrano, S.M., Quiring, S.M., Peña-Gallardo, M., Yuan, S. and Domínguez-Castro, F., 2019. A review of environmental droughts: Increased risk under global warming? *Earth-Science Reviews*: 102953.

Wen, Y., Liu, X., Pei, F., Li, X. and Du, G., 2018. Non-uniform time-lag effects of terrestrial vegetation responses to asymmetric warming. *Agricultural and forest meteorology*, 252: 130-143.

Wen, Y. et al., 2019. Cumulative effects of climatic factors on terrestrial vegetation growth. *Journal of Geophysical Research: Biogeosciences*, 124(4): 789-806.

Wu, D. et al., 2015. Time-lag effects of global vegetation responses to climate change. *Global Change Biology*, 21(9): 3520-3531.

Xu, C. et al., 2019. Increasing impacts of extreme droughts on vegetation productivity under climate change. *Nature Climate Change*, 9(12): 948-953.

Yang, X. et al., 2015. Solar-induced chlorophyll fluorescence that correlates with canopy photosynthesis on diurnal and seasonal scales in a temperate deciduous forest. *Geophysical Research Letters*, 42(8): 2977-2987.

Yoshida, Y. et al., 2015. The 2010 Russian drought impact on satellite measurements of solar-induced chlorophyll fluorescence: Insights from modeling and comparisons with parameters derived from satellite reflectances. *Remote Sensing of Environment*, 166: 163-177.

Yuan, W. et al., 2019. Increased atmospheric vapor pressure deficit reduces global vegetation growth. *Science Advances*, 5(8): eaax1396.

Zang, C.S. et al., 2020. Standardized drought indices in ecological research: Why one size does not fit all. *Global Change Biology*, 26(2): 322-324.

Zhang, A. and Jia, G., 2013. Monitoring meteorological drought in semiarid regions using multi-sensor microwave remote sensing data. *Remote Sensing of Environment*, 134: 12-23.

Zhang, L., Jiao, W., Zhang, H., Huang, C. and Tong, Q., 2017. Studying drought phenomena in the Continental United States in 2011 and 2012 using various drought indices. *Remote Sensing of Environment*, 190: 96-106.

Zhang, Q. et al., 2019. Response of ecosystem intrinsic water use efficiency and gross primary productivity to rising vapor pressure deficit. *Environmental Research Letters*, 14(7): 074023.

Zhao, M. and Running, S.W., 2010. Drought-induced reduction in global terrestrial net primary production from 2000 through 2009. *Science*, 329(5994): 940-943.

# CHAPTER 2 OVERVIEW OF MULTI-SENSOR REMOTE SENSING FOR DROUGHT CHARACTERIZATION: CURRENT STATUS, OPPORTUNITIES AND A ROADMAP FOR THE FUTURE

## 2.1 Introduction

Drought is routinely described as a naturally occurring phenomena induced by precipitation deficiency and consequent hydrological imbalance (Pachauri et al., 2014; Trenberth et al., 2014). Drought can occur over all climatic conditions and has a wide range of damaging impacts (Dai, 2011; Vicente-Serrano et al., 2019). For instance, it can cause crop failures, which may lead to substantial food security concerns and financial loses (Daryanto et al., 2015; Daryanto et al., 2016; Godfray et al., 2010; Pandey et al., 2007); it can decrease the volumes of source waters from rivers, lakes, and groundwater, directly impacting water availability, distribution and energy supply (Van Loon, 2015); it can also amplify tree mortality, trigger ecosystem fires, and decrease carbon uptake in vegetation (Allen et al., 2010; Ciais et al., 2005b; Zhao et al., 2010), thereby influencing terrestrial carbon storage and sequestration potential. Given the wide-ranging scope of influences and impacts that droughts can have, it is no surprise that it is often classified quite broadly, based on the different systems affected. These classifications generally fall into: i) agricultural; ii) hydrological; iii) meteorological, and iv) socioeconomic drought (Wilhite et al., 1985). Recent research has suggested additional drought types, such as ecological drought (Crausbay et al., 2017), environmental drought (Vicente-Serrano et al., 2019), and flash drought (Otkin et al., 2018; Svoboda et al., 2002). With the severity and frequency of droughts projected to increase under climate change, understanding the interrelated impacts and influence across and within sectors is an issue of considerable

importance (Dai, 2013; Trenberth et al., 2014; Xu et al., 2019; Zhou et al., 2019). Figure 2.1 illustrates a number of these drought impacts on different ecosystem components, together with the feedbacks between drought and climate.

Given the spatial and temporal advantage that remote sensing can offer, data from a range of satellite-based platforms have played an increasingly important role in drought studies over the last decade (AghaKouchak et al., 2015b; West et al., 2019). In addition, advances in algorithm development and the rise of cloud-based computing and storage capacity have greatly enhanced the application potential of remote sensing for drought studies (Abdelwahab et al., 2014; Faghmous et al., 2014; Huntington et al., 2017; Sellars et al., 2013; Zhou et al., 2016). Apart from offering an independent observational capacity, remote sensing data provides an opportunity to reduce uncertainty and constrain modelling efforts directed towards drought prediction (Smith et al., 2016). With all of these advances, there have been an increasing number of studies on the subject of drought monitoring and impacts (Agutu et al., 2017; Asner et al., 2016; Gonçalves et al., 2020; Hu, Renzullo, et al., 2020; Jiao, Chang, et al., 2019; Jiao, Tian, et al., 2019; Jiao, Wang, et al., 2019; Liu, Liao, et al., 2017; Nicolai-Shaw et al., 2017; Park et al., 2017; Schwantes et al., 2016; Thomas et al., 2017; Zhang, Chen, et al., 2017). However, while there has been considerable and important research reviewing drought monitoring and its various impacts, with a number of these studies highlighting the importance of integrated drought monitoring (AghaKouchak et al., 2015b; Liu, Zhu, et al., 2016; Trnka et al., 2018; Van Loon et al., 2016a; West et al., 2019; Zhang, Jiao, et al., 2017), there has been no systematic review focusing on some of the recent advances in multi-sensor remote

sensing for drought studies, and how these might further advance the modeling, assessment and prediction fields.

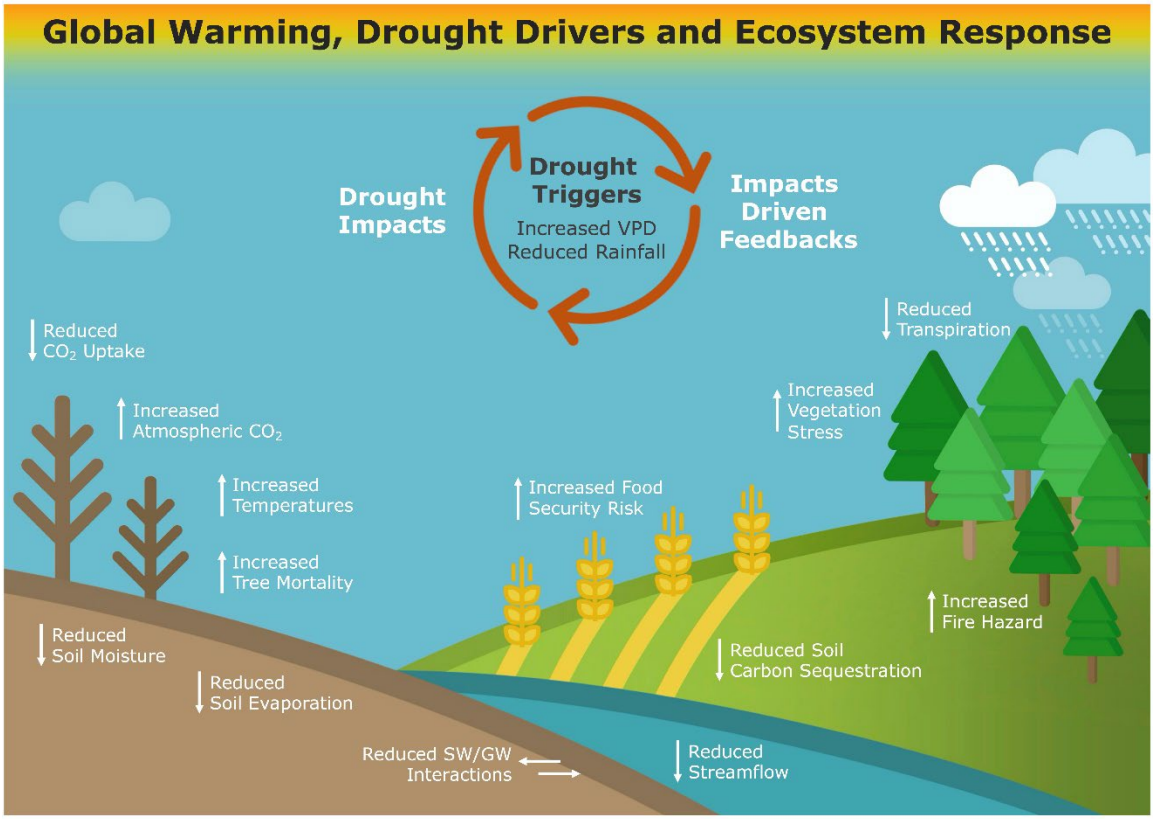


Figure 2.1: Conceptual diagram of a number of terrestrial drought impacts (e.g., increased fire risk, increased food security risk, reduced soil moisture) and potential ecosystem feedbacks (e.g., increased atmospheric $CO_2$, reduced carbon uptake) under global warming conditions. It is important to note that the diagram does not intend to map all of the direct links and multiple feedbacks between the various components of the terrestrial ecosystems (as these may vary based on landscape and condition), or that it captures all of the potential impacts, triggers and feedbacks. The intent is rather to provide a general overview of key impacts and process responses. Abbreviations in the figure refer to surface water/groundwater (SW/GW) and vapor pressure deficit (VPD).

In this section, we undertake a timely and systematic review of multi-sensor remote sensing based drought studies, motivated in part by recent and rapid developments in sensing capability, as well as the significant advantages that can be gained by coupling multi-platform/multi-sensor approaches to better understand drought phenomena and impacts. For example, many government agencies have space-based Earth observation programs, including the United States National Aeronautics and Space Administration (NASA), European Space Agency (ESA) and Japan Aerospace Exploration Agency (JAXA), all of which present opportunities for coupling multi-platform/multi-sensor approaches for enhanced monitoring (McCabe et al., 2008). A recent example is the effort to develop a Harmonized Landsat and Sentinel-2 (HLS) surface reflectance dataset, which combines United States Geological Survey (USGS)/NASA Landsat with ESA Sentinel-2 to provide near-daily reflectance observations at 30-meter resolution (Claverie et al., 2018). Such multi-sensor/multi-platform integration presents a number of advantages for the remote sensing of drought compared to single sensor approaches, including:

It is well recognized that drought has complex environmental impacts and can affect numerous ecosystems components in parallel (Vicente-Serrano et al., 2019). Used in isolation, a single drought index is unlikely to capture the complexity of process interactions and diverse impacts of drought, whereas multi-sensor platforms, facilitated by multivariate retrievals, may better reflect the extent and severity of drought conditions (Hao et al., 2013b; Hao and Singh, 2015).

Current remote sensing products already make it possible to observe drought from various perspectives, including through monitoring precipitation, air and land surface

temperature, soil moisture, evaporation, total water storage and vegetation health (AghaKouchak et al., 2015b; Alizadeh et al., 2018; Pan et al., 2008). A number of remote sensing platforms provide continuous long-term drought related information for use at large scales, with an obvious example being the series of National Oceanic and Atmospheric Administration (NOAA) satellites, which have provided global coverage from the Advanced Very High Resolution Radiometer (AVHRR) from 1979 to present (Van Leeuwen et al., 2006). Such long-term coverage is only possible through multi-sensor/multi-platform data fusion.

Up until the recent addition of CubeSat constellations to our Earth observation arsenal (McCabe, Aragon, et al., 2017; Rahmat-Samii et al., 2017; Woellert et al., 2011), single satellite sensors were unable to provide real-time drought information with high spatiotemporal resolution, as traditional remote sensing approaches generally require a compromise between spatial resolution and temporal frequency (Price, 1994; Zhu et al., 2010). New systems, together with the fusion of data from different sensors and platforms, or multi-sensors from satellite constellations, can provide drought information with both high spatial and temporal resolution (Feng et al., 2006; McCabe, Rodell, et al., 2017; Pohl et al., 1998; Zhu et al., 2010), overcoming this spatiotemporal divide.

Drought studies using multiple sources of data can provide multiple lines of evidence and improve the robustness of analysis. Sensors from different instruments observe the Earth independently, thus allowing analysis from a variety of data sources that can provide cross validation and an improved representation of prediction uncertainty.

Recent advances in both new sensors and improved observational techniques, such as space-borne solar-induced chlorophyll fluorescence (SIF) (Jiao, Chang, et al., 2019; Sun et al., 2015), light detection and ranging (LiDAR) and hyperspectral sensors (Asner et al., 2016; Brodrick et al., 2019; Zhu et al., 2019) offer complementary information that can be integrated into multi-sensor drought studies to better understand the mechanisms of drought development and impacts (Aubrecht et al., 2016; Smith, Dannenberg, et al., 2019; Yang, Shi, et al., 2018; Yang, Saatchi, et al., 2018).

This section provides an overview of the role of multi-sensor remote sensing for addressing knowledge gaps and driving advances in drought studies. To this end, we provide a systematic review of multi-sensor remote sensing drought studies from a number of critical aspects, including datasets, phenomena, mechanisms, and modeling. We first present a comprehensive summary of large-scale drought-related remote sensing datasets that could be used for multi-sensor drought studies (section 2.2). We then discuss the role of multi-sensor remote sensing for characterizing important drought related mechanisms, including evaluating mechanisms of vegetation response to drought (section 2.3.1) and monitoring land-atmosphere feedbacks (section 2.3.2). We follow this with a review of the role of multi-sensor remote sensing for identifying important drought related phenomena, including drought-induced tree mortality (section 2.3.3), ecosystem fires (section 2.3.4), post-drought recovery and drought legacy effects (section 2.3.5), flash drought (section 2.3.6), and drought trends under global warming (section 2.3.7). Recent modeling advances for developing integrated multi-sensor remote sensing drought indices are reviewed in section 2.4, followed by a discussion on some of the challenges (section 2.5) and a potential road map for the future (section 2.6). In combination, we

seek to establish the important role that multi-sensor remote sensing can play in bridging spatiotemporal divides, in improving our understanding of the underlying mechanisms and processes, as well as in advancing our ability to proactively monitor and predict drought events as they occur and develop.

## 2.2 Satellite-based products for multi-sensor drought characterization

Dataset selection is fundamental to multi-sensor remote sensing of drought (Zhang, Jiao, et al., 2017). Benefitting from an increasingly wide array of available satellite-based observations, remote sensing provides a capacity to characterize drought from a range of perspectives, including precipitation, temperature, soil moisture, terrestrial water storage, evaporation, snow, vegetation response and plant function. Table 2.1 collates a comprehensive overview of datasets that could be incorporated into multi-sensor drought studies. In the following paragraphs, we use this as a basis to explore the characteristics, strengths and constraints of major drought related remote sensing datasets.

### 2.2.1 Remote sensing based precipitation

Precipitation measurements are perhaps the most fundamental element for calibrating drought models (Orville, 1990; Wilhite et al., 1985), and most certainly the principal variable in identifying and defining meteorological drought (Palmer, 1965). The challenges of single-sensor satellite precipitation data have been well recognized by the community for many years, with multi-product and multi-sensor ensembles receiving much attention over the last decade (Beck et al., 2019; Martinaitis et al., 2017; Prakash et al., 2018; Sorooshian et al., 2011; Zhang, Howard, et al., 2016). The lack of consistency between different satellite precipitation datasets – even those from the same sensors –

further complicate dataset selection (Tapiador et al., 2017). Table 2.1 identifies the commonly used large scale satellite based precipitation datasets, with each having their own spatial, temporal, and regional coverages. A series of studies have attempted to inter-compare these various precipitation datasets at regional to global scales, with most finding that multi-sensor/multi-source ensemble products provide the highest quality (Beck et al., 2020; Derin et al., 2014; Gehne et al., 2016; Sun et al., 2014; Sun, Miao, et al., 2018; Zeng et al., 2018; Zhu et al., 2015). Some recent studies have focused inter-comparisons on drought monitoring using different precipitation products (Zhong et al., 2019), with the authors highlighting the benefit of integrated precipitation data (e.g., Multi-Satellite Precipitation Analysis, TMPA 3B42V7).

### 2.2.2 Remote sensing based land surface temperature

Land surface temperature (LST) is another key parameter for integrated drought monitoring, since it provides an indirect measure of the surface energy balance (Tomlinson et al., 2011). Thermal stress (or thermal inertia), which can be obtained from land surface temperature and air temperature, has also been shown to be a good indicator of drought condition (Anderson et al., 2008; Otkin et al., 2013; Seyednasrollah et al., 2019). Drought monitoring based on thermal stress has been shown to be capable of monitoring drought at early stages (Seyednasrollah et al., 2019). The combination of LST with vegetation indicators such as NDVI, which can reflect the vegetation response to drought, provides an excellent example of multi-sensor strategies (Orhan et al., 2014; Patel et al., 2012; Son et al., 2012; Sruthi et al., 2015). The triangle space relationship between LST and vegetation index (Ts-VI) (Goward et al., 1985) has been successfully applied to study soil water content and drought monitoring (Nemani et al., 1993; Nishida

et al., 2003; Running et al., 1994). Various Ts-VI drought indices, including the Temperature–Vegetation Dryness Index (TVDI) (Sandholt et al., 2002), Vegetation Temperature Condition Index (VTCI) (McVicar et al., 2001), Microwave Temperature Vegetation Drought Index (MTVDI) (Liu, Liao, et al., 2017), and the Temperature Vegetation Precipitation Dryness Index (TVPDI) (Wei et al., 2020) have been developed to leverage this relationship. In addition, the combination of LST with other metrics (e.g. soil moisture; see section 2.2.3 ) has also been explored and shown to have potential for improved drought monitoring (Hao, Zhang, et al., 2015; Jiao, Tian, et al., 2019).

There are numerous remote sensing LST datasets from different satellite platforms that can be used for multi-sensor integrated drought monitoring (see Table 2.1). The listed datasets present different observation periods, temporal and spatial resolutions, overpass times, and accuracies, and as a result, have differing strengths. Several factors, such as difficulties in atmospheric correction and emissivity estimation, the accessibility of data or having restrictions on its use (e.g., ASTER LST and other GOES datasets) (Tomlinson et al., 2011), may have limited wider application of LST data (Gutman, 1999; Li et al., 2014). Although a number of efforts have sought to overcome these constraints (Pinheiro et al., 2004; Pouliot et al., 2009), widely used datasets (e.g., MODIS and AVHRR LST datasets) offer a compromise between regular satellite revisit time and a reasonable spatial resolution. Higher-resolution Landsat data, as well as the improved spatio-temporal insights of the exploratory ECOSTRESS mission (Fisher et al., 2020), highlight the added value of thermal data for a range of hydrological studies, including drought monitoring.

### 2.2.3 Remote sensing based soil moisture

Soil moisture is a key variable for agricultural planning and water resources management, and remote sensing based products have seen extensive application to define and identify agricultural drought (Keshavarz et al., 2014; Vicente-Serrano et al., 2019; Wang et al., 2009). Soil moisture also plays a key role in the climate system, since its deficit can trigger changes in precipitation and energy storage within the soil-vegetation-atmosphere system, resulting in local to regional scale impacts (Seneviratne et al., 2010). As such, drought detection using soil moisture data not only benefits agricultural related systems, but also broadly enhances our understanding of land-atmosphere interactions for weather and climate predictions. Remotely sensed datasets can be obtained from at least four different types of sensors, comprising optical, thermal, passive microwave and active microwave systems (Wang et al., 2009), with each type having its relative advantages and limitations. The most commonly used remote sensing based soil moisture products are listed in Table 2.1. Numerous studies have evaluated the utility of remotely sensed soil moisture products for drought characterization (Bolten et al., 2009; Martínez-Fernández et al., 2016; Nicolai-Shaw et al., 2017). However, quantitative soil moisture estimation remains difficult, especially under vegetation cover (Dorigo et al., 2017; Wang et al., 2009). Moreover, any non-linear relationship between soil moisture and drought indices makes the application of soil moisture data more complicated (Sims et al., 2002). Development of soil moisture from multi-sensor remote sensing data show clear advantages, especially in terms of developing long-term datasets. As part of the European Space Agencies (ESA) Climate Change Initiative (CCI), Gruber,

Scanlon, van der Schalie, et al. (2019) developed one of the longest temporal sequences of global soil moisture, providing the opportunity to explore a range of related process.

### 2.2.4 Remote sensing based groundwater and surface water storage

Groundwater, streamflow and surface water storage are key variables to identify and define hydrological drought (Tallaksen et al., 2004; Van Loon, 2015; West et al., 2019). Hydrological drought (i.e., deficit of groundwater and/or surface water storage) can have longer and broader impacts than meteorological and agricultural drought, particularly in terms of drinking water supply, irrigation, and even electricity production via hydropower (Van Loon, 2015). Frappart et al. (2018) presented a detailed discussion on the potential for groundwater monitoring from satellite remote sensing, highlighting the potential to measure groundwater potential, storage, and fluxes when combined with numerical modeling and ground-based measurements. A number of recent studies have illustrated that terrestrial water storage observations derived from NASA's Gravity Recovery and Climate Experiment (GRACE) satellite can provide important insights into drought behavior (Bhanja et al., 2016; Feng et al., 2013; Thomas et al., 2017). Interferometric Synthetic Aperture Radar (InSAR) sensors have also been used for groundwater and terrestrial water studies (Bell et al., 2008; Castellazzi et al., 2018; Normand et al., 2015). These systems are able to precisely determine the magnitude of surface deformation and subsidence, even under challenging atmospheric conditions, and represent a cost-efficient approach for large scale monitoring (Galloway et al., 2007). However, both GRACE and InSAR data have their limitations. The coarse spatial resolution (i.e., pixel sizes of roughly 300-400 km) and post-processing demands of GRACE, present considerable constraints (Chen et al., 2016). In addition, GRACE based

terrestrial water storage estimates were found to have larger bias in humid regions, due to large seasonal water storage changes and propagation uncertainty of signal from all hydrological processes (Shamsudduha et al., 2012). While several novel strategies have been proposed to improve the spatial resolution (Bruinsma et al., 2010; Save et al., 2012), ongoing research is needed to address the issues, including algorithmic improvements, noise reduction and signal decomposition. InSAR presents its own limitations in terms of the signal coherence in areas with dense vegetation or regions with existing surface disturbance (e.g., agricultural areas) (Castellazzi et al., 2016). Recent efforts to combine GRACE and InSAR data have illustrated the benefit of multi-sensor approaches for both resolution improvements and for necessary monitoring of groundwater depletion (Castellazzi et al., 2018).

### 2.2.5 Remote sensing based snow data

Similar to soil moisture and precipitation data, remote sensing of snow can be broadly classified into optical and microwave approaches, and those that combine the two (Frei et al., 2012). Monitoring changes in snow coverage, depth, and duration are important for characterizing drought in areas where snow provides a substantial contribution to the hydrological cycle (Chang et al., 2019; Mote et al., 2005; Pederson et al., 2011; Stewart, 2009). It is worth noting that drought events (e.g., 2014/15 drought event in the state of Washington in the United States (Fosu et al., 2016)) can occur under normal precipitation, but deficiency of the winter snowpack. Deficit of snow cover in winter can cause severe hydrological and agricultural drought in summer, making the incorporation of snow cover information into integrated drought monitoring an important task (Hamlet et al., 2005; Kalra et al., 2008; Margulis et al., 2016). Drought indices

accounting for snow (e.g., Standardized Snow Melt and Rain Index (SMRI) (Staudinger et al., 2014)) have been shown to provide enhancements relative to traditional meteorological drought indices. Snowpack data has also been used in combination with soil moisture information to show improved indicators for drought estimation and disaster risk prediction (Kumar et al., 2014; Tachiiri et al., 2008). It is also important to note that global warming causes changes of snowpack in many regions and changes the sensitivity of snowpack to climate (Flanner et al., 2006; Mote et al., 2005; Stewart, 2009), so incorporating snow data into drought studies is likely to be an aspect of increasing importance.

### 2.2.6 Remote sensing based evaporation

Given its central role as a linking mechanism between the water and energy cycles, evaporation presents as an important metric for drought monitoring and estimation. Determining evaporation dynamics from satellite observations is complicated, since it is not directly observable from any sensor, but rather inferred through combining meteorological, radiation, vegetation and other data with an interpretive model. Evaporation also represents the integration of a range of water loss processes, from direct soil and canopy evaporation, as well as the transpiration deriving from plants, making its accurate modeling a challenging task (Anderson, Kustas, et al., 2011; Mu et al., 2011; Su et al., 2005). Numerous models and algorithms have been developed to infer evaporation from remote sensing observations, and the readers are referred to some of the extensive reviews undertaken by Kustas et al. (1996), Kalma et al. (2008), Li et al. (2009), Wang and Dickinson (2012) and Fisher et al. (2017) for further details. Drought monitoring studies have used evaporation as a parameter to develop drought indices, with the most

recognized being the Palmer Drought Severity Index (PDSI) (Palmer, 1965), Standardized Precipitation Evapotranspiration Index (SPEI) (Vicente-Serrano et al., 2010) and the Evaporative Stress Index (ESI) (Anderson, Hain, et al., 2011; Anderson et al., 2016). However, most of the commonly used long-term ET based drought monitoring indices are derived from coarse spatial resolution (e.g., 0.5$^{o}$ grid cell size for SPEI, 2.5$^{o}$ grid cell size for PDSI) with monthly temporal resolution, which limit their applicability for drought monitoring. Given the important role that evaporation plays, not just in drought studies, but also in monitoring ecosystem function, understanding water and carbon cycles (Wilkinson et al., 2020), and food and water security studies (López Valencia et al., 2020), the need for ongoing and improved satellite missions dedicated to its measurement is a critical requirement (Fisher et al., 2017; Wang, D'Odorico, et al., 2012a). Efforts exploring the recently commissioned ECOsystem Spaceborne Thermal Radiometer Experiment on Space Station (ECOSTRESS) (Fisher et al., 2020) provide an example of current capabilities for multi-sensor high spatiotemporal observations of evaporation. Future multi-instrument satellite systems, such as the Hyperspectral Infrared Imager mission (HyspIRI), may provide the combination of spectral, spatial and temporal resolution needed for global evaporation derivation (Lee et al., 2015).

### 2.2.7 Remote sensing based vegetation vigor

Vegetation plays the most active role in modulating the water and carbon cycles of most ecosystems (Jasechko et al., 2013; Lanning et al., 2019; Lanning et al., 2020; Wang, Good, et al., 2014). Plants respond quickly and dynamically to hydrologic stress and control the land-atmosphere exchanges of water and energy (Novick et al., 2016). Over the past few decades, remote sensing based vegetation observations have explored

the optical and microwave domains of the electromagnetic spectrum, with a large number of available multi- and hyperspectral sensors at ground-, air- and space-borne level. An historical overview of vegetation estimation based on leaf spectral properties can go back to the 1970s (Ryu et al., 2019). With the launch of Landsat in 1972, pioneering studies sought to explore drought impacts on vegetation growth at the landscape to regional scales (e.g., Thompson et al. (1977); Short (1976). The launch of active and passive microwave and hyperspectral sensors (e.g., Hyperion data from Earth Observing-1 (EO-1) satellite, launched November 21, 2000), provided further data to study drought impacts on vegetation beyond more traditional observations from broad-band optical sensors. In more recent times, active light detection and ranging (LiDAR), especially in combination with Unmanned Aerial System (UAS) platforms (Sankey et al., 2018) have dramatically expanded the fine-scale application of remote sensing vegetation monitoring (Xue et al., 2017).

Vegetation indices are the primary approach towards monitoring vegetation greenness, with changes in the spectral characteristics of plant leaves and canopy being used to provide insights into health and condition (Bannari et al., 1995; Zargar et al., 2011). One of the most widely used remote sensing based vegetation indices is the Normalized Difference Vegetation Index (NDVI) (Rouse, Haas, Schell and Deering, 1974). However, as with many such indices, NDVI has a range of limitations related to its sensitivity to background factors, such as shading and soil brightness, atmospheric effects, as well as saturation issues (Huete, 1988; Richardson et al., 1990). A suite of other NDVI type indices were subsequently developed in an attempt to improve such limitations, or to provide a more focused retrieval of plant physiological features. For

example, the Soil-Adjusted Vegetation Index (SAVI) (Huete, 1988), modified SAVI (MSAVI) (Qi et al., 1994), or the Global Environment Monitoring Index (GEMI) (Xue et al., 2017) were all developed to eliminate the soil background effect of vegetation indices, while the enhanced vegetation index (EVI) was developed to simultaneously correct soil and atmospheric effects (Huete et al., 2002). More recently, Badgley et al. (2017) developed near-infrared reflectance of vegetation ($NIR_V$) with the aim of minimizing both the effects of soil contamination and variable viewing geometry from satellite observations.

While broad-band based indices have provided numerous opportunities for vegetation sensing, hyperspectral sensors can provide an order of magnitude increase in spectral information relative to multispectral systems. Hyperspectral reflectance derived indices such as the Photochemical Reflectance Index (PRI) (Thenot et al., 2002) or the MERIS terrestrial chlorophyll index (MTCI) (Dash et al., 2007), were shown to have good performance in monitoring early plant water stress by reflecting drought-induced vegetation physiological and biochemical processes change (He et al., 2016; Suárez et al., 2008).

The main advantage of microwave sensors is that they have higher penetration ability and are less affected by weather and atmospheric influences. While the value of microwave remote sensing has been well detailed in the context of oceanographic applications and soil moisture estimation, an increasing number of recent studies have explored its sensitivity to plant water content (Konings et al., 2019; Liu et al., 2011), particularly via examination of the vegetation optical depth (VOD). However, the drawbacks of passive microwave observations include the relatively low spatial

resolution and the sensitivity to both temperature and single-scattering albedo, which can affect the derivation of VOD accuracy (Vreugdenhil et al., 2019).

Besides vegetation indices, other variables that are more directly linked to vegetation photosynthesis have been used to estimate drought impacts. Vegetation Gross Primary Productivity (GPP) is one of the most commonly used photosynthesis proxies that can be employed to infer drought impact and prediction (Meng et al., 2014; Zhao et al., 2010). Current satellite GPP can be generally estimated from four types of modeling: process-based model (Farquhar et al., 1980), light use efficiency (LUE) models (Zhao et al., 2005), machine learning techniques based on eddy covariance measurements (Tramontana et al., 2016), and solar induced chlorophyll fluorescence (SIF) based statistical model (Guanter et al., 2014a). However, there remain considerable uncertainties in using GPP datasets for drought studies. For example, Stocker et al. (2019) found that satellite GPP data underestimated the drought impact on terrestrial primary production due to the lack of consideration of soil moisture information. Studies also indicate the divergent ability of reflecting drought impact among different GPP models and products (Chang et al., 2020; Li and Xiao, 2020). Remote sensing based solar induced chlorophyll fluorescence (SIF) is a rapidly advancing research front in studies of global vegetation (Guan et al., 2016; Guanter et al., 2007; Joiner et al., 2013), with recent research indicating its potential to monitor the drought impact on vegetation dynamics (Jiao, Chang, et al., 2019; Sun et al., 2015; Yoshida et al., 2015). Although there have yet to be any satellites specifically designed to measure SIF, the planned FLuorescence EXplorer (FLEX) (scheduled to launch in 2022) will be the first (Mohammed et al., 2019). Remote sensing based SIF retrieval mechanisms have been studied for decades,

with detailed reviews provided by Mohammed et al. (2019), Ni et al. (2019), Aasen et al. (2019), and Bandopadhyay et al. (2020). Several satellite-based SIF datasets have been compiled from other satellite missions and directed towards the study of drought. SIF products derived from the Greenhouse gases Observing Satellite (GOSAT) provided regional to global scale availability (Frankenberg et al., 2011; Joiner et al., 2011). Datasets from other satellite sensors such as the SCanning Imaging Absorption spectroMeter for Atmospheric CartograpHY (SCIAMACHY) (Joiner et al., 2012), the Global Monitoring Ozone Experiment 2 (GOME-2) (Joiner et al., 2013), Orbiting Carbon Observatory-2 (OCO-2) (Sun, Frankenberg, et al., 2018; Taylor et al., 2020), the TROPOspheric Monitoring Instrument (TROPOMI) (Köhler et al., 2018), and Orbiting Carbon Observatory-3 (OCO-3) (Taylor et al., 2020) have also provided global SIF retrievals. The use of recent TROPOMI observations for providing relatively high spatiotemporal resolutions revolutionized satellite-based SIF application for drought studies (Köhler et al., 2018). However, current SIF data also have a number of limitations, including noise from clouds and aerosols, coarse spatial resolution and sensor degradation (Mohammed et al., 2019), all of which may introduce uncertainties for drought study. Despite such uncertainties, SIF presents several key advantages over other vegetation proxies and may provide an alternative perspective to study the impact of drought on vegetation photosynthesis. Indeed, SIF has been shown to track the seasonality of photosynthesis and be more consistent with site-observed GPP variability than vegetation indices such as EVI and photochemical reflectivity index (PRI) (Magney et al., 2019; Smith et al., 2018; Verma et al., 2017). Incorporating satellite SIF could also improve global estimates of important plant traits, such as GPP and photosynthetic

capacity (He et al., 2019; Smith et al., 2018; Zuromski et al., 2018). Recent studies have indicated that SIF is more sensitive to drought related water and heat stress than greenness indices (Qiu et al., 2020; Song et al., 2018a), highlighting this potential.

Table 2.1: Summary of major drought related satellite products that can be incorporated into integrated drought characterization.

| | Data | Temporal resolution | Spatial resolution | Coverage | Data period | References |
|---|---|---|---|---|---|---|
| Precipitation | CPC-Global | Daily | 0.5° | Global | 2006-present | (Xie et al., 2010) |
| | GPCP | Daily/Monthly | 1°/2.5° | Global | 1979-present | (Adler et al., 2003) |
| | GPM | 30 min/3h/Daily | 0.1° | 60°S-60°N | 2015-present | (Hou et al., 2008; Hou et al., 2014) |
| | GSMaP | 1h/Daily/Monthly | 0.1° | 60°S-60°N | 2002-2012 | (Kubota et al., 2007) |
| | CMAP | Monthly | 2.5° | Global | 1979-present | (Xie et al., 1997; Xie et al., 2007) |
| | TRMM | 3h/Daily/Monthly | 0.25°/0.5° | 50°S-50°N | 1998-2015 | (Huffman et al., 2007) |
| | PERSIANN-CCS | 30 min/3h/6h | 0.04° | 60°S-60°N | 2003-present | (Sorooshian et al., 2000) |
| | PERSIANN-CDR | 3h/6h/Daily | 0.25° | 60°S-60°N | 1983-present | (Ashouri et al., 2015) |
| Land Surface Temperature | Landsat | 16 days | 60 m | Global | 1999-present | (Sobrino et al., 2004) |

| | | | | | | |
|---|---|---|---|---|---|---|
| | MODIS | Twice daily | 0.01° | Global | 2000-present | (Wan et al., 1997; Wan, 2008) |
| | ASTER | Twice daily | 90 m | Global | 1999-present | (Jiménez-Muñoz et al., 2009) |
| | AVHRR | Twice daily | ~1.1 km | Global | 1978-present | (Kerr et al., 1992) |
| | AATSR | 35 days | ~1 km | Global | 2004-present | (Prata, 2002) |
| Soil Moisture | AMSR-E | Daily | 25 km | Global | 2002-2011 | (Paloscia et al., 2006) |
| | AMSR2 | Daily | 25 km | Global | 2012-present | (Kim et al., 2015) |
| | SSM/I | Daily | 25 km | Global | 1987-present | (Paloscia et al., 2001) |
| | ASCAT | 3 Days | 12.5/25 km | Global | 2007-present | (Brocca et al., 2011) |
| | SMAP | 2-3 Days | 3 /9 /36 km | Global | 2015-present | (Das et al., 2010) |
| | SMOS | 2-3 days | 35 km | Global | 2010-present | (Kerr et al., 2012) |
| Groundwater/Surface water storage | GRACE | Monthly | 220 km | Global | 2002-present | (Ruzmaikin et al., 2014) |
| | GRACE-FO | Monthly | 180 km | Global | 2017-present | (Flechtner et al., 2016) |
| Snow | MODIS | 5 min/Daily/8 days/Monthly | 1 km | Global | 2000-present | (Hall et al., 2002) |

| | | | | | | |
|---|---|---|---|---|---|---|
| | IMS | Daily | 1 km /4 km/24 km | 0-90°N | 1997-present | (Helfrich et al., 2007) |
| | CMC | Daily | 24 km | 0-90°N | 1998-present | (Brown et al., 2003) |
| | AMSR-E | Daily/5 days | 25 km | Global | 2002-2011 | (Chang et al., 2000) |
| | SSM/I | Daily | 25 km | Global | 1978-present | (Pulliainen et al., 2001) |
| | AMSR2 | Daily | 25 km | Global | 2012-present | (Kim et al., 2015) |
| Evapotranspiration | MODIS | 8 Days | 500 m | Global | 2000-present | (Mu et al., 2011) |
| | GLEAM | Daily | 0.25° | Global | 1980-2018 | (Miralles et al., 2011) |
| | GLDAS | 3 h/month | 1° | Global | 1979-2016 | (Liu, Wang, et al., 2016) |
| | METRIC | 16 days | 30 m | Global | 2011-present | (Allen et al., 2007) |
| Vegetation vigor | AVHRR NDVI/EVI | bi-week | 0.083° | Global | 1982-present | (Tucker et al., 2005) |
| | MODIS NDVI/EVI | 8 Days/Monthly | 500 m | Global | 2000-present | (Beck et al., 2006) |
| | Landsat NDVI | 16 days | 30 m | Global | 1972-present | (Beck et al., 2011) |
| | MODIS LAI | 8 days | 500 m | Global | 2000-present | (Myneni et al., 2002) |
| | SMOS VOD | Daily | ~40 km | Global | 2009-present | (Vittucci et al., 2016) |

| | | | | | |
|---|---|---|---|---|---|
| GOME-2 SIF | Daily | 0.5° | Global | 2007-present | (Joiner et al., 2011) |
| TROPOMI SIF | Daily | 7 km×3.5 km | Global | 2017-present | (Köhler et al., 2018) |
| OCO-2 SIF | Daily | 2.25 km × 1.29 km | Global | 2014-present | (Frankenberg et al., 2014; Sun et al., 2017) |
| SCIAMACHY SIF | Daily/Monthly | 1.5°/1° | Global | 2002-2012 | (Köhler et al., 2014) |
| MODIS GPP/NPP | 8 days | 500 m | Global | 2000-present | (Zhao et al., 2005) |

### 2.3. The role of multi-sensor remote sensing for drought related phenomena and mechanisms

Drought can substantially impact global and regional carbon cycling and cause irreversible damage to ecosystem function in a warming climate (Anderegg, 2015; Dai, 2011; Garcia et al., 2014; Hao et al., 2017b; Seddon et al., 2016; Sippel et al., 2018; Willis et al., 2018). Recent research suggests that drought associated with extreme high temperatures are leading to negative impacts on carbon uptake, slowing down carbon dioxide and nitrogen fertilization effects on terrestrial ecosystem vegetation (Peñuelas et al., 2017). In addition, drought has been reported to have increasing impacts on ecosystem carbon uptake. In a related study, Yuan, Zheng, et al. (2019) indicated an increasing impact of drought related vapor pressure deficit on vegetation growth over the past three decades. However, drought impact on ecosystems is complex and many uncertainties and questions remain unresolved (Trnka et al., 2018). Due to the complexity of drought interactions within ecosystems, single sensor remote sensing observation are

unlikely to provide a comprehensive and convincing accounting of their characterization. On the other hand, multi-sensor based evaluations can offer deeper insights across a range of drought-related research. For instance, multi-sensor based evaluations can improve the understanding of drought related phenomena such as drought-induced tree mortality, drought-related ecosystem fire, and developing trends under climate change. Multi-sensor based evaluations can also enhance the understanding of drought related mechanisms, including those behind vegetation response and land-atmospheric feedbacks during drought. Here we provide a review of these research aspects as well as identify some of the current gaps in drought research that could benefit from multi-sensor observations.

### 2.3.1 Monitoring mechanisms of vegetation response to drought using remote sensing

Drought can have a direct impact on the terrestrial carbon sink, with vegetation response being a key indicator of this influence (Piao et al., 2019). Drought impact on the terrestrial carbon cycle has been evaluated using remote sensing observations (AghaKouchak et al., 2015b), with decreases in vegetation productivity acting to reduce $CO_2$ uptake (Chen, Van der Werf, et al., 2013; Ciais et al., 2005b; Donohue, Petchey, et al., 2013). However, vegetation response to drought can vary considerably, both physiologically and structurally across leaf to canopy levels, let alone for different biome types and species (Zhang, Peng, et al., 2013). The structural and physiological responses of plants to droughts are not well understood at large scales (Van der Molen, Dolman, Ciais, Eglin, Gobron, Law, Meir, Peters, Phillips, Reichstein, et al., 2011). Physiological responses vary depending on the photosynthesis related enzymatic activities and stomatal

closure, which act to prevent water loss (Chang et al., 2020; Meir et al., 2008a; Meir et al., 2010). Two contrasting stomatal closure strategies for water use under drought have been identified: isohydric, where species decrease stomatal conductance to prevent reducing leaf water potential; and anisohydric, where species exert little or no stomatal control in response to drought (Klein, 2014; Lanning et al., 2020; Roman et al., 2015). Due to the different stomatal closure strategies under drought, isohydric species are generally expected to experience a larger reduction of short-term gross primary productivity (GPP) than anisohydric species (Van der Molen, Dolman, Ciais, Eglin, Gobron, Law, Meir, Peters, Phillips, Reichstein, et al., 2011). A recent multi-sensor approach by Hwang et al. (2017) indicated that photochemical reflectance index (PRI), derived from Moderate Resolution Imaging Spectroradiometer (MODIS) observations and field spectroradiometer data, can capture the divergent isohydric and anisohydric behavior under drought stress at both leaf and canopy scales, from sunlit and shaded portions of the canopy. Their study provided a theoretical framework for observing the vegetation physiological response to drought at large scales. GPP reduction caused by drought can also be determined from structural changes in the vegetation canopy (Van der Molen, Dolman, Ciais, Eglin, Gobron, Law, Meir, Peters, Phillips, Reichstein, et al., 2011).

Structural change under drought stress can include reductions in leaf area, leaf shed, and the alteration of leaf angle distribution within the canopy (Kull et al., 1999). Such change has often been inferred via remote sensing based leaf area index (LAI) measurements (Zhang, Peng, et al., 2013). However, accurate LAI estimation at regional to global scales remains a longstanding challenge (Richardson et al., 2009). Remote

sensing of LAI can be determined from passive optical sensors, microwave sensors, and active light detection and ranging (LiDAR) instruments, with each method having its relative strengths and limitations (Fang et al., 2019; Zheng et al., 2009). For example, passive optical sensors can provide multispectral imagery, which is beneficial to object discrimination (Chen et al., 2004). However, passive optical sensor based LAI estimations can be affected by multiple factors, such as saturation of vegetation index based derivation of LAI, sensor degradation, mitigating leaf pigment effects, and atmospheric contaminations (Xie et al., 2018; Yan et al., 2019). Microwave based LAI estimation has the potential to overcome the impacts from cloud and other atmospheric influences (Fang et al., 2019). However, few microwave based LAI estimations are based on radar physical models, and the accuracy of large regional scale microwave based LAI retrievals need further evaluations (Fang et al., 2019; Tao et al., 2016). LiDAR based LAI can be estimated by separating canopy woody and foliage components (Zhao et al., 2011). In addition, LiDAR observations are have the potential to characterize the vertical vegetation structure at different heights, and provide accurate three-dimensional (3D) point cloud data (Liu, Baret, et al., 2017). Such data provides new opportunities for detailed assessments of drought impact on canopy structure. For example, a recent study by Smith, Stark, et al. (2019) indicated that LiDAR showed great potential in capturing canopy structural heterogeneity in response to drought and seasonality. However, limitations such as the uncertainty of LiDAR based LAI estimation models, and the issue of converting effective LAI ($LAI_{eff}$) to LAI can also hamper the applications of LiDAR based LAI. (Fang et al., 2019). More generally, the combined use of multi-sensor information from LiDAR and optical observation (Ma et al., 2014), tend to show capacity

for a more comprehensive description of the biophysical characteristics of forest ecosystems, making for a promising opportunity for further exploration in multi-senor drought studies. Besides remote sensing LAI data, multi-angle reflectance based observations have been linked to canopy structure characteristics such as canopy roughness (Strahler, 1997), foliage clumping (Chen et al., 2005), and leaf angle distribution (Roujean et al., 2002). Recent multi-angle approaches such as MODIS derived Multi-Angle Implementation of Atmospheric Correction (MAIAC) has identified anomalies in Amazon forest canopy structure under drought (De Moura et al., 2015).

Species composition could change in response to drought, and multi-sensor based evaluations have the capacity to capture such changes. Recent studies indicate that ecosystems tend to change species composition towards deeper rooted varieties in order to stabilize ecosystem primary production under drying conditions (Griffin-Nolan et al., 2019; Liu, Mi, et al., 2018; Luo et al., 2019). Ecosystem with more species exhibiting lower productivity declines during droughts, tend to recover faster after extreme droughts (Anderegg et al., 2018; Anderegg et al., 2019). The reason is that different species can have different drought tolerances, and although some species may die during prolonged droughts, other species are able to persist. For example, Coates et al. (2015) used hyperspectral and thermal observations to study the impacts of the 2013-2014 drought on Southern California chaparral species and established that Ceanothus were the least well-adapted species, while deeply rooted species were the least impacted.

Drought impacts on an ecosystems carbon cycle can be examined via multi-sensor observations of vegetation greenness and other biophysical variables. Due to the complexity of drought response and the inherent uncertainties in any single remote

sensing product, attempting to answer the same question using different remote sensing observations and platforms has the potential to produce conflicting (and sometime erroneous) conclusions. For example, a number of early studies exploring the impacts of the 2005 Amazon drought used observed LAI and spectral reflectance data in the near infrared region (NIR) to suggest that severe drought caused reductions in LAI and carbon storage (Brando et al., 2008). Another study based on MODIS EVI proposed a finding that the Amazon forest showed a greening-up, even during a severe drought, and indicated that Amazon forests might be more resilient to severe drought than previously thought (Saleska et al., 2007). However, a later study by Samanta et al. (2010) indicated that Amazon forests did not green up during 2005 drought. In another later study exploring the Amazon's response to drought, Liu, van Dijk, et al. (2018) used AMSR-E derived vegetation optical depth (VOD), MODIS based LAI, EVI, aerosol optical depth (AOD) and cloud optical thickness (COT), CERES derived photosynthetically active radiation (PAR), GRACE based terrestrial water storage (TWS), and AIRS based surface skin temperature, air temperature and relative humidity data. Multiple lines of evidence from the change of VOD, LAI, and EVI indicated that during the early drought stage, sufficient soil moisture enhanced leaf development and ecosystem photosynthesis, while prolonged intense drought in the dry season negatively impacted forest growth (Liu, van Dijk, et al., 2018). The divergent results highlight the challenges in using single sensor observations that cannot always resolve the inherent uncertainties of complex interactions (Asner et al., 2010) and the importance of exploiting multiple lines of evidence.

Indeed, multi-sensor observation strategies allow for the introduction of alternative and complementary sources of information to help disentangle complex

phenomena. For example, SIF has been used to provide insight beyond more standard greenness approaches, with a number of studies exploring its potential for drought impact monitoring (Sun et al., 2015; Yoshida et al., 2015). Other studies have evaluated the SIF sensitivity to drought under various conditions. For example, Liu, Yang, Zhou, Liu, Zhou, Li, Yang, Han, et al. (2018) showed that SIF is better than NDVI for early drought detection, although NDVI remains useful in reflecting long lasting droughts. Multi-sensor observations have also been used to examine drought impact on carbon uptake. Wigneron et al. (2020) used MODIS based EVI and GOME-2 based SIF data to test the robustness of spatial patterns of anomalies in aboveground biomass carbon (AGC) to indicate that tropical forests did not recover from the 2015–2016 El Niño event. Other studies have employed multi-platform and multi-sensor approaches. For example, Zhou et al. (2014) conducted a comprehensive evaluation of the impacts of chronic drought on the Congo rainforest, using multi-sensor satellite products of EVI, VOD, backscatter anomaly, photosynthetically active radiation (PAR), terrestrial water storage (TWS), aerosol optical thickness (AOD), cloud optical thickness (COT), and land surface temperature (LST) to show the widespread decline of Congo rainforest greenness due to the long-term drying trend over the past decade. In another case, Wang, Kessner, et al. (2016) used MODIS LST, NDVI, fire count, fire radiative power, fire density, atmospheric water vapor, cloud fraction, and TRMM accumulated rainfall to study the characteristics of the 2012 Central Plains drought. Li, Li, et al. (2019) used MODIS NDVI, EVI, and GIMMS NDVI3g to provide robust analysis of the impact of the 2009/2010 South China drought on vegetation growth and terrestrial carbon balance. Park et al. (2020) used multi-sensor based Scaled Drought Condition Index (SDCI) and Evaporative Stress Index (ESI) to

explore the influence of El Nino-Southern Oscillation (ENSO) on East African drought during rainy seasons. More recently, a study from Jiao et al. (2020) used multiple sensors to examine the drought responses of biophysical variables including fraction of absorbed photosynthetic active radiation (fPAR), canopy density, photosynthetic vegetation cover, and aboveground biomass carbon, with all showing increased sensitivity during Australia's millennium drought.

### 2.3.2 Monitoring land-atmospheric feedbacks mechanisms

Land–atmospheric feedbacks play an important role in water and carbon cycles during droughts (Baldocchi et al., 2001; Roundy et al., 2017). It is generally acknowledged that severe droughts dry out soils and vegetation and reduce land evaporation, hence making the near-surface air even drier, which may in turn decrease the likelihood of rainfall and further exacerbate the occurrence of droughts (Roundy et al., 2014; Seneviratne et al., 2010; Zaitchik et al., 2013). However, our knowledge of how droughts start and evolve, and how climate change will affect their occurrence, remains incomplete (Miralles et al., 2019). There has been a strong focus on climate modeling of large scale land–atmospheric feedback during droughts over the last decade (Fischer et al., 2007; Stegehuis et al., 2015). One particular challenge of these studies is the degree of variability in modeling the strength of the land-atmosphere coupling, which has a strong impact on accurately forecasting and predicting climate extremes such as drought. Multi-sensor remote sensing provides large-scale observational variables and parameters for land–atmospheric feedbacks that can be used to reduce such uncertainties. For example, evaporation is a key linking mechanism in land–atmosphere feedback studies and is a direct modulator of climates trends and hydro-meteorological extremes through a

series of feedbacks acting on air temperature, precipitation, cloud cover, and photosynthesis (Douville et al., 2013; Miralles et al., 2014; Seneviratne et al., 2006; Teuling et al., 2010). To date, global climate model based land evaporation estimates remain unreliable (Dolman et al., 2014; Jimenez et al., 2011; Mueller et al., 2011; Wang and Dickinson, 2012), making their use as diagnostic tools challenging. On the other hand, multi-sensor based remote sensing approaches have been applied to provide more realistic observationally-based estimates of evaporation (Martens et al., 2017), offering the capacity for new insights into land-atmosphere behavior. A number of recent efforts have evaluated multi-sensor remote sensing data in land-atmosphere coupling studies exploring drought, and illustrated their considerable advantages (Hao, Singh and Xia, 2018; Roundy et al., 2017; Santanello Jr et al., 2018). Further work is required, but with the advent of an increasing number of sensors and complementary platforms, additional insights and clearer identification of patterns and trends in land–atmospheric feedbacks during droughts are anticipated.

### 2.3.3 Exploring drought-induced tree mortality

Severe drought acts not only to reduce vegetation productivity, but may also cause large-scale plant mortality (Allen et al., 2015). Myriad studies on the mechanisms of plant response to drought may not necessarily involve drought-induced tree mortality, which can also lead to ecosystem recession and impact ecosystem water and carbon cycles (Huang et al., 2019; Piao et al., 2019). Hydraulic failure and carbon starvation have been widely reported as two nonexclusive mechanisms of drought-induced tree mortality (Anderegg et al., 2012; Hartmann, 2015; McDowell et al., 2018). Hydraulic failure occurs when drought-caused embolisms block xylem cells and impair hydraulic

transport systems (Huang et al., 2019). Carbon starvation occurs when isohydric species close stomata to avoid excessive water loss. However, the closure of stomata not only avoids water loss, but also forgoes access to atmospheric carbon dioxide, and if respiratory consumption of the needed carbon exceeds stored resources, tree mortality may occur (Adams et al., 2010). One of the main approaches for studying drought-induced tree mortality is to estimate the plant water content (Huang et al., 2019; McDowell et al., 2010). Historically, satellite multispectral sensors were used to extract vegetation water status (Kokaly et al., 2009; Zarco-Tejada et al., 2003). However, it is challenging to accurately extract canopy water content for forest regions via traditional remote sensing observations, due to the cloud cover and the fact that those observations primarily sense the top of the canopy only (Asner et al., 2004; Konings et al., 2019). New large-scale datasets such as satellite-based VOD are emerging (Rao et al., 2019) and can be used as indicators of drought-induced tree mortality. Currently, high spatial resolution images are the most commonly used datasets to monitor regional forest health (Huang et al., 2019). Recent integrations of multi-sensor airborne hyperspectral and LiDAR have shown potential to provide accurate estimation of leaf water content at regional scales. Stovall et al. (2019) combined airborne LiDAR and optical data to track tree mortality rates and indicated that higher trees are more vulnerable than small trees during extreme droughts. Zhu et al. (2019) combined LiDAR and hyperspectral data using radiative transfer models (RTM) and an invertible forest reflectance model to address the effects of canopy structure variation, and to estimate leaf water content over the Bavarian Forest National Park in southeastern Germany. Related studies show that the integrated use of airborne high-fidelity imaging spectroscopy (HiFIS) and LiDAR scanning improves the

ability for monitoring forest canopy water content (Shugart et al., 2015). The integrated application of HiFIS and LiDAR provides three dimensional forest measurements and allows for excluding non-forest covers, such as grass, bare ground and rock cover, which could affect the analysis (Asner et al., 2007). Recently, Asner et al. (2016) provided a multi-sensor remote sensing canopy water content observation strategy by fusing HiFIS and LiDAR with Landsat data, and illustrated a progressive canopy water loss across California forests during 2012-2015 that allowed improved predictions of tree mortality. Research from Brodrick et al. (2017) used a similar strategy to monitor progressive canopy water content loss to tree mortality during the 2015-2016 Sierra Nevada mountain drought in California. The NASA Global Ecosystem Dynamics Investigation (GEDI) LiDAR, which launched to the International Space Station in December 2018 and has been collecting observation data since March 2019 (Hancock et al., 2019), serves as an exploratory mission to study tree mortality from canopy structure measurements (Qi et al., 2019). The combination of simulated GEDI with other measurements such as TerraSAR-X add-on for Digital Elevation Measurement (Tandem-X) InSAR (Lee et al., 2018; Qi et al., 2016) and Ice, cloud, and land elevation satellite-2 (ICESat-2) and NASA-ISRO Synthetic Aperture Radar (NISAR) (Fatoyinbo et al., 2017; Silva et al., 2018) highlights the potential of mapping tree health from a forest structure perspective.

### 2.3.4 Investigating drought-related ecosystem fires

Drought may cause an increase in the frequency of ecosystem fires, which is an important factor in the decline of ecosystem carbon uptake (Brando et al., 2014). Remote sensing may be the only technology that can provide for drought-induced wildfire observations at regional to global scales. Thermal remote sensing has been widely used to

establish the location of active fires (Asner et al., 2010). However, due to the spatial resolution and observation period, it is challenging for single sensor based remote sensing observations to provide long time period and accurate detection, and thus integrated use of multi-sensor remote sensing observations has often been applied to improve long-term fire detection. Van Der Werf et al. (2004) combined multi-sensor satellite observations of global fire activity over the 1997 to 2001 El Niño/La Niña period from TRMM, European Remote Sensing Satellite–Along Track Scanning Radiometer (ERS-ATSR), and MODIS Terra satellite sensors, showing increases in tropical fires during droughts associated with ENSO. For datasets related to global fires, the widely used Global Fire Emissions Database (GFED) was developed based on the integrated use of fire products from Terra and Aqua MODIS and the ATSR-based World Fire Atlas, to provide global daily, monthly, and annual burned area from 1995 onwards (Giglio et al., 2013). A particular challenge for single sensor observations for drought-induced fire studies is to detect ground-covering fires from space, since a moist and highly foliated canopy could block the fire signal on the ground (Goetz et al., 2006; Meng et al., 2017; Yi et al., 2013). Integrated use of multi-sensor satellite products by overlying fire detections (e.g., TRMM fire detections) on satellite deforestation maps (e.g., multi-sensor remote sensing based Brazilian National Institute of Space Research, INPE deforestation map) was shown to provide good indications for detecting ground-covering fire signals above the moist and highly foliated canopy (Asner et al., 2005; Asner et al., 2010). In addition, the integrated use of multi-sensor observations from airborne imaging spectroscopy and LiDAR was tested to quantify the post-fire forest recovery rate and demonstrated that integrated multi-sensor observation can separate canopy recovery from understory recovery,

providing reliable information of post-fire forest recovery over large scales (Meng et al., 2018). Apart from reliable detection of burned areas, satellite estimation of fire-induced CO and $CO_2$ emission measurements are useful for understanding the impact of drought-induced wildfire to ecosystem carbon and water cycles. The combination of satellite-derived burned areas with atmospheric CO and $CO_2$ measurements is likely to assist in quantitatively estimating the impact of drought-induced fires on ecosystem carbon cycle (Piao et al., 2019).

Live fuel moisture content (LFMC), which is defined as the mass of water contained within vegetation in relation to the total dry mass, is another primary variable that has been widely used in drought-related fire prediction and fire risk models (Yebra et al., 2013). Remote sensing observations could provide the opportunity of frequent monitoring of LFMC over large areas. However, there are a number of challenges for existing estimations of LFMC from remote sensing, with the retrieval of LFMC influenced by multiple factors. The physical basis for remote sensing based estimation of LFMC is via the different absorption and reflectance of radiation in NIR and SWIR spectral regions due to water content within vegetation (Tucker, 1980). As such, traditional indices such as the Normalized Difference Infrared Index (NDII) (Hardisky et al., 1983), Normalized Difference Water Index (NDWI) (Gao, 1996), and Normalized Difference Vegetation Index (NDVI) (Rouse, Haas, Schell and Deering, 1974) have all been applied to estimate the LFMC over large regions. Indices based on the optical and thermal bands provide important information on LFMC estimation via vegetation vigor and water content. However, observations from optical regions are limited in their ability to provide accurate estimation of LFMC. First, the optical and thermal wavelengths are

affected by contamination such as clouds, smoke, and atmospheric aerosols. In addition, remote sensing based retrieval of LFMC are affected by confounding factors such as canopy structure and biomass (Yebra et al., 2013). Apart from observations across optical wavelengths, signals from the microwave portion of the electromagnetic spectrum have been explored as alternatives for monitoring LFMC (Fan et al., 2018) due to the advantage that they can detect changes in canopy structure, biomass, soil and vegetation water content, while being less sensitive to atmospheric and cloud contamination (Al-Yaari et al., 2016). As such, exploiting multi-sensor remote sensing to estimate LFMC can offer multiple advantages. First, the multi-sensor approach can provide insights into the many complementary sensitives to needed parameters (such as vegetation water content, greenness, canopy structure) required by LFMC retrievals. Second, multi-sensor observations alleviate individual limitations from any specific sensor. Third, multi-sensor observations can provide high temporal and spatial LFMC estimations needed for fire risk and prediction. One recent example of multi-sensor remote sensing based LFMC estimation is the study of Rao et al. (2020), which presents an improved LFMC estimation every 15 days at 250 m resolution.

### 2.3.5 Identifying post-drought recovery and drought legacy effects

Drought extremes not only have immediate impacts on ecosystem functioning, but can also impart long-lasting lagged effects, hindering a comprehensive understanding of terrestrial ecosystem response to drought (Anderegg et al., 2015). Our understanding of drought legacy is challenged by the fact that such effects can be highly variable for species, ecosystems, climate conditions, and can even have both positive or negative impacts on plants (Kannenberg et al., 2020; Wu et al., 2018; Xu et al., 2010). A number

of recent studies have examined drought recovery and legacy effects from organism to ecosystem scales based on tree ring chronologies, flux towers, and remote sensing datasets (Kannenberg et al., 2020). Compared with flux towers and tree ring observations, remote sensing has been widely used for drought recovery and legacy effects at both ecosystem and global scales due to the large spatial support scales (Schwalm, Anderegg, Michalak, Fisher, Biondi, Koch, Litvak, Ogle, Shaw, Wolf, et al., 2017; Wu et al., 2018). However, due to the complexity of ecosystem drought legacy impacts and difficulties in quantifying drought recovery time, large uncertainties still exist for regional to global drought recovery and legacy effect studies (Liu, Gudmundsson, et al., 2019). Multi-sensor remote sensing can provide drought identification from various aspects that enhance our understanding of these drought recovery and legacy effects. For example, the recovery of photosynthetic capacity can be relatively quick and can be quantified via greenness indices. The combination of optical/NIR sensors with airborne SAR may be useful for quantifying the canopy recovery, and the recovery of below canopy structure in forests can be extracted by LiDAR and microwave imagery, since they are sensitive to properties of the below canopy (Frolking et al., 2009). Characterization of drought recovery legacy effects can be further complicated, since droughts not only have legacy impacts on vegetation structure and photosynthetic capacity, but also on other aspects such as phenology. Recent studies such as Peng et al. (2019), indicated that drought has both lagged and cumulative impacts on autumn leaf senescence over the Northern Hemisphere. Yuan et al. (2020) found that pre-season drought could impact vegetation spring phenology. Buermann et al. (2018a) highlighted the growing adverse negative lagged effect of spring warmth on northern hemisphere vegetation productivity. Shi et al.

(2019) examined the legacy effects of precipitation and evaporation changes during the 2005 Amazon drought based on multiple satellite observations of precipitation and evaporation, and found that the drought effect induced evaporation reductions, triggering a delay of the wet season onset. Gonçalves et al. (2020) confirmed the 2005 Amazon drought legacy effects on tropical forest leaf phenology using multi-sensor observations of near-surface and satellite remote sensing. Overall, like many of the other aspects explored herein, observations from multi-sensor remote sensing provide multiple lines of evidence for the study of drought recovery and legacy effects.

### 2.3.6 Capturing and monitoring flash droughts

While drought is generally described as a slowly evolving phenomena (Wilhite et al., 2007), recent rapidly developing drought events (e.g., 2012 United States summer drought) have caused a growing interests in the study of so-called "flash drought" within the scientific community. Flash droughts are generally defined as a short term but severe drought with rapid onset and evolving processes (Ford et al., 2017; Otkin et al., 2018; Senay et al., 2008). Flash droughts can cause severe environmental and agricultural impacts in a short time period, and since they have a sudden onset and rapid intensification, can bring particular challenges for drought monitoring, forecasting, and mitigation (Christian et al., 2019; Ford et al., 2017; Pendergrass et al., 2020). The identification of flash droughts is of great importance. Distinct from conventional droughts, high evaporation rates are usually found before their developments (Chen et al., 2019). Thus, remote sensing based evaporation products have been used to identify these events. A good example is the satellite-based evaporative stress index (ESI) (Anderson et al., 2016), which was shown to provide early warning of flash drought impacts on

agricultural system. More recently, a series of ESI based drought indices, including the rapid change index (RCI) (Otkin et al., 2014), evaporative demand drought index (EDDI) (Hobbins et al., 2016), and standardized evaporative stress ratio (SESR) (Christian et al., 2019) were developed for flash drought characterization. Studies have also identified that other drought characteristics, such as rapid declines in precipitation, soil moisture and abnormally high temperature, were also important to identify flash droughts (Haile et al., 2020; Mo et al., 2015). The combined information of soil moisture, temperature, and evaporation was applied by Wang, Yuan, et al. (2016) to identify a flash drought in China and indicated an increasing number of flash droughts from 1979 to 2010 due to global warming. Other multi-sensor remote sensing based integrated drought indices have also been developed for characterizing flash droughts. For example, the Quick Drought Response Index (QuickDRI) (Svoboda et al., 2017), which integrated satellite based ESI and Standardized Vegetation Index (SVI) (Peters et al., 2002) with climate indicators such as SPEI, Standardized Precipitation Index (SPI), and North American Land Data Assimilation System-2 (NLDAS-2) based soil moisture data, was developed to characterize shorter-term and quickly evolving droughts. Although a relatively new drought classification, the characteristics of flash droughts, including sudden onset, rapid evolution, and severe impacts on ecosystem (Mo et al., 2015; Yuan, Wang, et al., 2019), make their further study and description of considerable importance. Multi-sensor remote sensing observations provide a unique platform for providing the needed high spatial-temporal resolutions for flash droughts, and will undoubtedly play a key role in enhancing aspects of their description.

### 2.3.7 Drought trends under climate change

There is ongoing scientific debate on whether climate change will cause global drying, and how drought will evolve under such conditions (Vicente‐Serrano et al., 2020). Climate metrics such as the self-calibrated Palmer drought severity index (scPDSI), PDSI with potential evapotranspiration estimated using the Penman-Monteith equation (sc_PDSI_pm) and climate model predictions themselves, suggest a likely strong increase of drought severity and severe drought impacts in the future (Baig et al., 2020; Dai, 2013; Trenberth et al., 2014; Xu et al., 2019). However, other research providing a retrospective assessment has indicated that relatively little change in global drought has occurred over the past 60 years (Sheffield et al., 2012). Some climate model simulations suggest that global drying may not happen due to predicted increases in runoff, and that the effect of an increase in evaporation could be offset by a decrease in evaporation driven by increased surface resistance responding to elevated $CO_2$ (Berg et al., 2019; Yang et al., 2019). However, other studies have indicated that vegetation will reduce future runoff despite the increased surface resistance to evaporation, due to increasing canopy water demands and freshwater availability that will be reduced due to climate change (Mankin et al., 2019).

Studies of global drought trends based on multi-sensor remote sensing can provide a range of informative metrics, including their use as signals to evaluate climate model output. Damberg et al. (2014) indicated that there was no significant drying trend from 1980-2012 by combining multi-sensor satellite precipitation data from the Global Precipitation Climatology Project (GPCP), Multi-satellite Precipitation Analysis – Near Real Time (TMPA) (TMPA-RT), and Precipitation Estimation from Remotely Sensed

Information using Artificial Neural Networks (PERSIANN) satellite data. Dorigo et al. (2012) analyzed the global trend in a multi-sensor soil moisture product from 1988-2010, which indicated a strong tendency towards drying soil moisture. They also found that the drying soil moisture trends were not consistent with the patterns of precipitation, which indicated that even though precipitation is the main driver of variations in soil moisture, other factors such as evaporation, soil type, and vegetation cannot be neglected (Dorigo et al., 2012). Recently, a drought trend study over the United States using multi-sensor satellite data from the Scanning Multi-channel Microwave Radiometer (SMMR), the Special Sensor Microwave Imager (SSM/I), the Advanced Scatterometer (ASCAT), MODIS, AMSR-E, AMSR-2, and SMOS and SMAP soil moisture data (Kumar et al., 2019), indicated a trend of longer and more severe droughts over parts of the Western United States. Despite these and related studies, the complexity of spatially heterogeneous trends, limited coverage periods of individual satellite data, and inherent uncertainties from single satellite datasets, all suggest that further integration of multi-sensor observations are needed to disentangle the development of global scale drought trends under a changing climate.

### 2.4. Recent modeling advances for developing integrated multi-sensor remote sensing drought indices

Drought indices integrate various drought related variables (e.g., precipitation, temperature, evaporation, snow, groundwater, and soil moisture) to monitor and assess physical characteristics such as onset, duration, severity, and spatial extent (Hao and Singh, 2015; Hayes et al., 2007; Mishra et al., 2010). Drought has multiple aspects, examples of which might be high temperature with low soil moisture along with declines

in plant function: all of which can occur independently or simultaneously (Wilhite, 2000). As such, a single drought index that is developed based on one particular element is unlikely to capture many complex processes and diverse impacts (Jiao, Tian, et al., 2019). For example, a precipitation based drought index may fail to characterize plant water stress linked to rising vapor pressure deficit (VPD) during a heat wave, since drought can have independent impacts on both meteorology and plant function (Novick et al., 2016; Stocker et al., 2018). Not surprisingly, multivariate drought indices developed using multiple models and indices, and including drought properties such as severity and duration or alternative data sources, have proved to better and more comprehensively characterize drought than any single index (Andreadis et al., 2005; Hao et al., 2013b; Touma et al., 2015).

Many studies have sought to develop multivariate indices by combining observations from *in-situ* observations, gridded climate datasets, and single-sensor remote sensing dataset (AghaKouchak, 2015b; Brown et al., 2008; Hao et al., 2013b; Hao and AghaKouchak, 2014; Huang, Huang, et al., 2016; Kao et al., 2010; Niemeyer, 2008; Sepulcre-Canto et al., 2012; Tabari et al., 2013; Vasiliades et al., 2011; Waseem et al., 2015; Westra et al., 2007). Integrated drought indices that only exploit multi-sensor remote sensing data is an emerging research topic (AghaKouchak et al., 2015b; West et al., 2019). While a number of multi-variable drought indices have been developed, few have been applied using multi-sensor remote sensing observations. One reason is the relatively short length of satellite records (AghaKouchak et al., 2015b; Lettenmaier et al., 2015). On the other hand, numerous recent efforts have been made towards integrated multi-sensor drought indices based on multiple models. These multi-sensor based drought

indices can generally be divided into three categories: data-driven models, water balance models, and process-based models.

### 2.4.1 Data-driven models

Data-driven models are the most commonly used models for multi-sensor integrated drought indices development. The primary strategy of data-driven models is combining the input variables using a set of statistical models, and often with limited knowledge about the physical mechanism of the system (Solomatine, 2002). Some recent examples can be summarized through their use of simple linear combination models, principal component analysis (PCA) combination models, machine learning models, and fuzzy weighting models, and all of which are described below.

#### *2.4.1.1 Simple linear combination models*

One of the most commonly employed statistical models to integrate drought variables from multiple sensors is simple linear combination. Several multi-sensor integrated drought indices were developed by linearly assigning weights to single drought variables. For example, the Microwave Integrated Drought Index (MIDI) (Zhang and Jia, 2013) combines the Soil Moisture Condition Index (SMCI) from AMSR-E data, the Precipitation Condition Index (PCI) using TRMM, and the Temperature Condition Index (TCI) from MODIS LST data. Similarly, the Scaled Drought Condition Index (SDCI), Optimized Meteorological Drought Index (OMDI) and Optimized Vegetation Drought Index (OVDI) integrate drought variables including precipitation, soil moisture, vegetation indices, and LST, also using linear weighting (Hao, Zhang, et al., 2015; Rhee et al., 2010). The advantage of simple linear combination models is that they are relatively easy to calculate and straightforward to implement. While they have been

shown to present good performance for drought monitoring at local scales (Zhang, Jiao, et al., 2017), simple linear combination model have limitations for large scale implementation. For instance, they often assume that the sub-areas of a particular study area contribute the same weight for a particular single variable. Also, assigned weights for each drought variable are likely to vary in different climate regions, and may thus lead to poor performance when applied to diverse climate conditions (Hao and Singh, 2015; Jiao, Tian, et al., 2019).

#### *2.4.1.2 Principal component analysis models*

Since the basic purpose of principal component analysis (PCA) is to distill a large number of variables into a new data set with low dimensionality (Wold et al., 1987), it is no surprise that it has been commonly used to develop drought indices from multi-variables. Numerous studies have developed integrated drought indices based on site observation data using PCA (Arabzadeh et al., 2016; Barua et al., 2011; Bazrafshan et al., 2014; Bazrafshan et al., 2015; Keyantash et al., 2004; Liu, Zhu, et al., 2019), while others have also applied PCA to develop multi-sensor remote sensing based drought indices. Du et al. (2013) developed a synthesized drought index (SDI) using PCA to combine vegetation, temperature, and precipitation variables from TRMM and MODIS data. PCA has also been combined with other models to developed integrated multi-sensor based drought indices. For example, PCA was applied with a partial least squares regression (PLSR) model to assess agricultural drought in East Africa (Agutu et al., 2017), while Jiao, Wang, et al. (2019) used PCA with a geographically weighted regression (GWR) model to developed a station-enabled Geographically Independent Integrated Drought Index (GIIDI_station), which showed good performance under diverse climate regions.

One of the main limitations of the PCA based indices is the linearity assumption of the input variables and the assumption that the maximum information of the input variables is oriented along the direction of maximum variance of data transformation (Wold et al., 1987). However, the Gaussianity of input variables and their linearity may not always be met in reality (Azmi et al., 2016; Hao and Singh, 2015). To avoid those limitations, it may be helpful to explore other feature extraction models, such as kernel entropy component analysis (KECA), kernel PCA, and sparse KPCA (SKPCA), which have recently been developed as modified PCA models to overcome the linearity assumption (Rajsekhar et al., 2015a; Waseem et al., 2015).

#### *2.4.1.3 Machine learning models*

Big data is a term that is well associated with the collection and storage of vast amounts of remote sensing data (Ma et al., 2015). Recent studies have used multiple machine learning algorithms to incorporate multi-sensor remote sensing information for drought assessment at regional scales. Park et al. (2016) monitored meteorological and agricultural drought in the arid region of Arizona and New Mexico and the humid region of North Carolina and South Carolina by incorporating sixteen remote sensing based drought factors from MODIS and TRMM satellite sensors using random forest, boosted regression trees, and Cubist models. Similarly, Park et al. (2017) developed the High resolution Soil Moisture Drought Index (HSMDI) for meteorological, agricultural, and hydrological droughts over the Korean peninsula using Random Forest, Cubist, and Boosted Regression Trees based on AMSR-E soil moisture, MODIS NDVI, ET, albedo and LST data. Han et al. (2019) developed the combined drought monitoring index (CDMI) in Shaanxi province in China by combining MODIS LST, NDVI and ET data

with TRMM precipitation data using a random forest model. Feng et al. (2019) adopted a bias-corrected random forest, support vector machine, and multi-layer perceptron neural network using thirty remotely sensed drought factors from the TRMM and the MODIS satellite sensors to reproduce drought conditions in South-Eastern Australia. Their results indicated strong correlation between machine learning based satellite drought observations and ground-based crop yield and drought indices (Feng et al., 2019). Similar to the development of the Vegetation Drought Response Index (VegDRI) (Brown et al., 2008), Wu, Zhou, et al. (2015) developed an Integrated Surface Drought Index (ISDI) using a classification and regression tree (CART) approach based on MODIS NDVI and LST and climate data in China. Rahmati et al. (2020) mapped agricultural drought using CART, boosted regression trees (BRT), random forests (RF), multivariate adaptive regression splines (MARS), flexible discriminant analysis (FDA) and support vector machines (SVM) in the south-east region of Queensland Australia. Son et al. (2021) developed a Vector Projection Index of Drought (VPID) based on Vector Projection Analysis (VPA) by integrating site observation based SPI, SPEI, PDSI, and Z-index with multi-sensor satellite based precipitation, evaporation, vegetation, and soil moisture data.

Of course, the advantage of using machine learning models for integrated drought monitoring is that such models are good at handling multi-dimensional and multi-variable data in different environments and without human intervention (Lary et al., 2016; Ma et al., 2015). However, machine learning based integrated drought monitoring relies heavily on the selection of training data. They also require massive data sets to train on, and are highly susceptible to errors that often exist when a training set is not representative of diverse environmental conditions or climate states (Ali et al., 2015; Lary et al., 2016).

The transferability issue means that for regions with limited available ground observation, machine learning models may have limited application. Whether this can be overcome with the availability of spatiotemporal remote sensing records is a topic of ongoing research.

#### *2.4.1.4 Fuzzy weighting models*

The lack of a widely accepted drought definition is one of the primary obstacles to effectively investigate drought events (Lloyd-Hughes, 2014). The majority of research divides drought into different types: meteorological, agricultural, hydrological, and social-economic (Wilhite et al., 1985). However, the boundaries separating these drought conceptions are vague, and it is difficult to set a specific boundary for drought impacts of certain rates to meteorology, agriculture, hydrology, and social-economic (Pesti et al., 1996). To address these concerns, fuzzy analysis methods have been used to monitor drought based on multi-sensor remote sensing observations. Alizadeh et al. (2018) applied an Ordered Weighted Averaged approach using multi-sensor data from CHOMPS, GPCP, CMAP, PERSIANN-CD, TRMM, GLDAS-2, MERRA-2, with results indicating that the model significantly improved drought estimation. Jiao, Tian, et al. (2019) proposed a framework for developing a Geographically Independent Integrated Drought Index (GIIDI), based on local OWA models and multi-sensor data from MODIS NDVI, TRMM precipitation, and AMSR-E soil moisture data, which could have applicability for various climate regions. Huang et al. (2015) developed the Integrated Drought Index (IDI), combining meteorological, hydrological, and agricultural factors across the Yellow River basin in North China based on variable fuzzy set theory. In another approach, Nasab et al. (2018) developed a Fuzzy Integrated Drought Index

(FIDI) based on an entropy weighting fuzzy model, utilizing the Anomaly Percentage Index of precipitation, runoff, actual ET, and soil moisture in the Neyshabour basin, Iran. Fuzzy weighting models are widely used in the multi-criteria decision making field (Aruldoss et al., 2013). These models aim to address the uncertainty and interior related relationship between the single variables (Jiang et al., 2000; Yager, 1996). However, the limitation of weights determined by fuzzy weighting algorithms are not straightforward and the development of fuzzy models is often tedious (Grabisch, 1996; Reshmidevi et al., 2009; Velasquez et al., 2013). In addition, other studies argue that the min-max ordered rule of fuzzy weighting models may not be able to best reflect the conjunctive and disjunctive reasoning, and integrated fuzzy models should be applied in the real world (Simić et al., 2017).

### 2.4.2 Process based models

Drought is a complex natural hazard with gradual dynamic transition between drought and non-drought conditions (Rulinda et al., 2012). Different stages of drought, cumulative impacts, or even different drought timings, can all affect the environment differently (Fukai et al., 1995; Pasho et al., 2011; Peng et al., 2019; Sippel et al., 2018). Drought monitoring indices that are based on the evolution of the drought process may better reflect the dynamic of drought severity changes. Zhang, Chen, et al. (2017) recently proposed an Evolution Process-based Multi-sensor Collaboration (EPMC) framework and developed the Process-based Accumulated Drought Index (PADI) based on multi-sensor data that included GPCC precipitation data, GLDAS soil moisture data, and AVHRR NDVI data. The various phases of drought latency, onset, development, and recovery were quantified differently by the authors, and their results showed that the

process based drought monitoring framework could provide robust multi-sensor remote sensing based agricultural drought monitoring analysis (Zhang, Chen, et al., 2017).

### 2.4.3 Water balance models

While there are various definitions of drought and different classification types, it is a well-accepted theme that drought is a condition of insufficient water to meet needs (Redmond, 2002). A range of water budget based drought indices have been developed and widely used for a number of decades. One of the most widely employed indices is the PDSI, which is based on a water balance model of soil moisture supply and water demand of evaporation, with the input data including precipitation, temperature, and soil water content (Palmer, 1965). The Palmer Hydrologic Drought Index (PHDI) (Karl et al., 1987) and Surface Water Supply Index (SWSI) (Shafer et al., 1982) are other examples of widely used water budget models for monitoring drought. Similarly, the standardized precipitation evapotranspiration index (SPEI) monitors drought by estimating the water balance using the difference between precipitation and PET (Vicente-Serrano et al., 2010). Remote sensing based water balance models offer an important means to monitor droughts, since they are able to map the physical mechanisms behind ecosystem water supply and demand at regional to global scales, and previous multi-sensor remote sensing studies have shown the potential for the estimation of regional terrestrial water cycles (Pan et al., 2008; Sheffield, Ferguson, et al., 2009). In related efforts, Zhang, Xia, et al. (2019) developed the Standardized Moisture Anomaly Index (SZI) using a water-energy balance approach that combined remote sensing estimates of precipitation, potential evaporation, and runoff. A global evaluation of SZI indicated that it has strong performance for drought monitoring in different climate regions and could physically

capture surface water-energy balances (Zhang, AghaKouchak, et al., 2019). However, while effectively capturing natural water balance behavior is important, there are other elements that effect budget calculations. Anthropogenic effects associated with land use change, irrigation efficiency, and rapid increases in population can all effect the physical consistency of hydrological processes, yet the vast majority of water budget based drought indices fail to consider these (Mukherjee et al., 2018). If truly integrated approaches are to be developed, incorporation of the anthropogenic effects into multi-sensor drought index approaches are required.

**2.5. Challenges**

While there is general recognition that multi-sensor remote sensing presents a great opportunity for integrated drought studies, it remains very much in its infancy, and multiple challenges to effective implementation remain. Foremost amongst these is the inconsistency between variables derived from different sensors, which may lead to uncertainties in multi-sensor integration efforts. Differences arising from spatial, temporal, and spectral resolution, spatial extent, overpass time, and length of record all contribute to complicate data synthesis. The recent advances in new satellite data acquisition such as SIF serve as a notable example of the future need for more focused efforts on data fusion techniques. For example, current methods for observing SIF require the exploitation of different features of the electromagnetic spectrum, resulting in SIF observation across different platforms that are specific to different wavelengths (Cendrero-Mateo et al., 2019; Mohammed et al., 2019), challenging data fusion techniques. Additionally, SIF varies considerably with time, and thus moving from instantaneous to daily SIF, together with any associated data fusion across platforms, may

prove to be challenging. For SIF, as well as other land surface variables including LST, observations at different times of the day are critically needed (e.g., OCO3 and ECOSTRESS), as are geostationary missions (e.g., GeoCarb and GOES). However, this is not a problem unique to drought studies. Indeed, it is an area that is being actively explored in topics such as the development of remote sensing based climate records and essential climate variables (Hamaguchi et al., 2018; McCabe et al., 2008; Zhang, 2010), so much can be learned from these efforts. Related advances in data fusion and merging approaches provide a natural pathway for progress in this area.

Another challenge relates to what precisely "drought severity" might mean for multi-sensor remote sensing based drought indices. Drought indices such as SPI and SPEI (McKee et al., 1993; Vicente-Serrano et al., 2010) define severity using drought frequency based on probability distributions (e.g., gamma and log-logistic distribution) from long-term observations. Other indices arbitrarily define drought severity based on the abnormal degree of the current state compared with an historical calendric "normal" status over a period of years (without calculating probability distributions). For instance, the vegetation condition index (VCI), temperature condition index (TCI), and precipitation condition index (PCI) are widely used in multi-sensor integrated drought index models, and are all based on the similar standardization method, i.e., $\frac{V_{i,j}-V_{i,min}}{V_{i,max}-V_{i,min}}$, where $V_{i,j}$ represents the monthly PCI, TCI, and VCI for month *i* in year *j*, and $V_{i,max}$ and $V_{i,min}$ denote the multiyear minimum and maximum PCI, TCI, and VCI, respectively, for month i in year j. The arbitrary definition that VCI is less than 0.1 for extreme drought may not be accurate. In addition, the same value of VCI, TCI, and PCI may not reflect the same degree of drought anomaly, since the relationships between vegetation indices,

soil moisture, precipitation and temperature are rarely linear. The problem is also exacerbated by the fact that remote sensing observations do not generally extend beyond 5-10 years of continuous observation (sometimes, much less), meaning that anomaly records must be developed based on multi-sensor integrations, which can introduce biases. Future multi-sensor remote sensing drought monitoring studies may need to develop more objective, rather than arbitrary, definitions of drought severity.

In addition, there is still a lack of cause-and-effect based drought monitoring studies. Most current multi-sensor drought monitoring strategies are based on data-driven models, which lack mechanisms detailing how droughts impact ecosystems. For example, few current drought indices can directly reflect vegetation water stress. Due to the complexity of the Earth system, there are multiple factors other than drought (e.g., insects, disease, and hail damage) that could cause ecosystem anomalies (Brown et al., 2008). The compound feature of hazards (e.g., drought and heat waves) makes cause-and-effect studies even more needed in order to explicitly understand drought characteristics and their underlying features (AghaKouchak et al., 2020; Hao, Singh and Hao, 2018; Zscheischler et al., 2020). Causal models based on multi-sensor remote sensing data are needed to augment widely used linear correlation studies, since correlations do not impart causality.

## 2.6. A road map for the future

### 2.6.1 Integrating new and emerging sensors/platforms into physical models

With an increasing level of both remote sensing and *in-situ* data availability (McCabe, Rodell, et al., 2017), there are new and emerging opportunities that have the potential to further advance multi-sensor remote sensing drought characterization.

Physical models that integrate such data are likely to improve our understanding of the complex mechanisms of immediate and lagged drought effects across spatial, spectral and temporal scales. For example, hyperspectral remote sensing presents an opportunity to more directly detect the plant physiological and biochemical changes under water stress than traditional broad optical wavelengths. Hyperspectral remote sensing missions under operation or development, including the Hyperspectral Imager Suite (HISUI) (Iwasaki et al., 2011), High-resolution Temperature and Spectral Emissivity Mapping (HiTeSEM) (Udelhoven et al., 2017), hyperspectral infrared imager (HyspIRI) (Abrams et al., 2013), Environmental Mapping And Analysis Program (EnMAP) (Kaufmann et al., 2008), Precursore Iperspettrale Della Missione Applicativa (PRISMA) (Labate et al., 2009), and FLuorescence EXplorer (FLEX) (Mohammed et al., 2019) offer possibilities for regional to global hyperspectral remote sensing for future multi-sensor drought studies.

As noted in Section 2.2.7, hyperspectral based approaches offer just one of the pathways for improving our drought observation capacity. Leveraging LiDAR observations also provides opportunities for future multi-sensor drought characterization since LiDAR data have advantages in mapping canopy vertical change and 3-D reproduction. The LiDAR on the Global Ecosystem Dynamics Investigation (GEDI) instrument (Coyle et al., 2015), provides global LiDAR data availability that is suitable for use in multi-sensor drought studies. Recent studies synergizing LiDAR with hyperspectral data at regional scales have shown potential for multi-sensor early warning of plant water stress (Degerickx et al., 2018; Sankey et al., 2018; Shivers et al., 2019; Sobejano-Paz et al., 2020).

Drought studies based on Unmanned Aerial Systems (UAS) also present new opportunities to improve our understanding of the underlying mechanisms and processes, as well as in advancing our ability to proactively monitor and predict drought events as they occur and develop. The benefits of incorporating UAS observations into multi-sensor drought studies include the relatively low costs, sensor agnostic capability, and the on-demand capability combined with high spatial resolution. These UAS-based advantages make it possible to detect local-to-regional scale water deficit before they become widespread and this is particularly useful for agriculture and forest management applications.

Likewise, leveraging geostationary satellite systems provides another opportunity for advancing multi-sensor drought studies. The high temporal frequency of geostationary satellites affords a unique platform for monitoring rapid-development in drought response (i.e., flash droughts) (Otkin et al., 2013). Studies indicate that geostationary satellite systems such as Himawari-8/9 showed great insight for agricultural drought monitoring (e.g., Hu, van Dijk, et al. (2020). The upcoming Geostationary Carbon Cycle Observatory (GeoCarb) mission will provide $CO_2$ and SIF measurement at higher than 3-hour temporal resolution (Moore III et al., 2018), which makes it possible to study large-scale drought impacts on carbon cycles and vegetation photosynthesis at sub-daily scales. Fusing geostationary satellite observations with polar-orbiting sensors would provide a pathway towards high spatiotemporal resolution of drought related variables, following similar efforts with evaporation and land surface temperature (Smith, Dannenberg, et al., 2019).

### 2.6.2 Establishing the spatiotemporal resolution needed to deliver effective drought monitoring

Effective drought monitoring often require both high spatial and temporal resolution observations (e.g., flash drought and vegetation photosynthesis dynamics under droughts). Over the last decade, there have been a number of major international efforts to address both model development and inter-comparison activities across various hydrological variables (McCabe et al., 2016; Miralles et al., 2016) with an assessment of both limitations and advantages forming key areas of focus (Chen et al., 2014; Liou et al., 2014; Yang, Long, et al., 2015; Zhang, Kimball, et al., 2016). One of the major limitations identified in many of those studies relates to the trade-off between spatial resolution and temporal frequency: that is, a compromise is routinely required, whereby you can have one, but only at the expense of the other (McCabe, Aragon, et al., 2017). Observations with both high spatial resolution and temporal frequency are urgently needed for a range of applications. Emerging constellations of space-based data offer an enhanced observation capacity for drought characterization that can overcome such constraints. For example, the application of constellations such as ASCAT onboard the Metop-A, B, and C platforms can provide sub-daily microwave soil moisture products, which are capable of leading the next generation high spatiotemporal soil moisture observation (Peng et al., 2020). New opportunities such as the Multi-Radar Multi-Sensor (MRMS) system, which integrated about 180 operational radars to provide a three dimensional radar mosaic with both high spatial (1km) and high temporal (2 min) resolution is another good example, although the current MRMS only covers the United States and Canada (Zhang, Howard, et al., 2016). New approaches exploiting

constellations of small CubeSat systems, provide an enhanced capacity that also collapses this spatiotemporal constraint (Aragon et al., 2018). Figure 2.2 shows an example of the competing resolution of CubeSat imagery alongside Sentinel-2 and Landsat, illustrating the spatial advantage. With its fleet of more than 170 CubeSats, Planet is able to provide multi-spectral reflectance data at ~3 m spatial and daily resolution (Houborg et al., 2018b). While presenting clear spatiotemporal advantages, the commercial-off-the-shelf sensors have lower radiometric quality compared to more traditional satellite platforms (McCabe, Aragon, et al., 2017; Ryu et al., 2019). However, sensor harmonization strategies, such as the CubeSat Enabled Spatiotemporal Enhancement Method (CESTEM) of Houborg et al. (2018a) have overcome such sensor limitations, offering an analysis ready product comparable to Sentinel-2 and Landsat systems. The approach has enabled atmospherically corrected high-spatiotemporal surface reflectance and vegetation variables such as LAI and NDVI to be developed at unprecedented resolutions (Houborg et al., 2018b; Houborg et al., 2018a). Such sensor fusion and harmonization approaches offer much potential for drought studies and characterization in the future. Geostationary platforms such as the Geostationary Operational Environmental Satellites (GOES) also provide multi-sensor data opportunities for drought characterizations. The GOES series of satellites (R, S, T, and U), which cover the western hemisphere (from the west coast of Africa to New Zealand) could provide both multichannel passive imaging and near-infrared optical observations with up to 1-min imagery research request (Goodman, 2020), making it possible for nearly continuous monitoring of drought impacts (e.g., vegetation photosynthesis) for the covered regions.

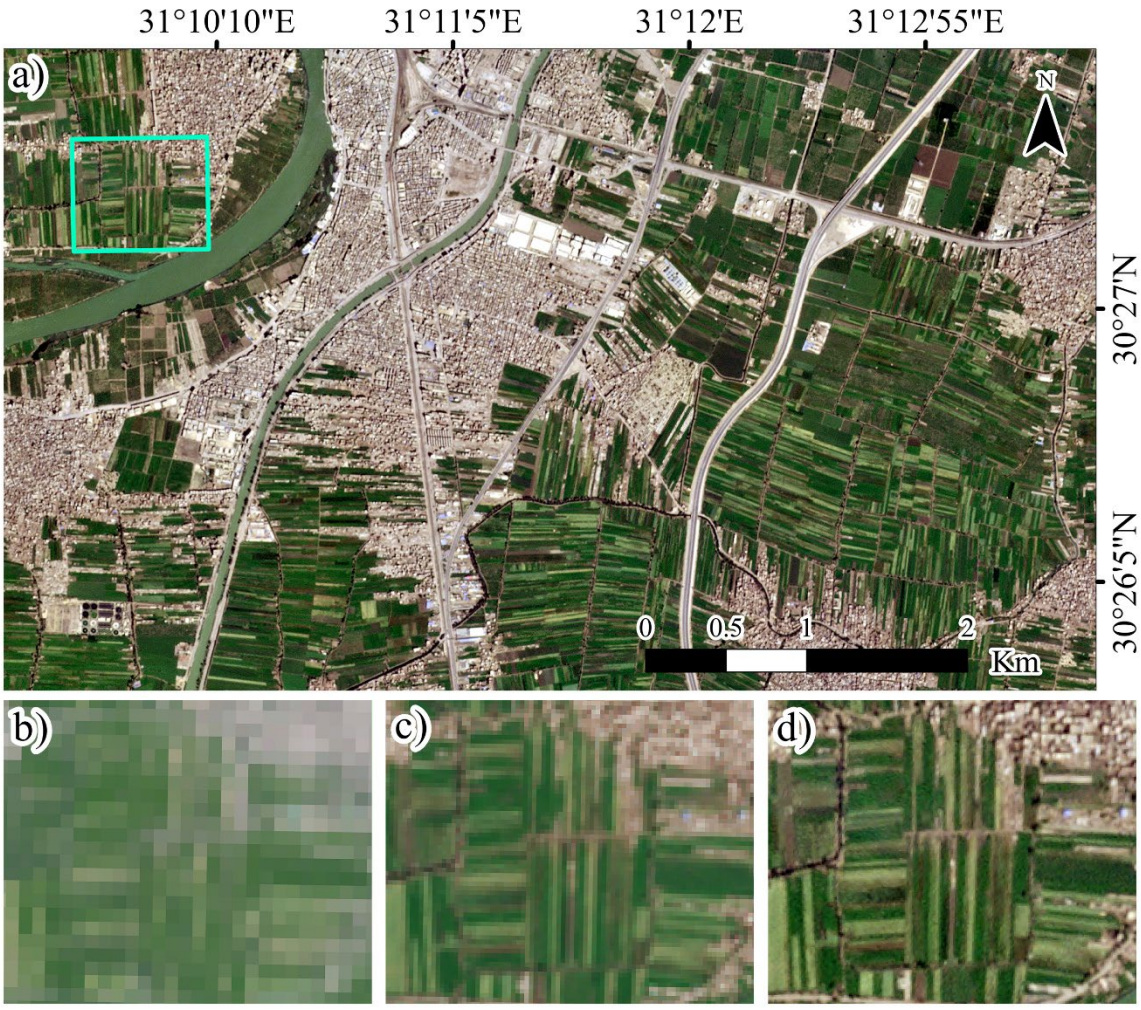


Figure 2.2: Natural color representation of an agricultural area along the Nile River near Banha, Egypt that demonstrates the spatial resolution advantage of CubeSats. Panel a) shows a 3 m spatial resolution CubeSat image from Planet, where small agricultural fields and urban structures can be discerned. Panels b) to d) show a zoomed-in view of the area contained by the cyan rectangle for b) Landsat 8, c) Sentinel-2A and d) Planet at 30, 10, and 3 m resolutions, respectively. The Landsat image was acquired on March 31, 2020, and both Planet and Sentinel-2A images were acquired on March 29, 2020.

### 2.6.3 Retrospective assessment of long-term multi-sensor remote sensing record

As noted in section 2.2, a suite of regional to global satellite observations of drought-related variables have been collected from as early as the 1970s. However, those satellite observations for drought-related variables often suffer from various uncertainties (e.g., data contamination, sensor degradation, and model retrieval uncertainties) and result in data inconsistency (e.g., GPP inconsistency revealed by O'Sullivan et al. (2020)). Such uncertainties may cause overestimation or underestimation of drought impacts (Stocker et al., 2019; Zhang, Song, et al., 2017). Retrospective assessment of long-term remote sensing record for multi-sensor drought studies provide opportunities to more accurately evaluate the drought impacts. In addition, the development of multi-sensor remote sensing data fusion models has the potential to curate long-term remote sensing records with high spatiotemporal resolutions. Retrospective drought studies based on the long-term multi-sensor remote sensing record present opportunities to better evaluate the underlying drought mechanisms and improving modelling accuracy.

### 2.6.4 Exploiting the new multi-sensor capabilities based on existing sensors

Together with new and emerging sensors/platforms (as noted in section 2.6.1), exploring novel applications of existing sensor records also provides new opportunities for drought characterization. Many remote sensing sensors originally designed for a specific application have been subsequently utilized to produce new capabilities (so-called "signals of opportunity" as in McCabe, Rodell, et al. (2017)). For example, several atmospheric satellite sensors have been shown to have the capability to measure vegetation SIF (Mohammed et al., 2019). Likewise, many of the existing microwave

vegetation water content observations are a by-product of microwave soil moisture retrievals, with a good example of the development of a long-term global multi-sensor based VOD dataset (Liu et al. (2011). Likewise, other existing sensors also provide opportunities for new multi-sensor capabilities of drought studies. The Global Navigation Satellite System (GNSS), which was originally designed for navigation and communication, has illustrated the potential for constellation-based precipitation monitoring and prediction (Asgarimehr et al., 2018; Cardellach et al., 2019), with further studies exploring its capability for soil moisture retrieval. Leveraging our existing networks of both *in-situ* and space-based sensors for such purposes offers further data and needed insights to better understand drought.

### 2.6.5 Identifying the capabilities of drought prediction and early warning through target experiments

Drought prediction and early warning are effective approaches to mitigate drought impacts. Current drought prediction methods can be generally divided into statistical drought prediction models, dynamical drought prediction approaches, or combinations of both (Hao et al., 2017b). All need multi-sensor remote sensing observations to improve large-scale drought prediction reliabilities. For the statistical approaches, predictions require a long-term observation records to build reliable historical relationship between predictors and observations. The dynamical method is based on climate/hydrologic models linked to the physical processes of land-atmospheric interactions (Hao, Singh and Xia, 2018). Multi-sensor remote sensing can not only provide long-term record for statistical prediction but also multiple components of observations for the land, ocean, and atmospheric for better simulation of description of linked processes. Target

experiments can be performed to evaluate drought prediction models, providing evidence-based assessment of drought-climate links and confidence in the chosen prediction approach. Indeed, establishing the physical basis and/or empirical links between drought extent, severity and duration and changing features of the climate system remains one of the outstanding questions where multi-sensor methods may play an important role. Moreover, identifying the interlinked variables responsible for driving the initiation, prolongation and completion of drought events may only be possible through such studies.

### 2.6.6 Identifying the missing elements in drought assessment

Given the complexity of the various direct and indirect elements of drought impacts, drought characterization demands interdisciplinary expertise. Over the decades of remote sensing-based drought studies, some drought features have been relatively well studied, while other elements remain less studied or even missing. For example, much of our understanding of remote sensing-based drought characterization has focused on natural ecosystems, while drought impacts on social-hydrological systems (Sivapalan et al., 2012) remain less studied. Multi-sensor drought studies that include human interventions (e.g., irrigation and water pumping to mitigate agriculture drought) will provide opportunities to physically improve water budget models for multi-sensor drought monitoring, providing capacity to not just monitor, but also manage the water resource systems under drought conditions. Incorporating key aspects of socio-economic impacts, social response, needs of governments, business/insurance companies is a much needed future objective to translate the science into actionable response.

### 2.6.7 Leveraging new strategies of data processing

Relative to single sensor drought studies, one of the obvious differences for multi-sensor drought studies is the increased data volumes with high dimensionality and metadata. Indeed, this is true not just for future multi-sensor drought studies, but for future remote sensing applications in general, due to the exponential increases in remote sensing data being produced. The data volume and velocity comes with particular challenges for data storage, management, transfer and processing. In this regard, efficient drought identification and characterization strategies that significantly reduce data redundancy and improve generality and transferability are critically needed. Leveraging high-performance computing (HPC) and cloud-based resources (e.g., Google Earth Engine, GEE) provide an obvious path to deal with the such storage and processing challenges.

## 2.7. Conclusions

Leveraging advances in our capacity to monitor and characterize droughts not only improves our understanding of their initiation and development, but also provides a pathway for improved conceptual understanding and physical description of the underlying process. Likewise, enhancing our understanding and description of key vegetation-water-carbon interactions, which is becoming increasingly viable due to opportunities provided by multi-sensor remote sensing, may not only drive these needed improvements, but also provide a path towards developing mechanism-based drought prediction. Exploiting the expanding array of remote sensing platforms, whether *in-situ*, airborne or satellite-based, and recognizing that each system provides independent insights and supporting evidence, is an obvious way to drive these needed developments

in process understanding. The expanding capacity of multi-sensor observations also increases our capacity to develop the mechanistic descriptions required to deliver improved drought monitoring, early warning and prediction systems in the coming decades. Such knowledge will be central to disentangling the complex interplays that define the drought process. Importantly, these knowledge advances are not just key to resolving the influences and fingerprints of climate change on drought occurrence, severity and duration, but also in developing the socio-economic links that are desperately needed for drought monitoring and prediction systems that can be applied towards planning, management and mitigation efforts.

**References**

Aasen, H. et al., 2019. Sun-induced chlorophyll fluorescence II: Review of passive measurement setups, protocols, and their application at the leaf to canopy level. *Remote Sensing*, 11(8): 927.

Abdelwahab, S., Hamdaoui, B., Guizani, M. and Rayes, A., 2014. Enabling smart cloud services through remote sensing: An internet of everything enabler. *IEEE Internet of Things Journal*, 1(3): 276-288.

Abrams, M.J. and Hook, S.J., 2013. NASA's hyperspectral infrared imager (HyspIRI), Thermal infrared remote sensing. Springer, pp. 117-130.

Adams, H.D. et al., 2010. Climate-induced tree mortality: Earth system consequences. *Eos, Transactions American Geophysical Union*, 91(17): 153-154.

Adler, R.F. et al., 2003. The version-2 global precipitation climatology project (GPCP) monthly precipitation analysis (1979–present). *Journal of Hydrometeorology*, 4(6): 1147-1167.

AghaKouchak, A., 2015b. A multivariate approach for persistence-based drought prediction: Application to the 2010–2011 East Africa drought, Journal of Hydrology, pp. 127-135.

AghaKouchak, A. et al., 2020. Climate Extremes and Compound Hazards in a Warming World. *Annual Review of Earth and Planetary Sciences*, 48.

AghaKouchak, A. et al., 2015b. Remote sensing of drought: Progress, challenges and opportunities. *Reviews of Geophysics*, 53(2): 452-480.

Agutu, N. et al., 2017. Assessing multi-satellite remote sensing, reanalysis, and land surface models' products in characterizing agricultural drought in East Africa. *Remote Sensing of Environment*, 194: 287-302.

Al-Yaari, A. et al., 2016. Testing regression equations to derive long-term global soil moisture datasets from passive microwave observations. *Remote Sensing of Environment*, 180: 453-464.

Ali, I., Greifeneder, F., Stamenkovic, J., Neumann, M. and Notarnicola, C., 2015. Review of machine learning approaches for biomass and soil moisture retrievals from remote sensing data. *Remote Sensing*, 7(12): 16398-16421.

Alizadeh, M.R. and Nikoo, M.R., 2018. A fusion-based methodology for meteorological drought estimation using remote sensing data. *Remote Sensing of Environment*, 211: 229-247.

Allen, C.D., Breshears, D.D. and McDowell, N.G., 2015. On underestimation of global vulnerability to tree mortality and forest die-off from hotter drought in the Anthropocene. *Ecosphere*, 6(8): 1-55.

Allen, C.D. et al., 2010. A global overview of drought and heat-induced tree mortality reveals emerging climate change risks for forests. *Forest Ecology and Management*, 259(4): 660-684.

Allen, R.G., Tasumi, M. and Trezza, R., 2007. Satellite-based energy balance for mapping evapotranspiration with internalized calibration (METRIC)—Model. *Journal of Irrigation and Drainage Engineering*, 133(4): 380-394.

Anderegg, W.R., 2015. Spatial and temporal variation in plant hydraulic traits and their relevance for climate change impacts on vegetation. *New Phytologist*, 205(3): 1008-1014.

Anderegg, W.R., Anderegg, L.D., Kerr, K.L. and Trugman, A.T., 2019. Widespread drought-induced tree mortality at dry range edges indicates that climate stress exceeds species' compensating mechanisms. *Global Change Biology*, 25(11): 3793-3802.

Anderegg, W.R., Berry, J.A. and Field, C.B., 2012. Linking definitions, mechanisms, and modeling of drought-induced tree death. *Trends in Plant Science*, 17(12): 693-700.

Anderegg, W.R. et al., 2018. Hydraulic diversity of forests regulates ecosystem resilience during drought. *Nature*, 561(7724): 538.

Anderegg, W.R. et al., 2015. Pervasive drought legacies in forest ecosystems and their implications for carbon cycle models. *Science*, 349(6247): 528-532.

Anderson, M. et al., 2008. A thermal-based remote sensing technique for routine mapping of land-surface carbon, water and energy fluxes from field to regional scales. *Remote Sensing of Environment*, 112(12): 4227-4241.

Anderson, M.C. et al., 2011. Evaluation of drought indices based on thermal remote sensing of evapotranspiration over the continental United States. *Journal of Climate*, 24(8): 2025-2044.

Anderson, M.C. et al., 2011. Mapping daily evapotranspiration at field to continental scales using geostationary and polar orbiting satellite imagery. *Hydrology and Earth System Sciences*.

Anderson, M.C. et al., 2016. The Evaporative Stress Index as an indicator of agricultural drought in Brazil: An assessment based on crop yield impacts. *Remote Sensing of Environment*, 174: 82-99.

Andreadis, K.M., Clark, E.A., Wood, A.W., Hamlet, A.F. and Lettenmaier, D.P., 2005. Twentieth-century drought in the conterminous United States. *Journal of Hydrometeorology*, 6(6): 985-1001.

Arabzadeh, R., Kholoosi, M.M. and Bazrafshan, J., 2016. Regional hydrological drought monitoring using principal components analysis. *Journal of Irrigation and Drainage Engineering*, 142(1): 04015029.

Aragon, B., Houborg, R., Tu, K., Fisher, J.B. and McCabe, M., 2018. CubeSats enable high spatiotemporal retrievals of crop-water use for precision agriculture. *Remote Sensing*, 10(12): 1867.

Aruldoss, M., Lakshmi, T.M. and Venkatesan, V.P., 2013. A survey on multi criteria decision making methods and its applications. *American Journal of Information Systems*, 1(1): 31-43.

Asgarimehr, M., Zavorotny, V., Wickert, J. and Reich, S., 2018. Can GNSS reflectometry detect precipitation over oceans? *Geophysical Research Letters*, 45(22): 12,585-12,592.

Ashouri, H. et al., 2015. PERSIANN-CDR: Daily precipitation climate data record from multisatellite observations for hydrological and climate studies. *Bulletin of the American Meteorological Society*, 96(1): 69-83.

Asner, G.P. and Alencar, A., 2010. Drought impacts on the Amazon forest: the remote sensing perspective. *New phytologist*, 187(3): 569-578.

Asner, G.P. et al., 2016. Progressive forest canopy water loss during the 2012–2015 California drought. *Proceedings of the National Academy of Sciences*, 113(2): E249-E255.

Asner, G.P. et al., 2005. Selective logging in the Brazilian Amazon. *Science*, 310(5747): 480-482.

Asner, G.P. et al., 2007. Carnegie airborne observatory: in-flight fusion of hyperspectral imaging and waveform light detection and ranging for three-dimensional studies of ecosystems. *Journal of Applied Remote Sensing*, 1(1): 013536.

Asner, G.P., Nepstad, D., Cardinot, G. and Ray, D., 2004. Drought stress and carbon uptake in an Amazon forest measured with spaceborne imaging spectroscopy. *Proceedings of the National Academy of Sciences*, 101(16): 6039-6044.

Aubrecht, D.M. et al., 2016. Continuous, long-term, high-frequency thermal imaging of vegetation: Uncertainties and recommended best practices. *Agricultural and forest Meteorology*, 228: 315-326.

Azmi, M., Rüdiger, C. and Walker, J.P., 2016. A data fusion-based drought index. *Water Resources Research*, 52(3): 2222-2239.

Badgley, G., Field, C.B. and Berry, J.A., 2017. Canopy near-infrared reflectance and terrestrial photosynthesis. *Science Advances*, 3(3): e1602244.

Baig, M.H.A. et al., 2020. Assessing Meteorological and Agricultural Drought in Chitral Kabul River Basin Using Multiple Drought Indices. *Remote Sensing*, 12(9): 1417.

Baldocchi, D. et al., 2001. FLUXNET: A new tool to study the temporal and spatial variability of ecosystem-scale carbon dioxide, water vapor, and energy flux densities. *Bulletin of the American Meteorological Society*, 82(11): 2415-2434.

Bandopadhyay, S., Rastogi, A. and Juszczak, R., 2020. Review of Top-of-Canopy Sun-Induced Fluorescence (SIF) studies from ground, UAV, airborne to spaceborne observations. *Sensors*, 20(4): 1144.

Bannari, A., Morin, D., Bonn, F. and Huete, A., 1995. A review of vegetation indices. *Remote Sensing Reviews*, 13(1-2): 95-120.

Barua, S., Ng, A. and Perera, B., 2011. Comparative evaluation of drought indexes: case study on the Yarra River catchment in Australia. *Journal of Water Resources Planning and Management*, 137(2): 215-226.

Bazrafshan, J., Hejabi, S. and Rahimi, J., 2014. Drought monitoring using the multivariate standardized precipitation index (MSPI). *Water Resources Management*, 28(4): 1045-1060.

Bazrafshan, J., Nadi, M. and Ghorbani, K., 2015. Comparison of empirical copula-based joint deficit index (JDI) and multivariate standardized precipitation index (MSPI) for drought monitoring in Iran. *Water Resources Management*, 29(6): 2027-2044.

Beck, H.E. et al., 2011. Global evaluation of four AVHRR–NDVI data sets: Intercomparison and assessment against Landsat imagery. *Remote Sensing of Environment*, 115(10): 2547-2563.

Beck, H.E. et al., 2020. Global-scale evaluation of 22 precipitation datasets using gauge observations and hydrological modeling, Satellite Precipitation Measurement. Springer, pp. 625-653.

Beck, H.E. et al., 2019. MSWEP V2 global 3-hourly 0.1 precipitation: methodology and quantitative assessment. *Bulletin of the American Meteorological Society*, 100(3): 473-500.

Beck, P.S., Atzberger, C., Høgda, K.A., Johansen, B. and Skidmore, A.K., 2006. Improved monitoring of vegetation dynamics at very high latitudes: A new method using MODIS NDVI. *Remote Sensing of Environment*, 100(3): 321-334.

Bell, J.W., Amelung, F., Ferretti, A., Bianchi, M. and Novali, F., 2008. Permanent scatterer InSAR reveals seasonal and long-term aquifer-system response to groundwater pumping and artificial recharge. *Water Resources Research*, 44(2).

Berg, A. and Sheffield, J., 2019. Historic and projected changes in coupling between soil moisture and evapotranspiration (ET) in CMIP5 models confounded by the role of different ET components. *Journal of Geophysical Research: Atmospheres*, 124(11): 5791-5806.

Bhanja, S.N., Mukherjee, A., Saha, D., Velicogna, I. and Famiglietti, J.S., 2016. Validation of GRACE based groundwater storage anomaly using in-situ groundwater level measurements in India. *Journal of Hydrology*, 543: 729-738.

Bolten, J.D., Crow, W.T., Zhan, X., Jackson, T.J. and Reynolds, C.A., 2009. Evaluating the utility of remotely sensed soil moisture retrievals for operational agricultural drought monitoring. *IEEE Journal of Selected Topics in Applied Earth Observations and Remote Sensing*, 3(1): 57-66.

Brando, P.M. et al., 2014. Abrupt increases in Amazonian tree mortality due to drought–fire interactions. *Proceedings of the National Academy of Sciences*, 111(17): 6347-6352.

Brando, P.M. et al., 2008. Drought effects on litterfall, wood production and belowground carbon cycling in an Amazon forest: results of a throughfall reduction experiment. *Philosophical Transactions of the Royal Society B: Biological Sciences*, 363(1498): 1839-1848.

Brocca, L. et al., 2011. Soil moisture estimation through ASCAT and AMSR-E sensors: An intercomparison and validation study across Europe. *Remote Sensing of Environment*, 115(12): 3390-3408.

Brodrick, P., Anderegg, L. and Asner, G., 2019. Forest drought resistance at large geographic scales. *Geophysical Research Letters*, 46(5): 2752-2760.

Brodrick, P. and Asner, G., 2017. Remotely sensed predictors of conifer tree mortality during severe drought. *Environmental Research Letters*, 12(11): 115013.

Brown, J.F., Wardlow, B.D., Tadesse, T., Hayes, M.J. and Reed, B.C., 2008. The Vegetation Drought Response Index (VegDRI): A new integrated approach for

monitoring drought stress in vegetation. *GIScience & Remote Sensing*, 45(1): 16-46.

Brown, R.D., Brasnett, B. and Robinson, D., 2003. Gridded North American monthly snow depth and snow water equivalent for GCM evaluation. *Atmosphere-Ocean*, 41(1): 1-14.

Bruinsma, S., Lemoine, J.-M., Biancale, R. and Valès, N., 2010. CNES/GRGS 10-day gravity field models (release 2) and their evaluation. *Advances in Space Research*, 45(4): 587-601.

Buermann, W. et al., 2018a. Widespread seasonal compensation effects of spring warming on northern plant productivity. *Nature*, 562(7725): 110-114.

Cardellach, E. et al., 2019. Sensing heavy precipitation with GNSS polarimetric radio occultations. *Geophysical Research Letters*, 46(2): 1024-1031.

Castellazzi, P. et al., 2018. Quantitative mapping of groundwater depletion at the water management scale using a combined GRACE/InSAR approach. *Remote Sensing of Environment*, 205: 408-418.

Castellazzi, P., Martel, R., Galloway, D.L., Longuevergne, L. and Rivera, A., 2016. Assessing groundwater depletion and dynamics using GRACE and InSAR: potential and limitations. *Groundwater*, 54(6): 768-780.

Cendrero-Mateo, M.P. et al., 2019. Sun-induced chlorophyll fluorescence III: Benchmarking retrieval methods and sensor characteristics for proximal sensing. *Remote Sensing*, 11(8): 962.

Chang, A. and Rango, A., 2000. Algorithm theoretical basis document (ATBD) for the AMSR-E snow water equivalent algorithm. *NASA/GSFC, Nov*.

Chang, Q. et al., 2019. Assessing consistency of spring phenology of snow-covered forests as estimated by vegetation indices, gross primary production, and solar-induced chlorophyll fluorescence. *Agricultural and Forest Meteorology*, 275: 305-316.

Chang, Q. et al., 2020. Estimating site-specific optimum air temperature and assessing its effect on the photosynthesis of grasslands in mid-to high-latitudes. *Environmental Research Letters*, 15(3): 034064.

Chen, J., Famigliett, J.S., Scanlon, B.R. and Rodell, M., 2016. Groundwater storage changes: present status from GRACE observations, Remote Sensing and Water Resources. Springer, pp. 207-227.

Chen, J., Menges, C. and Leblanc, S., 2005. Global mapping of foliage clumping index using multi-angular satellite data. *Remote Sensing of Environment*, 97(4): 447-457.

Chen, L.-C., Teo, T.-A., Shao, Y.-C., Lai, Y.-C. and Rau, J.-Y., 2004. Fusion of LIDAR data and optical imagery for building modeling. *International Archives of Photogrammetry and Remote Sensing*, 35(B4): 732-737.

Chen, L.G. et al., 2019. Flash drought characteristics based on US Drought Monitor. *Atmosphere*, 10(9): 498.

Chen, T., Van der Werf, G., De Jeu, R., Wang, G. and Dolman, A., 2013. A global analysis of the impact of drought on net primary productivity. *Hydrology and Earth System Sciences*, 17: 3885-3894.

Chen, Y. et al., 2014. Comparison of satellite-based evapotranspiration models over terrestrial ecosystems in China. *Remote Sensing of Environment*, 140: 279-293.

Christian, J.I. et al., 2019. A methodology for flash drought identification: Application of flash drought frequency across the United States. *Journal of Hydrometeorology*, 20(5): 833-846.

Ciais, P. et al., 2005b. Europe-wide reduction in primary productivity caused by the heat and drought in 2003. *Nature*, 437(7058): 529.

Claverie, M. et al., 2018. The Harmonized Landsat and Sentinel-2 surface reflectance data set. *Remote Sensing of Environment*, 219: 145-161.

Coates, A.R., Dennison, P.E., Roberts, D.A. and Roth, K.L., 2015. Monitoring the impacts of severe drought on southern California chaparral species using hyperspectral and thermal infrared imagery. *Remote Sensing*, 7(11): 14276-14291.

Coyle, D.B., Stysley, P.R., Poulios, D., Clarke, G.B. and Kay, R.B., 2015. Laser transmitter development for NASA's Global Ecosystem Dynamics Investigation (GEDI) lidar, Lidar Remote Sensing for Environmental Monitoring XV. International Society for Optics and Photonics, pp. 961208.

Crausbay, S.D. et al., 2017. Defining ecological drought for the twenty-first century. *Bulletin of the American Meteorological Society*, 98(12): 2543-2550.

Dai, A., 2011. Drought under global warming: a review. *Wiley Interdisciplinary Reviews: Climate Change*, 2(1): 45-65.

Dai, A., 2013. Increasing drought under global warming in observations and models. *Nature Climate Change*, 3(1): 52.

Damberg, L. and AghaKouchak, A., 2014. Global trends and patterns of drought from space. *Theoretical and Applied Climatology*, 117(3-4): 441-448.

Daryanto, S., Wang, L. and Jacinthe, P.-A., 2015. Global synthesis of drought effects on food legume production. *PloS one*, 10(6): e0127401.

Daryanto, S., Wang, L. and Jacinthe, P.-A., 2016. Global synthesis of drought effects on maize and wheat production. *PloS One*, 11(5): e0156362.

Das, N.N., Entekhabi, D. and Njoku, E.G., 2010. An algorithm for merging SMAP radiometer and radar data for high-resolution soil-moisture retrieval. *IEEE Transactions on Geoscience and Remote Sensing*, 49(5): 1504-1512.

Dash, J. and Curran, P., 2007. Evaluation of the MERIS terrestrial chlorophyll index (MTCI). *Advances in Space Research*, 39(1): 100-104.

De Moura, Y.M. et al., 2015. Seasonality and drought effects of Amazonian forests observed from multi-angle satellite data. *Remote Sensing of Environment*, 171: 278-290.

Degerickx, J., Roberts, D.A., McFadden, J.P., Hermy, M. and Somers, B., 2018. Urban tree health assessment using airborne hyperspectral and LiDAR imagery. *International Journal of Applied Earth Observation and Geoinformation*, 73: 26-38.

Derin, Y. and Yilmaz, K.K., 2014. Evaluation of multiple satellite-based precipitation products over complex topography. *Journal of Hydrometeorology*, 15(4): 1498-1516.

Dolman, A.J., Miralles, D.G. and de Jeu, R.A., 2014. Fifty years since Monteith's 1965 seminal paper: the emergence of global ecohydrology. *Ecohydrology*, 7(3): 897-902.

Donohue, I. et al., 2013. On the dimensionality of ecological stability. *Ecology Letters*, 16(4): 421-429.

Dorigo, W. et al., 2012. Evaluating global trends (1988–2010) in harmonized multi-satellite surface soil moisture. *Geophysical Research Letters*, 39(18).

Dorigo, W. et al., 2017. ESA CCI Soil Moisture for improved Earth system understanding: State-of-the art and future directions. *Remote Sensing of Environment*, 203: 185-215.

Douville, H., Ribes, A., Decharme, B., Alkama, R. and Sheffield, J., 2013. Anthropogenic influence on multidecadal changes in reconstructed global evapotranspiration. *Nature Climate Change*, 3(1): 59-62.

Du, L. et al., 2013. A comprehensive drought monitoring method integrating MODIS and TRMM data. *International Journal of Applied Earth Observation and Geoinformation*, 23: 245-253.

Faghmous, J.H. and Kumar, V., 2014. A big data guide to understanding climate change: The case for theory-guided data science. *Big Data*, 2(3): 155-163.

Fan, L. et al., 2018. Evaluation of microwave remote sensing for monitoring live fuel moisture content in the Mediterranean region. *Remote Sensing of Environment*, 205: 210-223.

Fang, H., Baret, F., Plummer, S. and Schaepman-Strub, G., 2019. An overview of global leaf area index (LAI): Methods, products, validation, and applications. *Reviews of Geophysics*, 57(3): 739-799.

Farquhar, G.D., von Caemmerer, S.v. and Berry, J.A., 1980. A biochemical model of photosynthetic CO 2 assimilation in leaves of C 3 species. *Planta*, 149(1): 78-90.

Fatoyinbo, L. et al., 2017. The 2016 NASA AfriSAR campaign: Airborne SAR and Lidar measurements of tropical forest structure and biomass in support of future satellite missions, 2017 IEEE International Geoscience and Remote Sensing Symposium (IGARSS). IEEE, pp. 4286-4287.

Feng, G., Masek, J., Schwaller, M. and Hall, F., 2006. On the blending of the Landsat and MODIS surface reflectance: predicting daily Landsat surface reflectance. *IEEE Transactions on Geoscience and Remote Sensing*, 44(8): 2207-2218.

Feng, P., Wang, B., Li Liu, D. and Yu, Q., 2019. Machine learning-based integration of remotely-sensed drought factors can improve the estimation of agricultural drought in South-Eastern Australia. *Agricultural Systems*, 173: 303-316.

Feng, W. et al., 2013. Evaluation of groundwater depletion in North China using the Gravity Recovery and Climate Experiment (GRACE) data and ground-based measurements. *Water Resources Research*, 49(4): 2110-2118.

Fischer, E.M., Seneviratne, S.I., Lüthi, D. and Schär, C., 2007. Contribution of land-atmosphere coupling to recent European summer heat waves. *Geophysical Research Letters*, 34(6).

Fisher, J.B. et al., 2020. ECOSTRESS: NASA's next generation mission to measure evapotranspiration from the International Space Station. *Water Resources Research*, 56(4).

Fisher, J.B. et al., 2017. The future of evapotranspiration: Global requirements for ecosystem functioning, carbon and climate feedbacks, agricultural management, and water resources. *Water Resources Research*, 53(4): 2618-2626.

Flanner, M.G. and Zender, C.S., 2006. Linking snowpack microphysics and albedo evolution. *Journal of Geophysical Research: Atmospheres*, 111(D12).

Flechtner, F. et al., 2016. What can be expected from the GRACE-FO laser ranging interferometer for Earth science applications?, Remote Sensing and Water Resources. Springer, pp. 263-280.

Ford, T.W. and Labosier, C.F., 2017. Meteorological conditions associated with the onset of flash drought in the eastern United States. *Agricultural and Forest Meteorology*, 247: 414-423.

Fosu, B.O., Simon Wang, S.-Y. and Yoon, J.-H., 2016. The 2014/15 snowpack drought in Washington State and its climate forcing. *Bulletin of the American Meteorological Society*, 97(12): S19-S24.

Frankenberg, C. et al., 2011. New global observations of the terrestrial carbon cycle from GOSAT: Patterns of plant fluorescence with gross primary productivity. *Geophysical Research Letters*, 38(17).

Frankenberg, C. et al., 2014. Prospects for chlorophyll fluorescence remote sensing from the Orbiting Carbon Observatory-2. *Remote Sensing of Environment*, 147: 1-12.

Frappart, F. and Ramillien, G., 2018. Monitoring groundwater storage changes using the Gravity Recovery and Climate Experiment (GRACE) satellite mission: A review. *Remote Sensing*, 10(6): 829.

Frei, A. et al., 2012. A review of global satellite-derived snow products. *Advances in Space Research*, 50(8): 1007-1029.

Frolking, S. et al., 2009. Forest disturbance and recovery: A general review in the context of spaceborne remote sensing of impacts on aboveground biomass and canopy structure. *Journal of Geophysical Research: Biogeosciences*, 114(G2).

Fukai, S. and Cooper, M., 1995. Development of drought-resistant cultivars using physiomorphological traits in rice. *Field Crops Research*, 40(2): 67-86.

Galloway, D.L. and Hoffmann, J., 2007. The application of satellite differential SAR interferometry-derived ground displacements in hydrogeology. *Hydrogeology Journal*, 15(1): 133-154.

Gao, B., 1996. NDWI—A normalized difference water index for remote sensing of vegetation liquid water from space. *Remote Sensing of Environment*, 58(3): 257-266.

Garcia, R.A., Cabeza, M., Rahbek, C. and Araújo, M.B., 2014. Multiple dimensions of climate change and their implications for biodiversity. *Science*, 344(6183): 1247579.

Gehne, M., Hamill, T.M., Kiladis, G.N. and Trenberth, K.E., 2016. Comparison of global precipitation estimates across a range of temporal and spatial scales. *Journal of Climate*, 29(21): 7773-7795.

Giglio, L., Randerson, J.T. and van der Werf, G.R., 2013. Analysis of daily, monthly, and annual burned area using the fourth-generation global fire emissions database (GFED4). *Journal of Geophysical Research: Biogeosciences*, 118(1): 317-328.

Godfray, H.C.J. et al., 2010. Food security: the challenge of feeding 9 billion people. *Science*, 327(5967): 812-818.

Goetz, S.J., Fiske, G.J. and Bunn, A.G., 2006. Using satellite time-series data sets to analyze fire disturbance and forest recovery across Canada. *Remote Sensing of Environment*, 101(3): 352-365.

Gonçalves, N.B. et al., 2020. Both near-surface and satellite remote sensing confirm drought legacy effect on tropical forest leaf phenology after 2015/2016 ENSO drought. *Remote Sensing of Environment*, 237: 111489.

Goodman, S.J., 2020. GOES-R series introduction, The GOES-R Series. Elsevier, pp. 1-3.

Goward, S.N., Cruickshanks, G.D. and Hope, A.S., 1985. Observed relation between thermal emission and reflected spectral radiance of a complex vegetated landscape. *Remote Sensing of Environment*, 18(2): 137-146.

Grabisch, M., 1996. The application of fuzzy integrals in multicriteria decision making. *European Journal of Operational Research*, 89(3): 445-456.

Griffin-Nolan, R.J. et al., 2019. Shifts in plant functional composition following long-term drought in grasslands. *Journal of Ecology*, 107(5): 2133-2148.

Gruber, A., Scanlon, T., van der Schalie, R., Wagner, W. and Dorigo, W., 2019. Evolution of the ESA CCI Soil Moisture climate data records and their underlying merging methodology. *Earth System Science Data*: 1-37.

Guan, K. et al., 2016. Improving the monitoring of crop productivity using spaceborne solar-induced fluorescence. *Global Change Biology*, 22(2): 716-726.

Guanter, L. et al., 2007. Estimation of solar-induced vegetation fluorescence from space measurements. *Geophysical Research Letters*, 34(8).

Guanter, L. et al., 2014a. Global and time-resolved monitoring of crop photosynthesis with chlorophyll fluorescence. *Proceedings of the National Academy of Sciences*, 111(14): E1327-E1333.

Gutman, G., 1999. On the monitoring of land surface temperatures with the NOAA/AVHRR: removing the effect of satellite orbit drift. *International Journal of Remote Sensing*, 20(17): 3407-3413.

Haile, G.G., Tang, Q., Li, W., Liu, X. and Zhang, X., 2020. Drought: Progress in broadening its understanding. *Wiley Interdisciplinary Reviews: Water*, 7(2): e1407.

Hall, D.K., Riggs, G.A., Salomonson, V.V., DiGirolamo, N.E. and Bayr, K.J., 2002. MODIS snow-cover products. *Remote Sensing of Environment*, 83(1-2): 181-194.

Hamaguchi, R., Fujita, A., Nemoto, K., Imaizumi, T. and Hikosaka, S., 2018. Effective use of dilated convolutions for segmenting small object instances in remote sensing imagery, 2018 IEEE winter conference on applications of computer vision (WACV). IEEE, pp. 1442-1450.

Hamlet, A.F., Mote, P.W., Clark, M.P. and Lettenmaier, D.P., 2005. Effects of temperature and precipitation variability on snowpack trends in the western United States. *Journal of Climate*, 18(21): 4545-4561.

Han, H., Bai, J., Yan, J., Yang, H. and Ma, G., 2019. A combined drought monitoring index based on multi-sensor remote sensing data and machine learning. *Geocarto International*: 1-16.

Hancock, S. et al., 2019. The GEDI simulator: A large-footprint waveform lidar simulator for calibration and validation of spaceborne missions. *Earth and Space Science*, 6(2): 294-310.

Hao, C., Zhang, J. and Yao, F., 2015. Combination of multi-sensor remote sensing data for drought monitoring over Southwest China. *International Journal of Applied Earth Observation and Geoinformation*, 35: 270-283.

Hao, Z. and AghaKouchak, A., 2013b. Multivariate standardized drought index: a parametric multi-index model. *Advances in Water Resources*, 57: 12-18.

Hao, Z. and AghaKouchak, A., 2014. A nonparametric multivariate multi-index drought monitoring framework. *Journal of Hydrometeorology*, 15(1): 89-101.

Hao, Z. and Singh, V.P., 2015. Drought characterization from a multivariate perspective: A review. *Journal of Hydrology*, 527: 668-678.

Hao, Z., Singh, V.P. and Hao, F., 2018. Compound extremes in hydroclimatology: a review. *Water*, 10(6): 718.

Hao, Z., Singh, V.P. and Xia, Y., 2018. Seasonal drought prediction: advances, challenges, and future prospects. *Reviews of Geophysics*, 56(1): 108-141.

Hao, Z., Yuan, X., Xia, Y., Hao, F. and Singh, V.P., 2017b. An overview of drought monitoring and prediction systems at regional and global scales. *Bulletin of the American Meteorological Society*.

Hardisky, M.A., Klemas, V. and Smart, R.M., 1983. The influence of soil salinity, growth form, and leaf moisture on the spectral radiance of Spartina alterniflora canopies. *Photogrammetric Engineering & Remote Sensing*, 49(1): 77-83.

Hartmann, H., 2015. Carbon starvation during drought-induced tree mortality–are we chasing a myth?

Hayes, M.J., Alvord, C. and Lowrey, J., 2007. Drought indices. *Intermountain West Climate Summary*, 3(6): 2-6.

He, L. et al., 2019. Diverse photosynthetic capacity of global ecosystems mapped by satellite chlorophyll fluorescence measurements. *Remote Sensing of Environment*, 232: 111344.

He, M. et al., 2016. Satellite detection of soil moisture related water stress impacts on ecosystem productivity using the MODIS-based photochemical reflectance index. *Remote Sensing of Environment*, 186: 173-183.

Helfrich, S.R., McNamara, D., Ramsay, B.H., Baldwin, T. and Kasheta, T., 2007. Enhancements to, and forthcoming developments in the Interactive Multisensor Snow and Ice Mapping System (IMS). *Hydrological Processes: An International Journal*, 21(12): 1576-1586.

Hobbins, M.T. et al., 2016. The evaporative demand drought index. Part I: Linking drought evolution to variations in evaporative demand. *Journal of Hydrometeorology*, 17(6): 1745-1761.

Hou, A.Y. et al., 2014. The global precipitation measurement mission. *Bulletin of the American Meteorological Society*, 95(5): 701-722.

Hou, A.Y., Skofronick-Jackson, G., Kummerow, C.D. and Shepherd, J.M., 2008. Global precipitation measurement, Precipitation: Advances in Measurement, Estimation and Prediction. Springer, pp. 131-169.

Houborg, R. and McCabe, M.F., 2018a. A cubesat enabled spatio-temporal enhancement method (cestem) utilizing planet, landsat and modis data. *Remote Sensing of Environment*, 209: 211-226.

Houborg, R. and McCabe, M.F., 2018b. Daily Retrieval of NDVI and LAI at 3 m Resolution via the Fusion of CubeSat, Landsat, and MODIS Data. *Remote Sensing*, 10(6): 890.

Hu, T. et al., 2020. Monitoring agricultural drought in Australia using MTSAT-2 land surface temperature retrievals. *Remote Sensing of Environment*, 236: 111419.

Hu, T. et al., 2020. On agricultural drought monitoring in Australia using Himawari-8 geostationary thermal infrared observations. *International Journal of Applied Earth Observation and Geoinformation*, 91: 102153.

Huang, C., Anderegg, W.R. and Asner, G.P., 2019. Remote sensing of forest die-off in the Anthropocene: From plant ecophysiology to canopy structure. *Remote Sensing of Environment*, 231: 111233.

Huang, S., Chang, J., Leng, G. and Huang, Q., 2015. Integrated index for drought assessment based on variable fuzzy set theory: a case study in the Yellow River basin, China. *Journal of Hydrology*, 527: 608-618.

Huang, S., Huang, Q., Leng, G. and Chang, J., 2016. A hybrid index for characterizing drought based on a nonparametric kernel estimator. *Journal of Applied Meteorology and Climatology*, 55(6): 1377-1389.

Huete, A., 1988. Huete, AR A soil-adjusted vegetation index (SAVI). Remote Sensing of Environment. *Remote Sensing of Environment*, 25: 295-309.

Huete, A. et al., 2002. Overview of the radiometric and biophysical performance of the MODIS vegetation indices. *Remote Sensing of Environment*, 83(1-2): 195-213.

Huffman, G.J. et al., 2007. The TRMM multisatellite precipitation analysis (TMPA): Quasi-global, multiyear, combined-sensor precipitation estimates at fine scales. *Journal of Hydrometeorology*, 8(1): 38-55.

Huntington, J.L. et al., 2017. Climate Engine: cloud computing and visualization of climate and remote sensing data for advanced natural resource monitoring and process understanding. *Bulletin of the American Meteorological Society*, 98(11): 2397-2410.

Hwang, T. et al., 2017. Capturing species-level drought responses in a temperate deciduous forest using ratios of photochemical reflectance indices between sunlit and shaded canopies. *Remote Sensing of Environment*, 199: 350-359.

Iwasaki, A., Ohgi, N., Tanii, J., Kawashima, T. and Inada, H., 2011. Hyperspectral Imager Suite (HISUI)-Japanese hyper-multi spectral radiometer, 2011 IEEE International Geoscience and Remote Sensing Symposium. IEEE, pp. 1025-1028.

Jasechko, S. et al., 2013. Terrestrial water fluxes dominated by transpiration. *Nature*, 496(7445): 347-350.

Jiang, H. and Eastman, J.R., 2000. Application of fuzzy measures in multi-criteria evaluation in GIS. *International Journal of Geographical Information Science*, 14(2): 173-184.

Jiao, T., Williams, C.A., Rogan, J., De Kauwe, M.G. and Medlyn, B.E., 2020. Drought impacts on Australian vegetation during the Millennium drought measured with

multisource spaceborne remote sensing. *Journal of Geophysical Research: Biogeosciences*, 125(2).

Jiao, W., Chang, Q. and Wang, L., 2019. The Sensitivity of Satellite Solar-Induced Chlorophyll Fluorescence to Meteorological Drought. *Earth's Future*, 7(5): 558-573.

Jiao, W., Tian, C., Chang, Q., Novick, K.A. and Wang, L., 2019. A new multi-sensor integrated index for drought monitoring. *Agricultural and Forest Meteorology*, 268: 74-85.

Jiao, W., Wang, L., Novick, K.A. and Chang, Q., 2019. A new station-enabled multi-sensor integrated index for drought monitoring. *Journal of Hydrology*, 574: 169-180.

Jiménez-Muñoz, J.C. and Sobrino, J.A., 2009. A single-channel algorithm for land-surface temperature retrieval from ASTER data. *IEEE Geoscience and Remote Sensing Letters*, 7(1): 176-179.

Jimenez, C. et al., 2011. Global intercomparison of 12 land surface heat flux estimates. *Journal of Geophysical Research: Atmospheres*, 116(D2).

Joiner, J. et al., 2013. Global monitoring of terrestrial chlorophyll fluorescence from moderate spectral resolution near-infrared satellite measurements: methodology, simulations, and application to GOME-2. *Atmospheric Measurement Techniques*, 6(2): 2803-2823.

Joiner, J., Yoshida, Y., Vasilkov, A. and Middleton, E., 2011. First observations of global and seasonal terrestrial chlorophyll fluorescence from space. *Biogeosciences*, 8(3): 637-651.

Joiner, J. et al., 2012. Filling-in of near-infrared solar lines by terrestrial fluorescence and other geophysical effects: simulations and space-based observations from SCIAMACHY and GOSAT. *Atmospheric Measurement Techniques*, 5(4): 809-829.

Kalma, J.D., McVicar, T.R. and McCabe, M.F., 2008. Estimating land surface evaporation: A review of methods using remotely sensed surface temperature data. *Surveys in Geophysics*, 29(4-5): 421-469.

Kalra, A., Piechota, T.C., Davies, R. and Tootle, G.A., 2008. Changes in US streamflow and western US snowpack. *Journal of Hydrologic Engineering*, 13(3): 156-163.

Kannenberg, S.A., Schwalm, C.R. and Anderegg, W.R., 2020. Ghosts of the past: how drought legacy effects shape forest functioning and carbon cycling. *Ecology Letters*, 23(5): 891-901.

Kao, S.-C. and Govindaraju, R.S., 2010. A copula-based joint deficit index for droughts. *Journal of Hydrology*, 380(1-2): 121-134.

Karl, T., Quinlan, F. and Ezell, D., 1987. Drought termination and amelioration: Its climatological probability. *Journal of Climate and Applied Meteorology*, 26(9): 1198-1209.

Kaufmann, H. et al., 2008. Environmental mapping and analysis program (EnMAP)-Recent advances and status, IGARSS 2008-2008 IEEE International Geoscience and Remote Sensing Symposium. IEEE, pp. IV-109-IV-112.

Kerr, Y.H., Lagouarde, J.P. and Imbernon, J., 1992. Accurate land surface temperature retrieval from AVHRR data with use of an improved split window algorithm. *Remote Sensing of Environment*, 41(2-3): 197-209.

Kerr, Y.H. et al., 2012. The SMOS soil moisture retrieval algorithm. *IEEE Transactions on Geoscience and Remote Sensing*, 50(5): 1384-1403.

Keshavarz, M.R., Vazifedoust, M. and Alizadeh, A., 2014. Drought monitoring using a Soil Wetness Deficit Index (SWDI) derived from MODIS satellite data. *Agricultural Water Management*, 132: 37-45.

Keyantash, J.A. and Dracup, J.A., 2004. An aggregate drought index: Assessing drought severity based on fluctuations in the hydrologic cycle and surface water storage. *Water Resources Research*, 40(9).

Kim, S., Liu, Y.Y., Johnson, F.M., Parinussa, R.M. and Sharma, A., 2015. A global comparison of alternate AMSR2 soil moisture products: Why do they differ? *Remote Sensing of Environment*, 161: 43-62.

Klein, T., 2014. The variability of stomatal sensitivity to leaf water potential across tree species indicates a continuum between isohydric and anisohydric behaviours. *Functional Ecology*, 28(6): 1313-1320.

Köhler, P. et al., 2018. Global Retrievals of Solar-Induced Chlorophyll Fluorescence With TROPOMI: First Results and Intersensor Comparison to OCO-2. *Geophysical Research Letters*, 45(19): 10,456-10,463.

Köhler, P., Guanter, L. and Joiner, J., 2014. A linear method for the retrieval of sun-induced chlorophyll fluorescence from GOME-2 and SCIAMACHY data. *Atmospheric Measurement Techniques*, 7(12): 12,173-12,217.

Kokaly, R.F., Asner, G.P., Ollinger, S.V., Martin, M.E. and Wessman, C.A., 2009. Characterizing canopy biochemistry from imaging spectroscopy and its application to ecosystem studies. *Remote Sensing of Environment*, 113: S78-S91.

Konings, A.G., Rao, K. and Steele-Dunne, S.C., 2019. Macro to micro: microwave remote sensing of plant water content for physiology and ecology. *New Phytologist*, 223(3): 1166-1172.

Kubota, T. et al., 2007. Global precipitation map using satellite-borne microwave radiometers by the GSMaP project: Production and validation. *IEEE Transactions on Geoscience and Remote Sensing*, 45(7): 2259-2275.

Kull, O., Broadmeadow, M., Kruijt, B. and Meir, P., 1999. Light distribution and foliage structure in an oak canopy. *Trees*, 14(2): 55-64.

Kumar, S.V. et al., 2019. NCA-LDAS land analysis: Development and performance of a multisensor, multivariate land data assimilation system for the National Climate Assessment. *Journal of Hydrometeorology*, 20(8): 1571-1593.

Kumar, S.V. et al., 2014. Assimilation of remotely sensed soil moisture and snow depth retrievals for drought estimation. *Journal of Hydrometeorology*, 15(6): 2446-2469.

Kustas, W. and Norman, J., 1996. Use of remote sensing for evapotranspiration monitoring over land surfaces. *Hydrological Sciences Journal*, 41(4): 495-516.

Labate, D. et al., 2009. The PRISMA payload optomechanical design, a high performance instrument for a new hyperspectral mission. *Acta Astronautica*, 65(9-10): 1429-1436.

Lanning, M., Wang, L. and Novick, K.A., 2020. The importance of cuticular permeance in assessing plant water–use strategies. *Tree Physiology*, 40(4): 425-432.

Lanning, M. et al., 2019. Intensified vegetation water use under acid deposition. *Science Advances*, 5(7): eaav5168.

Lary, D.J., Alavi, A.H., Gandomi, A.H. and Walker, A.L., 2016. Machine learning in geosciences and remote sensing. *Geoscience Frontiers*, 7(1): 3-10.

Lee, C.M. et al., 2015. An introduction to the NASA Hyperspectral InfraRed Imager (HyspIRI) mission and preparatory activities. *Remote Sensing of Environment*, 167: 6-19.

Lee, S.-K. et al., 2018. GEDI and TanDEM-X fusion for 3D forest structure parameter retrieval, IGARSS 2018-2018 IEEE International Geoscience and Remote Sensing Symposium. IEEE, pp. 380-382.

Lettenmaier, D.P. et al., 2015. Inroads of remote sensing into hydrologic science during the WRR era. *Water Resources Research*, 51(9): 7309-7342.

Li, H. et al., 2014. Evaluation of the VIIRS and MODIS LST products in an arid area of Northwest China. *Remote Sensing of Environment*, 142: 111-121.

Li, X. et al., 2019. The impact of the 2009/2010 drought on vegetation growth and terrestrial carbon balance in Southwest China. *Agricultural and Forest Meteorology*, 269: 239-248.

Li, X. and Xiao, J., 2020. Global climatic controls on interannual variability of ecosystem productivity: Similarities and differences inferred from solar-induced chlorophyll fluorescence and enhanced vegetation index. *Agricultural and Forest Meteorology*: 108018.

Li, Z.-L. et al., 2009. A review of current methodologies for regional evapotranspiration estimation from remotely sensed data. *Sensors*, 9(5): 3801-3853.

Liou, Y.-A. and Kar, S.K., 2014. Evapotranspiration estimation with remote sensing and various surface energy balance algorithms—A review. *Energies*, 7(5): 2821-2849.

Liu, H. et al., 2018. Shifting plant species composition in response to climate change stabilizes grassland primary production. *Proceedings of the National Academy of Sciences*, 115(16): 4051-4056.

Liu, L. et al., 2019. Revisiting assessments of ecosystem drought recovery. *Environmental Research Letters*, 14(11): 114028.

Liu, L. et al., 2017. The Microwave Temperature Vegetation Drought Index (MTVDI) based on AMSR-E brightness temperatures for long-term drought assessment across China (2003–2010). *Remote Sensing of Environment*, 199: 302-320.

Liu, L. et al., 2018. Evaluating the utility of solar-induced chlorophyll fluorescence for drought monitoring by comparison with NDVI derived from wheat canopy. *Science of The Total Environment*, 625: 1208-1217.

Liu, S. et al., 2017. Estimating wheat green area index from ground-based LiDAR measurement using a 3D canopy structure model. *Agricultural and Forest Meteorology*, 247: 12-20.

Liu, W. et al., 2016. A worldwide evaluation of basin-scale evapotranspiration estimates against the water balance method. *Journal of Hydrology*, 538: 82-95.

Liu, X. et al., 2016. Agricultural drought monitoring: Progress, challenges, and prospects. *Journal of Geographical Sciences*, 26(6): 750-767.

Liu, Y. et al., 2019. On the mechanisms of two composite methods for construction of multivariate drought indices. *Science of the Total Environment*, 647: 981-991.

Liu, Y.Y., de Jeu, R.A., McCabe, M.F., Evans, J.P. and van Dijk, A.I., 2011. Global long-term passive microwave satellite-based retrievals of vegetation optical depth. *Geophysical Research Letters*, 38(18).

Liu, Y.Y. et al., 2018. Enhanced canopy growth precedes senescence in 2005 and 2010 Amazonian droughts. *Remote Sensing of Environment*, 211: 26-37.

Lloyd-Hughes, B., 2014. The impracticality of a universal drought definition. *Theoretical and Applied Climatology*, 117(3-4): 607-611.

López Valencia, O.M. et al., 2020. Mapping groundwater abstractions from irrigated agriculture: big data, inverse modeling, and a satellite–model fusion approach. *Hydrology and Earth System Sciences*, 24(11): 5251-5277.

Luo, W. et al., 2019. Long term experimental drought alters community plant trait variation, not trait means, across three semiarid grasslands. *Plant and Soil*, 442(1-2): 343-353.

Ma, H., Song, J., Wang, J., Xiao, Z. and Fu, Z., 2014. Improvement of spatially continuous forest LAI retrieval by integration of discrete airborne LiDAR and remote sensing multi-angle optical data. *Agricultural and Forest Meteorology*, 189: 60-70.

Ma, Y. et al., 2015. Remote sensing big data computing: Challenges and opportunities. *Future Generation Computer Systems*, 51: 47-60.

Magney, T.S. et al., 2019. Mechanistic evidence for tracking the seasonality of photosynthesis with solar-induced fluorescence. *Proceedings of the National Academy of Sciences*, 116(24): 11640-11645.

Mankin, J.S., Seager, R., Smerdon, J.E., Cook, B.I. and Williams, A.P., 2019. Mid-latitude freshwater availability reduced by projected vegetation responses to climate change. *Nature Geoscience*: 1-6.

Margulis, S.A. et al., 2016. Characterizing the extreme 2015 snowpack deficit in the Sierra Nevada (USA) and the implications for drought recovery. *Geophysical Research Letters*, 43(12): 6341-6349.

Martens, B. et al., 2017. GLEAM v3: Satellite-based land evaporation and root-zone soil moisture. *Geoscientific Model Development*, 10(5): 1903-1925.

Martinaitis, S.M. et al., 2017. The HMT multi-radar multi-sensor hydro experiment. *Bulletin of the American Meteorological Society*, 98(2): 347-359.

Martínez-Fernández, J., González-Zamora, A., Sánchez, N., Gumuzzio, A. and Herrero-Jiménez, C., 2016. Satellite soil moisture for agricultural drought monitoring: Assessment of the SMOS derived Soil Water Deficit Index. *Remote Sensing of Environment*, 177: 277-286.

McCabe, M., Aragon, B., Houborg, R. and Mascaro, J., 2017. CubeSats in hydrology: Ultrahigh-resolution insights into vegetation dynamics and terrestrial evaporation. *Water Resources Research*, 53(12): 10017-10024.

McCabe, M. et al., 2008. Hydrological consistency using multi-sensor remote sensing data for water and energy cycle studies. *Remote Sensing of Environment*, 112(2): 430-444.

McCabe, M.F. et al., 2016. The GEWEX LandFlux project: Evaluation of model evaporation using tower-based and globally gridded forcing data. *Geoscientific Model Development*, 9(1): 283-305.

McCabe, M.F. et al., 2017. The future of Earth observation in hydrology. *Hydrology and Earth System Sciences*, 21(7): 3879.

McDowell, N. et al., 2018. Drivers and mechanisms of tree mortality in moist tropical forests. *New Phytologist*, 219(3): 851-869.

McDowell, N.G. and Sevanto, S., 2010. The mechanisms of carbon starvation: how, when, or does it even occur at all? *New Phytologist*, 186(2): 264-266.

McKee, T.B., Doesken, N.J. and Kleist, J., 1993. The relationship of drought frequency and duration to time scales, Proceedings of the 8th Conference on Applied Climatology. American Meteorological Society Boston, MA, pp. 179-183.

McVicar, T. and Bierwirth, P., 2001. Rapidly assessing the 1997 drought in Papua New Guinea using composite AVHRR imagery. *International Journal of Remote Sensing*, 22(11): 2109-2128.

Meir, P., Metcalfe, D.B., Costa, A. and Fisher, R.A., 2008a. The fate of assimilated carbon during drought: impacts on respiration in Amazon rainforests. *Philosophical Transactions of the Royal Society B: Biological Sciences*, 363(1498): 1849-1855.

Meir, P. and Woodward, F.I., 2010. Amazonian rain forests and drought: response and vulnerability. *New Phytologist*, 187(3): 553-557.

Meng, R. et al., 2017. Using high spatial resolution satellite imagery to map forest burn severity across spatial scales in a Pine Barrens ecosystem. *Remote Sensing of Environment*, 191: 95-109.

Meng, R. et al., 2018. Measuring short-term post-fire forest recovery across a burn severity gradient in a mixed pine-oak forest using multi-sensor remote sensing techniques. *Remote Sensing of Environment*, 210: 282-296.

Meng, X.H., Evans, J.P. and McCabe, M.F., 2014. The Impact of Observed Vegetation Changes on Land–Atmosphere Feedbacks During Drought. *Journal of Hydrometeorology*, 15(2): 759-776.

Miralles, D., De Jeu, R., Gash, J., Holmes, T. and Dolman, A., 2011. Magnitude and variability of land evaporation and its componentsat the global scale. *Hydrology and Earth System Sciences*, 15(3): 967-981.

Miralles, D.G., Gentine, P., Seneviratne, S.I. and Teuling, A.J., 2019. Land–atmospheric feedbacks during droughts and heatwaves: state of the science and current challenges. *Annals of the New York Academy of Sciences*, 1436(1): 19.

Miralles, D.G. et al., 2016. The WACMOS-ET project-Part 2: Evaluation of global terrestrial evaporation data sets. *Hydrology and Earth System Sciences*, 20(2): 823-842.

Miralles, D.G., Teuling, A.J., Van Heerwaarden, C.C. and De Arellano, J.V.-G., 2014. Mega-heatwave temperatures due to combined soil desiccation and atmospheric heat accumulation. *Nature Geoscience*, 7(5): 345-349.

Mishra, A.K. and Singh, V.P., 2010. A review of drought concepts. *Journal of Hydrology*, 391(1): 202-216.

Mo, K.C. and Lettenmaier, D.P., 2015. Heat wave flash droughts in decline. *Geophysical Research Letters*, 42(8): 2823-2829.

Mohammed, G.H. et al., 2019. Remote sensing of solar-induced chlorophyll fluorescence (SIF) in vegetation: 50 years of progress. *Remote Sensing of Environment*, 231: 111177.

Moore III, B. et al., 2018. The potential of the geostationary Carbon Cycle Observatory (GeoCarb) to provide multi-scale constraints on the carbon cycle in the Americas. *Frontiers in Environmental Science*, 6: 109.

Mote, P.W., Hamlet, A.F., Clark, M.P. and Lettenmaier, D.P., 2005. Declining mountain snowpack in western North America. *Bulletin of the American Meteorological Society*, 86(1): 39-50.

Mu, Q., Zhao, M. and Running, S.W., 2011. Improvements to a MODIS global terrestrial evapotranspiration algorithm. *Remote Sensing of Environment*, 115(8): 1781-1800.

Mueller, B. et al., 2011. Evaluation of global observations-based evapotranspiration datasets and IPCC AR4 simulations. *Geophysical Research Letters*, 38(6).

Mukherjee, S., Mishra, A. and Trenberth, K.E., 2018. Climate change and drought: a perspective on drought indices. *Current Climate Change Reports*, 4(2): 145-163.

Myneni, R.B. et al., 2002. Global products of vegetation leaf area and fraction absorbed PAR from year one of MODIS data. *Remote Sensing of Environment*, 83(1-2): 214-231.

Nasab, A.H., Ansary, H. and Sanaei-Nejad, S.H., 2018. Analyzing drought history using Fuzzy Integrated Drought Index (FIDI): a case study in the Neyshabour basin, Iran. *Arabian Journal of Geosciences*, 11(14): 390.

Nemani, R., Pierce, L., Running, S. and Goward, S., 1993. Developing satellite-derived estimates of surface moisture status. *Journal of Applied Meteorology*, 32(3): 548-557.

Ni, Z., Lu, Q., Huo, H. and Zhang, H., 2019. Estimation of chlorophyll fluorescence at different scales: A review. *Sensors*, 19(13): 3000.

Nicolai-Shaw, N., Zscheischler, J., Hirschi, M., Gudmundsson, L. and Seneviratne, S.I., 2017. A drought event composite analysis using satellite remote-sensing based soil moisture. *Remote Sensing of Environment*, 203: 216-225.

Niemeyer, S., 2008. New drought indices. *Options Méditerranéennes. Série A: Séminaires Méditerranéens*, 80: 267-274.

Nishida, K., Nemani, R.R., Running, S.W. and Glassy, J.M., 2003. An operational remote sensing algorithm of land surface evaporation. *Journal of Geophysical Research: Atmospheres*, 108(D9).

Normand, J.C. and Heggy, E., 2015. InSAR assessment of surface deformations in urban coastal terrains associated with groundwater dynamics. *IEEE Transactions on Geoscience and Remote Sensing*, 53(12): 6356-6371.

Novick, K.A. et al., 2016. The increasing importance of atmospheric demand for ecosystem water and carbon fluxes. *Nature Climate Change*, 6(11): 1023-1027.

O'Sullivan, M. et al., 2020. Climate-driven variability and trends in plant productivity over recent decades based on three global products. *Global Biogeochemical Cycles*: e2020GB006613.

Orhan, O., Ekercin, S. and Dadaser-Celik, F., 2014. Use of landsat land surface temperature and vegetation indices for monitoring drought in the Salt Lake Basin Area, Turkey. *The Scientific World Journal*, 2014.

Orville, H.D., 1990. AMS statement on meteorological drought. *Bulletin of the American Meteorological Society*, 71(7): 1021-1025.

Otkin, J.A. et al., 2013. Examining rapid onset drought development using the thermal infrared–based evaporative stress index. *Journal of Hydrometeorology*, 14(4): 1057-1074.

Otkin, J.A., Anderson, M.C., Hain, C. and Svoboda, M., 2014. Examining the relationship between drought development and rapid changes in the evaporative stress index. *Journal of Hydrometeorology*, 15(3): 938-956.

Otkin, J.A. et al., 2018. Flash droughts: a review and assessment of the challenges imposed by rapid-onset droughts in the United States. *Bulletin of the American Meteorological Society*, 99(5): 911-919.

Pachauri, R.K. et al., 2014. Climate change 2014: synthesis report. Contribution of Working Groups I, II and III to the fifth assessment report of the Intergovernmental Panel on Climate Change. IPCC.

Palmer, W.C., 1965. Meteorological drought, 30. US Department of Commerce, Weather Bureau.

Paloscia, S., Macelloni, G. and Santi, E., 2006. Soil moisture estimates from AMSR-E brightness temperatures by using a dual-frequency algorithm. *IEEE Transactions on Geoscience and Remote Sensing*, 44(11): 3135-3144.

Paloscia, S., Macelloni, G., Santi, E. and Koike, T., 2001. A multifrequency algorithm for the retrieval of soil moisture on a large scale using microwave data from SMMR and SSM/I satellites. *IEEE Transactions on Geoscience and Remote Sensing*, 39(8): 1655-1661.

Pan, M., Wood, E.F., Wójcik, R. and McCabe, M.F., 2008. Estimation of regional terrestrial water cycle using multi-sensor remote sensing observations and data assimilation. *Remote Sensing of Environment*, 112(4): 1282-1294.

Pandey, S., Bhandari, H.S. and Hardy, B., 2007. Economic costs of drought and rice farmers' coping mechanisms: a cross-country comparative analysis. International Rice Research Institute, 203 pp.

Park, S., Im, J., Jang, E. and Rhee, J., 2016. Drought assessment and monitoring through blending of multi-sensor indices using machine learning approaches for different climate regions. *Agricultural and Forest Meteorology*, 216: 157-169.

Park, S., Im, J., Park, S. and Rhee, J., 2017. Drought monitoring using high resolution soil moisture through multi-sensor satellite data fusion over the Korean peninsula. *Agricultural and Forest Meteorology*, 237: 257-269.

Park, S., Kang, D., Yoo, C., Im, J. and Lee, M.-I., 2020. Recent ENSO influence on East African drought during rainy seasons through the synergistic use of satellite and reanalysis data. *ISPRS Journal of Photogrammetry and Remote Sensing*, 162: 17-26.

Pasho, E., Camarero, J.J., de Luis, M. and Vicente-Serrano, S.M., 2011. Impacts of drought at different time scales on forest growth across a wide climatic gradient in north-eastern Spain. *Agricultural and Forest Meteorology*, 151(12): 1800-1811.

Patel, N., Parida, B., Venus, V., Saha, S. and Dadhwal, V., 2012. Analysis of agricultural drought using vegetation temperature condition index (VTCI) from Terra/MODIS satellite data. *Environmental Monitoring and Assessment*, 184(12): 7153-7163.

Pederson, G.T. et al., 2011. The unusual nature of recent snowpack declines in the North American Cordillera. *Science*, 333(6040): 332-335.

Pendergrass, A.G. et al., 2020. Flash droughts present a new challenge for subseasonal-to-seasonal prediction. *Nature Climate Change*, 10(3): 191-199.

Peng, J. et al., 2020. A roadmap for high-resolution satellite soil moisture applications – confronting product characteristics with user requirements. *Remote Sensing of Environment*: 112162.

Peng, J., Wu, C., Zhang, X., Wang, X. and Gonsamo, A., 2019. Satellite detection of cumulative and lagged effects of drought on autumn leaf senescence over the Northern Hemisphere. *Global Change Biology*, 25(6): 2174-2188.

Peñuelas, J. et al., 2017. Shifting from a fertilization-dominated to a warming-dominated period. *Nature Ecology & Evolution*, 1(10): 1438-1445.

Pesti, G., Shrestha, B.P., Duckstein, L. and Bogárdi, I., 1996. A fuzzy rule-based approach to drought assessment. *Water Resources Research*, 32(6): 1741-1747.

Peters, A.J. et al., 2002. Drought monitoring with NDVI-based standardized vegetation index. *Photogrammetric Engineering and Remote Sensing*, 68(1): 71-75.

Piao, S. et al., 2019. The impacts of climate extremes on the terrestrial carbon cycle: A review. *Science China Earth Sciences*: 1-13.

Pinheiro, A.C., Privette, J.L., Mahoney, R. and Tucker, C.J., 2004. Directional effects in a daily AVHRR land surface temperature dataset over Africa. *IEEE Transactions on Geoscience and Remote Sensing*, 42(9): 1941-1954.

Pohl, C. and Van Genderen, J.L., 1998. Review article multisensor image fusion in remote sensing: concepts, methods and applications. *International Journal of Remote Sensing*, 19(5): 823-854.

Pouliot, D., Latifovic, R. and Olthof, I., 2009. Trends in vegetation NDVI from 1 km AVHRR data over Canada for the period 1985–2006. *International Journal of Remote Sensing*, 30(1): 149-168.

Prakash, S. et al., 2018. A preliminary assessment of GPM-based multi-satellite precipitation estimates over a monsoon dominated region. *Journal of Hydrology*, 556: 865-876.

Prata, A., 2002. Land surface temperature measurement from space: AATSR algorithm theoretical basis document. *Contract Report to ESA, CSIRO Atmospheric Research, Aspendale, Victoria, Australia*, 2002: 1-34.

Price, J.C., 1994. How unique are spectral signatures? *Remote Sensing of Environment*, 49(3): 181-186.

Pulliainen, J. and Hallikainen, M., 2001. Retrieval of regional snow water equivalent from space-borne passive microwave observations. *Remote Sensing of Environment*, 75(1): 76-85.

Qi, J., Chehbouni, A., Huete, A.R., Kerr, Y.H. and Sorooshian, S., 1994. A modified soil adjusted vegetation index. *Remote Sensing of Environment*, 48(2): 119-122.

Qi, W. and Dubayah, R.O., 2016. Combining Tandem-X InSAR and simulated GEDI lidar observations for forest structure mapping. *Remote Sensing of Environment*, 187: 253-266.

Qi, W., Saarela, S., Armston, J., Ståhl, G. and Dubayah, R., 2019. Forest biomass estimation over three distinct forest types using TanDEM-X InSAR data and simulated GEDI lidar data. *Remote Sensing of Environment*, 232: 111283.

Qiu, B., Ge, J., Guo, W., Pitman, A.J. and Mu, M., 2020. Responses of Australian Dryland Vegetation to the 2019 Heat Wave at a Subdaily Scale. *Geophysical Research Letters*, 47(4).

Rahmat-Samii, Y., Manohar, V. and Kovitz, J.M., 2017. For Satellites, Think Small, Dream Big: A review of recent antenna developments for CubeSats. *IEEE Antennas and Propagation Magazine*, 59(2): 22-30.

Rahmati, O. et al., 2020. Machine learning approaches for spatial modeling of agricultural droughts in the south-east region of Queensland Australia. *Science of the Total Environment*, 699: 134230.

Rajsekhar, D., Singh, V.P. and Mishra, A.K., 2015a. Multivariate drought index: An information theory based approach for integrated drought assessment. *Journal of Hydrology*, 526: 164-182.

Rao, K., Anderegg, W.R., Sala, A., Martínez-Vilalta, J. and Konings, A.G., 2019. Satellite-based vegetation optical depth as an indicator of drought-driven tree mortality. *Remote Sensing of Environment*, 227: 125-136.

Rao, K., Williams, A.P., Flefil, J.F. and Konings, A.G., 2020. SAR-enhanced mapping of live fuel moisture content. *Remote Sensing of Environment*, 245: 111797.

Redmond, K.T., 2002. The depiction of drought: A commentary. *Bulletin of the American Meteorological Society*, 83(8): 1143-1148.

Reshmidevi, T., Eldho, T. and Jana, R., 2009. A GIS-integrated fuzzy rule-based inference system for land suitability evaluation in agricultural watersheds. *Agricultural Systems*, 101(1-2): 101-109.

Rhee, J., Im, J. and Carbone, G.J., 2010. Monitoring agricultural drought for arid and humid regions using multi-sensor remote sensing data. *Remote Sensing of Environment*, 114(12): 2875-2887.

Richardson, A.J. and Wiegand, C.L., 1990. Comparison of two models for simulating the soil-vegetation composite reflectance of a developing cotton canopy. *Remote Sensing*, 11(3): 447-459.

Richardson, J.J., Moskal, L.M. and Kim, S.-H., 2009. Modeling approaches to estimate effective leaf area index from aerial discrete-return LIDAR. *Agricultural and Forest Meteorology*, 149(6-7): 1152-1160.

Roman, D. et al., 2015. The role of isohydric and anisohydric species in determining ecosystem-scale response to severe drought. *Oecologia*, 179(3): 641-654.

Roujean, J.L. and Lacaze, R., 2002. Global mapping of vegetation parameters from POLDER multiangular measurements for studies of surface-atmosphere interactions: A pragmatic method and its validation. *Journal of Geophysical Research: Atmospheres*, 107(D12): ACL 6-1-ACL 6-14.

Roundy, J.K., Ferguson, C.R. and Wood, E.F., 2014. Impact of land-atmospheric coupling in CFSv2 on drought prediction. *Climate Dynamics*, 43(1-2): 421-434.

Roundy, J.K. and Santanello, J.A., 2017. Utility of satellite remote sensing for land–atmosphere coupling and drought metrics. *Journal of Hydrometeorology*, 18(3): 863-877.

Rouse, J., Haas, R., Schell, J. and Deering, D., 1974. Monitoring vegetation systems in the Great Plains with ERTS. *NASA special publication*, 351: 309.

Rulinda, C.M., Dilo, A., Bijker, W. and Stein, A., 2012. Characterising and quantifying vegetative drought in East Africa using fuzzy modelling and NDVI data. *Journal of Arid Environments*, 78: 169-178.

Running, S.W. et al., 1994. Terrestrial remote sensing science and algorithms planned for EOS/MODIS. *International Journal of Remote sensing*, 15(17): 3587-3620.

Ruzmaikin, A., Aumann, H.H. and Manning, E.M., 2014. Relative humidity in the troposphere with AIRS. *Journal of the Atmospheric Sciences*, 71(7): 2516-2533.

Ryu, Y., Berry, J.A. and Baldocchi, D.D., 2019. What is global photosynthesis? History, uncertainties and opportunities. *Remote Sensing of Environment*, 223: 95-114.

Saleska, S.R., Didan, K., Huete, A.R. and Da Rocha, H.R., 2007. Amazon forests green-up during 2005 drought. *Science*, 318(5850): 612-612.

Samanta, A. et al., 2010. Amazon forests did not green-up during the 2005 drought. *Geophysical Research Letters*, 37(5).

Sandholt, I., Rasmussen, K. and Andersen, J., 2002. A simple interpretation of the surface temperature/vegetation index space for assessment of surface moisture status. *Remote Sensing of Environment*, 79(2-3): 213-224.

Sankey, T.T. et al., 2018. UAV hyperspectral and lidar data and their fusion for arid and semi-arid land vegetation monitoring. *Remote Sensing in Ecology and Conservation*, 4(1): 20-33.

Santanello Jr, J.A. et al., 2018. Land–atmosphere interactions: the LoCo perspective. *Bulletin of the American Meteorological Society*, 99(6): 1253-1272.

Save, H., Bettadpur, S. and Tapley, B.D., 2012. Reducing errors in the GRACE gravity solutions using regularization. *Journal of Geodesy*, 86(9): 695-711.

Schwalm, C.R. et al., 2017. Global patterns of drought recovery. *Nature*, 548(7666): 202-205.

Schwantes, A.M., Swenson, J.J. and Jackson, R.B., 2016. Quantifying drought-induced tree mortality in the open canopy woodlands of central Texas. *Remote Sensing of Environment*, 181: 54-64.

Seddon, A.W., Macias-Fauria, M., Long, P.R., Benz, D. and Willis, K.J., 2016. Sensitivity of global terrestrial ecosystems to climate variability. *Nature*, 531(7593): 229.

Sellars, S. et al., 2013. Computational Earth science: Big data transformed into insight. *Eos, Transactions American Geophysical Union*, 94(32): 277-278.

Senay, G.B., Budde, M., Brown, J. and Verdin, J., 2008. Mapping flash drought in the US: Southern Great Plains, 22nd Conference on Hydrology. American Meteorological Society New Orleans, LA.

Seneviratne, S.I. et al., 2010. Investigating soil moisture–climate interactions in a changing climate: A review. *Earth-Science Reviews*, 99(3-4): 125-161.

Seneviratne, S.I., Lüthi, D., Litschi, M. and Schär, C., 2006. Land–atmosphere coupling and climate change in Europe. *Nature*, 443(7108): 205-209.

Sepulcre-Canto, G., Horion, S., Singleton, A., Carrao, H. and Vogt, J., 2012. Development of a Combined Drought Indicator to detect agricultural drought in Europe. *Natural Hazards & Earth System Sciences*, 12(11).

Seyednasrollah, B., Domec, J.-C. and Clark, J.S., 2019. Spatiotemporal sensitivity of thermal stress for monitoring canopy hydrological stress in near real-time. *Agricultural and Forest Meteorology*, 269-270: 220-230.

Shafer, B. and Dezman, L., 1982. Development of surface water supply index (SWSI) to assess the severity of drought condition in Snowpack runoff areas. Proceding of The Western Snow Conference.

Shamsudduha, M., Taylor, R. and Longuevergne, L., 2012. Monitoring groundwater storage changes in the highly seasonal humid tropics: Validation of GRACE measurements in the Bengal Basin. *Water Resources Research*, 48(2).

Sheffield, J., Ferguson, C.R., Troy, T.J., Wood, E.F. and McCabe, M.F., 2009. Closing the terrestrial water budget from satellite remote sensing. *Geophysical Research Letters*, 36(7).

Sheffield, J., Wood, E.F. and Roderick, M.L., 2012. Little change in global drought over the past 60 years. *Nature*, 491(7424): 435-438.

Shi, M. et al., 2019. The 2005 Amazon drought legacy effect delayed the 2006 wet season onset. *Geophysical Research Letters*, 46(15): 9082-9090.

Shivers, S.W., Roberts, D.A. and McFadden, J.P., 2019. Using paired thermal and hyperspectral aerial imagery to quantify land surface temperature variability and assess crop stress within California orchards. *Remote Sensing of Environment*, 222: 215-231.

Short, N.M., 1976. Mission to Earth: Landsat views the world, 1. Scientific and Technical Office, National Aeronautics and Space Administration.

Shugart, H.H. et al., 2015. Computer and remote-sensing infrastructure to enhance large-scale testing of individual-based forest models. *Frontiers in Ecology and the Environment*, 13(9): 503-511.

Silva, C.A. et al., 2018. Fusing GEDI, ICESat-2 and NISAR data for aboveground biomass mapping in Sonoma County, California, USA. *AGUFM*, 2018: B44E-05.

Simić, D., Kovačević, I., Svirčević, V. and Simić, S., 2017. 50 years of fuzzy set theory and models for supplier assessment and selection: A literature review. *Journal of Applied Logic*, 24: 85-96.

Sims, A.P., Niyogi, D.d.S. and Raman, S., 2002. Adopting drought indices for estimating soil moisture: A North Carolina case study. *Geophysical Research Letters*, 29(8): 24-1-24-4.

Sippel, S. et al., 2018. Drought, Heat, and the Carbon Cycle: a Review. *Current Climate Change Reports*: 1-21.

Sivapalan, M., Savenije, H.H. and Blöschl, G., 2012. Socio-hydrology: A new science of people and water. *Hydrology Process*, 26(8): 1270-1276.

Smith, M.N. et al., 2019. Seasonal and drought-related changes in leaf area profiles depend on height and light environment in an Amazon forest. *New Phytologist*, 222(3): 1284-1297.

Smith, W. et al., 2018. Chlorophyll fluorescence better captures seasonal and interannual gross primary productivity dynamics across dryland ecosystems of southwestern North America. *Geophysical Research Letters*, 45(2): 748-757.

Smith, W.K. et al., 2019. Remote sensing of dryland ecosystem structure and function: Progress, challenges, and opportunities. *Remote Sensing of Environment*, 233: 111401.

Smith, W.K. et al., 2016. Large divergence of satellite and Earth system model estimates of global terrestrial $CO_2$ fertilization. *Nature Climate Change*, 6(3): 306.

Sobejano-Paz, V. et al., 2020. Hyperspectral and Thermal Sensing of Stomatal Conductance, Transpiration, and Photosynthesis for Soybean and Maize under Drought. *Remote Sensing*, 12(19): 3182.

Sobrino, J.A., Jiménez-Muñoz, J.C. and Paolini, L., 2004. Land surface temperature retrieval from LANDSAT TM 5. *Remote Sensing of Environment*, 90(4): 434-440.

Solomatine, D.P., 2002. Data-driven modelling: paradigm, methods, experiences, Proc. 5th International Conference on Hydroinformatics, pp. 1-5.

Son, B. et al., 2021. A new drought monitoring approach: Vector Projection Analysis (VPA). *Remote Sensing of Environment*, 252: 112145.

Son, N., Chen, C., Chen, C., Chang, L. and Minh, V.Q., 2012. Monitoring agricultural drought in the Lower Mekong Basin using MODIS NDVI and land surface temperature data. *International Journal of Applied Earth Observation and Geoinformation*, 18: 417-427.

Song, L. et al., 2018a. Satellite sun-induced chlorophyll fluorescence detects early response of winter wheat to heat stress in the Indian Indo-Gangetic Plains. *Global Change Biology*, 24(9): 4023-4037.

Sorooshian, S. et al., 2011. Advanced concepts on remote sensing of precipitation at multiple scales. *Bulletin of the American Meteorological Society*, 92(10): 1353-1357.

Sorooshian, S. et al., 2000. Evaluation of PERSIANN system satellite-based estimates of tropical rainfall. *Bulletin of the American Meteorological Society*, 81(9): 2035-2046.

Sruthi, S. and Aslam, M.M., 2015. Agricultural drought analysis using the NDVI and land surface temperature data; a case study of Raichur district. *Aquatic Procedia*, 4: 1258-1264.

Staudinger, M., Stahl, K. and Seibert, J., 2014. A drought index accounting for snow. *Water Resources Research*, 50(10): 7861-7872.

Stegehuis, A. et al., 2015. An observation-constrained multi-physics WRF ensemble for simulating European mega heat waves. *Geoscientific Model Development*, 8(7): 2285-2298.

Stewart, I.T., 2009. Changes in snowpack and snowmelt runoff for key mountain regions. *Hydrological Processes: An International Journal*, 23(1): 78-94.

Stocker, B.D. et al., 2018. Quantifying soil moisture impacts on light use efficiency across biomes. *New Phytologist*, 218(4): 1430-1449.

Stocker, B.D. et al., 2019. Drought impacts on terrestrial primary production underestimated by satellite monitoring. *Nature Geoscience*, 12(4): 264.

Stovall, A.E., Shugart, H. and Yang, X., 2019. Tree height explains mortality risk during an intense drought. *Nature Communications*, 10(1): 1-6.

Strahler, A.H., 1997. Vegetation canopy reflectance modeling—Recent developments and remote sensing perspectives. *Remote Sensing Reviews*, 15(1-4): 179-194.

Su, H., McCabe, M., Wood, E.F., Su, Z. and Prueger, J., 2005. Modeling evapotranspiration during SMACEX: Comparing two approaches for local-and regional-scale prediction. *Journal of Hydrometeorology*, 6(6): 910-922.

Suárez, L. et al., 2008. Assessing canopy PRI for water stress detection with diurnal airborne imagery. *Remote Sensing of Environment*, 112(2): 560-575.

Sun, Q. et al., 2014. Variations in global temperature and precipitation for the period of 1948 to 2010. *Environmental Monitoring and Assessment*, 186(9): 5663-5679.

Sun, Q. et al., 2018. A review of global precipitation data sets: Data sources, estimation, and intercomparisons. *Reviews of Geophysics*, 56(1): 79-107.

Sun, Y. et al., 2018. Overview of Solar-Induced chlorophyll Fluorescence (SIF) from the Orbiting Carbon Observatory-2: Retrieval, cross-mission comparison, and global monitoring for GPP. *Remote Sensing of Environment*, 209: 808-823.

Sun, Y. et al., 2017. OCO-2 advances photosynthesis observation from space via solar-induced chlorophyll fluorescence. *Science*, 358(6360).

Sun, Y. et al., 2015. Drought onset mechanisms revealed by satellite solar-induced chlorophyll fluorescence: Insights from two contrasting extreme events. *Journal of Geophysical Research: Biogeosciences*, 120(11): 2427-2440.

Svoboda, M. et al., 2002. The drought monitor. *Bulletin of the American Meteorological Society*, 83(8): 1181-1190.

Svoboda, M. et al., 2017. NDMC Annual Report 2017.

Tabari, H., Nikbakht, J. and Talaee, P.H., 2013. Hydrological drought assessment in Northwestern Iran based on streamflow drought index (SDI). *Water Resources Management*, 27(1): 137-151.

Tachiiri, K., Shinoda, M., Klinkenberg, B. and Morinaga, Y., 2008. Assessing Mongolian snow disaster risk using livestock and satellite data. *Journal of Arid Environments*, 72(12): 2251-2263.

Tallaksen, L.M. and Van Lanen, H.A., 2004. Hydrological drought: processes and estimation methods for streamflow and groundwater, 48. Elsevier.

Tao, L., Li, J., Jiang, J. and Chen, X., 2016. Leaf area index inversion of winter wheat using modified water-cloud model. *IEEE Geoscience and Remote Sensing Letters*, 13(6): 816-820.

Tapiador, F. et al., 2017. Global precipitation measurements for validating climate models. *Atmospheric Research*, 197: 1-20.

Taylor, T.E. et al., 2020. OCO-3 early mission operations and initial (vEarly) XCO2 and SIF retrievals. *Remote Sensing of Environment*, 251: 112032.

Teuling, A.J. et al., 2010. Contrasting response of European forest and grassland energy exchange to heatwaves. *Nature Geoscience*, 3(10): 722-727.

Thenot, F., Méthy, M. and Winkel, T., 2002. The Photochemical Reflectance Index (PRI) as a water-stress index. *International Journal of Remote Sensing*, 23(23): 5135-5139.

Thomas, B.F. et al., 2017. GRACE groundwater drought index: Evaluation of California Central Valley groundwater drought. *Remote Sensing of Environment*, 198: 384-392.

Thompson, D. and Wehmanen, O., 1977. The use of Landsat digital data to detect and monitor vegetation water deficiencies.

Tomlinson, C.J., Chapman, L., Thornes, J.E. and Baker, C., 2011. Remote sensing land surface temperature for meteorology and climatology: a review. *Meteorological Applications*, 18(3): 296-306.

Touma, D., Ashfaq, M., Nayak, M.A., Kao, S.-C. and Diffenbaugh, N.S., 2015. A multi-model and multi-index evaluation of drought characteristics in the 21st century. *Journal of Hydrology*, 526: 196-207.

Tramontana, G. et al., 2016. Predicting carbon dioxide and energy fluxes across global FLUXNET sites with regression algorithms. *Biogeosciences Discussions*, 13(14): 4291-4313.

Trenberth, K.E. et al., 2014. Global warming and changes in drought. *Nature Climate Change*, 4(1): 17.

Trnka, M. et al., 2018. Priority questions in multidisciplinary drought research. *Climate Research*, 75(3): 241-260.

Tucker, C.J., 1980. Remote sensing of leaf water content in the near infrared. *Remote Sensing of Environment*, 10(1): 23-32.

Tucker, C.J. et al., 2005. An extended AVHRR 8-km NDVI dataset compatible with MODIS and SPOT vegetation NDVI data. *International Journal of Remote Sensing*, 26(20): 4485-4498.

Udelhoven, T. et al., 2017. A satellite-based imaging instrumentation concept for hyperspectral thermal remote sensing. *Sensors*, 17(7): 1542.

Van der Molen, M.K. et al., 2011. Drought and ecosystem carbon cycling. *Agricultural and Forest Meteorology*, 151(7): 765-773.

Van Der Werf, G.R. et al., 2004. Continental-scale partitioning of fire emissions during the 1997 to 2001 El Nino/La Nina period. *Science*, 303(5654): 73-76.

Van Leeuwen, W.J., Orr, B.J., Marsh, S.E. and Herrmann, S.M., 2006. Multi-sensor NDVI data continuity: Uncertainties and implications for vegetation monitoring applications. *Remote Sensing of Environment*, 100(1): 67-81.

Van Loon, A.F., 2015. Hydrological drought explained. *Wiley Interdisciplinary Reviews: Water*, 2(4): 359-392.

Van Loon, A.F. et al., 2016a. Drought in a human-modified world: reframing drought definitions, understanding, and analysis approaches. *Hydrology and Earth System Sciences*, 20(9): 3631-3650.

Vasiliades, L., Loukas, A. and Liberis, N., 2011. A water balance derived drought index for Pinios River Basin, Greece. *Water Resources Management*, 25(4): 1087-1101.

Velasquez, M. and Hester, P.T., 2013. An analysis of multi-criteria decision making methods. *International Journal of Operations Research*, 10(2): 56-66.

Verma, M. et al., 2017. Effect of environmental conditions on the relationship between solar-induced fluorescence and gross primary productivity at an OzFlux grassland site. *Journal of Geophysical Research: Biogeosciences*, 122(3): 716-733.

Vicente-Serrano, S.M., Beguería, S. and López-Moreno, J.I., 2010. A multiscalar drought index sensitive to global warming: the standardized precipitation evapotranspiration index. *Journal of Climate*, 23(7): 1696-1718.

Vicente-Serrano, S.M., Quiring, S.M., Peña-Gallardo, M., Yuan, S. and Domínguez-Castro, F., 2019. A review of environmental droughts: Increased risk under global warming? *Earth-Science Reviews*: 102953.

Vicente-Serrano, S.M. et al., 2020. Global characterization of hydrological and meteorological droughts under future climate change: The importance of timescales, vegetation-CO2 feedbacks and changes to distribution functions. *International Journal of Climatology*, 40(5): 2557-2567.

Vittucci, C. et al., 2016. SMOS retrieval over forests: Exploitation of optical depth and tests of soil moisture estimates. *Remote Sensing of Environment*, 180: 115-127.

Vreugdenhil, M., Hahn, S., Dorigo, W., Steele-Dunne, S. and Wagner, W., 2019. Sentinel-1 backscatter dynamics for vegetation monitoring: Synergies and discordances with Vegetation Optical Depth, Geophysical Research Abstracts.

Wan, Z., 2008. New refinements and validation of the MODIS land-surface temperature/emissivity products. *Remote Sensing of Environment*, 112(1): 59-74.

Wan, Z. and Li, Z.-L., 1997. A physics-based algorithm for retrieving land-surface emissivity and temperature from EOS/MODIS data. *IEEE Transactions on Geoscience and Remote Sensing*, 35(4): 980-996.

Wang, J. et al., 2016. A multi-sensor view of the 2012 central plains drought from space. *Frontiers in Environmental Science*, 4: 45.

Wang, K. and Dickinson, R.E., 2012. A review of global terrestrial evapotranspiration: Observation, modeling, climatology, and climatic variability. *Reviews of Geophysics*, 50(2).

Wang, L. et al., 2012a. Dryland ecohydrology and climate change: critical issues and technical advances. *Hydrology and Earth System Sciences*, 16(8): 2585-2603.

Wang, L., Good, S.P. and Caylor, K.K., 2014. Global synthesis of vegetation control on evapotranspiration partitioning. *Geophysical Research Letters*, 41(19): 6753-6757.

Wang, L. and Qu, J.J., 2009. Satellite remote sensing applications for surface soil moisture monitoring: A review. *Frontiers of Earth Science in China*, 3(2): 237-247.

Wang, L., Yuan, X., Xie, Z., Wu, P. and Li, Y., 2016. Increasing flash droughts over China during the recent global warming hiatus. *Scientific Reports*, 6: 30571.

Waseem, M., Ajmal, M. and Kim, T.-W., 2015. Development of a new composite drought index for multivariate drought assessment. *Journal of Hydrology*, 527: 30-37.

Wei, W. et al., 2020. Temperature Vegetation Precipitation Dryness Index (TVPDI)-based dryness-wetness monitoring in China. *Remote Sensing of Environment*, 248: 111957.

West, H., Quinn, N. and Horswell, M., 2019. Remote sensing for drought monitoring & impact assessment: Progress, past challenges and future opportunities. *Remote Sensing of Environment*, 232: 111291.

Westra, S., Brown, C., Lall, U. and Sharma, A., 2007. Modeling multivariable hydrological series: Principal component analysis or independent component analysis? *Water Resources Research*, 43(6).

Wilhite, D.A., 2000. Drought as a natural hazard: concepts and definitions. I: 3-18.

Wilhite, D.A. and Glantz, M.H., 1985. Understanding: the drought phenomenon: the role of definitions. *Water International*, 10(3): 111-120.

Wilhite, D.A., Svoboda, M.D. and Hayes, M.J., 2007. Understanding the complex impacts of drought: A key to enhancing drought mitigation and preparedness. *Water Resources Management*, 21(5): 763-774.

Wilkinson, S.L., Verkaik, G.J., Moore, P.A. and Waddington, J.M., 2020. Threshold peat burn severity breaks evaporation-limiting feedback. *Ecohydrology*, 13(1): e2168.

Willis, K.J., Jeffers, E.S. and Tovar, C., 2018. What makes a terrestrial ecosystem resilient? *Science*, 359(6379): 988-989.

Woellert, K., Ehrenfreund, P., Ricco, A.J. and Hertzfeld, H., 2011. Cubesats: Cost-effective science and technology platforms for emerging and developing nations. *Advances in Space Research*, 47(4): 663-684.

Wold, S., Esbensen, K. and Geladi, P., 1987. Principal component analysis. *Chemometrics and Intelligent Laboratory Systems*, 2(1-3): 37-52.

Wu, J. et al., 2015. Drought monitoring and analysis in China based on the Integrated Surface Drought Index (ISDI). *International Journal of Applied Earth Observation and Geoinformation*, 41: 23-33.

Wu, X. et al., 2018. Differentiating drought legacy effects on vegetation growth over the temperate Northern Hemisphere. *Global Change Biology*, 24(1): 504-516.

Xie, P. and Arkin, P.A., 1997. Global precipitation: A 17-year monthly analysis based on gauge observations, satellite estimates, and numerical model outputs. *Bulletin of the American Meteorological Society*, 78(11): 2539-2558.

Xie, P., Arkin, P.A. and Janowiak, J.E., 2007. CMAP: The CPC merged analysis of precipitation, Measuring Precipitation from Space. Springer, pp. 319-328.

Xie, Q. et al., 2018. Vegetation indices combining the red and red-edge spectral information for leaf area index retrieval. *IEEE Journal of Selected Topics in Applied Earth Observations and Remote Sensing*, 11(5): 1482-1493.

Xie, S. et al., 2010. Global warming pattern formation: Sea surface temperature and rainfall. *Journal of Climate*, 23(4): 966-986.

Xu, C. et al., 2019. Increasing impacts of extreme droughts on vegetation productivity under climate change. *Nature Climate Change*, 9(12): 948-953.

Xu, Z., Zhou, G. and Shimizu, H., 2010. Plant responses to drought and rewatering. *Plant Signaling & Behavior*, 5(6): 649-654.

Xue, J. and Su, B., 2017. Significant Remote Sensing Vegetation Indices: A Review of Developments and Applications. *Journal of Sensors*, 2017: 1353691.

Yager, R.R., 1996. Quantifier guided aggregation using OWA operators. *International Journal of Intelligent Systems*, 11(1): 49-73.

Yan, G. et al., 2019. Review of indirect optical measurements of leaf area index: Recent advances, challenges, and perspectives. *Agricultural and forest meteorology*, 265: 390-411.

Yang, X. et al., 2018. FluoSpec 2—an automated field spectroscopy system to monitor canopy solar-induced fluorescence. *Sensors*, 18(7): 2063.

Yang, Y. et al., 2015. Comparison of three dual-source remote sensing evapotranspiration models during the MUSOEXE-12 campaign: Revisit of model physics. *Water Resources Research*, 51(5): 3145-3165.

Yang, Y., Roderick, M.L., Zhang, S., McVicar, T.R. and Donohue, R.J., 2019. Hydrologic implications of vegetation response to elevated $CO_2$ in climate projections. *Nature Climate Change*, 9(1): 44-48.

Yang, Y. et al., 2018. Post-drought decline of the Amazon carbon sink. *Nature Communications*, 9(1): 1-9.

Yebra, M. et al., 2013. A global review of remote sensing of live fuel moisture content for fire danger assessment: Moving towards operational products. *Remote Sensing of Environment*, 136: 455-468.

Yi, Y. et al., 2013. Recent climate and fire disturbance impacts on boreal and arctic ecosystem productivity estimated using a satellite-based terrestrial carbon flux model. *Journal of Geophysical Research: Biogeosciences*, 118(2): 606-622.

Yoshida, Y. et al., 2015. The 2010 Russian drought impact on satellite measurements of solar-induced chlorophyll fluorescence: Insights from modeling and comparisons with parameters derived from satellite reflectances. *Remote Sensing of Environment*, 166: 163-177.

Yuan, M. et al., 2020. Impacts of preseason drought on vegetation spring phenology across the Northeast China Transect. *Science of The Total Environment*, 738: 140297.

Yuan, W. et al., 2019. Increased atmospheric vapor pressure deficit reduces global vegetation growth. *Science Advances*, 5(8): eaax1396.

Yuan, X. et al., 2019. Anthropogenic shift towards higher risk of flash drought over China. *Nature Communications*, 10(1): 1-8.

Zaitchik, B.F., Santanello, J.A., Kumar, S.V. and Peters-Lidard, C.D., 2013. Representation of soil moisture feedbacks during drought in NASA Unified WRF (NU-WRF). *Journal of Hydrometeorology*, 14(1): 360-367.

Zarco-Tejada, P.J., Rueda, C. and Ustin, S., 2003. Water content estimation in vegetation with MODIS reflectance data and model inversion methods. *Remote Sensing of Environment*, 85(1): 109-124.

Zargar, A., Sadiq, R., Naser, B. and Khan, F.I., 2011. A review of drought indices. *Environmental Reviews*, 19(NA): 333-349.

Zeng, Q. et al., 2018. Inter-comparison and evaluation of remote sensing precipitation products over China from 2005 to 2013. *Remote Sensing*, 10(2): 168.

Zhang, A. and Jia, G., 2013. Monitoring meteorological drought in semiarid regions using multi-sensor microwave remote sensing data. *Remote Sensing of Environment*, 134: 12-23.

Zhang, B., AghaKouchak, A., Yang, Y., Wei, J. and Wang, G., 2019. A water-energy balance approach for multi-category drought assessment across globally diverse hydrological basins. *Agricultural and Forest Meteorology*, 264: 247-265.

Zhang, B. et al., 2019. A Framework for Global Multicategory and Multiscalar Drought Characterization Accounting for Snow Processes. *Water Resources Research*, 55(11): 9258-9278.

Zhang, J., 2010. Multi-source remote sensing data fusion: status and trends. *International Journal of Image and Data Fusion*, 1(1): 5-24.

Zhang, J. et al., 2016. Multi-Radar Multi-Sensor (MRMS) quantitative precipitation estimation: Initial operating capabilities. *Bulletin of the American Meteorological Society*, 97(4): 621-638.

Zhang, K., Kimball, J.S. and Running, S.W., 2016. A review of remote sensing based actual evapotranspiration estimation. *Wiley Interdisciplinary Reviews: Water*, 3(6): 834-853.

Zhang, L., Jiao, W., Zhang, H., Huang, C. and Tong, Q., 2017. Studying drought phenomena in the Continental United States in 2011 and 2012 using various drought indices. *Remote Sensing of Environment*, 190: 96-106.

Zhang, X., Chen, N., Li, J., Chen, Z. and Niyogi, D., 2017. Multi-sensor integrated framework and index for agricultural drought monitoring. *Remote Sensing of Environment*, 188: 141-163.

Zhang, Y. et al., 2013. Monitoring and estimating drought-induced impacts on forest structure, growth, function, and ecosystem services using remote-sensing data: recent progress and future challenges. *Environmental Reviews*, 21(2): 103-115.

Zhang, Y., Song, C., Band, L.E., Sun, G. and Li, J., 2017. Reanalysis of global terrestrial vegetation trends from MODIS products: Browning or greening? *Remote Sensing of Environment*, 191: 145-155.

Zhao, F. et al., 2011. Measuring effective leaf area index, foliage profile, and stand height in New England forest stands using a full-waveform ground-based lidar. *Remote Sensing of Environment*, 115(11): 2954-2964.

Zhao, M., Heinsch, F.A., Nemani, R.R. and Running, S.W., 2005. Improvements of the MODIS terrestrial gross and net primary production global data set. *Remote Sensing of Environment*, 95(2): 164-176.

Zhao, M. and Running, S.W., 2010. Drought-induced reduction in global terrestrial net primary production from 2000 through 2009. *Science*, 329(5994): 940-943.

Zheng, G. and Moskal, L.M., 2009. Retrieving leaf area index (LAI) using remote sensing: theories, methods and sensors. *Sensors*, 9(4): 2719-2745.

Zhong, R. et al., 2019. Drought monitoring utility of satellite-based precipitation products across mainland China. *Journal of Hydrology*, 568: 343-359.

Zhou, L., Chen, N., Chen, Z. and Xing, C., 2016. ROSCC: an efficient remote sensing observation-sharing method based on cloud computing for soil moisture mapping in precision agriculture. *IEEE Journal of Selected Topics in Applied Earth Observations and Remote Sensing*, 9(12): 5588-5598.

Zhou, L. et al., 2014. Widespread decline of Congo rainforest greenness in the past decade. *Nature*, 509(7498): 86.

Zhou, S., Zhang, Y., Park Williams, A. and Gentine, P., 2019. Projected increases in intensity, frequency, and terrestrial carbon costs of compound drought and aridity events. *Science Advances*, 5(1): eaau5740.

Zhu, X., Chen, J., Gao, F., Chen, X. and Masek, J.G., 2010. An enhanced spatial and temporal adaptive reflectance fusion model for complex heterogeneous regions. *Remote Sensing of Environment*, 114(11): 2610-2623.

Zhu, X., Skidmore, A.K., Darvishzadeh, R. and Wang, T., 2019. Estimation of forest leaf water content through inversion of a radiative transfer model from LiDAR and

hyperspectral data. *International Journal of Applied Earth Observation and Geoinformation*, 74: 120-129.

Zhu, X. et al., 2015. Comparison of monthly precipitation derived from high-resolution gridded datasets in arid Xinjiang, central Asia. *Quaternary International*, 358: 160-170.

Zscheischler, J. et al., 2020. A typology of compound weather and climate events. *Nature Reviews Earth & Environment*: 1-15.

Zuromski, L.M. et al., 2018. Solar-induced fluorescence detects interannual variation in gross primary production of coniferous forests in the Western United States. *Geophysical Research Letters*, 45(14): 7184-7193.

# CHAPTER 3 DEVELOPING A NEWLY INTEGRATED DROUGHT INDEX BASED ON IN-SITU METEOROLOGICAL OBSERVATION AND MULTI-SENSOR REMOTE SENSING DATA

## 3.1 Introduction

There is an increasing need for comprehensive and reliable drought monitoring to aid planning and mitigation of drought impacts, since the frequency and consequences of droughts are expected to intensify under climate change (Halwatura et al., 2017; Keyantash et al., 2004; Wilhelmi et al., 2002; Zhou et al., 2012). Historically, droughts have been classified and assessed using point observations from networks of meteorological stations. For instance, the widely-used Standardized Precipitation Index (SPI), which is the World Meteorological Organization's (WMO) recommended indicator for meteorological drought, is based on ground-based precipitation observations (Hayes et al., 1999b; McKee et al., 1993). More recently, global and near-real-time observations of remote sensing technology open the door for comprehensively characterizing drought conditions regionally and globally, especially in regions with limited sampling gauges (Jiao, Tian, et al., 2019; Lu, Wang, Pan, et al., 2016; Rhee et al., 2010; Wu et al., 2013; Zhang, Jiao, et al., 2017). Various drought indices building on remote sensing observations have been developed to estimate drought conditions. Table 3.1 provides a summary of the commonly used drought indices.

However, many of the existing remote-sensing drought indices are linked to a single biophysical variable (e.g., precipitation, soil moisture, greenness), and may not be sufficient to capture the complex processes and diverse impacts of drought (AghaKouchak et al., 2015a; Hao and Singh, 2015). There is an urgent need to develop

integrated indices which could combine station data and remote sensing observations to alleviate the shortcomings of drought characterization from a single index. Several studies have focused on developing integrated remote-sensing drought indices to provide a more robust and comprehensive estimation of drought. For example, the Microwave Integrated Drought Index (MIDI) (Zhang and Jia, 2013), Scaled Drought Condition Index (SDCI) (Rhee et al., 2010), Optimized Meteorological Drought Index (OMDI) and Optimized Vegetation Drought Index (OVDI) (Hao, Zhang, et al., 2015), Synthesized Drought Index (SDI) (Du et al., 2013) combined variables from multiple perspectives (e.g., Soil Moisture Condition Index (SMCI), Precipitation Condition Index (PCI), Temperature Condition Index (TCI) and Vegetation Condition Index (VCI)). These indices have been shown to perform well in selected study areas (Du et al., 2013; Hao, Zhang, et al., 2015; Rhee et al., 2010; Zhang and Jia, 2013).

A major challenge for these integrated, remote-sensing indices is their relatively poor performance when applied to climate regions different from those in which they were developed since they were optimized under a narrow range of environmental conditions. Another major issue is their inability to adequately represent spatial variability, due to their reliance on traditional composition methods (Park et al., 2016). Specifically, it is often assumed that all areas within a study region contribute the same weight for a particular single index. This type of integration is straightforward to implement and is commonly used to develop multivariate drought indices. However, this type of integration is not well suited for capturing the covariability of drought-related indices, since it may miss local details that can be significant if the relationship of the related indices is spatially non-stationary (AghaKouchak et al., 2015a). A third limitation

is that traditionally integrated drought indices only use a single *in-situ* based drought index as the dependent variable to combine the multi-source remote sensing data. For example, OVDI uses SPI as the dependent variable to determine the weights of PCI, TCI, SMCI and VCI (Hao, Zhang, et al., 2015). Similarly, Vegetation Drought Response Index (VegDRI) only uses Palmer Drought Severity Index (PDSI) as the dependent variable to composite multi-source data (Brown et al., 2008). However, only one dependent variable may not be sufficient to estimate comprehensive drought conditions as they affect hydrological, vegetative, and meteorological conditions. For the regions with both station data and remote sensing images, the integration of ground observation information from multiple perspectives and the remote sensing observations from multi-sensors could be a better way to comprehensively monitor drought.

To address these issues, the objective of this study is to develop and evaluate a new integrated drought index based on multi-sensor remote sensing data for drought monitoring under different climate conditions. In this study, Geographically Weighted Regression (GWR) model and Principal Component Analysis (PCA) were used to composite and integrate multiple remote sensing based drought indices. GWR and PCA were used because they can take the local details into consideration (e.g., using different weights in different parts of the study area for a particular single index), thus the newly developed index can be applied to diverse climate regions. We also used three *in-situ* based drought indices (PDSI, moisture anomaly index (Z-index) and SPI) as dependent variables to composite multi-source single indices. We call the new product the station-enabled Geographically Independent Integrated Drought Index (GIIDI_station) indicating its universal applicability for diverse climate regions. To evaluate the performance of

GIIDI_station, it was compared with both integrated drought indices (MIDI, OMDI) and single drought indices (PCI, TCI, VCI, and SMCI). We also evaluated whether environmental factors impact the performance of GIIDI_station across spatial climate gradients.

Table 3.1: Description of commonly used drought indices. The data source column indicates the satellite name, meteorological observation data or single drought indices used for the integrated drought indices (MIDI and OMDI). The method column shows the main method for establishing drought indices.

| Drought index | Data source | Method | Source |
|---|---|---|---|
| PDSI | Precipitation, temperature, and soil moisture | Based on water balance model | (Palmer, 1965) |
| SPI | Precipitation | Based on the historical precipitation occurrence probability distribution function | (McKee et al., 1993) |
| Z-index | PDSI | Based on PDSI anomaly | (Palmer, 1965) |
| SPEI | Potential evapotranspiration and precipitation | Based on the historical deficiency of precipitation (P-PET) occurrence probability distribution function | (Vicente-Serrano et al., 2010) |
| USDM | SPI, PDSI, soil moisture, NDVI and other indicators | Local expert knowledge | (Svoboda et al., 2002) |
| RDI | Precipitation and evapotranspiration | Similar to SPEI but using $\frac{P}{ET}$ | (Mu et al., 2013) |
| VegDRI | NDVI, Phenology and other indicators | Classification and regression tree (CART) | (Brown et al., 2008) |
| SWI | Precipitation and $ET_o$ | Based on residual water-energy ratio and probability-based function | (Liu, Xu, et al., 2017) |
| VCI | MODIS NDVI | $(NDVI_{ikj}-NDVI_{i,min})/(NDVI_{i,max}-NDVI_{i,min})$ | (Kogan, 1995b) |
| TCI | MOIDS LST | $(LST_{i,max}-LST_{ijk})/(LST_{i,max}-LST_{i,min})$ | (Kogan, 1997) |
| SMCI | AMSR-E Soil moisture | $(SM_{ikj}-SM_{i,min})/(SM_{i,max}-SM_{i,min})$ | (Rhee et al., 2010) |
| PCI | TRMM precipitation | $(TRMM_{ikj}-TRMM_{i,min})/(TRMM_{i,max}+TRMM_{i,min})$ | (Zhang and Jia, 2013) |

| | | | |
|---|---|---|---|
| MIDI | TCI, SMCI, PCI | Empirical weights | (Zhang and Jia, 2013) |
| OMDI | TCI, SMCI, PCI | Constrained optimization | (Hao, Zhang, et al., 2015) |

*$LST_{ijk}$, $SM_{ijk}$, $TRMM_{ijk}$—monthly LST, SM, TRMM for pixel i, in month j, for year k, respectively. $LST_{i,min}$, $SM_{i,min}$, $TRMM_{i,min}$—multi-year minimum LST, SM, TRMM, respectively, for pixel i. $LST_{i,max}$, $SM_{i,max}$, $TRMM_{i,max}$—multi-year maximum LST, SM, TRMM, respectively.

## 3.2. Data

Both *in-situ* and remote sensing datasets were used to develop and assess the performance of our GIIDI_station. These data were also used to compare GIIDI_stations's performance with other remote sensing-based drought indices in various climate divisions over the continental United States (CONUS), focusing on the growing season from 2002 to 2011. The product of Advanced Microwave Scanning Radiometer for EOS (AMSR-E) was used in the development of GIIDI_station and the AMSR-E data was available from 2002 to 2011.

### 3.2.1 *In-situ* based drought indices

Three monthly *in-situ* drought indices, PDSI, moisture anomaly index (Z-index), and Standardized Precipitation Index (SPI) were selected for incorporation into GIIDI_station because they are among the most commonly used indicators for drought monitoring in the United States. These *in-situ* drought indices, which provide general assessment of soil moisture and precipitation conditions, were obtained from the NOAA's National Climatic Data Center (NCDC–NOAA) repository for 344 climatic divisions in the CONUS (http://www1.ncdc.noaa.gov/pub/data/cirs/). These selected *in-situ* indices also have been widely applied by various studies to evaluate remote sensing drought indices (Brown et al., 2008; Caccamo et al., 2011; Ji et al., 2003; Rhee et al., 2010). In our study, the PDSI, Z-index and SPI from 1012 observation stations were used

as training data, and climate division level based PDSI, Z-index and SPI were used as evaluation data.

### 3.2.2 Remote sensing data

Four remote based drought indices -- Moderate Resolution Imaging Spectroradiometer (MODIS) data based VCI and TCI, AMSR-E based SMCI, and TRMM-based PCI -- were selected for incorporation into GIIDI_station. These four remote sensing based drought indices estimate drought conditions from unique perspectives. The VCI, which is derived from Vegetation Index based on the Universal Pattern Decomposition method (VIUPD), estimates drought conditions based on the vegetative response. It was calculated using MODIS land surface data (MOD09A1) downloaded from the Land Processes Distributed Active Center (LPDAAC; http://lpdaac.usgs.gov/). TCI describes temperature anomaly during the drought events. Monthly TCI was calculated using MODIS Land Surface Temperature (LST) data (MOD11A2), which was obtained from the National Aeronautics and Space Administration's (NASA) earth observing system data and information system (EOSDIS; http://reverb.echo.nasa.gov). PCI provides information on precipitation deficiency. It was calculated based on TRMM 3B43 data, which was available at the NASA Data and Information Services Center (DISC) (http://mirador.gsfc.nasa.gov/). SMCI was selected to describe the soil moisture perspective. We compute SMCI based on the AMSR-E product, obtained from Vrije Universtiteit Amsterdam (http://nsidc.org/).

### 3.2.3 Other data

United States Drought Monitor (USDM) data was chosen as a proxy for evaluating the performance of GIIDI_station. USDM combines information from

multiple ground-observation based drought indicators and local reports from state climatologists and observers throughout the country, and it is used as a trigger for federal drought relief programs (Brown et al., 2008; Hayes et al., 2012). The USDM map has a spatial resolution at the approximate scale of a climate division (Svoboda et al., 2002). The USDM classifies droughts as D0 (abnormally dry), D1 (moderate drought), D2 (severe drought), D3 (extreme drought), and D4 (exceptional drought) events. Detailed information about USDM is available at http://drought.unl/dm/.

In order to further evaluate the performance of GIIDI_station, nine additional datasets including land use/land cover (LULC) data, climate data, and soil data were selected to explore whether the performance of GIIDI_station for drought monitoring depends on common environmental factors. The U.S. Geological Survey National Land Cover Data (NLCD) (http://landcover.usgs.gov) was used to describe LULC state. Mean annual precipitation and temperature data were selected to describe climate conditions. Data on estimated mean annual precipitation and temperature in each climate division was obtained from the Oregon State University PRISM group (http://prism.oregonstate.edu) and DISC (http://mirador.gsfc.nasa.gov/), respectively. Information on five soil properties, including permeability, water table depth, available water holding capacity, hydrologic groups and soil drainage, were obtained from the Center for Environmental Informatics at Penn State University (http://www.soilinfo.psu.edu/). A more detailed description of these indices is available from Quiring et al. (2010).

## 3.3. Methodology

To develop the composite GIIDI_station index, we first calculated VCI using VIUPD instead of the commonly used NDVI, since the former has been shown to better estimate drought conditions (Jiao et al., 2016). Next, we used the GWR model to composite TCI, VCI, PCI and SMCI. We used three different *in-situ* drought indices (SPI, PDSI and Z-index) as the dependent variables to composite the remote sensing based condition indices (TCI, VCI, PCI and SMCI). There are three outcomes of GWR model based composition: SPI-targeted integrated drought index, PDSI-targeted integrated drought index and Z-index targeted integrated drought index. The PCA method was then used to composite these three outcomes of the GWR into GIIDI_station. To validate the product, we first evaluated the correlation between *in-situ* drought indices and GIIDI_station in different climate divisions. Then the LULC data, climate data and soil data were used to explore whether the performance of GIIDI_station for drought estimation was affected by LULC, precipitation, temperature and soil conditions. More details about our methodology are given in Sections 3.1 - 3.3, and the overall approach is illustrated in Figure 3.1.

### 3.3.1 Scaled remote sensing indices

Table 3.1 shows detailed information about the remote sensing based drought indices used in this study. To reiterate, TCI, PCI, VCI and SMCI were used to develop GIIDI_station, while MIDI and OMDI were used to assess its drought monitoring performance. The analysis in this study focused primarily on the months from April to October in order to avoid noise from the snow and ice in the winter.

### 3.3.2 GIIDI_station development and evaluation

The development of GIIDI_station incorporated *in-situ* drought indices (SPI, PDSI, and Z-index) from 1012 observation stations. GIIDI_station was calculated using GWR model based on the following equations:

$$Y=\beta_0(\mu,v)+\beta_1(\mu,v)TCI+\beta_2(\mu,v)VCI+\beta_3(\mu,v)PCI+\beta_4(\mu,v)SMCI, \quad (3.1)$$

$$Y=\begin{cases} SPI \\ PDSI \\ Z\text{-}index \end{cases}, \quad (3.2)$$

where $(\mu,v)$ denotes the geographical coordinates of the 1012 observation stations. $\beta_i(u,v)$ represents the weighting of single indices (TCI, VCI, PCI and SMCI). Y is the dependent variable which includes the three widely used *in-situ* drought indices: SPI, PDSI and Z-index. In geographically weighted regression, the parameter estimates are made using an approach in which the contribution of a sample to the analysis is weighted based on its spatial proximity to the specific location under consideration. Data from observations close to the location under consideration are weighted more than data from observations further away. The parameters were estimated from

$$\hat{\beta}(\mu,v)=(X^TW(\mu,v)X)^{-1}X^TW(\mu,v)Y, \quad (3.3)$$

where $\hat{\beta}(\mu,v)$ represents an estimate of $\beta$, $W(\mu,v)$ is the weighting matrix, which ensures that observations close to the location at which the parameter estimates are to be made have more influence on the analysis than those further away. $W(\mu,v)$ is a matrix of weights relative to the position of (μ,v) in our study area. W(μ,v) is computed from a weighting scheme that is also known as a kernel (Fotheringham et al., 1998). Gaussian-shaped kernel was used in our study:

$$W_i(u,v) = e^{-0.5(\frac{d_i(u,v)}{h})^2}, \quad (3.4)$$

where $W_i(u,v)$ is the geographical weight of the *i*th observation relative to the location (u,v), and (u,v) is the coordinate of observation points. $d_i(u,v)$ is the distance between the grid cells and the location (u,v). h is known as the bandwidth. In our study, the bandwidth was determined based on the corrected Akaike Information Criterion (AICc) (Hurvich et al., 1998) which takes the form below:

$$AIC_c = 2n\log_e(\hat{\sigma}) + n\log_e(2\pi) + n(\frac{n+tr(S)}{n-2-tr(S)}), \quad (3.5)$$

where n is the number of observations in the dataset, $\hat{\sigma}$ is the estimate of the standard deviation of the residuals, and tr(S) is the trace of the hat matrix. The optimum of h could be found based on the least AICc. In this study, GWR model was established using arcpy module in Python. Given that there were three different *in-situ* based drought indices (SPI, PDSI and Z-index) as the dependent variables in equation (1), there were three outcomes of the GWR model: SPI-targeted integrated drought indices, PDSI-targeted integrated drought indices and Z-index targeted integrated drought indices. In order to better integrate these three GWR model outputs into one variable, the PCA method was used to composite the three different outcomes into GIIDI_station (see equations 3.6 and 3.7). The basic purpose of using PCA is to reduce the dimensionality of a data set from a large set of variables into a small set of variables (Wold et al., 1987). The first principal component (PC1) of the PCA was selected and the values of the PC1 were normalized as the range of -6 to 6 in corresponding to the range of PDSI. Then the normalized PC1 was defined as GIIDI_station since it accounts for as much of the variability of these three GWR outputs, which were based on the dependent variables of SPI, PDSI and Z-index, respectively. The PCA process was finished in environment for visualizing images

(IDL/ENVI) software environment. It also should be noted that 1-month SPI was used as the dependent variable to produce SPI-targeted integrated index as an example. Our framework could also include different time-scales of SPI to obtain different time scales of GIIDI_station.

$$\begin{cases} Y_1\text{=SPI-targeted integrated drought index} \\ Y_2\text{=PDSI-targeted integrated drought index} \\ Y_3\text{=Z index-targeted integreated drought index} \end{cases}, \tag{3.6}$$

$$\text{GIIDI\_station} = \text{PCA}(Y_1, Y_2, Y_3)\,, \tag{3.7}$$

The drought severity category definition was based on the drought severity classification system of USDM (abnormally dry, moderate drought, severe drought, extreme drought, and exceptional drought). Similar to USDM, we defined each drought severity category based on the cumulative frequency for historical GIIDI_station value distribution. The evaluation of GIIDI_station includes three stages. In the first stage, we compared GIIDI_station with PCI, MIDI and OMDI during the growing season (April–October) using the visual comparison method. Here, the years of 2007, 2009 and 2011 were selected as the examples of severe, moderate and extreme drought years, respectively. Pearson correlation between remote sensing drought indices and *in-situ* indices was then used in the second stage to assess the performance of the compared remotely sensed drought indices. In the third stage, nine independent variables were selected in a multivariate regression model to evaluate whether the environmental factors (e.g., LULC, climate and soil variables) could affect the applicability of GIIDI_station.

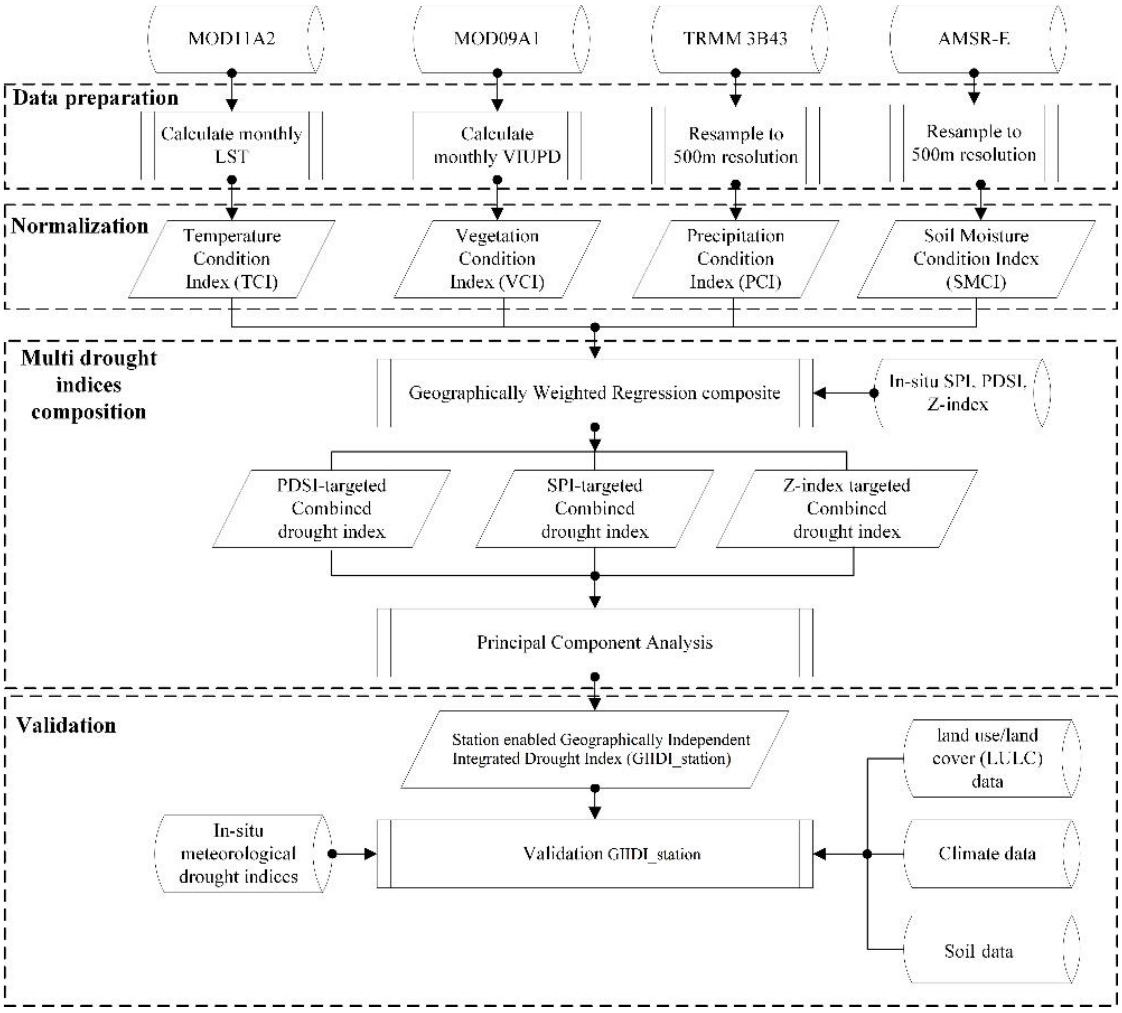


Figure 3.1: Flowchart of comprehensive drought estimation based on multi-source remote sensing data.

## 3.4. Results

### 3.4.1 The significance of GWR and PCA models

Figure. 3.2 shows an example of the weighting of PCI, TCI, VCI and SMCI, when taking PDSI in July 2011 as the response variable using the GWR model. In Figure. 3.2, different colors of the points indicate different weighting of each remote sensing based drought index. According to Figure. 3.2, we can see the weighting of PCI, TCI,

VCI and SMCI was spatially heterogeneous. For example, in the southern Great Plains, VCI took higher weighting than other indices, but in the Southeast, the weighting of VCI was lower than other indices. Unlike the spatial homogeneity models, GWR model could provide the criterion weights depend on the spatial variable range of criterion values.

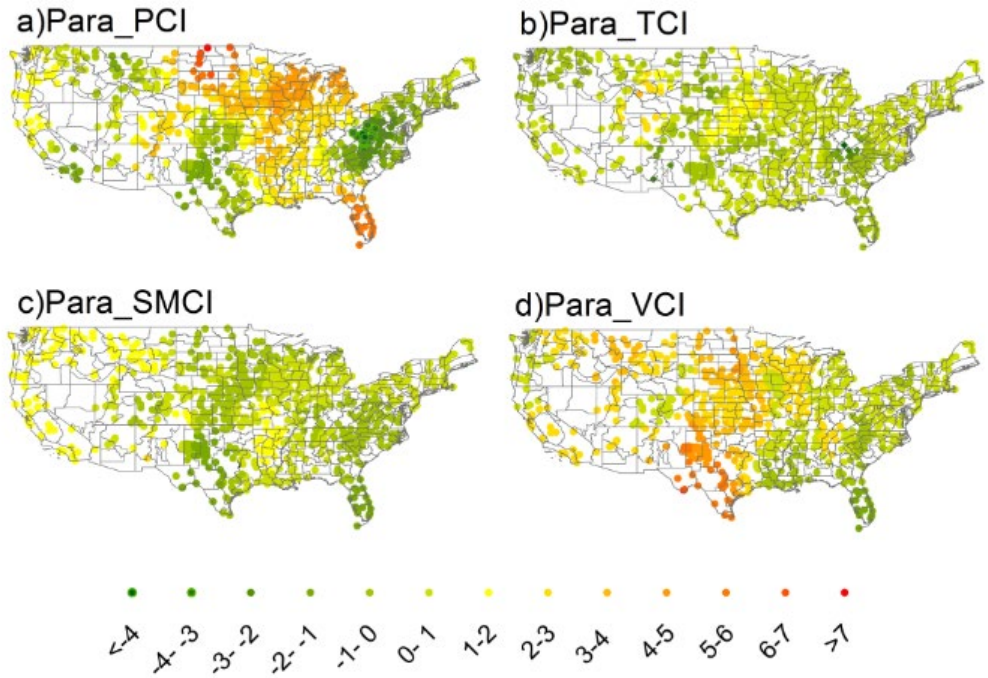


Figure 3.2: Spatial distributions of GWR estimated parameters for PDSI simulation in July 2011: (a) parameter for PCI; (b) parameter for TCI; (c) parameter for SMCI; and (d) parameter for VCI.

For clarity, in the process of PCA composition, we referred to the integrated drought index developed using PDSI as the dependent variable in GWR as the "PDSI targeted Combined Drought Index (CDI)". Similarly, SPI targeted CDI and Z-index targeted CDI were named when using SPI and Z-index as the dependent variables, respectively. Figure 3.3 shows the relationships between GIIDI_station, SPI targeted CDI, PDSI targeted CDI and Z-index targeted CDI for July 2011. According to Figure

3.3, there were still differences between SPI-, PDSI- and Z-index targeted CDI, and GIIDI_station achieved better agreement with *in-situ* drought indices after the three CDIs were integrated by PCA. The determination of coefficients ($R^2$) between PDSI targeted CDI and SPI-, Z-index targeted CDI were 0.318 and 0.259, respectively, while the determination of coefficients ($R^2$) between GIIDI_station and SPI-, Z-index targeted CDI were 0.737 and 0.612, respectively (Figure 3.3). Thus, PCA can effectively combine different information from each *in-situ* drought index based CDI into a newly integrated drought index.

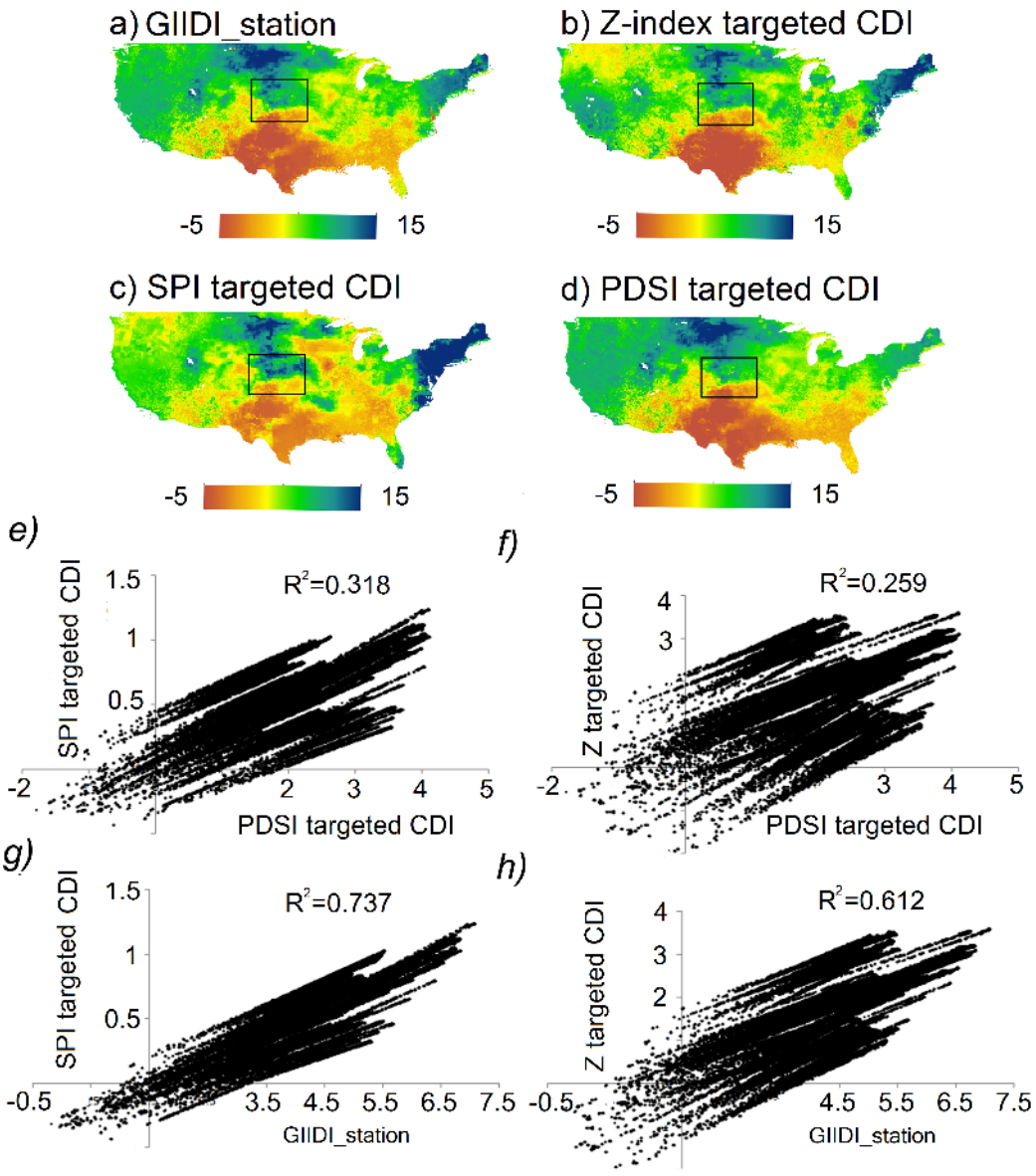


Figure 3.3: The correlations between GIIDI_station, SPI-, PDSI- and Z-index targeted CDI. Panel a) stands for the values of GIIDI_station for July 2011; b) to d) represents the values of SPI targeted CDI, PDSI targeted CDI and Z-index targeted CDI for July 2011, respectively. Panel e) – f) show the correlations between GIIDI_station, PDSI-, SPI- and Z-index targeted CDIs for the specified regions using squares in panel a) to d).

### 3.4.2 GIIDI_station drought category definition

To define the categories of drought indices, we calculated the frequency of the county level GIIDI_station values. The historical frequency and cumulative frequency of GIIDI_station distribution for all the grid cells over CONUS from the year 2002 to 2011 is shown in Figure 3.4. Referring to the drought classification schemes of USDM, we classified GIIDI_station into six levels based on the historical GIIDI_station frequency distribution. Table 3.2 shows the drought severity classification ranges for GIIDI_station for each dryness level.

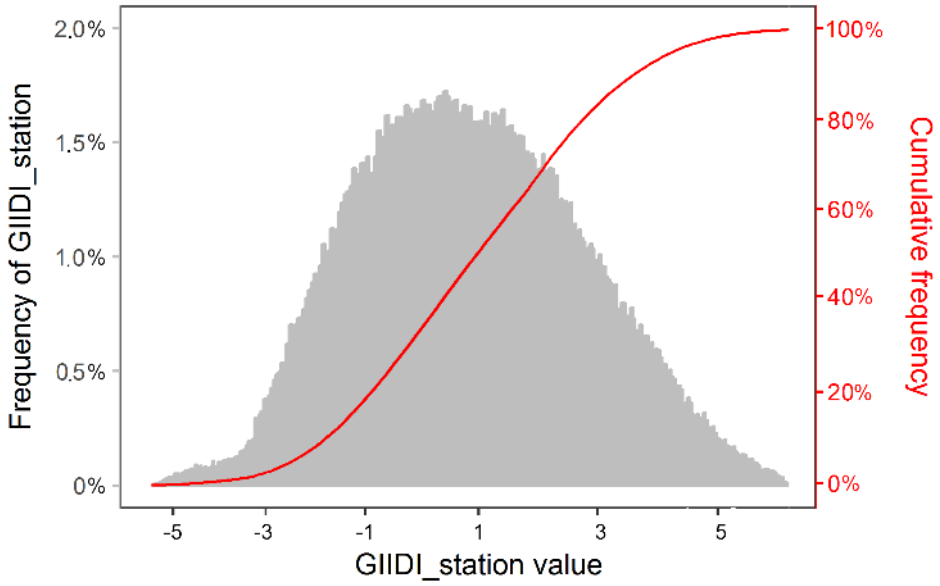


Figure 3.4: Frequency and cumulative frequency distribution of GIIDI_station values.

Table 3.2: Drought classification scheme of GIIDI_station

| GIIDI_station Values | Drought Category | Cumulative Percentiles |
|---|---|---|
| -0.49 to 0.50 | Abnormally Dry | 33.9% |

| | | |
|---|---|---|
| -1.49 to -0.50 | Moderate Drought | 23.8% |
| -2.49 to -1.5 | Severe Drought | 12.4% |
| -3.49 to -2.5 | Extreme Drought | 5.6% |
| < -3.5 | Exceptional Drought | 1.8% |
| >0.5 | No Drought | ~ 66% |

### 3.4.3 Regional drought pattern comparisons

The similarity of the remote sensing drought indices to USDM, and to each other, was assessed by mapping drought conditions over the CONUS during the growing seasons of 2007, 2009, and 2011. As described above, these years were selected to exemplify moderate, slight and severe drought years, respectively. Maps of monthly drought conditions monitored by the USDM, GIIDI_station, OMDI, MIDI and PCI are shown in Figs. 3.5 to 3.7. These figures demonstrate the diversity of information provided by different drought indicators, highlighting the complexity of developing an integrated drought index in various climate regions at the continental scale. Generally, as show in Figs. 5 to 7, GIIDI_station shows greater similarity to USDM under all drought conditions when compared to the other drought indices.

In 2011, USDM indicated that the majority of Texas, New Mexico and Georgia experienced extreme drought (D1) beginning in April. The drought then began to expand into northern regions (e.g., Michigan, Iowa and Illinois) and throughout the southeastern by August (see USDM in Figure 3.5). All the compared indices indicated a general extreme drought condition from April to May in the south. However, patterns in PCI, OMDI and MIDI were similar but not identical to those in the USDM and GIIDI_station.

They showed expansion of the extreme drought areas into the northern Great Plains and northwestern CONUS in June, when these regions were identified as drought free by USDM and GIIDI_station. Figure 3.6 provides additional insights about the performance of the indices during the moderate drought of 2009. The USDM indicated moderate drought in western regions along the coast, and a small region of extreme drought in south Texas. GIIDI_station generally captured the drought features in the USDM, while other drought indices showed different patterns. For example, from April to May, PCI, OMDI and MIDI diagnosed drought conditions in the northwestern Great Plains. In September, these indices classified areas of the western and northeastern CONUS as experience severe drought, severe drought in these areas was not identified by USDM and GIIDI_station in 2009. As shown in Figure 3.7, similar results were obtained for the severe drought year of 2007. Based on the USDM data, western regions and areas of the Southeast (Georgia, Alabama, North and South Carolina) experienced D1 (moderate drought) to D2 (severe drought). The drought condition became even more severe (D2 and D3) in southeastern regions by October 2007. PCI, MIDI and OMDI maps showed high inter-index agreement but were less similar to USDM when compared to GIIDI_station. Unlike MIDI, PCI and OMDI, GIIDI_station identified drought conditions in the west and southeastern regions that did not change much in terms of severity from April to October 2007, in reasonable agreement with predictions from the USDM.

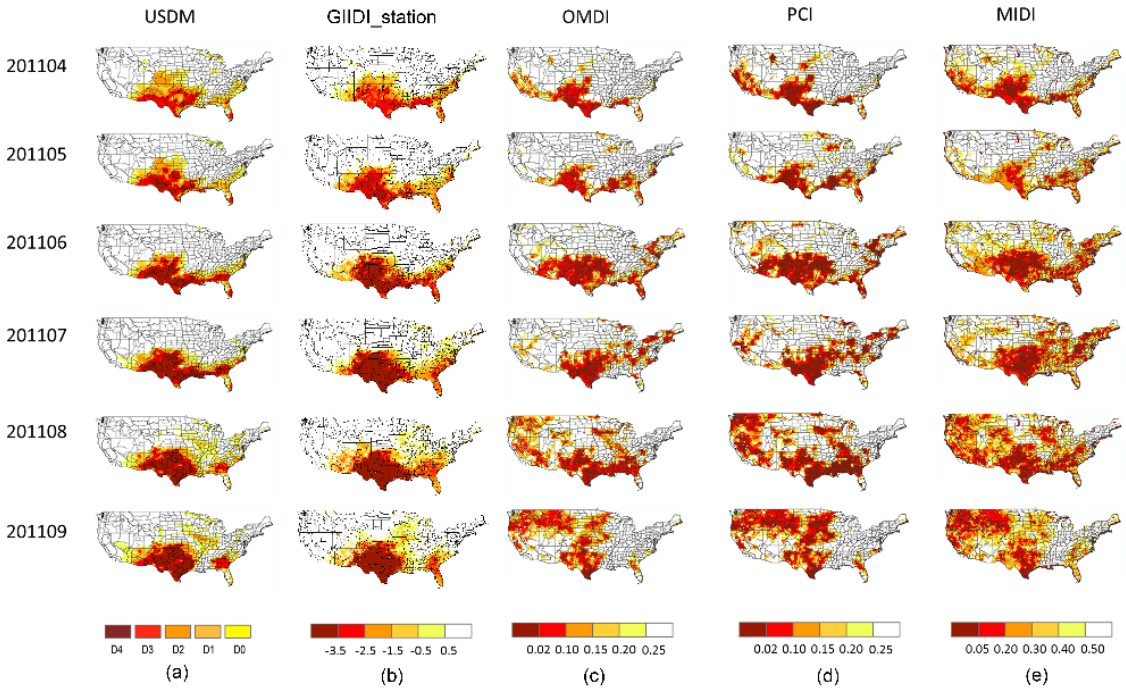


Figure 3.5: Drought conditions in the US monitored by multiple drought indices from April to September in 2011. The first column displays the observed USDM drought data for the period of April to October, while the second to fifth columns show the GIIDI_station, OMDI, PCI and MIDI, respectively. For USDM, D0-D4 represents the different severities of drought conditions; for columns 2 to 5, lower values stand for more severe drought.

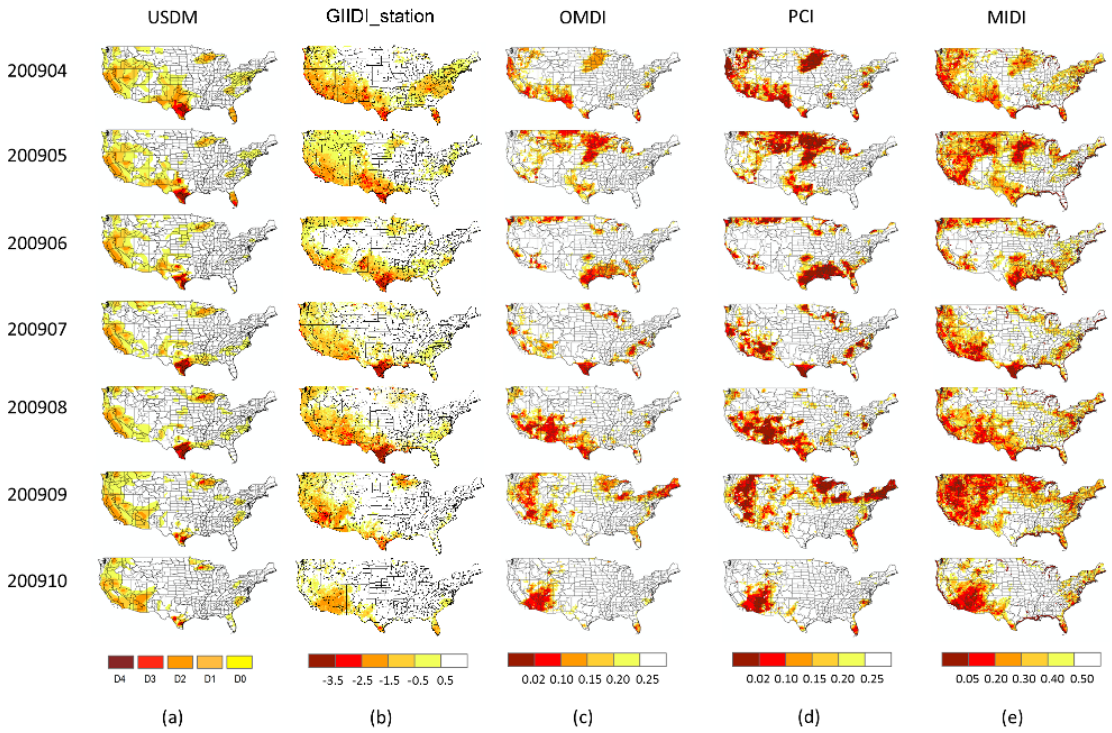


Figure 3.6: Drought conditions in the US monitored by multiple drought indices from April to October in 2009. The first column displays the observed USDM drought data for the period of April to October, while the second to fifth columns show the GIIDI_station, OMDI, PCI and MIDI, respectively. For USDM, D0-D4 represents the different severities of drought conditions; for columns 2 to 5, lower values stand for more severe drought.

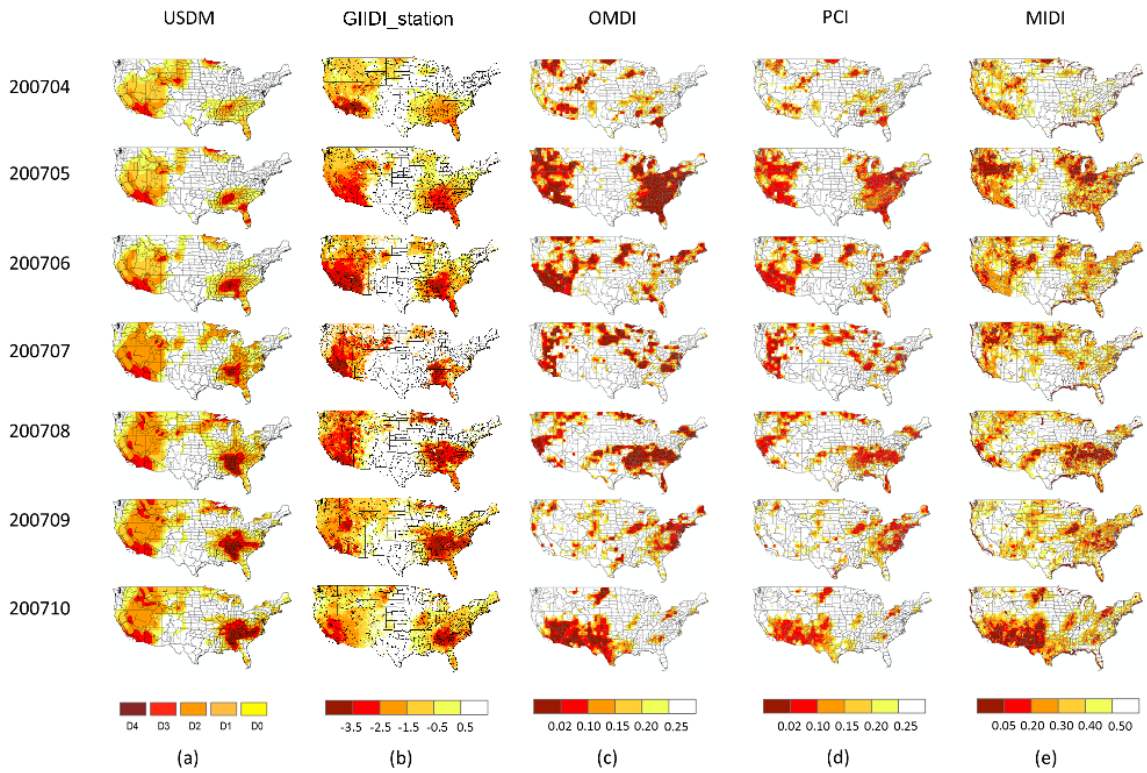


Figure 3.7: Drought conditions in the US monitored by multiple drought indices from April to October in 2007. The first column displays the observed USDM drought data for the period of April to October, while the second to fifth columns show the GIIDI_station, OMDI, PCI and MIDI, respectively. For USDM, D0-D4 represents the different severities of drought conditions; for columns 2 to 5, lower values stand for more severe drought.

### 3.4.4 Monthly temporal and spatial correlation comparisons

We compared the correlations between seven remotely sensed drought indices (GIIDI_station, MIDI, OMDI, PCI, TCI, VCI and SMCI) and *in-situ* drought indices (PDSI, Z-Index, 1-, 2-, 3-, 6-, 9-, 12-, and 24-month SPI). Of the remote sensing based

indices considered here, GIIDI_station was the most similar to the *in-situ* indices in their temporal ranking of drought conditions (see Tables 3.3 and 3.4).

Table 3.3: Comparison of the performance of GIIDI_station with six commonly used remote sensing drought indices using 8 *in-situ* drought indices. r is the correlation coefficient between two variables. *denotes the maximum value in each column. GIIDI_station, MIDI, OMDI, PCI, TCI, VCI and SMCI are seven remotely sensed drought indices; PDSI, Z-Index, 1-, 2-, 3-, 6-, 9-, 12-, and 24-month SPI are *in-situ* drought indices.

| Drought indices | r (n = 24080) | | | | | | | |
|---|---|---|---|---|---|---|---|---|
| | PDSI | Z | SPI-1 | SPI-3 | SPI-6 | SPI-9 | SPI-12 | SPI-24 |
| GIIDI_station | 0.801* | 0.877* | 0.892* | 0.803* | 0.795* | 0.671* | 0.632* | 0.493* |
| OMDI | 0.496 | 0.825 | 0.871 | 0.686 | 0.592 | 0.449 | 0.395 | 0.354 |
| MIDI | 0.504 | 0.788 | 0.807 | 0.662 | 0.580 | 0.445 | 0.399 | 0.345 |
| VCI | 0.622 | 0.313 | 0.234 | 0.564 | 0.582 | 0.584 | 0.548 | 0.390 |
| PCI | 0.440 | 0.806 | 0.865 | 0.559 | 0.398 | 0.350 | 0.303 | 0.211 |
| TCI | 0.542 | 0.589 | 0.487 | 0.515 | 0.471 | 0.423 | 0.379 | 0.278 |
| SMCI | 0.370 | 0.451 | 0.426 | 0.389 | 0.331 | 0.297 | 0.259 | 0.197 |

Table 3.4: Comparisons of the RMSE between GIIDI_station and other commonly used remote sensing based drought indices. *denotes the minimum value in each column. GIIDI_station, MIDI, OMDI, PCI, TCI, VCI and SMCI are seven remotely sensed drought indices; PDSI, Z-Index, 1-, 2-, 3-, 6-, 9-, 12-, and 24-month SPI are *in-situ* drought indices.

| | RMSE (n = 24080) |
|---|---|

| Drought indices | PDSI | Z | SPI-1 | SPI-3 | SPI-6 | SPI-9 | SPI-12 | SPI-24 |
|---|---|---|---|---|---|---|---|---|
| GIIDI_station | 0.858* | 0.783* | 0.709* | 0.849* | 0.861* | 0.956* | 0.998* | 1.223* |
| OMDI | 3.011 | 0.803 | 0.732 | 1.305 | 1.805 | 2.303 | 2.499 | 2.667 |
| MIDI | 2.985 | 0.823 | 0.776 | 1.344 | 1.878 | 2.397 | 2.589 | 2.697 |
| VCI | 2.658 | 2.244 | 1.159 | 1.075 | 1.082 | 1.058 | 2.068 | 3.074 |
| PCI | 3.440 | 0.865 | 0.801 | 2.559 | 2.598 | 2.650 | 2.703 | 2.811 |
| TCI | 2.709 | 2.289 | 1.166 | 1.145 | 1.271 | 1.223 | 1.379 | 1.278 |
| SMCI | 2.856 | 2.234 | 1.183 | 1.324 | 1.245 | 1.255 | 1.265 | 1.278 |

Figure. 3.8 shows the temporal similarity between the *in-situ* drought indices and each of the remote-sensing drought indices, evaluated as linear correlation within each climate division. GIIDI_station yielded higher performance than the other remote sensing based indices. High correlation values (r-value >0.6) between GIIDI_station and the *in-situ* drought indices were obtained in almost all the climate divisions, and across the multiple timescales associated with the *in-situ* indices. In the western and northeastern United States, most of the remote sensing based drought indices showed weak correlation (e.g., $r < 0.4$) with *in-situ* drought indices. For example, as shown in Figure 3.8, VCI generally correlated significantly only in the southern CONUS. PCI exhibited strong correlations with SPI-1 but not with long-term SPI (SPI-3 and SPI-6) in most of the CONUS.

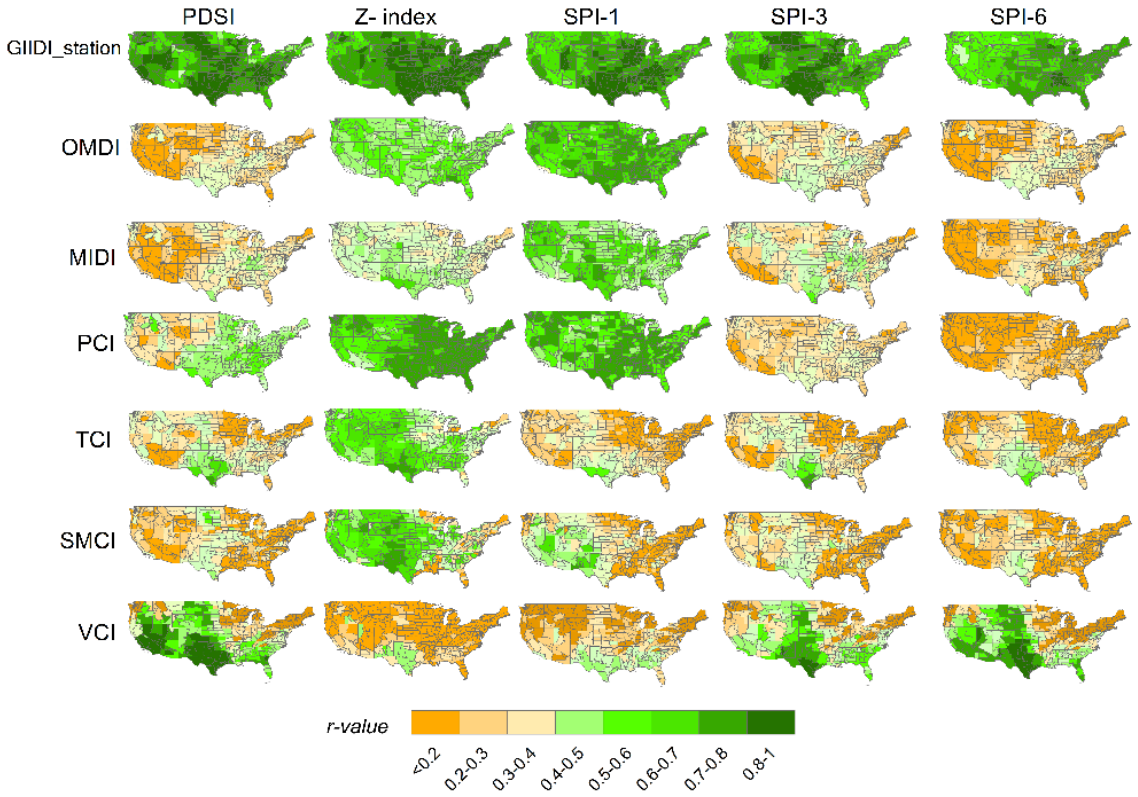


Figure 3.8: Spatial distribution across climate divisions of the correlations (r-value) between remote-sensing-based and *in-situ*-based drought indices for the entire growing season (April to October) of 2002–2011.

### 3.4.5 Factors influencing the relationships between GIIDI_station and *in-situ* drought indices

Nine independent variables (LULC, mean annual precipitation, mean annual temperature, permeability, mean soil moisture, organic material in soil, available water holding capacity, hydrologic groups, and soil drainage class) were entered into a stepwise multivariate regression model where the dependent variable was the r-values between GIIDI_station and PDSI, Z-index and SPI. Results showed that there was no significant correlation between the nine independent variables and the performance of GIIDI_station

(p >0.05). The stepwise regression model results showed that if four or five variables were included in the regression model, it provided the best regression result (Figure 3.9). However, the top four or five significant variables all together explained only 8.3% of the GIIDI_station performance (Figure 3.9). This indicates that the performance of GIIDI_station for monitoring drought conditions is not dependent on these nine common environmental factors. In comparison, some previous studies have shown that the performance of other remotely sensed drought indices is strongly dependent on environmental factors (Brown et al., 2008; Ji et al., 2003; Quiring et al., 2010; Zhang, Jiao, et al., 2017). For example, Quiring et al. (2010) demonstrated that the response of VCI to drought conditions is modulated by vegetation type, land use practices and soil type.

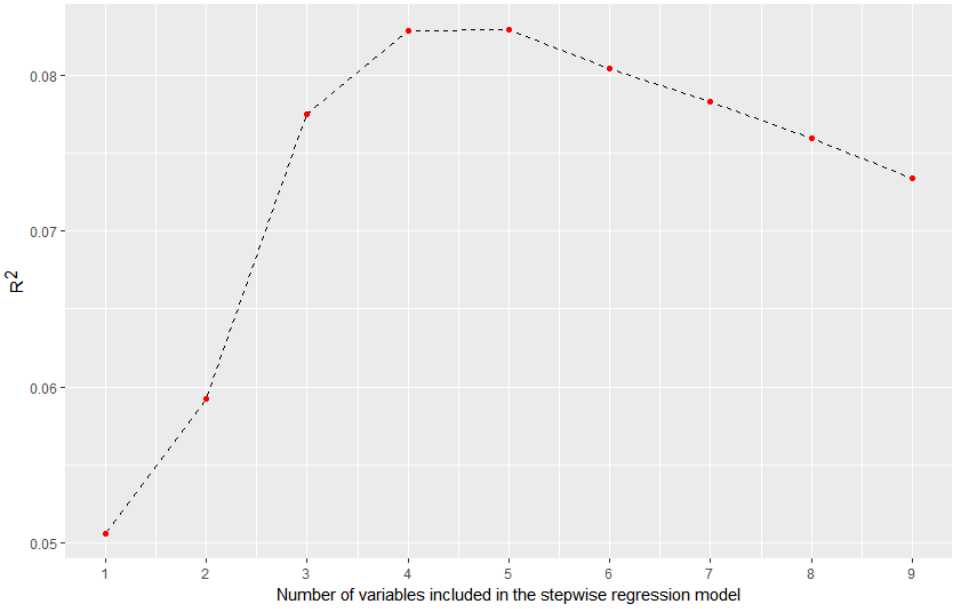


Figure 3.9: Results of regression model showing the number of variables included in the regression model and the performance of GIIDI_station. Values on the y-axis are the adjusted $R^2$, x-axis stands for the number of variables included in the stepwise regression model.

### 3.5. Discussion

Based on the comparison results, we can draw some general conclusions regarding the applicability of GIIDI_station for drought monitoring across climate divisions. The GIIDI_station provides several unique characteristics for drought monitoring. The most unique characteristics of GIIDI_station for drought monitoring is its potential as a reliable index for drought monitoring across climate regions, linked to the fact that its performance is independent of environmental factors. Previous work indicated that the performances of traditional remote sensing based indices such as VCI depend on precipitation, land cover and other factors (Bayarjargal et al., 2006; Quiring et al., 2010; Singh et al., 2003; Vicente-Serrano, 2007), and therefore have limited applicability across different regions. For example, for the fifteen remote sensing based drought indices assessed by Zhang, Jiao, et al. (2017), performance of most remote sensing based drought indices is generally good only in Texas and the central CONUS, and is poorer in western and northeastern regions. Compared with these indices, GIIDI_station can perform reasonably well across all different climate regions. Our results indicate that GIIDI_station has high correlation with *in-situ* evaluation drought indices located in almost all the climate regions. In addition, the performance of GIIDI_station for drought monitoring is not influenced by the common environmental factors such as LULC, mean annual precipitation, mean annual temperature, permeability, mean soil moisture, organic material in soil, available water holding capacity, hydrologic groups, and soil drainage class. Another unique characteristic of GIIDI_station for drought monitoring is that it could monitor different severity of drought

conditions. We selected 2007, 2009 and 2011 as the severe, moderate and extreme drought examples in our study, and GIIDI_station shows the best match with USDM according to our visual interpretation. In addition, compared with USDM, GIIDI_station does not require knowledge from local experts, which makes the establishmentof GIIDI_station is much less expensive and time-consuming than USDM.

Several factors could contribute to the superior performance of GIIDI_station for drought monitoring. Firstly, the GWR model, which is used to combine multiple single drought indices and includes the spatial coordinates of the sample sites in the analysis, has the potential to provide a more appropriate basis for the spatial integration of the relationship between variables. Different single indices have different characters and they also have different applicability. Previous studies indicated that VIUPD based VCI performed worse in regions with lower temperature and SMCI performed worse in regions with high density of vegetation cover (Jiao et al., 2016; Zhang, Jiao, et al., 2017), so in relatively cold regions the weighting of VCI should be lower than other indices, and in the high density vegetation covered regions, the weighting of SMCI should be lower. The GWR model is a preferable choice for combining single drought indices because it permits this flexibility in weighting. Because GWR model is a local regression model for spatially varying relationships, it leads to the single indices have their high weights in the regions where they best suitable for. As the parameters from GWR model shown in Figure 3.2, high weighting of VCI mainly located on warm regions such as Texas. Similarly, the relatively higher weighting of SMCI mainly located on the sparse vegetation covered region in the West. Our spatial distributions of the weights for the single drought indices are in accordance with the findings of previous studies.

Secondly, the selection of multiple dependent variables is another factor that potentially contributes to the good performance of GIIDI_station. Many previous studies only use one *in-situ* based drought index as the dependent variable to combine multiple dependent variables. For example, Hao, Zhang, et al. (2015) used the *in-situ* based SPEI as the dependent variable to composite TCI, PCI and SMCI for establishing OMDI. Brown et al. (2008) only used PDSI as the dependent variable to combine the multi-variable when calculating VegDRI. Such approach reflects a limited perspective on drought, as there are differences between the station-based drought indices. We used three different *in-situ* based drought indices (PDSI, Z-index and SPI) as the dependent variables to composite the integrated drought indices. The evaluation of PCA output in our results indicates that GIIDI_station could synthetically contain the most information from dependent of variable from PDSI, Z-index and SPI. The integration of the information from PDSI, Z-index and SPI makes GIIDI_station shows better consistence with USDM in different severity of drought conditions since USDM itself contains the combined information from different drought indices such as PDSI, Z-index and SPI.

Third, the selection of single indices is another factor that potentially contributes to the good performance of GIIDI_station. Previous studies indicate that the time series analysis based single drought indices (PCI, TCI, VCI and SMCI) performed better than other types of single drought indices such as Perpendicular Drought Index (PDI), Modified Perpendicular Drought Index (MPDI) and Temperature Vegetation Dryness Index (TVDI) (Zhang et al. 2017a). PCI is derived from the scaled precipitation information based on TRMM data, TCI is derived from land surface temperature information, VCI is about the condition of vegetation growth, and the SMCI is soil

moisture condition from AMSR-E data. These indices are not fully correlated with each other. In this regard, PCI, SMCI, VCI and TCI were selected to composite GIIDI_station. To summarize, GIIDI_station can be more confidently applied across different environmental regions when compared to the existing remotely-sensed drought indices and it has potential to be used as a mixture of meteorological drought and agricultural drought index. However, the application of GIIDI_station is limited to regions with available meteorological ground observations. Establishing reliable integrated remote sensing based drought indices which could be applied in various environmental regions without relying on ground observations is an important avenue for future work.

### 3.6. Conclusions

Reliable drought monitoring is fundamental to planning and mitigation of drought impacts. Given the complexity of drought, a drought index from single data source, which typically represents a limited perspective on drought impacts, may not be sufficient for comprehensive drought detection. This study outlines a multi-index drought monitoring framework (GIIDI_station). GWR model and PCA were used to integrate multi-sensor remote sensing data and *in situ* based drought indices in this framework. The GIIDI_station, along with the USDM, PCI, OMDI and MIDI, were assessed for their ability to characterize moderate, severe and extreme drought examples in the United States. Their performance was also compared to information provided by *in-situ* drought indices (PDSI, Z-index, SPI-1, SPI-3, SPI-6, SPI-9, SPI-12, and SPI-24), and the relationship between GIIDI_station and a range of environmental factors was also investigated.

Based on the case studies, the GIIDI_station generally captures the drought severity as indicated by USDM. The results also indicated that the GIIDI_station had the strongest correlation with *in-situ* drought indices when compared to the other remote sensing based indices in most climate divisions, and its applicability is not significantly affected by environmental factors such as precipitation, temperature, soil available water holding capacity, soil moisture, soil permeability, soil drainage class, hydrological group, organic material in soil and LULC. We emphasize that GIIDI_station is not meant to replace any other drought indices but as an additional source of information and a new framework, which combines different perspectives afforded by remote sensing and *in-situ* data, and has great potential for monitoring drought conditions across diverse climate conditions.

**References**

AghaKouchak, A. et al., 2015a. Remote sensing of drought: Progress, challenges and opportunities. *Reviews of Geophysics*, 53(2): 452-480.

Bayarjargal, Y. et al., 2006. A comparative study of NOAA–AVHRR derived drought indices using change vector analysis. *Remote Sensing of Environment*, 105(1): 9-22.

Brown, J.F., Wardlow, B.D., Tadesse, T., Hayes, M.J. and Reed, B.C., 2008. The Vegetation Drought Response Index (VegDRI): A new integrated approach for monitoring drought stress in vegetation. *GIScience & Remote Sensing*, 45(1): 16-46.

Caccamo, G., Chisholm, L.A., Bradstock, R.A. and Puotinen, M.L., 2011. Assessing the sensitivity of MODIS to monitor drought in high biomass ecosystems. *Remote Sensing of Environment*, 115(10): 2626-2639.

Du, L. et al., 2013. A comprehensive drought monitoring method integrating MODIS and TRMM data. *International Journal of Applied Earth Observation and Geoinformation*, 23: 245-253.

Fotheringham, A.S., Charlton, M.E. and Brunsdon, C., 1998. Geographically weighted regression: a natural evolution of the expansion method for spatial data analysis. *Environment and planning A*, 30(11): 1905-1927.

Halwatura, D., McIntyre, N., Lechner, A.M. and Arnold, S., 2017. Capability of meteorological drought indices for detecting soil moisture droughts. *Journal of Hydrology: Regional Studies*: 396-412.

Hao, C., Zhang, J. and Yao, F., 2015. Combination of multi-sensor remote sensing data for drought monitoring over Southwest China. *International Journal of Applied Earth Observation and Geoinformation*, 35: 270-283.

Hao, Z. and Singh, V.P., 2015. Drought characterization from a multivariate perspective: A review. *Journal of Hydrology*, 527: 668-678.

Hayes, M.J., Svoboda, M.D., Wardlow, B.D., Anderson, M.C. and Kogan, F., 2012. Drought monitoring: Historical and current perspectives.

Hayes, M.J., Svoboda, M.D., Wilhite, D.A. and Vanyarkho, O.V., 1999b. Monitoring the 1996 Drought Using the Standardized Precipitation Index. *Bulletin of the American Meteorological Society*, 80(80): 429-438.

Hurvich, C.M., Simonoff, J.S. and Tsai, C.L., 1998. Smoothing parameter selection in nonparametric regression using an improved Akaike information criterion. *Journal of the Royal Statistical Society: Series B (Statistical Methodology)*, 60(2): 271-293.

Ji, L. and Peters, A.J., 2003. Assessing vegetation response to drought in the northern Great Plains using vegetation and drought indices. *Remote Sensing of Environment*, 87(1): 85-98.

Jiao, W., Tian, C., Chang, Q., Novick, K.A. and Wang, L., 2019. A new multi-sensor integrated index for drought monitoring. *Agricultural and Forest Meteorology*, 268: 74-85.

Jiao, W. et al., 2016. Evaluating an enhanced vegetation condition index based on VIUPD for drought monitoring in the continental United States. *Remote Sensing*, 8(3): 224.

Keyantash, J.A. and Dracup, J.A., 2004. An aggregate drought index: Assessing drought severity based on fluctuations in the hydrologic cycle and surface water storage. *Water Resources Research*, 40(9).

Kogan, F.N., 1995b. Droughts of the late 1980s in the United States as derived from NOAA polar-orbiting satellite data. *Bulletin of the American Meteorological Society*, 76(5): 655-668.

Kogan, F.N., 1997. Global drought watch from space. *Bulletin of the American Meteorological Society*, 78(4): 621-636.

Liu, M. et al., 2017. A new drought index that considers the joint effects of climate and land surface change. *Water Resources Research*, 53(4): 3262-3278.

Lu, X., Wang, L., Pan, M., Kaseke, K.F. and Li, B., 2016. A multi-scale analysis of Namibian rainfall over the recent decade–Comparing TMPA satellite estimates and ground observations. *Journal of Hydrology: Regional Studies*, 8: 59-68.

McKee, T.B., Doesken, N.J. and Kleist, J., 1993. The relationship of drought frequency and duration to time scales, Proceedings of the 8th Conference on Applied Climatology. American Meteorological Society Boston, MA, pp. 179-183.

Mu, Q., Zhao, M., Kimball, J.S., McDowell, N.G. and Running, S.W., 2013. A remotely sensed global terrestrial drought severity index. *Bulletin of the American Meteorological Society*, 94(1): 83-98.

Palmer, W.C., 1965. Meteorological drought, 30. US Department of Commerce, Weather Bureau.

Park, S., Im, J., Jang, E. and Rhee, J., 2016. Drought assessment and monitoring through blending of multi-sensor indices using machine learning approaches for different climate regions. *Agricultural and Forest Meteorology*, 216: 157-169.

Quiring, S.M. and Ganesh, S., 2010. Evaluating the utility of the Vegetation Condition Index (VCI) for monitoring meteorological drought in Texas. *Agricultural and Forest Meteorology*, 150(3): 330-339.

Rhee, J., Im, J. and Carbone, G.J., 2010. Monitoring agricultural drought for arid and humid regions using multi-sensor remote sensing data. *Remote Sensing of Environment*, 114(12): 2875-2887.

Singh, R.P., Roy, S. and Kogan, F., 2003. Vegetation and temperature condition indices from NOAA AVHRR data for drought monitoring over India. *International Journal of Remote Sensing*, 24(22): 4393-4402.

Svoboda, M. et al., 2002. The drought monitor. *Bulletin of the American Meteorological Society*, 83(8): 1181-1190.

Vicente-Serrano, S.M., 2007. Evaluating the impact of drought using remote sensing in a Mediterranean, semi-arid region. *Natural Hazards*, 40(1): 173-208.

Vicente-Serrano, S.M., Beguería, S. and López-Moreno, J.I., 2010. A multiscalar drought index sensitive to global warming: the standardized precipitation evapotranspiration index. *Journal of Climate*, 23(7): 1696-1718.

Wilhelmi, O.V. and Wilhite, D.A., 2002. Assessing vulnerability to agricultural drought: a Nebraska case study. *Natural Hazards*, 25(1): 37-58.

Wold, S., Esbensen, K. and Geladi, P., 1987. Principal component analysis. *Chemometrics and Intelligent Laboratory Systems*, 2(1-3): 37-52.

Wu, J. et al., 2013. Establishing and assessing the Integrated Surface Drought Index (ISDI) for agricultural drought monitoring in mid-eastern China. *International Journal of Applied Earth Observation and Geoinformation*, 23(0): 397-410.

Zhang, A. and Jia, G., 2013. Monitoring meteorological drought in semiarid regions using multi-sensor microwave remote sensing data. *Remote Sensing of Environment*, 134: 12-23.

Zhang, L., Jiao, W., Zhang, H., Huang, C. and Tong, Q., 2017. Studying drought phenomena in the Continental United States in 2011 and 2012 using various drought indices. *Remote Sensing of Environment*, 190: 96-106.

Zhou, L. et al., 2012. Comparison of remotely sensed and meteorological data-derived drought indices in mid-eastern China. *International Journal of Remote Sensing*, 33(6): 1755-1779.

# CHAPTER 4 DEVELOPING A NEWLY INTEGRATED DROUGHT INDEX APPLICABLE ACROSS DIVERSE CLIMATE REGIONS ONLY BASED ON MULTI-SENSOR REMOTE SENSING DATA

## 4.1 Introduction

Drought is a naturally occurring hazard that has significant damaging effects on socioeconomic development and ecosystems. It results in major famines in different parts of world and causes global economic losses of 6–8 billion dollars, on average, each year (Pandey et al., 2007; Sheffield, Andreadis, et al., 2009; Zhou et al., 2012). Drought reduces ecosystem CO2 uptake and increases atmospheric CO2 concentrations (Ciais et al., 2005a; Mk et al., 2011; Vetter et al., 2008). Long and severe droughts could also trigger lasting changes in vegetation canopy structure and function (Donohue et al., 2009; Donohue, Roderick, et al., 2013; Parida et al., 2008). International research on droughts is of increasing importance since the frequency and consequences of droughts are expected to intensify in the future (Halwatura et al., 2017; Keyantash et al., 2004; Wilhelmi et al., 2002; Zhou et al., 2012).

Droughts are broadly classified into four types: (1) “Meteorological drought” is a period of months or even years with precipitation below normal condition; (2) “Agricultural drought” when soil moisture is reduced below the level at which plant function becomes impaired; (3) “Hydrological drought” occurs when streamflow, groundwater, or total water storages are below the long term mean level; and (4) “Socioeconomic drought” is used when moisture deficits cause the demand of certain commodities to exceed supply (Du et al., 2013; Hao, Zhang, et al., 2015; Quiring et al., 2010; Rhee et al., 2010). This classification importantly acknowledges that a range of

factors, including topography, antecedent conditions, vegetation type, and land use, work together to determine the consequences of precipitation shortfalls, and that a deficit of a given magnitude will not affect all landscapes in the same way. However, in reality, it can be difficult to neatly classify a drought event into a single category. For example, an agricultural drought can also become a socioeconomic drought if drought-driven declines in plant function reduce yield. In another case, declines in plant function may not be immediately apparent if they do not affect greenness or LAI, in which case an "agricultural drought" may be difficult to diagnose. Thus, efforts to diagnose and monitoring drought may benefit from holistic frameworks that consider a range of variables that affect local meteorology, hydrology, and plant function.

Historically, droughts have been estimated and investigated based on station-based point observations (AghaKouchak et al., 2015b; Mishra et al., 2010; Zhang and Jia, 2013). However, in regions with limited sampling gauges, the station-based based drought indices are not sufficient to characterize drought conditions, whereas remote sensing could be very useful since it could provide continuous and consistent observations of relevant variables linked to the hydrologic cycle (Lu, Wang, Pan, et al., 2016; Rhee et al., 2010; Rhee et al., 2017; Wu et al., 2013; Zhang, Jiao, et al., 2017). There are different drought indices with different emphasis. For instance, the Precipitation Condition Index (PCI), which was established based on precipitation information from the Tropical Rainfall Measuring Mission (TRMM) data, and the Temperature Condition Index (TCI) derived from Land Surface Temperature (LST) data, are commonly used remote sensing drought indexes that have a clear climatological perspective (Hao, Zhang, et al., 2015; Rhee et al., 2010; Zhang and Jia, 2013). From the

ecological perspective, drought can be estimated based on observed changes in vegetation growth indicators (e.g., Normalized Difference Vegetation Index (NDVI) and Vegetation Condition Index (VCI)) from remotely sensed data (Di et al., 1994; Hielkema et al., 1986; Kogan, 1995a; Rouse, Haas, Schell, Deering, et al., 1974).

However, a more complete view of drought conditions could rely on variables from multiple perspectives. For example, drought conditions can be aggravated by high temperature and low relative humidity, and can impact meteorology, hydrology, and plant function (Hao et al., 2017b; Park et al., 2016)). A single drought index may not be sufficient to capture the complex processes and diverse impacts of drought (AghaKouchak et al., 2015a; Hao and Singh, 2015). To this end, integrated drought indices, which are based on multiple perspectives, are urgently needed to alleviate the shortcomings of drought characterization from a single index. For example, an index based only on precipitation would not be able to characterize hydrologic stress linked to rising VPD during a heat wave (Almeida et al., 2003; Stocker et al., 2018); an index based only on vegetation condition may not detect drought-related reductions in plant function that are not manifested as a change in greenness (Zhang, Xiao, et al., 2016). Several studies have focused on developing remote sensing based integrated drought indices to provide a more robust and integrated estimation of drought. Table 4.1 lists a summary of several commonly used integrated drought indices. For example, the Microwave Integrated Drought Index (MIDI), which integrates Soil Moisture Condition Index (SMCI), PCI and TCI, has been shown to be an optimum drought index for meteorological drought monitoring over semiarid regions in China (Zhang and Jia, 2013). Similarly, the Scaled Drought Condition Index (SDCI) combines PCI with TCI and VCI

for agricultural drought monitoring in both arid/semiarid and humid states in the United States (U.S., (Rhee et al., 2010). The Optimized Meteorological Drought Index (OMDI) and Optimized Vegetation Drought Index (OVDI), which are based on VCI, TCI, PCI, and SMCI, have been investigated as tools to detect and monitor both agricultural and meteorological drought in Southwest China (Hao, Zhang, et al., 2015). Finally, the Synthesized Drought Index (SDI), which was developed using TCI, PCI, and VCI, was shown to be a good indicator for agricultural drought monitoring in Shandong province in China (Du et al., 2013).

One of the major issues for most remote sensing based integrated indices is that those indices were established and evaluated for a specific climate or geographic location. As shown in Table 4.1, the study areas over which the indices were developed are typically confined to one or two climate regions. Few of these indices were developed under diverse environmental conditions covering large spatial scales. This could result in a poor performance if some indices are applied in different climate regions from which they are developed (Quiring et al., 2010; Zhang, Jiao, et al., 2017). The second major issue is that for the typical composition method, spatial homogeneity of its parameters is often assumed (Hao, Zhang, et al., 2015; Zhang and Jia, 2013). For example, it is often assumed that all the sub-areas of a particular study area contribute the same weight for a particular single index, and an empirical linear combination method is used to derive a relationship that is believed to be uniformly applicable across the study area (Malczewski et al., 2014; Tang et al., 2018). This type of integration is straightforward to implement and has gained popularity in recent developments of multivariate drought indices (AghaKouchak, 2015a). However, this type of integration may not be applicable to

characterize the covariability of drought related indices, since it may miss local details that can be significant if the relationship of the related indices is spatially non-stationary(AghaKouchak, 2015a) . A third issue is that satellite observations of are subject to various uncertainties due to errors in retrieval algorithms, data acquisition, data postprocessing, infrequent overpasses, etc. (AghaKouchak et al., 2012; Damberg et al., 2014; Hong et al., 2006). These challenges have historically motivated the use of in-situ data when developing drought indices. However, in regions with limited ground observation sites, inadequacy of in-situ data has hampered drought monitoring. Thus, a reliable remote sensing based integrated drought index which could be independent on in-situ data proxy is of great importance.

To address these issues, the objective of this section is to develop and evaluate a new integrated drought index based on multi-sensor remote sensing data for drought monitoring under different climate conditions. In this study, the local ordered weighted averaging (OWA) was used as the composition method to integrate single remote sensing based drought indices. Local OWA was selected because it can accommodate heterogeneities in the land surface by using different weights in different parts of the study area for a particular single index. Thus, the newly developed index can be applied to diverse climate regions. We named the new index Geographically Independent Integrated Drought Index (GIIDI). To evaluate the performance of GIIDI, it was compared with both the integrated drought indices MIDI, OMDI and the single drought indices PCI, TCI, VCI and SMCI

Table 4.1: Summary of studies using multivariate analysis for drought estimation, including drought type, experiment region and year, data source and methodology.

| Index | Data | Method | Reference |
|---|---|---|---|
| ESI | MODIS LAI; MODIS LST; MERRA; TRMM | Integrated multisource data using evaporative stress mechanism | (Anderson et al., 2016) |
| ISDI | MODIS NDVI; MODIS LST; ecological zoning; AWC; irrigation water management distribution; DEM | integrated multisource data mining technology (CART) | (Wu et al., 2013) |
| MDI | NOAA precipitation; runoff; actual evapotranspiration | MDI extraction based on KECA | (Rajsekhar et al., 2015b) |
| MIDI | AVHRR LST;AMSR-E soil moisture; TRMM precipitation | Combine TCI, SMCI and PCI using empirical weights | (Zhang and Jia, 2013) |
| MSDI | CPC precipitation; CPC soil moisture | SPI and SSI preparation; copulas based conjunction | (Hao et al., 2013a) |
| OMDI | AVHRR LST;AMSR-E soil moisture; TRMM precipitation | Combine TCI, SMCI and PCI by Constrained Optimization | (Hao, Zhang, et al., 2015) |
| OVDI | AVHRR LST; AVHRR NDVI; AMSR-E soil moisture; TRMM precipitation | Combine VCI, TCI, SMCI and PCI by Constrained Optimization | (Hao, Zhang, et al., 2015) |
| PADI | GPCC precipitation; GLDAS soil moisture; AVHRR NDVI; | Evolution Process based Multi-sensor Collaboration framework | (Zhang, Chen, et al., 2017) |
| SDCI | AVHRR LST; AVHRR; TRMM precipitation | Combine VCI, TCI and PCI by empirical weights | (Rhee et al., 2010) |
| SDI | MODIS LST; MODIS NDVI, MODIS | Combine VCI, TCI and PCI by PCA | (Du et al., 2013) |

| | | | |
|---|---|---|---|
| | reflectance; TRMM precipitation | | |
| VegDRI | MODIS NDVI; MODIS LST; ecological zoning; AWC; irrigation water management distribution; DEM | Integrated multisource data mining technology (CART) | (Brown et al., 2008) |
| HSMDI | MODIS LST,NDVI,EVI, Albedo, LAI, ET; TRMM precipitation and AMSR-E soil moisture | Downscaling soil moisture through Random forest | (Park et al., 2017) |
| VegDRI-Canada | NDVI, land cover/land use, soil data and in-situ climate data | Integrated multisource data mining technology (CART) | (Tadesse et al., 2017) |

## 4.2. Data

Datasets collected both *in-situ* and with remote sensing were used to assess the performance of our newly developed drought index in various climate divisions over the continental United States (CONUS) from 2002 to 2011. The analysis in this study focused primarily on the months from April to October in order to avoid complications arising from snow and ice in winter.

### 4.2.1 *In-situ* based drought indices

Monthly *in-situ* drought indices, including PDSI, moisture anomaly index (Z-index), and Standardized Precipitation Index (SPI), were selected as the reference data for evaluating GIIDI. These *in-situ* drought indices were obtained from the NOAA's National Climatic Data Center (NCDC–NOAA) repository for 344 climatic divisions in

CONUS (http://www1.ncdc.noaa.gov/pub/data/cirs/), and have been used in previous studies to evaluate remote sensing drought indices (Brown et al., 2008; Caccamo et al., 2011; Ji et al., 2003; Jiao et al., 2016; Rhee et al., 2010; Zhang, Jiao, et al., 2017).

### 4.2.2 Remote sensing data

GIIDI was established by integrating the single indices of MODIS data based VCI and TCI, AMSR-E based SMCI, and TRMM based PCI. The VCI, which was derived from Vegetation Index based on the Universal Pattern Decomposition method (VIUPD), was calculated using MODIS land surface data (MOD09A1) downloaded from the Land Processes Distributed Active Center (LPDAAC; http://lpdaac.usgs.gov/). MODIS Land Surface Temperature (LST) data (MOD11A2) was used to calculate TCI and it was obtained from the National Aeronautics and Space Administration's (NASA) earth observing system data and information system (EOSDIS; http://reverb.echo.nasa.gov). We composited the MOD11A2 and MOD09A1 into monthly data according to data quality flags and the number of days in each month. PCI was calculated based on TRMM 3B43 data, which provides an estimate of monthly precipitation. Data from 2002 to 2011 is available at the NASA Data and Information Services Center (DISC) (http://mirador.gsfc.nasa.gov/). The AMSR-E product was used to calculate SMCI. The AMSR-E data was available from 2002 to 2011 and could be obtained from Vrije Universtiteit Amsterdam (http://nsidc.org/)

### 4.2.3 Other data

A number of other datasets were used to validate the applicability of the GIIDI for drought monitoring in different climate divisions across CONUS. United States drought monitor (USDM) data was chosen as reference data for evaluating GIIDI, since it

combines information from multiple ground-observation based drought indicators and local reports from state climatologists and observers throughout the country (Hayes et al., 2012). It is worth noting that USDM is a categorical index, with the following classifications: abnormally dry (D0), moderate drought (D1), severe drought conditions (D2), extreme drought (D3), and exceptional drought (D4). More detailed information about USDM could be found at http://drought.unl/dm/.

**4.3. Methodology**

The methodology, illustrated in Figure 4.1, includes the following steps:
The first step is data preparation and re-processing. During this step, MOD11A2 data was used to composite 8-day LST to the monthly data. . It should be noted that VIUPD was used to calculate VCI instead of the commonly used NDVI, because previous work indicates that VIUPD-based VCI has better performance for drought monitoring in more climate regions than NDVI-based VCI (Jiao et al., 2016). More detailed information about the calculation of VIUPD is available in Zhang et al. (2007). In the second step, the condition indices (TCI, VCI, PCI and SMCI) were calculated using the multi-source remote sensing data mentioned in the first step. The condition indices were calculated scaling from 0 to 1 for each pixel from April to October for the period 2002-2011. The third step is to compose the multi drought indices. In this step, we used a local OWA model to composite TCI, VCI, PCI and SMCI (see section 4.3.2 for more details). The last step is validation. We used *in-situ* drought indices to evaluate the correlation between the *in-situ* drought indices and GIIDI in different climate divisions.

### 4.3.1 Scaled remote sensing indices

Table 4.2 shows detailed information about the remote sensing based drought indices used in this study. Among the listed indices, TCI, PCI, VCI and SMCI were used as the input single drought indices to establish GIIDI, while MIDI and OMDI were used to evaluate the performance of GIIDI. All these indices were calculated from April to October for the period 2002-2011.

Table 4.2: Descriptions of remote sensing based drought indices used in this study. The data source column indicates the satellite name or single drought indices (for integrated drought indices of MIDI, OMDI), the method column shows the main method for establishing drought indices. For the integrated drought indices (MIDI, OMDI), the method column indices the method of determining the weights of single drought indices.

| Drought index | Data source | Method | Source |
|---|---|---|---|
| VCI | MODIS | $(VIUPD_{ikj}-VIUPD_{i,min})/(VIUPD_{i,max}-VIUPD_{i,min})$ | (Kogan, 1995b) |
| TCI | MOIDS | $(LST_{i,max}-LST_{ijk})/(LST_{i,max}-LST_{i,min})$ | (Kogan, 1997) |
| SMCI | AMSR-E | $(SM_{ikj}-SM_{i,min})/(SM_{i,max}-SM_{i,min})$ | (Zhang and Jia, 2013) |
| PCI | TRMM | $(TRMM_{ikj}-TRMM_{i,min})/(TRMM_{i,max}+TRMM_{i,min})$ | (Rhee et al., 2010) |
| MIDI | TCI, SMCI, PCI | Empirical weights | (Zhang and Jia, 2013) |

| | | | |
|---|---|---|---|
| OMDI | TCI, SMCI, PCI | Constrained optimization | (Hao, Zhang, et al., 2015) |
| GIIDI | VCI, TCI, SMCI, PCI | Local OWA | This study |

Note: LSTijk, SMijk, TRMMijk—monthly LST, SM, TRMM for pixel i, in month j, for year k, respectively. LSTi,min, SMi,min, TRMMi,min—multi-year minimum LST, SM, TRMM, respectively, for pixel i. LSTi,max, SMi,max, TRMMi,max—multi-year maximum LST, SM, TRMM, respectively.

### 4.3.2 GIIDI development

The selection of single drought indices for establishing the integrated drought index is an important component of our approach. Previous studies have indicated that single drought indices based on time series analysis (PCI, TCI, VCI and SMCI) performed better than other types of single drought indices such as the Perpendicular Drought Index (PDI), Modified Perpendicular Drought Index (MPDI) and temperature Vegetation Dryness Index (TVDI) (Zhang, Jiao, et al., 2017). PCI is derived from the scaled precipitation information based on TRMM data, TCI is derived from land surface temperature information, VCI describes conditions related to vegetation growth, and the SMCI is soil moisture condition from AMSR-E data. These indices are not fully correlated with each other. In this regard, PCI, SMCI, VCI and TCI were selected to inform GIIDI.

The ordered weighted averaging (OWA), which was developed by Yager (1993), provides a general class of parameterized aggregation operators between the minimum and maximum. In the OWA, criteria weights and order weights are applied. Criteria

weights ($w_1$,$w_2 \ldots w_n$, $0 \leq w_k \leq 1,\ and\ \sum_{k=1}^{n} w_k = 1$) determines the relative importance of evaluation criteria, while order weights ($\lambda_1$, $\lambda_2$, ..., $\lambda_n$, $0 \leq \lambda_k \leq 1$, $and\ \sum_{k=1}^{n} \lambda_k = 1$) indicate the degree of tradeoff between "ANDness" (requiring all the criteria to be satisfied) and "ORness" (requiring at least one of the criteria to be satisfied) (Yager, 1993).

However, one issue of OWA model is the spatial homogeneity of its weights irrespectively of spatial heterogeneity. To address this issue, Malczewski et al. (2014) developed the local OWA model based on the range-sensitivity principle (Fischer, 1995). The local OWA model allocates criterion weights based on local spatial variations by subdividing the study area into different neighborhoods. In this study, the approach of moving window was used to define neighborhoods. Hence, for the given set of single drought indices $a_{i1}$, $a_{i2}$, ..., $a_{in}$ at the $i^{th}$ location (i = 1, 2,..., n), GIIDI was calculated using local OWA model based on the following equations:

$$OWA_{iq} = \sum_{k=1}^{n} \frac{\lambda_k u_{kq} z_{ikq}}{\sum_{k=1}^{n} \lambda_k u_{kq}} \quad (4.1),$$

where $OWA_{iq}$ is the OWA value of the $i^{th}$ pixel estimated in the $q^{th}$ neighborhood; $\lambda_k$, is the order weight associated with the $k^{th}$ single drought index among PCI, TCI, SMCI and VCI; $z_{i1q} \geq z_{i2q} \geq \ldots \geq z_{inq}$ is obtained by reordering the normalized values according to local value function $v(a_{ik}^{q})$ (see Equation (4.3)); $u_{kq}$ is the reordered $w_{kq}$ according to $z_{ikq}$. The local criterion weight, $w_{kq}$, is defined as a function below:

$$w_{kq} = \frac{w_{kq}^{*}}{\sum_{k=1}^{n} w_{kq}^{*}}, 0 \leq w_{kq} \leq 1, and\ \sum_{k=1}^{n} w_{kq} = 1 \quad (4.2)$$

where $w_{kq}^{*} = (w_k r_{kq} / r_k)$ is the local weight of the $k^{th}$ single drought index in the $q^{th}$ neighborhood.

$$v(a_{ik}^q) = \begin{cases} \frac{a_{ik}^q - min_{iq}(a_{ik}^q)}{max_{iq}(a_{ik}^q) - min_{iq}(a_{ik}^q)} \text{ for the k}^{\text{th}} \text{ criterin to be maximized} \\ \frac{max_{iq}(a_{ik}^q) - a_{ik}^q}{max_{iq}(a_{ik}^q) - min_{iq}(a_{ik}^q)} \text{ for the k}^{\text{th}} \text{ criterion to be minimized} \end{cases} \quad (4.3)$$

where $max_{iq}(a_{ik}^q)$ and $min_{iq}(a_{ik}^q)$ are the maximum and minimum values of the k[th] drought index in q[th] neighborhood.

The degree of ORness was used to measure the weighting vector of the OWA operator. The degree of ORness is given as below (Yager, 1993):

$$\alpha = \sum_{k=1}^{n} \frac{n-k}{n-1} \lambda_k, 0 \leq \text{ORness} \leq 1 \quad (4.4)$$

where α measures the degree of similarity of OWA operator to the logical OR operator. If the value of α = 0.5, $\lambda_k$ = 1/n; when α = 0, $\lambda_k$ = 1 and all other weights are 0; and if α = 1 for $\lambda_n$ = 1, all other $\lambda_k$ weights are equal to 0. Table 4.3 shows the values of $\lambda_k$ for different values of α. The normalized form of the dispersion is given as below:

$$\varphi = -\sum_{k=1}^{n} \frac{\lambda_k ln \lambda_k}{\ln n} \quad (4.5)$$

where $\varphi$ indicates order weight dispersion. $0 \leq \varphi \leq 1$; $\varphi$ = 0 for $\lambda_k$= 1 and all other weights are 0; the value of $\varphi$ = 1 for all $\lambda_k$ = 1/n. The order weights $\lambda_k$ could be obtained by solving the following non-linear equation:

$$\text{maximize } \varphi = -\sum_{k=1}^{n} \frac{\lambda_k \ln \lambda_k}{\ln n} \quad (4.6)$$

subject to:

$$\sum_{k=1}^{n} \frac{n-k}{n-1} \lambda_k = \alpha, \sum_{k=1}^{n} \lambda_k = 1, 0 \leq \lambda_k \leq 1, for\ k = 1,2, \dots, n. \quad (4.7)$$

Table 4.3: Optimal order weights ($\lambda_k$) for selected values of the α parameter and the number of criteria n=4

| α | 0 | 0.1 | 0.2 | 0.3 | 0.4 | 0.5 | 0.6 | 0.7 | 0.8 | 0.9 | 1 |
|---|---|---|---|---|---|---|---|---|---|---|---|
| $\lambda_1$ | 0 | 0.084 | 0.117 | 0.135 | 0.167 | 0.250 | 0.347 | 0.405 | 0.494 | 0.491 | 1 |
| $\lambda_2$ | 0 | 0.150 | 0.179 | 0.209 | 0.213 | 0.250 | 0.273 | 0.284 | 0.284 | 0.308 | 0 |
| $\lambda_3$ | 0 | 0.272 | 0.280 | 0.286 | 0.272 | 0.250 | 0.214 | 0.171 | 0.157 | 0.163 | 0 |
| $\lambda_4$ | 1 | 0.494 | 0.424 | 0.363 | 0.347 | 0.250 | 0.166 | 0.140 | 0.066 | 0.041 | 0 |

The α parameter indicates the position of OWA on a continuum between the AND and OR operators (Malczewski et al., 2014; Tang et al., 2018). In this study, to investigate the effect of the analyst's risk attitude on the drought conditions, nine different risk attitudes of local OWA with α = 0.1, 0.2, 0.3, 0.4, 0.5,0.6, 0.7, 0.8 and 0.9 were evaluated by *in-situ* drought indices. From the different α profiles tested, the local OWA with α =3 showed the best correlation with SPI, PDS, and Z-indices of various timescales (see Table 4.4). α =3 was recommended for establishment of GIIDI.

Table 4.4: Correlation coefficients (r-values) between in situ drought indices (PDSI, Z-index and SPIs of differing timescales) and local OWAs with different α values. $p < 0.01$ in all cases. The largest r-value for each drought index weighting is shown in bold typeface.

| | r-value | | | | | |
|---|---|---|---|---|---|---|
| α | PDSI | Z-index | SPI-01 | SPI-02 | SPI-03 | SPI-06 |

| | | | | | | |
|---|---|---|---|---|---|---|
| 0.1 | 0.602 | 0.694 | 0.728 | 0.746 | 0.712 | 0.628 |
| 0.2 | 0.693 | 0.698 | 0.732 | 0.76 | 0.726 | 0.639 |
| 0.3 | 0.701 | 0.749 | 0.811 | 0.786 | 0.733 | 0.628 |
| 0.4 | 0.66 | 0.695 | 0.727 | 0.757 | 0.724 | 0.638 |
| 0.5 | 0.656 | 0.694 | 0.721 | 0.751 | 0.719 | 0.633 |
| 0.6 | 0.69 | 0.683 | 0.712 | 0.724 | 0.693 | 0.613 |
| 0.7 | 0.694 | 0.69 | 0.721 | 0.74 | 0.707 | 0.621 |
| 0.8 | 0.684 | 0.691 | 0.727 | 0.734 | 0.699 | 0.612 |
| 0.9 | 0.681 | 0.68 | 0.711 | 0.716 | 0.684 | 0.604 |

#### 4.3.3 Accuracy assessment

We evaluated GIIDI in three stages. During the first stage, we evaluated the indices using data from the growing seasons (April–October) in 2007, 2009 and 2011, which were identified as severe drought, moderate drought and extreme drought years. The drought conditions estimated from GIIDI were compared to the drought conditions monitored from SDCI, MIDI, OMDI and USDM. USDM was used as a standard for the comparison. OMDI, MIDI and SDCI were chosen to compare with GIIDI because previous comparative study indicated that those indices have top performance for drought monitoring in the compared drought indices (Zhang et al. 2017a). Our analysis at this stage was largely qualitative. In the second stage, the correlation values (r-value) and the root mean square error (RMSE) between GIIDI and *in-situ* drought indices were used to examine the performance of GIIDI.

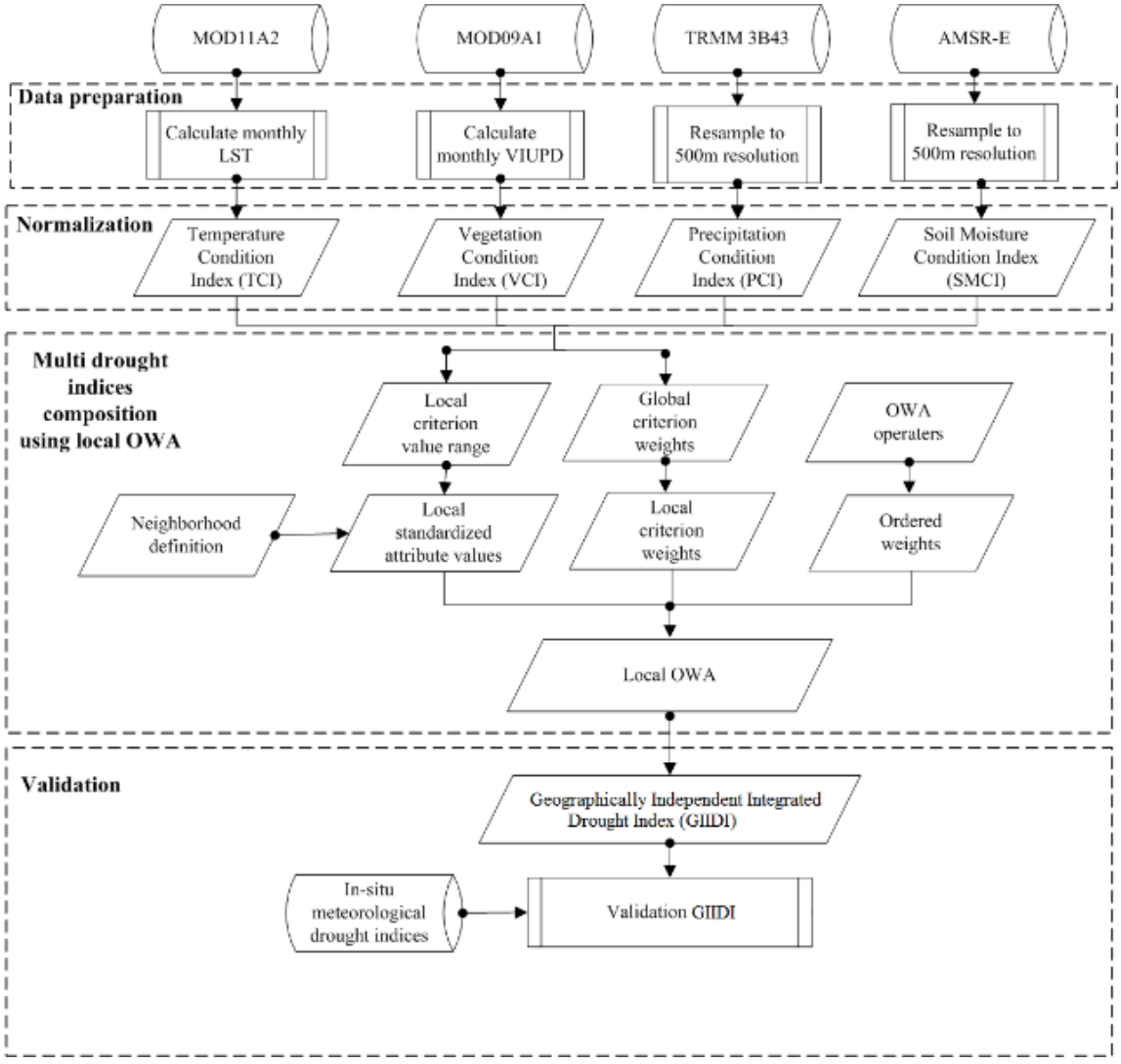


Figure 4.1: Flowchart of comprehensive drought estimation based on multi-source remote sensing data.

## 4.4. Results

### 4.4.1 Regional drought pattern comparisons

The months from April to October in 2007, 2009 and 2011 were selected to evaluate the spatial variation of GIIDI and other drought indices. In 2011, many parts of the U.S., and especially Texas, experienced one of the most extreme droughts in the

historical record (Long et al., 2013). Similarly, in 2007, much of the U.S. experienced as severe drought event, and in 2009, much of the country experienced moderate drought conditions. Figs.4.2-4.4 show the variation among the indices for 2011, 2009 and 2007, respectively. According to Figure 4.2 to Figure 4.4, by visual comparison, GIIDI generally shows greater similarity to USDM under all drought conditions than other drought indices.

For the extreme drought year of 2011, drought conditions were initially located in much of Texas, New Mexico and Georgia in April, then expanded North (e.g., to Michigan, Iowa and Illinois) to other parts of the Southeast (e.g. Alabama) by August (see USDM in Figure 4.2). OMDI, SDCI, MIDI and GIIDI all indicated extreme drought conditions from April to May in the South. However, SDCI, OMDI and MIDI also showed expansion of the extreme drought to parts of the Great Plains and the Northwestern CONUS in June, while these regions were not confirmed to be experiencing extreme drought conditions by USDM. GIIDI estimated the drought to be much more confined, and did not indicate extreme drought in the Plains or Northwestern US.

For the moderate drought year of 2009, the USDM indicated moderate drought in Western regions along the coast, and a small region of extreme drought in south Texas (Fig 4.3). GIIDI described the spatial extent of the drought better than other drought indices, using USDM as the reference. In general, other drought indices overestimated the drought conditions across the CONUS. For example, from April to May, these three indices showed large regions under extreme drought conditions in the Northwestern Great Plains. In June, these three indices indicated that the severe drought areas were

mainly located in The North and Southeastern regions. In September, they indicated the severe drought areas were mainly located in the West and Northeastern CONUS, in contrast to estimate from USDM and GIIDI.

In 2007, USM indicated that drought conditions were mainly located in Western regions and parts of the Southeast (Fig 4.4). Similar to the year of 2009 and 2011, GIIDI was more consistent with USDM than other three indices since they generally overestimated the drought severity. SDCI, MIDI and OMDI presented similar drought condition distributions. For SDCI, MIDI and OMDI, extreme drought appeared in May in the Eastern and Western CONUS. In October, the severe drought appeared in Southwestern regions such as Arizona, New Mexico and part of Texas. However, USDM and GIIDI showed only moderate or slight drought conditions in these regions. It was even more obvious that in October 2007, SDCI, MIDI and OMDI over-estimated drought conditions in the Southwest, where drought was not detected by USDM.

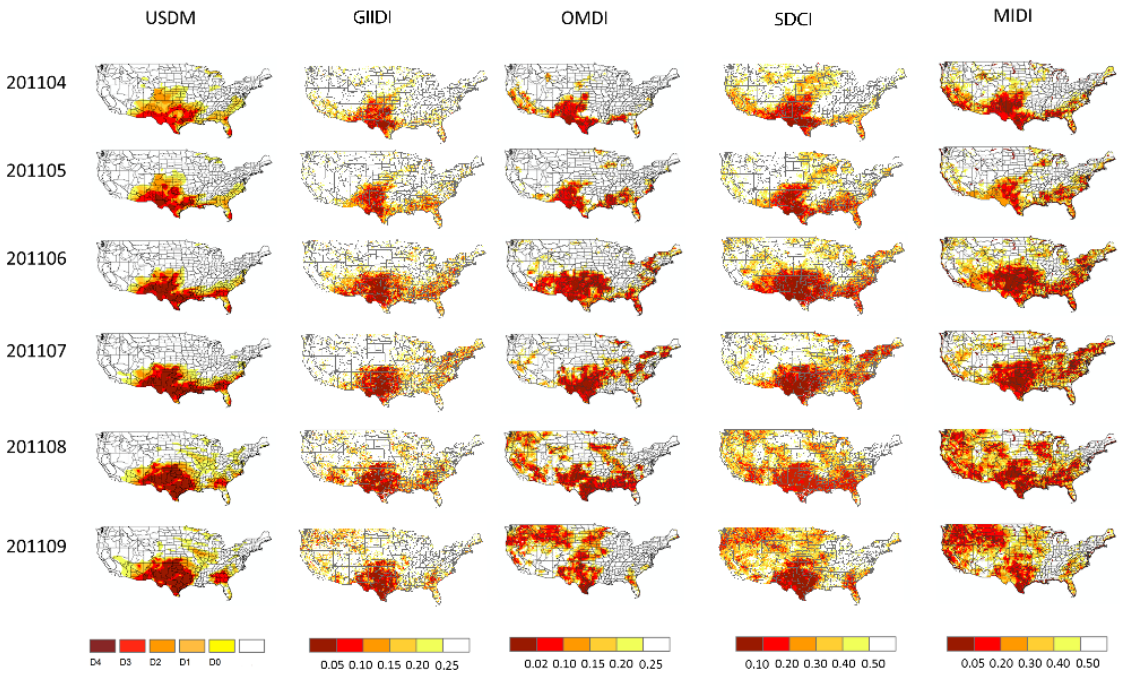


Figure 4.2: Drought conditions in the US monitored by multiple drought indices from April to September in 2011. The first column displays the observed USDM drought data for the period of April to October, while the second to fifth columns show the GIIDI, OMDI, SDCI and MIDI, respectively. For USDM, D0-D4 represents the different severities of drought conditions; for columns 2 to 5, lower values stands for more severe drought.

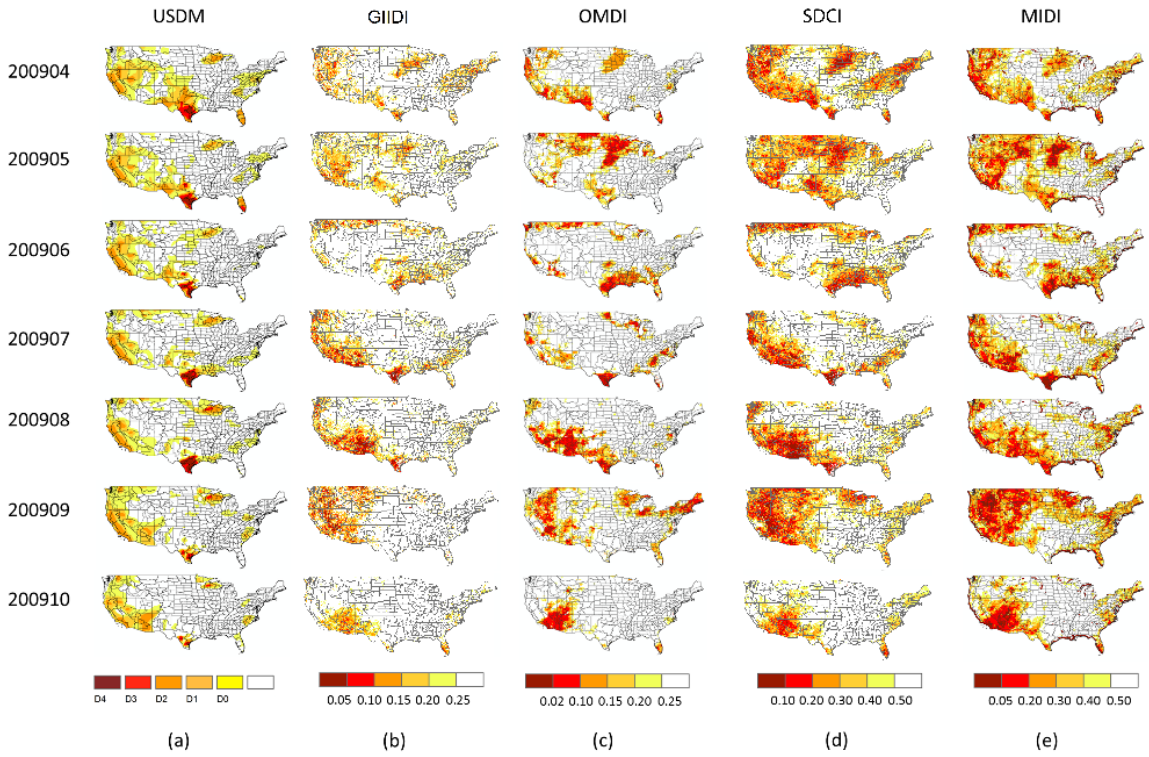


Figure 4.3: Same as Fig 4.2, but for the 2009 growing season

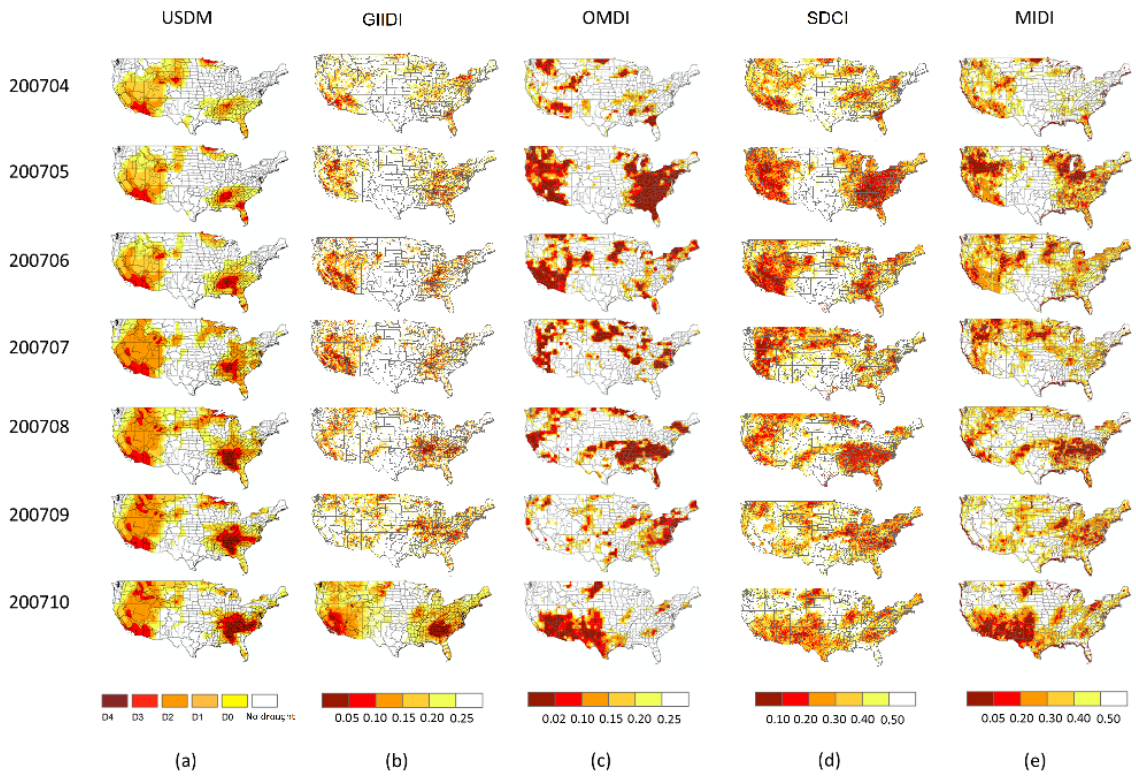


Figure 4.4: Same as Figure 4.2, but for the 2007 growing season.

### 4.4.2 Monthly temporal correlation comparisons

We compared the correlations between seven remotely sensed drought indices (GIIDI, MIDI, OMDI, PCI, TCI, VCI and SMCI) and *in-situ* drought indices (PDSI, Z-Index, 1-, 2-, 3-, 6-month SPI). Among the seven remotely sensed drought indices compared, GIIDI has superior performance than other indices in most goodness-of-fit measures. As shown in Table 4.4, GIIDI was more closely correlated with PDSI, Z-index, 1-, 3-, 6-month SPI ($r=0.701, 0.794, 0.811, 0.733, 0.628$, respectively, $p < 0.05$ for all cases) when compared with MIDI, OMDI, VCI, PCI, TCI and SMCI. Table 4.5 shows that GIIDI had smaller RMSE (RMSE = 1.979, 0.798, 0.729, 1.049, 1.071, respectively) when compared with MIDI, OMDI, VCI, PCI, TCI and SMCI.

Table 4.5: Comparison of the performance of GIIDI and six other commonly used remote sensing drought indices using 6 *in-situ* drought indexes as a reference. r is the correlation coefficient between two variables. *denotes the minimum maximum value in each column. GIIDI, MIDI, OMDI, PCI, TCI, VCI and SMCI are seven remotely sensed drought indices; PDSI, Z-Index, 1-, 2-, 3-, 6-month SPI are *in-situ* drought indices. *denotes the maximum value in each column.

| Drought indices | r (n = 24080) | | | | |
|---|---|---|---|---|---|
| | PDSI | Z | SPI-1 | SPI-3 | SPI-6 |
| GIIDI | 0.701* | 0.794 | 0.811* | 0.733* | 0.628* |
| OMDI | 0.496 | 0.825* | 0.871* | 0.686 | 0.592 |
| MIDI | 0.504 | 0.788 | 0.807 | 0.662 | 0.58 |
| VCI | 0.622 | 0.313 | 0.234 | 0.564 | 0.582 |
| PCI | 0.44 | 0.806 | 0.865 | 0.559 | 0.398 |
| TCI | 0.542 | 0.589 | 0.487 | 0.515 | 0.471 |
| SMCI | 0.37 | 0.451 | 0.426 | 0.389 | 0.331 |

Table 4.6: Comparisons of the RMSE between GIIDI and other commonly used remote sensing based drought indices. *denotes the minimum maximum value in each column. GIIDI, MIDI, OMDI, PCI, TCI, VCI and SMCI are seven remotely sensed drought indices; PDSI, Z-Index, 1-, 2-, 3-, 6-month SPI are *in-situ* drought indices. *denotes the minimum value in each column.

| Drought indices | RMSE (n = 24080) | | | | |
|---|---|---|---|---|---|
| | PDSI | Z | SPI-1 | SPI-3 | SPI-6 |
| GIIDI | 1.979* | 0.798* | 0.729* | 1.049* | 1.071* |
| OMDI | 3.011 | 0.803 | 0.732 | 1.305 | 1.805 |
| MIDI | 2.985 | 0.823 | 0.776 | 1.344 | 1.878 |
| VCI | 2.658 | 2.244 | 1.159 | 1.075 | 1.082 |
| PCI | 3.44 | 0.865 | 0.801 | 2.559 | 2.598 |
| TCI | 2.709 | 2.289 | 1.166 | 1.145 | 1.271 |
| SMCI | 2.856 | 2.234 | 1.183 | 1.324 | 1.245 |

### 4.4.3 Spatial variability comparisons

Spatially, GIIDI produced stronger correlations with PDSI, Z-index, SPI-1, SPI-3 and SPI-6 than other compared remote sensing-based indices almost over all the climate divisions (Figure 4.5). For GIIDI, high correlation values (r-value >0.6) were located in almost all the climate divisions. In, VCI was generally correlated only with long term *in-situ* drought indices (PDSI, 3- and 6-month SPI), with the strongest correlations limited to the Southeastern US. Both MIDI and OMDI only have good performance when

correlated to short-term drought indices (Z-index and 1-month SPI). PCI exhibited stronger correlations with SPI-1. However, the correlations of PCI and long-term SPI (SPI-3 and SPI-6) were low in most of the CONUS. TCI and SMCI generally had similar performance. They showed stronger correlation with *in-situ* indices than the short-term SPI indices but weak correlations with PDSI and long-term SPIs (3- and 6-SPI) for most areas.

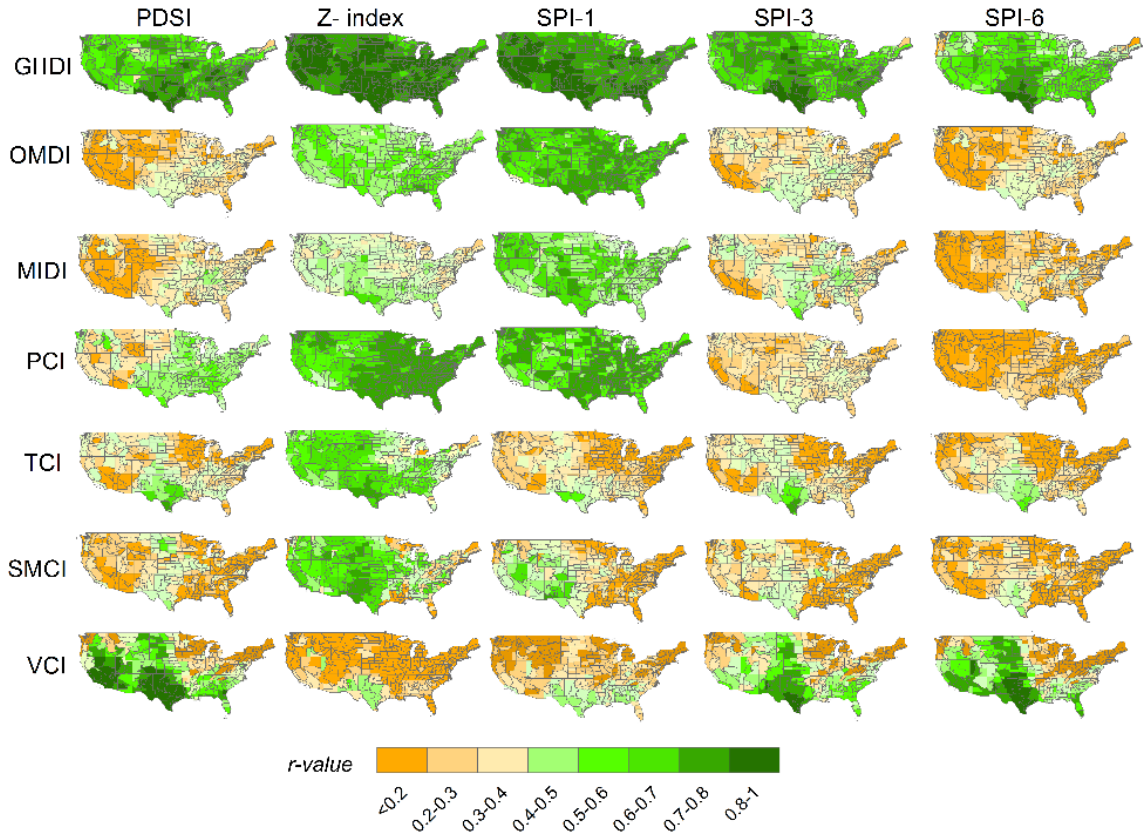


Figure 4.5: Spatial distribution of climate divisions with the correlations (r-value) between remote-sensing-based and *in-situ*-based drought indices for the entire growing season (April to October) of 2002–2011.

## 4.5. Discussion

Based on multiple comparisons, GIIDI is shown to have better performance in drought monitoring than MIDI, OMDI and other single remote sensing based indices across the CONUS. There are several reasons for the good performance of GIIDI. First, empirical linear combination approaches to build composite drought indices may not be applicable for the regions where the relationship between variables is spatially nonstationary, since it may miss significant local detail. In contrast, the local OWA model, in which the local criterion weight depends upon the local range, has the potential to provide a more appropriate basis for the spatial integration of the relationship between variables. To illustrate the advantages of the local OWA model, we take one of the most severe drought months -- August 2011-- as an example. As illustrated in Figure 4.6, GIIDI more accurately estimates drought conditions than OMDI, MIDI and SDCI. OMDI, MIDI and SDCI all indicated large regions in the Northern U.S experienced severe drought – a result that was not indicated by USDM (Figure 4.2) and GIIDI. The weighting of PCI, TCI, VCI and SMCI are spatially nonstationary (Figure 4.6 e-i), and the weighting of each index was not the same over the whole CONUS. For example, in the most of the Great Plains, VCI takes higher weighting than other indices, but in the Northeastern regions, the weighting of VCI is lower than other indices. The weighting of the difference indices by the OWA model reflects the fact that each index has different character and different applicability..

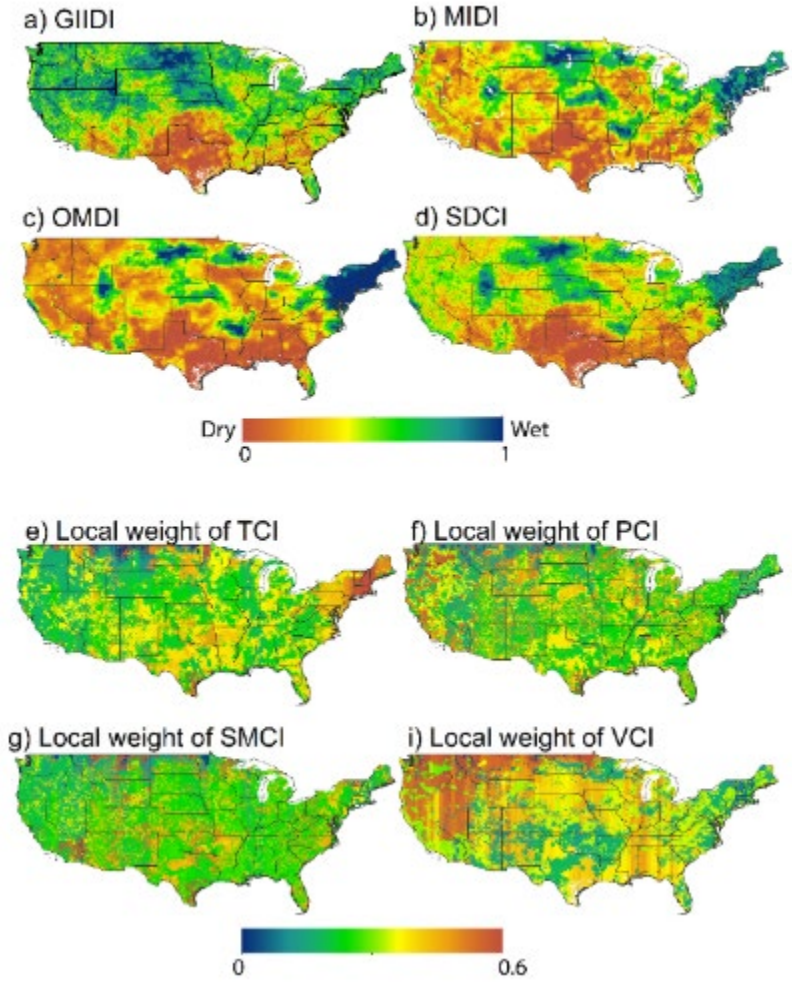


Figure 4.6: Spatial distributions of drought conditions estimated by compared remote sensing based drought indices and local criterion weights for GIIDI establishment in Augest 2011: (a) GIIDI; (b) MIDI; (c) OMDI; (d) SDCI; (e) local weight of TCI; (f) local weight of PCI; (g) local weight of SMCI; (i) local weight of VCI.

Second, the selection of single indices is another factor that potentially contributes to the good performance of GIIDI. A previous study indicated the condition indices (e.g., TCI, VCI, PCI and SMCI) have better performance than other drought indexes (Zhang, Jiao, et al., 2017). It also indicated that the VUA-based SMCI performed better than

National Snow and Ice Data Center (NSIDC)-based SMCI, and MODIS-based TCI performed better than VUA based TCI. In addition, Jiao et al. (2016) indicated that VIUPD-based VCI could improve the applicability of drought monitoring when compared to NDVI-based VCI. Informed by these, we used the MODIS LST-data based TCI, VUA-based SMCI, VIUPD-based VCI and TRMM-based PCI as the single indices to develop GIIDI, which potentially contributes to the good performance of GIIDI. Our results suggest hat GIIDI could be a reliable index for drought monitoring across wide climate gradients, since its performance is largely independent of environmental factors. Previous work indicated that the performances of traditional remote sensing based indices, such as VCI, depend on precipitation, land cover and other factors (Bayarjargal et al., 2006; Quiring et al., 2010; Singh et al., 2003; Vicente-Serrano, 2007). As a result, many remote sensing based indices have limited applicability across different regions. For example, all fifteen remote sensing based drought indices compared in the study of Zhang, Jiao, et al. (2017) performed well for Texas and other parts of the central CONUS, but did not perform well in Western and Northeastern regions. Compared with these indices, GIIDI can perform reasonably well across different climate regions. In addition, compared with USDM, the establishing of GIIDI do not need the knowledge of local experts.

Despite of all the advantages, there are some limitations that could affect the performance of GIIDI. First of all, there is no absolute "true" drought measure. By using USDM, SPI, PDSI and Z-index as the reference, we establish a benchmark for comparisons but cannot provide a true validations of GIIDI. Another limitation concerns the classification of GIIDI drought , which was based on an empirical comparison

between GIIDI and USDM. Future work could focus on quantitative determination of the drought severity classification of GIIDI.

### 4.6. Conclusions

This study developed a new integrated drought index (GIIDI) using the local OWA model to integrate multi-sensor remote sensing data based drought indices. The remote sensing based drought indices (GIIDI, OMDI, MIDI, SDCI, VIUPD-derived VCI, VUA based TCI, MODIS based TCI, TRMM based PCI, and AMSR-E based SMCI) were compared with the *in-situ* drought indices (PDSI, Z-index, SPI-1, SPI-3, SPI-6). The dependence of GIIDI performance on environmental factors was also investigated. When compared to the other remote-sensing based index, GIIDI had the strongest correlation with *in-situ* drought indices in most climate divisions. GIIDI can effectively combine the drought information from different single drought indices and overcome some of the shortcomings of single drought indices for drought monitoring in particular areas. Results also indicated that the performance of GIIDI was not significantly affected by common environmental factors such as precipitation, temperature, soil available water holding capacity, soil moisture, soil permeability, soil drainage class, hydrological group, organic material in soil and LULC. The results indicate that GIIDI has great potential for monitoring drought conditions across diverse climate conditions.

### References

AghaKouchak, A., 2015a. A multivariate approach for persistence-based drought prediction: Application to the 2010–2011 East Africa drought, Journal of Hydrology, pp. 127-135.

AghaKouchak, A. et al., 2015a. Remote sensing of drought: Progress, challenges and opportunities. *Reviews of Geophysics*, 53(2): 452-480.

AghaKouchak, A. et al., 2015b. Remote sensing of drought: Progress, challenges and opportunities. *Reviews of Geophysics*, 53(2): 452-480.

AghaKouchak, A., Mehran, A., Norouzi, H. and Behrangi, A., 2012. Systematic and random error components in satellite precipitation data sets. *Geophysical Research Letters*, 39(9).

Almeida, A.C. and Landsberg, J.J., 2003. Evaluating methods of estimating global radiation and vapor pressure deficit using a dense network of automatic weather stations in coastal Brazil. *Agricultural and Forest Meteorology*, 118(3-4): 237-250.

Anderson, M.C. et al., 2016. The Evaporative Stress Index as an indicator of agricultural drought in Brazil: An assessment based on crop yield impacts. *Remote Sensing of Environment*, 174: 82-99.

Bayarjargal, Y. et al., 2006. A comparative study of NOAA–AVHRR derived drought indices using change vector analysis. *Remote Sensing of Environment*, 105(1): 9-22.

Brown, J.F., Wardlow, B.D., Tadesse, T., Hayes, M.J. and Reed, B.C., 2008. The Vegetation Drought Response Index (VegDRI): A new integrated approach for monitoring drought stress in vegetation. *GIScience & Remote Sensing*, 45(1): 16-46.

Caccamo, G., Chisholm, L.A., Bradstock, R.A. and Puotinen, M.L., 2011. Assessing the sensitivity of MODIS to monitor drought in high biomass ecosystems. *Remote Sensing of Environment*, 115(10): 2626-2639.

Ciais, P. et al., 2005a. Europe-wide reduction in primary productivity caused by the heat and drought in 2003. *Nature*, 437(7058): 529-533.

Damberg, L. and AghaKouchak, A., 2014. Global trends and patterns of drought from space. *Theoretical and Applied Climatology*, 117(3-4): 441-448.

Di, L., Rundquist, D.C. and Han, L., 1994. Modelling relationships between NDVI and precipitation during vegetative growth cycles. *International Journal of Remote Sensing*, 15(10): 2121-2136.

Donohue, R.J., Mcvicar, T.R. and Roderick, M.L., 2009. Climate-related trends in Australian vegetation cover as inferred from satellite observations, 1981-2006. *Global Change Biology*, 15(4): 1025-1039.

Donohue, R.J., Roderick, M.L., Mcvicar, T.R. and Farquhar, G.D., 2013. Impact of CO2 fertilization on maximum foliage cover across the globe's warm, arid environments. *Geophysical Research Letters*, 40(12): 3031-3035.

Du, L. et al., 2013. A comprehensive drought monitoring method integrating MODIS and TRMM data. *International Journal of Applied Earth Observation and Geoinformation*, 23: 245-253.

Fischer, G.W., 1995. Range sensitivity of attribute weights in multiattribute value models. *Organizational Behavior and Human Decision Processes*, 62(3): 252-266.

Halwatura, D., McIntyre, N., Lechner, A.M. and Arnold, S., 2017. Capability of meteorological drought indices for detecting soil moisture droughts. *Journal of Hydrology: Regional Studies*: 396-412.

Hao, C., Zhang, J. and Yao, F., 2015. Combination of multi-sensor remote sensing data for drought monitoring over Southwest China. *International Journal of Applied Earth Observation and Geoinformation*, 35: 270-283.

Hao, Z. and Aghakouchak, A., 2013a. Multivariate Standardized Drought Index: A parametric multi-index model. *Advances in Water Resources*, 57(9): 12-18.

Hao, Z. and Singh, V.P., 2015. Drought characterization from a multivariate perspective: A review. *Journal of Hydrology*, 527: 668-678.

Hao, Z., Yuan, X., Xia, Y., Hao, F. and Singh, V.P., 2017b. An overview of drought monitoring and prediction systems at regional and global scales. *Bulletin of the American Meteorological Society*.

Hayes, M.J., Svoboda, M.D., Wardlow, B.D., Anderson, M.C. and Kogan, F., 2012. Drought monitoring: Historical and current perspectives.

Hielkema, J., Prince, S. and Astle, W., 1986. Rainfall and vegetation monitoring in the savanna zone of the Democratic Republic of Sudan using the NOAA Advanced Very High Resolution Radiometer. *International Journal of Remote Sensing*, 7(11): 1499-1513.

Hong, Y., Hsu, K.l., Moradkhani, H. and Sorooshian, S., 2006. Uncertainty quantification of satellite precipitation estimation and Monte Carlo assessment of the error propagation into hydrologic response. *Water resources research*, 42(8).

Ji, L. and Peters, A.J., 2003. Assessing vegetation response to drought in the northern Great Plains using vegetation and drought indices. *Remote Sensing of Environment*, 87(1): 85-98.

Jiao, W. et al., 2016. Evaluating an enhanced vegetation condition index based on VIUPD for drought monitoring in the continental United States. *Remote Sensing*, 8(3): 224.

Keyantash, J.A. and Dracup, J.A., 2004. An aggregate drought index: Assessing drought severity based on fluctuations in the hydrologic cycle and surface water storage. *Water Resources Research*, 40(9).

Kogan, F., 1995a. Application of vegetation index and brightness temperature for drought detection. *Advances in Space Research*, 15(11): 91-100.

Kogan, F.N., 1995b. Droughts of the late 1980s in the United States as derived from NOAA polar-orbiting satellite data. *Bulletin of the American Meteorological Society*, 76(5): 655-668.

Kogan, F.N., 1997. Global drought watch from space. *Bulletin of the American Meteorological Society*, 78(4): 621-636.

Long, D. et al., 2013. GRACE satellite monitoring of large depletion in water storage in response to the 2011 drought in Texas. *Geophysical Research Letters*, 40(13): 3395-3401.

Lu, X., Wang, L., Pan, M., Kaseke, K.F. and Li, B., 2016. A multi-scale analysis of Namibian rainfall over the recent decade–Comparing TMPA satellite estimates and ground observations. *Journal of Hydrology: Regional Studies*, 8: 59-68.

Malczewski, J. and Liu, X., 2014. Local ordered weighted averaging in GIS-based multicriteria analysis. *Annals of GIS*, 20(2): 117-129.

Mishra, A.K. and Singh, V.P., 2010. A review of drought concepts. *Journal of Hydrology*, 391(1): 202-216.

Mk, V.D.M. et al., 2011. Drought and ecosystem carbon cycling. *Agricultural & Forest Meteorology*, 151(7): 765-773.

Pandey, S., Bhandari, H.S. and Hardy, B., 2007. Economic costs of drought and rice farmers' coping mechanisms: a cross-country comparative analysis. International Rice Research Institute, 203 pp.

Parida, B.R., Collado, W.B., Borah, R., Hazarika, M.K. and Samarakoon, L., 2008. Detecting Drought-Prone Areas of Rice Agriculture Using a MODIS-Derived Soil Moisture Index. *Giscience & Remote Sensing*, 45(1): 109-129.

Park, S., Im, J., Jang, E. and Rhee, J., 2016. Drought assessment and monitoring through blending of multi-sensor indices using machine learning approaches for different climate regions. *Agricultural and Forest Meteorology*, 216: 157-169.

Park, S., Im, J., Park, S. and Rhee, J., 2017. Drought monitoring using high resolution soil moisture through multi-sensor satellite data fusion over the Korean peninsula. *Agricultural and Forest Meteorology*, 237: 257-269.

Quiring, S.M. and Ganesh, S., 2010. Evaluating the utility of the Vegetation Condition Index (VCI) for monitoring meteorological drought in Texas. *Agricultural and Forest Meteorology*, 150(3): 330-339.

Rajsekhar, D., Singh, V.P. and Mishra, A.K., 2015b. Multivariate drought index: An information theory based approach for integrated drought assessment. *Journal of Hydrology*, 526(s 11–12): 164-182.

Rhee, J. and Im, J., 2017. Meteorological drought forecasting for ungauged areas based on machine learning: Using long-range climate forecast and remote sensing data. *Agricultural and Forest Meteorology*, 237: 105-122.

Rhee, J., Im, J. and Carbone, G.J., 2010. Monitoring agricultural drought for arid and humid regions using multi-sensor remote sensing data. *Remote Sensing of Environment*, 114(12): 2875-2887.

Rouse, J.W., Haas, R.W., Schell, J.A., Deering, D.W. and Harlan, J.C., 1974. Monitoring the vernal advancement and retrogradation (Greenwave effect) of natural vegetation. NASA/GSFCT Type III final report. *Nasa*.

Sheffield, J., Andreadis, K.M., Wood, E.F. and Lettenmaier, D.P., 2009. Global and continental drought in the second half of the twentieth century: severity–area–duration analysis and temporal variability of large-scale events. *Journal of Climate*, 22(8): 1962-1981.

Singh, R.P., Roy, S. and Kogan, F., 2003. Vegetation and temperature condition indices from NOAA AVHRR data for drought monitoring over India. *International Journal of Remote Sensing*, 24(22): 4393-4402.

Stocker, B.D. et al., 2018. Quantifying soil moisture impacts on light use efficiency across biomes. *New Phytologist*, 218(4): 1430-1449.

Tadesse, T. et al., 2017. Building the vegetation drought response index for Canada (VegDRI-Canada) to monitor agricultural drought: first results. *GIScience & Remote Sensing*, 54(2): 230-257.

Tang, Z., Zhang, H., Yi, S. and Xiao, Y., 2018. Assessment of flood susceptible areas using spatially explicit, probabilistic multi-criteria decision analysis. *Journal of Hydrology*.

Vetter, M. et al., 2008. Analyzing the causes and spatial pattern of the European 2003 carbon flux anomaly using seven models. *Biogeosciences*, 5(2): 561-583.

Vicente-Serrano, S.M., 2007. Evaluating the impact of drought using remote sensing in a Mediterranean, semi-arid region. *Natural Hazards*, 40(1): 173-208.

Wilhelmi, O.V. and Wilhite, D.A., 2002. Assessing vulnerability to agricultural drought: a Nebraska case study. *Natural Hazards*, 25(1): 37-58.

Wu, J. et al., 2013. Establishing and assessing the Integrated Surface Drought Index (ISDI) for agricultural drought monitoring in mid-eastern China. *International Journal of Applied Earth Observation and Geoinformation*, 23(0): 397-410.

Yager, R.R., 1993. On ordered weighted averaging aggregation operators in multicriteria decisionmaking, Readings in Fuzzy Sets for Intelligent Systems. Elsevier, pp. 80-87.

Zhang, A. and Jia, G., 2013. Monitoring meteorological drought in semiarid regions using multi-sensor microwave remote sensing data. *Remote Sensing of Environment*, 134: 12-23.

Zhang, L. et al., 2007. A new vegetation index based on the universal pattern decomposition method. *International Journal of Remote Sensing*, 28(1): 107-124.

Zhang, L., Jiao, W., Zhang, H., Huang, C. and Tong, Q., 2017. Studying drought phenomena in the Continental United States in 2011 and 2012 using various drought indices. *Remote Sensing of Environment*, 190: 96-106.

Zhang, X., Chen, N., Li, J., Chen, Z. and Niyogi, D., 2017. Multi-sensor integrated framework and index for agricultural drought monitoring. *Remote Sensing of Environment*, 188: 141-163.

Zhang, Y. et al., 2016. Canopy and physiological controls of GPP during drought and heat wave. *Geophysical Research Letters*, 43(7): 3325-3333.

Zhou, L. et al., 2012. Comparison of remotely sensed and meteorological data-derived drought indices in mid-eastern China. *International Journal of Remote Sensing*, 33(6): 1755-1779.

# CHAPTER 5 EVALUATING THE APPLICABILITY OF SATELLITE SOLAR-INDUCED CHLOROPHYLL FLUORESCENCE (SIF) TO EXAMINE METEOROLOGICAL DROUGHT

## 5.1 Introduction

Drought is one of the least understood natural hazards that can have devastating impacts on agriculture, environment and social economics in many parts of the increasingly globalized world (Mishra et al., 2010; Sheffield et al., 2012). Drought occurs virtually in all climatic zones and the potential increase of drought frequency and severity due to climate change highlights the importance of a better understanding of drought to both policymakers and the scientific community (Dai, 2011; Griggs et al., 2002; Hao et al., 2017a; Van Loon et al., 2016b).

Over the last decades, satellite remote sensing technology has been proved to be a useful tool for drought monitoring since it could provide continuous observations for drought characterizations at regional to global scales, especially for regions with limited *in-situ* observations (Jiao et al., 2016; Jiao, Tian, et al., 2019; Rhee et al., 2010; Zhou et al., 2012). Satellite observations could also be applied to estimate the drought impact on ecosystems by assessing the photosynthetic process of plants since water stress can change plants' photosynthetic capacity (AghaKouchak et al., 2015b). Large-scale remotely sensed drought estimation often relies on optical, near-infrared (NIR), thermal and microwave reflectance observations. For example, satellite-based vegetation indices (VIs) have been widely used for detecting the severity and impact of drought globally through assessing the water-stress related vegetation conditions (Asner et al., 2010; Di et al., 1994; Mishra et al., 2010; Myneni et al., 1989; Singh et al., 2003; Tate et al., 2000;

Tucker et al., 1987; Van Loon et al., 2016b). Some of the research indicated that VIs are good indicators to monitor drought (Ji et al., 2003; Kogan, 1997; Liu et al., 1996; Zhang, Jiao, et al., 2017). However, other studies have shown that VIs should be used with caution for drought monitoring, as they fail to capture rapid changes in drought responses since these indices are not directly linked to photosynthetic functioning (Dobrowski et al., 2005; Sun et al., 2015).

Solar-induced fluorescence (SIF) is the fluorescence emission from plant chlorophyll as 1-2% of the energy absorbed by chlorophyll is re-emitted at longer wavelengths as fluorescence during the light reactions process of photosynthesis (Meroni et al., 2009). In this regard, SIF is considered to have a more close relationship to the functional status of photosynthetic machinery than VIs (Meroni et al., 2009). Satellite-based SIF provides a new method for observing vegetation function from space (Guanter et al., 2007; Guanter et al., 2012; Joiner et al., 2011; Joiner et al., 2013; Yang, Tang, et al., 2015). The main applications of satellite SIF products are to estimate gross primary production (GPP), light use efficiency (LUE), vegetation photosynthetic capacity and crop productivity (Damm et al., 2010; Frankenberg et al., 2011; Guan et al., 2016; Guanter et al., 2014b; Liu et al., 2010; Pérez‐Priego et al., 2015).

In recent years, researchers began to explore the impacts of drought on the ground observed SIF at local scales and satellite SIF at the regional scales. The results implied that SIF may have the potential to monitor the drought impacts on vegetation dynamics (Sun et al., 2015; Wang, Huang, et al., 2016; Yoshida et al., 2015). Research indicated that SIF anomaly, which is the departure of SIF from the corresponding multiyear mean monthly value, could reasonably capture the spatial and temporal dynamics of drought

severity (Sun et al., 2015). In these research work, soil moisture was used to indicate vegetation water stress and was correlated to SIF anomaly. This is because soil water deficit will lead to the closure of plant stomata and the reduction of transpiration and photosynthesis, which consequently limit plant function and decrease SIF signal (Sun et al., 2015; Yoshida et al., 2015). Recent studies also indicated that site-observed SIF performs better for early drought detection compared with VIs such as Normalized Difference Vegetation Index (NDVI) (Liu, Yang, Zhou, Liu, Zhou, Li, Yang, Han, et al., 2018; Liu, Yang, Zhou, Liu, Zhou, Li, Yang and Wu, 2018). However, the sensitivity of satellite SIF to the drought-related environmental variables is complicated and SIF anomaly is not responsive to soil water deficit alone. The change of vapor pressure deficit (VPD), LUE, fraction of photosynthetically active radiation (fPAR), and fluorescence yield under drought conditions have also been shown affecting the SIF anomaly (Sun et al., 2015; Yoshida et al., 2015). In addition, SIF dynamics could be affected by some other biotic and abiotic factors such as plant functional types, temperature, and evapotranspiration (Porcar-Castell et al., 2014).

Drought is a complex phenomenon which associated with multiple perspectives (e.g., low relative soil moisture, precipitation deficiency, and high temperature) (Hao and Singh, 2015). Apart from using soil moisture to represent drought severity, meteorological drought indices, which are based on the climate variables such as temperature, precipitation and potential evapotranspiration (PET), are among the most commonly used drought indices to indicate drought severity, onset, and duration. However, even if the meteorological drought indices indicate that there is drought, the vegetation may not necessarily experience water stress and decrease SIF signal. To what

extent satellite SIF responds to meteorological drought which are estimated from precipitation, temperature and PET perspectives, and how the responses vary under different climatic conditions remain unclear. In this study, we characterize and quantify the relationships between GOME-2 derived 0.5° spatial-resolution SIF dataset and four most commonly used meteorological drought indices (Standardized Precipitation-Evapotranspiration Index, SPEI; Standardized Precipitation Index, SPI; Temperature Condition Index, TCI; Palmer Drought Severity Index, PDSI) in 3,023 counties from diverse climate regions over the continental United States (CONUS) during the growing season in the years of 2007 to 2014. We aim to address the following questions: (1) What are the spatial patterns of the relationship between meteorological drought indices and SIF anomaly in different climate regions? (2) Is there any difference in SIF sensitivity to different meteorological drought indices estimated from temperature, precipitation, and PET? (3) What are the main factors influencing the spatiotemporal patterns of the relationship between SIF and meteorological drought indices at the regional scale? (4) Under what environmental conditions satellite SIF has high correlations to meteorological drought indices?

## 5.2. Data and methodology

### 5.2.1 SIF products

Satellite measurements of SIF from chlorophyll are based on the fact that a small fraction of the energy absorbed by vegetation is emitted as fluorescence during the process of photosynthesis. The fluorescence emission has red and far-red spectrum peaks (near 685 and 740 nm) and most of the satellite SIF measurements have been in the far-

red spectral region (Yoshida et al., 2015). The amount of SIF at the top-of-canopy is frequently expressed as:

$$SIF = PAR \times fPAR \times LUE_F(\lambda) \times f_{esc}(\lambda), \quad (5.1)$$

where PAR is the flux of photosynthetically active radiation received, fPAR is the fraction of PAR, $LUE_F(\lambda)$ can be considered as light use efficiency for SIF and $f_{esc}(\lambda)$ is the fraction of SIF photons escaping from the canopy to space. This expression of SIF is similar to LUE based GPP model and is widely used by the remote sensing community (Sun et al., 2015; Yang, Tang, et al., 2015; Yoshida et al., 2015). There are various types of satellite SIF products with different retrieval methods: SIF derived from GOME-2, Greenhouse gases Observing SATellite (GOSAT), Orbiting Carbon Observatory-2 (OCO-2), TROPOspheric Monitoring Instrument (TROPOMI), and Scanning Imaging Absorption Spectrometer for Atmospheric Chartography (SCIAMACHY) (Frankenberg et al., 2014; Guanter et al., 2007; Guanter et al., 2012; Joiner et al., 2011; Joiner et al., 2013; Köhler et al., 2018; Sun, Frankenberg, et al., 2018). As SCIAMACHY derived SIF product ended in 2012, TROPOMI derived SIF product has only covered a short observation period (launched on 13 October 2017), and other datasets could not provide a full spatial mapping of regional to global scale (Frankenberg et al., 2014; Guanter et al., 2016; Köhler et al., 2015; Köhler et al., 2018), this study only focuses on GOME-2 derived SIF product.

GOME-2 based SIF product with a spatial resolution of 0.5° latitude × 0.5° longitude (denoted as SIF hereafter) was extracted by Joiner et al. (2013) based on the GOME-2 data onboard the MetOp-A satellite. Level 3 of version 26 monthly product was used in this study. The GOME-2 based SIF used in this study has a morning overpass

time near 09:30 local time. The detailed information about 0.5° spatial resolution GOME-2 based SIF product is available at https://avdc.gsfc.nasa.gov/pub/data/satellite/MetOp/GOME_F/.

Since most vegetation in the northern regions of the United States is dormant in the winter, our analysis focused primarily on the growing season from April to October (representing the period of active photosynthesis activities) between 2007 and 2014. During the study period, frequent drought events occurred over the CONUS. For example, in 2008 and 2009, much of south and south-central Texas experienced exceptional drought (Nielsen-Gammon, 2011). California also experienced a multiyear exceptional drought which peaked in 2007-2009 and 2012-2013 (Griffin et al., 2014; Williams et al., 2015). The severe drought in California also contributed to the extreme severity of the California wildfires (Keeley et al., 2009). The California drought shifted east causing large parts of Southwest and Texas suffered a harsh drought in the summer of 2011 (Neitsch et al., 2011). In 2012, much of the United States experienced one of the worst droughts in the history of the country, creating the 2012 North American drought.

### 5.2.2 Meteorological drought indices

Standardized Precipitation–Evapotranspiration Index (SPEI), Standardized Precipitation Index (SPI), Temperature Condition Index (TCI), and Palmer Drought Severity Index (PDSI) were used as meteorological drought reference data in this study. SPEI, SPI, TCI, and PDSI are among the most commonly used meteorological drought indices. These four indices were selected to estimate meteorological drought condition from different perspectives. SPI characterizes meteorological drought from the perspective of the precipitation deficiency since it only relies on the historical distribution

of precipitation to quantify the wet and dry levels (McKee et al., 1993). The SPI is simple to calculate and reflects drought conditions over different timescales and recommended by the World Meteorological Organization (WMO) as a global measure of meteorological drought (Hayes et al., 1999a). TCI characterizes meteorological drought from the perspective of temperature anomaly and has been used for drought estimation by various studies (Bhuiyan et al., 2006; Kogan, 1995a; Kogan, 1997; Unganai et al., 1998). SPEI characterizes meteorological drought based on both precipitation and PET. It is based on the historical distribution of precipitation deficiency relative to atmospheric water demand (precipitation minus potential evapotranspiration) (Vicente-Serrano et al., 2010). SPEI has been widely used as the standard drought index by various studies for evaluating different drought monitoring methods since it is statistically robust and its multi-scalar characteristics enable identification of different drought types and impacts in the context of global warming (Banimahd et al., 2013; Hao, AghaKouchak, et al., 2014; Hao, Zhang, et al., 2015; Rajsekhar et al., 2015a). PDSI (Palmer, 1965) accounts for the balance of precipitation, temperature, and PET (Dai, 2011; Wang et al., 2018). Table 5.1 lists the detailed information about the four metrological drought indices.

Drought indices of a certain time-scale refer to the cumulative water deficit over the preceding months (McKee et al., 1993; Vicente-Serrano et al., 2010; Zhao et al., 2017). Different time-scales of SPI and SPEI were used in this study to explore the sensitivity of SIF to cumulative meteorological drought conditions ranging from 1 month to 12 months. Specifically, 1-, 2-, 3-, 4, 5-, 6-, 7-, 9-, and 12-month time-scale SPI and SPEI were used in this study.

The 0.5° monthly raster SPI was obtained from https://climatedataguide.ucar.edu/climate-data/standardized-precipitation-index-spi; a self-calibrating version of PDSI, was obtained from http://www.cgd.ucar.edu/cas/catalog/climind/pdsi.html, and the SPEI V2.5 dataset (monthly data with 0.5° spatial resolution) was obtained at http://spei.csic.es/database.html. Since daily SPEI, PDSI and SPI data covering the CONUS are not readily available, this study examines the monthly SIF responses to meteorological drought. Satellite-based TCI was calculated based on the MODIS Land Surface Temperature (LST) product (MOD11A2) using the minimum and maximum LST for each month ($TCI_i = (LST_{i,max} - LST_i) / (LST_{i,max} - LST_{i,min})$, where $LST_{i,max}$ and $LST_{i,min}$ are the maximum and minimum LST for month i from different years). Eight-day of MODIS LST was composited into monthly LST weighted by the number of days recorded in each month. MODIS LST product was obtained from the Land Processes Distributed Active Center (LPDAAC; http://lpdaac.usgs.gov/).

In this section, we used the county as the basic geographic unit to reduce the effect of low-quality SIF data or missing SIF observations in some pixels on our assessments. We excluded urban, barren and water dominated counties and focused on 3,023 vegetation covered counties in our study. In the county-level statistics, given that some small counties are smaller than the smallest grid cell for the raster SIF data and some large counties in the west may contain multiple grid cells, we divided each SIF grid cell into 10,000 small grid cells without changing the value, then we used the mean value of these small grid cells located in the corresponding counties to represent the county value. The mean SPEI, SPI, TCI and PDSI values were also calculated for each county.

In order to evaluate the sensitivity of satellite SIF to meteorological drought at the county level, we firstly calculated the mean SPEI, SPI, TCI and PDSI values in each county, then correlated these values to the mean SIF anomaly values in each county. We compared the sensitivity of SIF for each over CONUS. The sensitivity of SIF response to meteorological drought was determined based on spearman rank analysis between SIF anomalies and three meteorological drought indices of different time scales. High correlation coefficients indicate high sensitivity and *vice versa*.

Table 5.1: Summary of the meteorological drought indices used in this study.

| Drought index | Required metrological factors | Method | Source |
|---|---|---|---|
| SPI | Precipitation | Based on the historical precipitation occurrence probability distribution function | (McKee et al., 1993) |
| SPEI | Potential evapotranspiration and precipitation | Based on the historical deficiency of precipitation (P-PET) occurrence probability distribution function | (Vicente-Serrano et al., 2010) |
| TCI | Land surface temperature (LST) | Based on LST anomaly | (Kogan, 1997) |

| | | | |
|---|---|---|---|
| PDSI | Precipitation, temperature, and potential evapotranspiration | Based on water balance model | (Palmer, 1965) |

### 5.2.3 Ancillary data

In order to investigate the factors modulating the sensitivity of the satellite SIF to meteorological drought as comprehensive as possible, ten additional datasets were used as the explanatory covariates to explain the spatial variations in the relationships between satellite SIF product and meteorological drought indices. These additional datasets include climate data (historical mean annual growing season temperature and historical mean annual growing season precipitation), land use and land cover (LULC) data, historical mean annual growing season vegetation gross primary production (GPP), digital elevation model (DEM) data and soil property data (soil permeability, hydrology group, water holding capacity and soil drainage).

In this study, LULC information in each county was obtained from National Land Cover Database 2011 (NLCD 2011), which are available at the U.S. Geological Survey National Land Cover Data (NLCD) Institute (http://landcover.usgs.gov/). The majority of the land cover pixel was used to represent the county's LULC type. Each county's majority LULC type was calculated using Zonal statistical function in the ArcGIS software. Counties with LULC types of non-vegetation were excluded. The gridded historical mean annual precipitation was calculated for each county using seven years

(2007-2014) growing season (April to October) data obtained from the Oregon State University PRISM group (http://prism.oregonstate.edu). Mean annual temperature in each county was obtained using 2007-2014 growing season (April to October) MODIS land surface temperature (LST, MOD11A2, with 8-day temporal resolution and 1-km spatial resolution) data. Mean value of the gridded time series of MODIS LST was calculated for each county. For vegetation data, we calculated the mean annual GPP using MODIS GPP product (MOD17A2, with 8-day temporal resolution and 1-km spatial resolution) for the growing season from the year of 2007-2014. Detailed information about these vegetation and land surface temperature datasets are available at https://modis.gsfc.nasa.gov/data/. Gridded DEM for each county is obtained using Space Shuttle Radar Topography Mission (SRTM) product. Soil properties (permeability, water table depth, available water holding capacity, hydrologic groups, and soil drainage) in each county were derived from the STATSGO soil database which was downloaded from the Center for Environmental Informatics at Pennsylvania State University (http://www.soilinfo.psu.edu/). The mean value of the gridded precipitation, temperature, GPP and soil data was used to represent the county's precipitation, temperature, GPP and soil properties. Similar with LULC data, each county's mean precipitation, temperature, GPP, and soil property values were calculated using Zonal statistical function in the ArcGIS software.

### 5.2.4 Calculation of SIF anomaly

The z-score was used to represent the anomaly of GOME-2 SIF data from 2007 to 2014. The z-score of SIF anomaly was calculated as

$$A_{j,i} = \frac{SIF_{j,i} - \overline{SIF_J}}{\sigma}, \tag{5.2}$$

where $A_{j,i}$ denotes SIF anomaly for the month j in year i. $\overline{SIF_j}$ denotes the averaged SIF of month j over the year 2007-2014; $\sigma$ is the standard deviation of SIF for month j over the year 2007-2014. The SIF anomaly was compared with SPEI, SPI, TCI and PDSI in different counties across the CONUS. The Spearman rank correlation coefficients (r-values) between the SIF anomaly and four meteorological drought indices (SPEI, SPI, TCI, and PDSI) were used to evaluate the sensitivity of satellite SIF to the meteorological drought conditions in this study. High correlation coefficients indicate high sensitivity and *vice versa*.

### 5.2.5 Random forest regression

In order to quantify the factors modulating the sensitivity of the satellite SIF to meteorological drought, the random forest regression model was used to examine the relationship between the satellite SIF drought sensitivity and explanatory covariates. Random forest regression is a non-parametric statistical method requiring no distributional assumptions on covariate in relation to the response variable (Breiman, 2001). The random forest algorithm here uses 1000 binary decision trees. In standard trees, each node is split using the best split among all variables. The explanatory covariates used are: historical mean annual growing season temperature, mean annual growing season precipitation, LULC, mean annual growing season GPP, DEM, mean soil moisture, soil permeability, hydrology group, water holding capacity, and soil drainage. With the random forest regression model, variable importance ranking for variable selection was also calculated. The variable importance measures how much the error increases if we scramble the values of a variable. Larger error before and after

permutation means larger importance of the variable in the forest and contribute more to predictive accuracy than other variables (Breiman, 2001).

## 5.3 Results

### 5.3.1 Temporal correlations between SIF and meteorological drought indices

The SIF anomalies were compared against each of the four meteorological drought indices, specifically: PDSI, TCI, SPI (1-, 2-, 3-, 4-, 5-, 6-, 7-, 9- and 12-month time-scales) and SPEI (1-, 2-, 3-, 4-, 5-, 6-, 7-, 9- and 12-month time-scales) in all 3,023 counties across the CONUS. Table 5.2 summarized the mean correlations between SIF and meteorological drought indices. SIF has the highest correlation with PDSI (r =0.257) followed by TCI with a similar value (r=0.249). SIF has similar correlations with SPI and SPEI under different time-scales and the correlations were generally lower than those with PDSI and TCI (Table 5.2). Since the calculation of TCI is based on monthly data and there is no accumulative effect from previous months, TCI could be considered as 1-month time-scale. The correlation between SIF and TCI was 61.68 % higher than the correlation between SIF and 1-month SPI (SPEI), and 7.8% higher than the correlation between SIF and 3-month SPI (8.7% for 3-month SPEI). When comparing the correlations of SIF with meteorological drought indices from different time-scales, the correlation of 2-month time-scale SPI was 38% higher than that of 1-month SPI (37% for SPEI). The correlation of 3-month time-scale SPI was 8.4% higher than that of 2-month SPI (8.5% for SPEI). There was no significant difference for the correlations between SIF and SPI (SPEI) for time-scale longer than 3 months.

Table 5.2: Correlations between SIF and meteorological drought indices across 3,023 counties in the continental United States (* indicates p-value <0.05).

| Drought index | r-value |
|---|---|
| TCI | 0.249* |
| PDSI | 0.257* |
| 1-Month SPI | 0.154 |
| 1-Month SPEI | 0.154 |
| 2-Month SPI | 0.213* |
| 2-Month SPEI | 0.211* |
| 3-Month SPI | 0.231* |
| 3-Month SPEI | 0.229* |
| 4-Month SPI | 0.230* |
| 4-Month SPEI | 0.226* |
| 5-Month SPI | 0.230* |
| 5-Month SPEI | 0.229* |
| 6-Month SPI | 0.232* |
| 6-Month SPEI | 0.228* |
| 7-Month SPI | 0.231* |
| 7-Month SPEI | 0.229* |
| 9-Month SPI | 0.226* |
| 9-Month SPEI | 0.222* |
| 12-Month SPI | 0.226* |
| 12-Month SPEI | 0.225* |

### 5.3.2 Spatial patterns of the correlations between SIF and meteorological drought indices

Over the CONUS, there was significant spatial variability in the correlations between satellite SIF and SPEI, the r-values ranged from -0.4 to 0.9 (Figure 5.1). This was similar to the correlation ranges between satellite SIF and SPI (Figure 5.2), TCI, and PDSI (Figure 5.3). Generally, SIF showed similar spatial variability and their correlations with different meteorological drought indices of different time-scales were uniform (Figures 5.1-5.3). There were much stronger positive correlations between SIF and meteorological drought indices in the counties in the middle CONUS than counties in the eastern and western CONUS. For example, for the r-values between SIF and SPEI-3, SPI-3 and PDSI (denotes as $R_{SIF\text{-}SPEI03}$, $R_{SIF\text{-}SPI03}$, and $R_{SIF\text{-}PDSI}$) in Figures 5.1-5.3, many of the counties in the southwestern CONUS (e.g., some counties in Nevada, California, and Arizona) had $R_{SIF\text{-}SPEI03}$, $R_{SIF\text{-}SPI03}$ and $R_{SIF\text{-}PDSI}$ close to zero and p-value > 0.05, whereas most counties in the north-central and south-central CONUS (e.g., counties in Texas, Oklahoma, Kansas, Dakota, and Nebraska) had $R_{SIF\text{-}SPEI03}$, $R_{SIF\text{-}SPI03}$ and $R_{SIF\text{-}PDSI}$ exceeding 0.75 and p-value <0.05. Besides the significant positive correlations in the middle of CONUS, there are significantly negative correlations between SIF and meteorological drought indices mainly in the Pacific Northwest and Northeast regions.

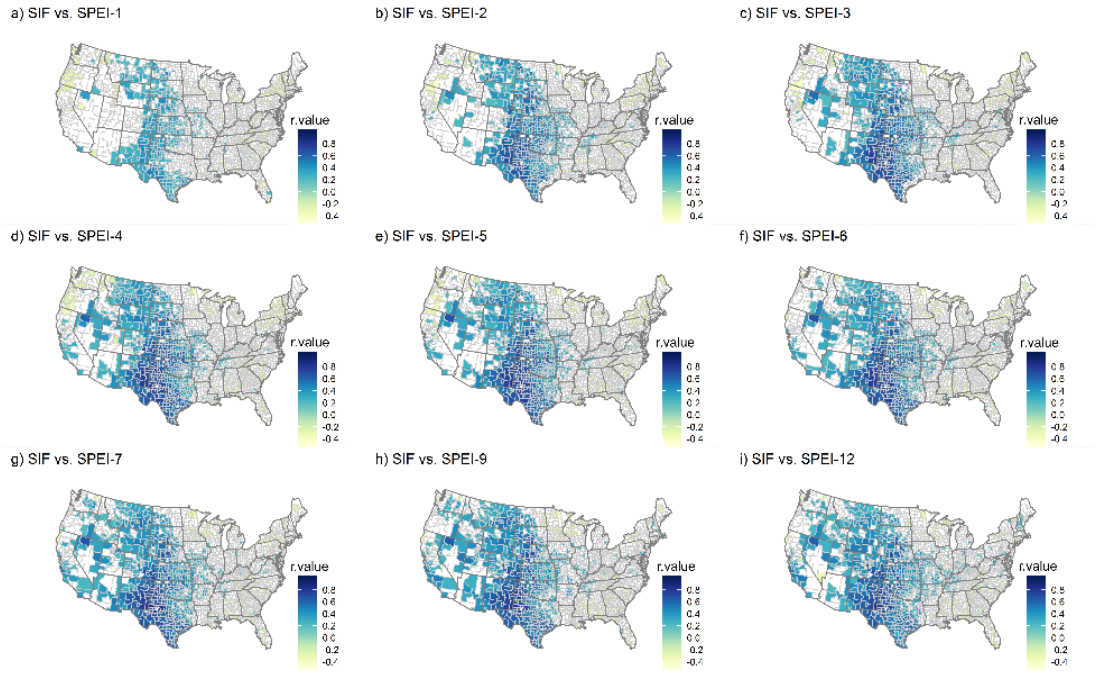


Figure 5.1: Spatial variations of the r-values between SIF and SPEI at 1-month (a), 2-month (b), 3-month (c), 4-month (d), 5-month (e), 6-month (f), 7-month (g), 9-month (h), 12-month (i) time scale. Counties with white color means insignificant correlations (p-value > 0.05) in those counties.

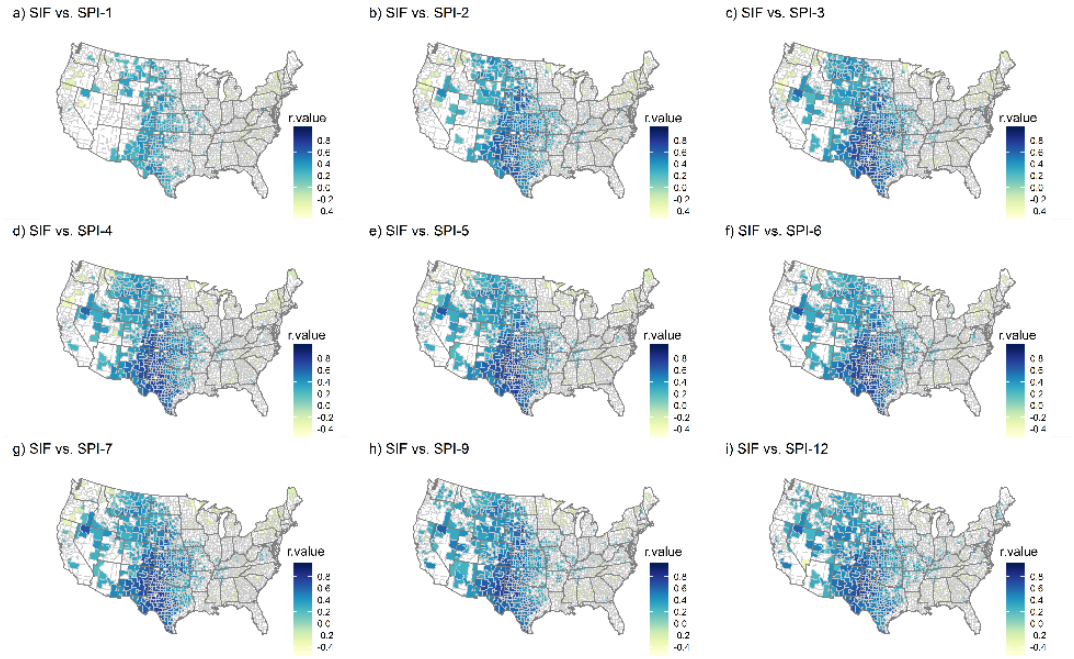


Figure 5.2: Spatial variations of the r-values between SIF and SPI at 1-month (a), 2-month (b), 3-month (c), 4-month (d), 5-month (e), 6-month (f), 7-month (g), 9-month (h), 12-month (i) time scale. Counties with white color means insignificant correlations (p-value > 0.05) in those counties.

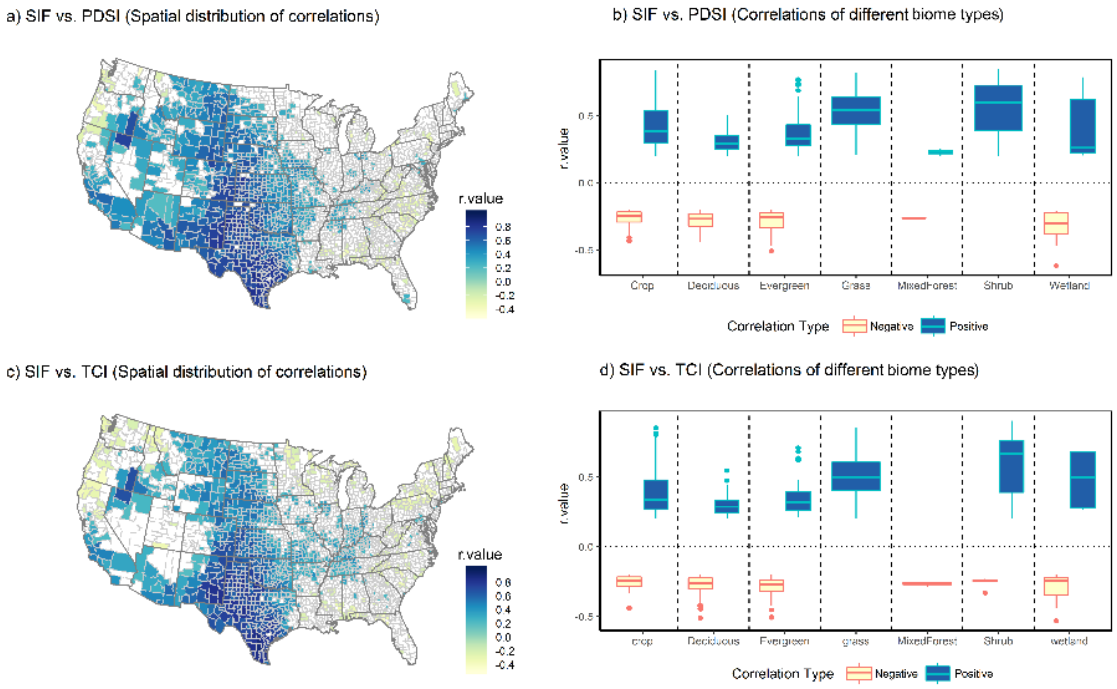


Figure 5.3: Spatial variations of the r-values between SIF and PDSI (a) as well as between SIF and TCI (c). Counties with white color means insignificant correlations (p-values > 0.05) in those counties. The correlations (r-value) between SIF and PDSI (b) as well as between SIF and TCI (d) for different ecosystem types.

The sensitivity of SIF to metrological drought were different for different ecosystem types (Figure 5.3). Figure 5.3 (b) and (d) show the correlations between SIF and PDSI as well as between SIF and TCI, respectively, for different ecosystem types. Generally, SIF had higher positive correlations with PDSI and TCI for grassland and shrubland ecosystems than other ecosystem types. Most of the grassland and shrubland ecosystems only had positive correlations with PDSI and TCI. SIF had lowest positive correlations for deciduous and evergreen forests than other ecosystem types. The sensitivity of SIF to the meteorological indices of different ecosystem types were also different for different time-scales (Figures 5.4 and 5.5). Grassland SIF had only positive correlations for all the time-scales of SPI and 2 to 12-month time-scales of SPEI. Mixed forest SIF had only negative correlations to SPI and SPEI for 1 to 7-month time-scales and only positive correlation with 12-month SPI. Shrubland SIF had both positive and negative correlations with SPI for the time-scale of 1 to 7 months and only positive correlations for the time-scale of 9 to 12 months. Similarly, shrubland SIF shows both positive and negative correlations to SPEI for time-scale from 1 to 5 months, and for time scale longer than 6 months, there were only positive correlations.

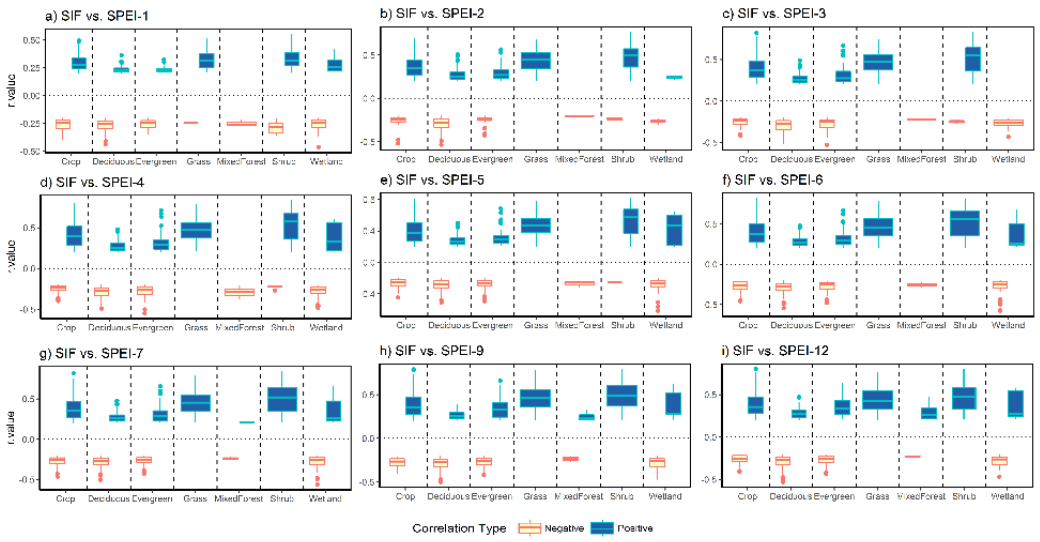


Figure 5.4: The correlations (r-value) between SIF and SPEI under different ecosystem types for the time-scale of 1-month (a), 2-month (b), 3-month (c), 4-month (d), 5-month (e), 6-month (f), 7-month (g), 9-month (h) and 12-month (i).

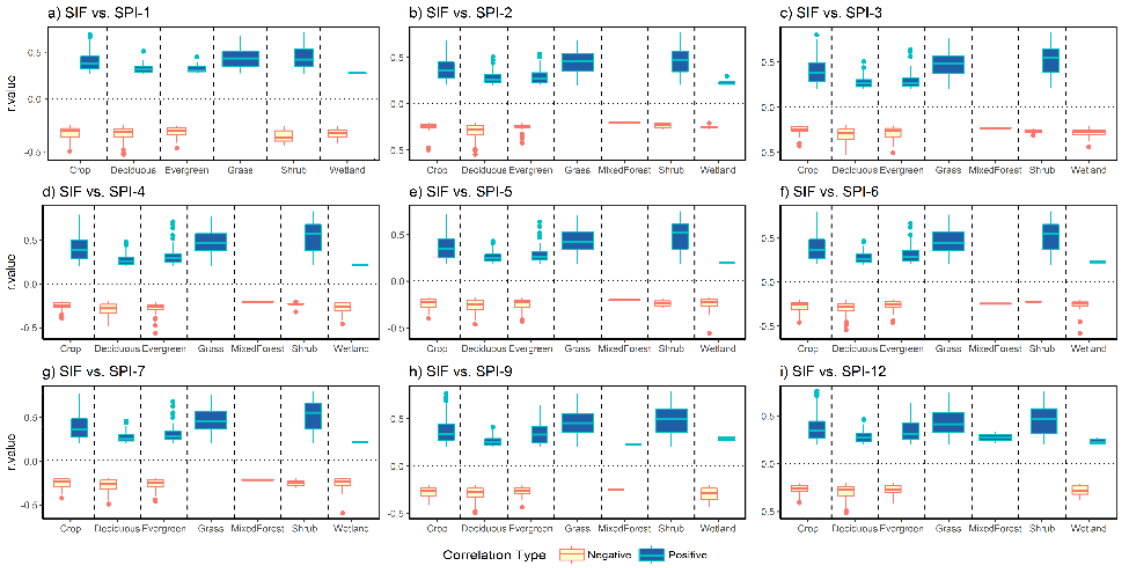


Figure 5.5: The correlations (r-value) between SIF and SPI under different ecosystem types for the time-scale of 1-month (a), 2-month (b), 3-month (c), 4-month (d), 5-month (e), 6-month (f), 7-month (g), 9-month (h) and 12-month (i).

### 5.3.3 Driving forces of the observed spatial variability

To examine the driving forces of the observed spatial variability in the relationships between the SIF anomaly and meteorological drought indices, ten independent variables (described in section 5.2.3) were evaluated using random forest regression. Because of the similar spatial variability and magnitude in correlation coefficients between SIF and those meteorological drought indices of different time-scales, we chose to focus on the relationships between the SIF and SPEI-5, SPI-5, TCI and PDSI in our analysis.

All the variables together explained 77.76% of the variation in the r-value between SIF and SPEI-5 (denotes as $R_{SIF\text{-}SPEI05}$). In comparison, these ten independent

variables explained 77.56%, 78.49%, and 78.68% of the variations in the r-values between SIF and SPI-5 ($R_{SIF\text{-}SPI05}$), between SIF and TCI ($R_{SIF\text{-}TCI}$), and between SIF and PDSI ($R_{SIF\text{-}PDSI}$), respectively. The variable importance function in the random forest model was used to quantify the rank of how each variable modulates the variance of $R_{SIF\text{-}SPEI05}$, $R_{SIF\text{-}SPI05}$, $R_{SIF\text{-}TCI}$ and $R_{SIF\text{-}PDSI}$. Figure 5.6 shows the rank of importance for the ten independent variables controlling the sensitivity of SIF to meteorological drought. Figure 5.6 shows each variable on the y-axis, and their importance on the x-axis, ordering from top-to-bottom as most to least important. The variable importance (x-axis value in Figure 5.6) is the difference in 'Out of Bag' (Breiman, 1996) prediction error before and after permutation. A larger variable importance value indicates that misspecification detracts from the predictive accuracy in the forest. Smaller variable importance value indicates the variable contributes less to the predictive accuracy (Ishwaran, 2007).

The results showed that mean annual temperature was the most important variable in explaining the spatiotemporal distributions of r-value distributions (Figure 5.6). Less important but still of major influence was mean annual growing season GPP. Mean annual growing season precipitation was the next significant variable. Compared with the factors described above, DEM, LULC and the soil conditions (soil drainage class, organic material, permeability, water holding capacity, and hydrologic group) were the less significant variables affecting the $R_{SIF\text{-}SPEI05}$ distributions. Similar to $R_{SIF\text{-}SPEI05}$, temperature appeared to be the most dominant driver for the spatial distribution of $R_{SIF\text{-}SPI05}$, $R_{SIF\text{-}TCI}$ and $R_{SIF\text{-}PDSI}$. Mean annual GPP and precipitation were the next top significant variables associated with the strength of $R_{SIF\text{-}SPI05}$, $R_{SIF\text{-}TCI}$ and $R_{SIF\text{-}PDSI}$ .

LULC was the fourth important factor. Also, DEM and the soil conditions were the less significant variables (Figure 5.6).

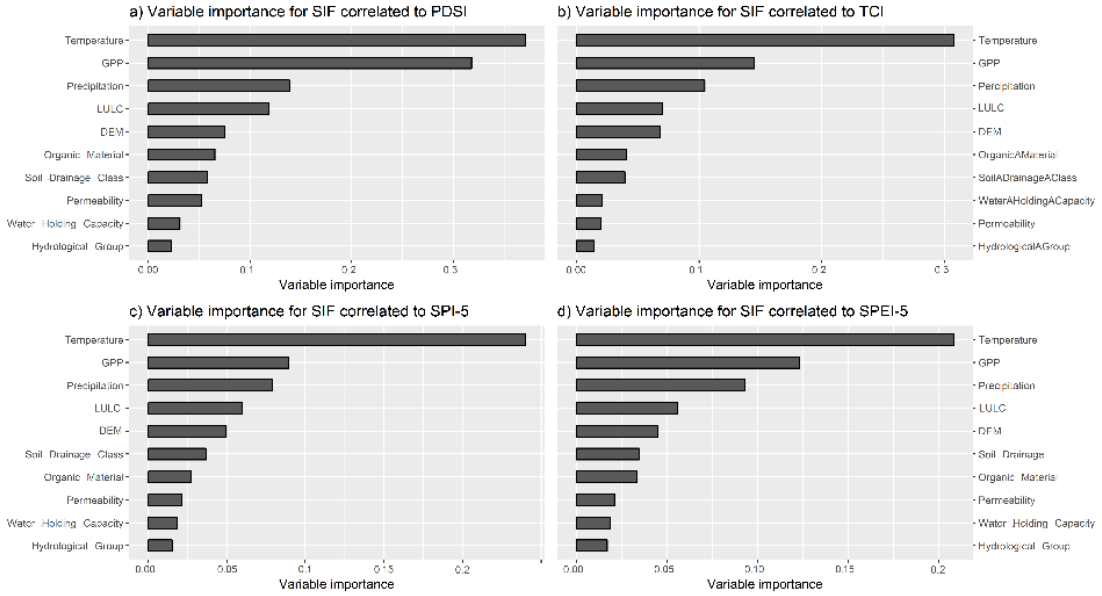


Figure 5.6: Variable importance of ten environmental variables for explaining the relationship between SIF anomaly and meteorological drought indices (SPEI, SPI, TCI and PDSI).

To demonstrate an environmental envelope for the sensitivity of satellite SIF to meteorological drought and show areas of high SIF sensitivity to meteorological drought, Figure 5.7 displays the dependence of SIF and meteorological drought index correlation on the top three independent environmental variables across a wide range of observed values. Since PDSI, TCI, different time-scales of SPI and SPEI showed similar spatial variability and their correlations with SIF anomaly were uniform (Figure 5.1-5.3), we focused on the relationship between SIF anomalies and SPEI-5. The black points with p-value $< 0.05$ indicate the points with a statistically significant relationship between SIF and SPEI-5.

In Figure 5.7, the blue and brown lines represent the thresholds of 90% and 80% of the counties with a significant correlation between SIF and SPEI-5, respectively. That is, for example, for the counties with mean annual growing season temperature higher than the blue line (i.e., >30.6°C), the percentage of counties with significant correlations between SIF and SPEI-5 (black points in Figure 5.7a) is more than 90% (all the points at the right side of the blue line in Figure 5.7a). That is, satellite SIF anomaly was sensitive to meteorological drought for areas with mean annual growing season temperature higher than 30.6 °C. Similarly, regions with mean annual growing season GPP less than 750 g C $m^{-2}$ $yr^{-1}$ or mean annual growing season precipitation less than 700 mm were areas with high sensitivity of satellite SIF to meteorological drought. Figure 5.7d) -f) displayed the suggested suitable areas for using satellite SIF to characterize meteorological drought based on 80% threshold in mean annual growing season temperature, GPP, and precipitation. Supplemental materials Figures S5.1 to S5.6 showed the detailed correlations between SIF and all the ten environmental variables.

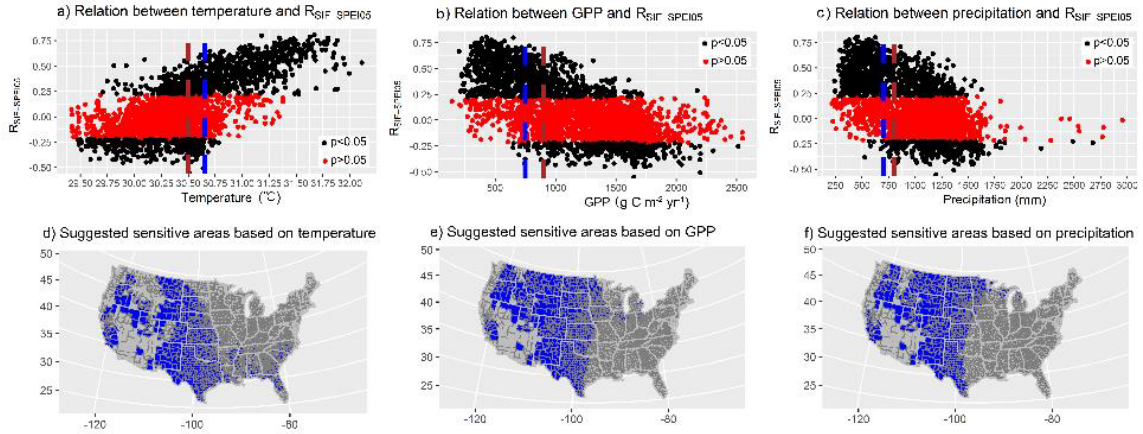


Figure 5.7: The dependence of SIF and 5-month SPEI correlation ($R_{SIF\text{-}SPEI05}$) on mean annual temperature (a), GPP (b) and precipitation (c). The blue and brown lines represent

the thresholds of 90% and 80% of the counties with significant relationship between SIF and SPEI, respectively. The blue colored regions represent the areas meet the 80% threshold regarding temperature (d), GPP (e) and precipitation (f) for SIF being sensitive to meteorological drought. Red points in (a)-(c) represent the counties with non-significant relationships between SIF and SPEI-5 ($p>0.05$) and black points represent counties with significant correlations ($p<0.05$).

## 5.4 Discussion

### 5.4.1 SIF sensitivity to different climate variables

The correlation of SIF to meteorological drought indices not only reflects SIF response to drought stress but also reflects the sensitivity of SIF to different climate variables. For example, SPI is only based on the historical distribution of precipitation and high SPI could indicate wet conditions(Hayes, 2000; Shahid, 2010). Therefore, the correlation between SIF anomaly and SPI could potentially reflect the sensitivity of SIF to precipitation dynamics. Similarly, TCI is only based on temperature variable, the correlation between SIF anomaly and TCI could potentially indicate the sensitivity of SIF to temperature variations. SPEI represents meteorological drought using the combination of precipitation and PET. The correlation between SIF anomaly and SPEI indicates the sensitivity of SIF to the dynamics of precipitation deficiency relative to PET. Similarly, the correlation between SIF anomaly and PDSI indicates the sensitivity of SIF to the dynamics of water balance.

Our results indicate that SIF is more sensitive to temperature than precipitation and PET since the correlation between SIF and TCI is much higher than the correlation

between SIF and SPI or SPEI. Though the correlation between SIF and PDSI is higher than the correlation between SIF and TCI, there is only a 3% difference. Consistent with the high correlation between SIF and TCI, variable importance from random forest regression also shows that temperature is the most important factor explaining the variance of SIF sensitivity to meteorological drought. Temperature has a significant positive correlation with $R_{SIF\text{-}SPEI05,}$ which means that there will be stronger SIF sensitivity to meteorological drought under higher temperature conditions. The reason could be that rising temperatures favorably influence vegetation activity and it is the main driver of many biological processes (such as enzyme-catalyzed reactions), which usually increase plant photosynthetic activity up to a certain point (Badeck et al., 2004; Karnieli et al., 2006). It should be noted that those very high temperatures (>31.5 $^{o}$C) decreases the sensitivity to meteorological drought (Figure 5.7). This is may be because vegetation under extremely high temperatures will decrease enzyme-catalyzed reactions and photosynthetic activity (Mu et al., 2007; Xiao et al., 2004; Zhao et al., 2005).

It is worth noting that although SIF is less sensitive to precipitation than to temperature, precipitation is still a very important climate variable affecting SIF dynamics. There is a significant correlation between SIF and SPI, and including PET into SPEI does not significantly improve the correlation with SIF. This indicates that precipitation is a more important factor than PET for affecting SIF dynamics. The negative relationship between the $R_{SIF\text{-}SPEI05}$ and mean annual growing season precipitation is similar to previous studies using other vegetation indices for drought monitoring. For example, Vicente-Serrano (2007) and Quiring et al. (2010) showed that the correlations between the *in-situ* meteorological drought index (SPI) and satellite-

based vegetation condition index (VCI) are generally higher in dry locations than in wet regions. In drylands where precipitation is the dominant factor for vegetation growth, precipitation is a key important factor for determining the vegetation dynamics (Wang, d'Odorico, et al., 2012b). While in wet regions, additional precipitation does not change SIF signal significantly. In these regions, vegetation response to drought and moisture variations will be much more muted.

### 5.4.2 SIF sensitivity to meteorological drought of different time scales and different ecosystem types

Our results indicate that different ecosystem types have different SIF sensitivity to meteorological drought. In this study, shrubland mainly refers to areas dominated by 5 m tall shrubs and young trees; grassland refers to areas dominated by grammanoid or herbaceous vegetation (Homer et al., 2004). Generally, shrubland, grassland, and cropland SIFs are sensitive to short-term (1-month) meteorological drought indices, which indicates SIF could have fast response to meteorological drought for these ecosystem types. Grassland SIF only shows positive correlations to all the meteorological drought indices, which indicates decreasing of precipitation and increasing of temperature will decrease SIF values for grassland. Shrubland SIF has the highest positive correlation with all the meteorological drought indices across different time scales, and as the time-scale increase more counties have positive correlations. This indicates that shrubland SIF is also a fast response signal to meteorological drought conditions since it has high correlation with short-term SPI and SPEI (1-month time-scale). The negative correlation indicates that 1 to 7 month's cumulative decreasing precipitation or increasing temperature could increase SIF values for some regions.

Generally, the patterns of SIF response to different time-scales of drought from different ecosystem types agree with the patterns from NDVI in Vicente-Serrano et al. (2013) that forests are more sensitive to long-term drought conditions since they have deeper rooting systems and grassland and shrubland are sensitive to short-term drought. Our results also agree with Anderegg et al. (2018) that higher diversity of mixed forests have higher drought resilience since the correlations between SIF and meteorological drought indices are lower for mixed forests than for other ecosystem types.

Spatially, the negative correlations in Pacific Northwest and Northeast regions are likely because these are wet regions and soil water is not limiting when meteorological drought occurs. Meteorological drought often occurs along with high temperature and low cloud cover, the increasing temperature and PAR during meteorological drought in these regions could increase satellite SIF values. It should be noted the heterogeneous pattern of the correlations in the Intermountain West may be due to data quality in this region. Due to the sparse coverage of vegetation in this region, there are many pixels without SIF data. Given the limited number of pixels in this region, the mean SIF pixel value of some counties may not reasonably reflect the large counties' value and therefore cause some statistical uncertainties. In this regard, the application of satellite SIF to meteorological drought response in this region should be treated with caution. The significant correlations in the middle regions of CONUS indicated that SIF signal in these regions has high sensitivity to meteorological drought.

Our results indicate that the overall correlations of SIF to 2-month time-scale of drought indices are significant higher than the correlations between SIF and 1-month time-scale drought indices. The overall sensitivity of SIF to 3-month time-scale

meteorological drought is slightly higher than to 2-month time-scale meteorological drought. One of the possible reasons for the overall lower correlation between SIF and 1-month drought indices than with longer term drought indices is that vegetation growth is controlled by soil moisture and changes in vegetation growth signal are buffered by soil water storage (Piao et al., 2003; Quiring et al., 2010). The occurrence of meteorological drought does not always mean plant water stress. For some regions when early meteorological droughts occur, vegetation could still have access to sufficient soil water to maintain functions without experiencing water stress for a period of time. In fact, the relationships between soil moisture and different time-scales of meteorological drought have been well documented. For example, Wang et al. (2015) indicated that there is a time-lag of soil moisture response to meteorological drought indices. It is shown that the SPEI of 1-3 month timescales has maximum correlations with soil moisture at soil depths of 0-5 cm, while SPEI of 9-12 month time scales has maximum correlations with soil moisture at soil depths of 90-100 cm. Another possible reason for the overall lower correlation between SIF and 1-month drought indices than with longer term drought indices is that the sensitivity of SIF is controlled by different ecosystem types. For 1-month drought indices, grassland and shrubland SIF have high correlations but not for the other types. As the time-scale increases, SIF from more ecosystem types become positively correlated to meteorological drought indices and grassland and shrubland SIF are still highly correlated to longer term drought indices, thus increasing the overall correlations with longer term meteorological drought indices. However, even SIF has lowest correlation with 1-month time-scale drought indices than with other time-scales, it has potential to detect ecosystem drought response earlier than other remote-sensing

based indices. For example, previous research studied the characteristic of VI based meteorological drought monitoring, which showed VIs have higher correlations with the 6- to 9-month time-scale meteorological drought indices (Quiring et al., 2010). Recent study also compared daily ground-based observations of SIF and NDVI against soil moisture and demonstrated that SIF has a quicker response to drought than NDVI (Liu, Yang, Zhou, Liu, Zhou, Li, Yang, Han, et al., 2018).

### 5.4.3 Potential use of satellite SIF to study vegetation response to environmental stresses

Satellite SIF is an emerging satellite retrieval product, which could provide measurements closely or directly related to plant photosynthetic activity. There are growing interests to examine the effects of drought on SIF in recent years. Our research indicates that SIF is highly sensitive to temperature variation in the short time-scale (e.g., 1 month). The high SIF sensitivity to temperature indicates the potential use of SIF to monitor plant heat stress. Recently, Song et al. (2018b) shows that SIF has the ability to detect winter wheat early response to heat stress in the Indian Indo-Gangetic Plains when comparing with NDVI and EVI. Future research could focus on SIF sensitivities to heat stress over regional to global scales and explore the mechanisms of plant functions involving heat stress. In addition, because SIF has high sensitivity to temperature variations it has potential to investigate changes in plant photosynthetic activity under global warming. This is important because there are uncertainties using existing VIs to evaluate plant photosynthetic activity responses to warming due to saturation issue, background effect or sensor degradation (Gao et al., 2000; Nicholson et al., 1994; Zhang, Song, et al., 2017).

With growing interests in satellite SIF, more satellite products at regional to global scale will become available such as TROPOMI SIF product with a global coverage (Köhler et al., 2018). Future study can also take advantage of satellite SIF products extracted from satellite observation models such as high resolution global contiguous OCO-2 based SIF product (Yu et al.). In this study, we compared the original GOME-2 SIF product and downscaled high spatial resolution GOME-2 SIF product by (Duveiller et al., 2016), they showed a similar pattern when correlated to the meteorological drought indices (Figures S7-S9).

Our research analyzed the characteristics of SIF responses to meteorological drought. However, it should be noted that several factors could potentially affect the sensitivity analysis of SIF to meteorological drought. Firstly, we assessed the sensitivity of SIF to meteorological drought based on the Spearman rank correlation analysis between SIF anomalies and meteorological drought indices. However, correlation does not always imply causation. Ground-based SIF measurements would be valuable to examine the mechanisms in the future. In addition, this study analyzed data at the county level. Small counties may be smaller than the smallest SIF grid cell, and large counties in the west may contain multiple SIF grid cells. This may add uncertainties to our evaluation results. At the same time, political boundaries, in general, and county boundaries, in particular, are commonly used for making drought-related decisions.

### 5.5 Conclusions

This study examines the spatial relationship between satellite SIF and four commonly used meteorological drought indices of different time-scales in different

climate regions across the CONUS. We found that satellite SIF is more sensitive to meteorological drought through temperature effect than through precipitation and potential evapotranspiration effects. We also demonstrate that the sensitivity of satellite SIF response to meteorological drought varied significantly in different climate regions and for different ecosystem types. SIF is sensitive to meteorological drought only in climate regions with high growing season temperature, low growing season precipitation and low GPP. Among the environment variables, mean annual growing season temperature is of the greatest importance affecting the satellite SIF sensitivity.

**References**

AghaKouchak, A. et al., 2015b. Remote sensing of drought: Progress, challenges and opportunities. *Reviews of Geophysics*, 53(2): 452-480.

Anderegg, W.R. et al., 2018. Hydraulic diversity of forests regulates ecosystem resilience during drought. *Nature*, 561(7724): 538.

Asner, G.P. and Alencar, A., 2010. Drought impacts on the Amazon forest: the remote sensing perspective. *New phytologist*, 187(3): 569-578.

Badeck, F.W. et al., 2004. Responses of spring phenology to climate change. *New Phytologist*, 162(2): 295-309.

Banimahd, S.A. and Khalili, D., 2013. Factors influencing Markov chains predictability characteristics, utilizing SPI, RDI, EDI and SPEI drought indices in different climatic zones. *Water Resources Management*, 27(11): 3911-3928.

Bhuiyan, C., Singh, R. and Kogan, F.N., 2006. Monitoring drought dynamics in the Aravalli region (India) using different indices based on ground and remote sensing data. *International Journal of Applied Earth Observation and Geoinformation*, 8(4): 289-302.

Breiman, L., 1996. Out-of-bag estimation. Citeseer.

Breiman, L., 2001. Random forests. *Machine Learning*, 45(1): 5-32.

Dai, A., 2011. Drought under global warming: a review. *Wiley Interdisciplinary Reviews: Climate Change*, 2(1): 45-65.

Damm, A. et al., 2010. Remote sensing of sun-induced fluorescence to improve modeling of diurnal courses of gross primary production. . *Global Change Biology*, 16(1): 171-186.

Di, L., Rundquist, D.C. and Han, L., 1994. Modelling relationships between NDVI and precipitation during vegetative growth cycles. *International Journal of Remote Sensing*, 15(10): 2121-2136.

Dobrowski, S., Pushnik, J., Zarco-Tejada, P. and Ustin, S., 2005. Simple reflectance indices track heat and water stress-induced changes in steady-state chlorophyll fluorescence at the canopy scale. *Remote Sensing of Environment*, 97(3): 403-414.

Duveiller, G. and Cescatti, A., 2016. Spatially downscaling sun-induced chlorophyll fluorescence leads to an improved temporal correlation with gross primary productivity. *Remote Sensing of Environment*, 182: 72-89.

Frankenberg, C. et al., 2011. New global observations of the terrestrial carbon cycle from GOSAT: Patterns of plant fluorescence with gross primary productivity. *Geophysical Research Letters*, 38(17).

Frankenberg, C. et al., 2014. Prospects for chlorophyll fluorescence remote sensing from the Orbiting Carbon Observatory-2. *Remote Sensing of Environment*, 147: 1-12.

Gao, X., Huete, A.R., Ni, W. and Miura, T., 2000. Optical–biophysical relationships of vegetation spectra without background contamination. *Remote Sensing of Environment*, 74(3): 609-620.

Griffin, D. and Anchukaitis, K.J., 2014. How unusual is the 2012–2014 California drought? *Geophysical Research Letters*, 41(24): 9017-9023.

Griggs, D.J. and Noguer, M., 2002. Climate change 2001: the scientific basis. Contribution of working group I to the third assessment report of the intergovernmental panel on climate change. *Weather*, 57(8): 267-269.

Guan, K. et al., 2016. Improving the monitoring of crop productivity using spaceborne solar-induced fluorescence. *Global Change Biology*, 22(2): 716-726.

Guanter, L. et al., 2007. Estimation of solar-induced vegetation fluorescence from space measurements. *Geophysical Research Letters*, 34(8).

Guanter, L. et al., 2012. Retrieval and global assessment of terrestrial chlorophyll fluorescence from GOSAT space measurements. *Remote Sensing of Environment*, 121: 236-251.

Guanter, L., Köhler, P., Walther, S. and Zhang, Y., 2016. Recent advances in global monitoring of terrestrial sun-induced chlorophyll fluorescence, Geoscience and Remote Sensing Symposium (IGARSS), 2016 IEEE International. IEEE, pp. 1714-1716.

Guanter, L. et al., 2014b. Reply to Magnani et al.: Linking large-scale chlorophyll fluorescence observations with cropland gross primary production. *Proceedings of the National Academy of Sciences*, 111(25): E2511-E2511.

Hao, C., Zhang, J. and Yao, F., 2015. Combination of multi-sensor remote sensing data for drought monitoring over Southwest China. *International Journal of Applied Earth Observation and Geoinformation*, 35: 270-283.

Hao, Z., AghaKouchak, A., Nakhjiri, N. and Farahmand, A., 2014. Global integrated drought monitoring and prediction system. *Scientific Data*, 1: 140001.

Hao, Z. and Singh, V.P., 2015. Drought characterization from a multivariate perspective: A review. *Journal of Hydrology*, 527: 668-678.

Hao, Z., Yuan, X., Xia, Y., Hao, F. and Singh, V.P., 2017a. An overview of drought monitoring and prediction systems at regional and global scales. *Bulletin of the American Meteorological Society*, 98(9): 1879-1896.

Hayes, M.J., 2000. Revisiting the SPI: clarifying the process.

Hayes, M.J., Svoboda, M.D., Wilhite, D.A. and Vanyarkho, O.V., 1999a. Monitoring the 1996 drought using the standardized precipitation index. *Bulletin of the American Meteorological Society*, 80(3): 429-438.

Homer, C., Huang, C., Yang, L., Wylie, B. and Coan, M., 2004. Development of a 2001 national land-cover database for the United States. *Photogrammetric Engineering & Remote Sensing*, 70(7): 829-840.

Ishwaran, H., 2007. Variable importance in binary regression trees and forests. *Electronic Journal of Statistics*, 1: 519-537.

Ji, L. and Peters, A.J., 2003. Assessing vegetation response to drought in the northern Great Plains using vegetation and drought indices. *Remote Sensing of Environment*, 87(1): 85-98.

Jiao, W., Tian, C., Chang, Q., Novick, K.A. and Wang, L., 2019. A new multi-sensor integrated index for drought monitoring. *Agricultural and Forest Meteorology*, 268: 74-85.

Jiao, W. et al., 2016. Evaluating an enhanced vegetation condition index based on VIUPD for drought monitoring in the continental United States. *Remote Sensing*, 8(3): 224.

Joiner, J. et al., 2013. Global monitoring of terrestrial chlorophyll fluorescence from moderate spectral resolution near-infrared satellite measurements: methodology, simulations, and application to GOME-2. *Atmospheric Measurement Techniques*, 6(2): 2803-2823.

Joiner, J., Yoshida, Y., Vasilkov, A. and Middleton, E., 2011. First observations of global and seasonal terrestrial chlorophyll fluorescence from space. *Biogeosciences*, 8(3): 637-651.

Karnieli, A. et al., 2006. Comments on the use of the vegetation health index over Mongolia. *International Journal of Remote Sensing*, 27(10): 2017-2024.

Keeley, J.E., Safford, H., Fotheringham, C., Franklin, J. and Moritz, M., 2009. The 2007 southern California wildfires: lessons in complexity. *Journal of Forestry*, 107(6): 287-296.

Kogan, F., 1995a. Application of vegetation index and brightness temperature for drought detection. *Advances in Space Research*, 15(11): 91-100.

Kogan, F.N., 1997. Global drought watch from space. *Bulletin of the American Meteorological Society*, 78(4): 621-636.

Köhler, P. et al., 2018. Global Retrievals of Solar-Induced Chlorophyll Fluorescence With TROPOMI: First Results and Intersensor Comparison to OCO-2. *Geophysical Research Letters*, 45(19): 10,456-10,463.

Köhler, P., Guanter, L. and Joiner, J., 2015. A linear method for the retrieval of sun-induced chlorophyll fluorescence from GOME-2 and SCIAMACHY data. *Atmospheric Measurement Techniques*, 8(6): 2589-2608.

Liu, L. and Cheng, Z., 2010. Detection of vegetation light-use efficiency based on solar-induced chlorophyll fluorescence separated from canopy radiance spectrum. *IEEE Journal of Selected Topics in Applied Earth Observations and Remote Sensing*, 3(3): 306-312.

Liu, L. et al., 2018. Evaluating the utility of solar-induced chlorophyll fluorescence for drought monitoring by comparison with NDVI derived from wheat canopy. *Science of The Total Environment*, 625: 1208-1217.

Liu, L. et al., 2018. Relationship of root zone soil moisture with solar-induced chlorophyll fluorescence and vegetation indices in winter wheat: A comparative study based on continuous ground-measurements. *Ecological Indicators*, 90: 9-17.

Liu, W. and Kogan, F., 1996. Monitoring regional drought using the vegetation condition index. *International Journal of Remote Sensing*, 17(14): 2761-2782.

McKee, T.B., Doesken, N.J. and Kleist, J., 1993. The relationship of drought frequency and duration to time scales, Proceedings of the 8th Conference on Applied Climatology. American Meteorological Society Boston, MA, pp. 179-183.

Meroni, M. et al., 2009. Remote sensing of solar-induced chlorophyll fluorescence: Review of methods and applications. *Remote Sensing of Environment*, 113(10): 2037-2051.

Mishra, A.K. and Singh, V.P., 2010. A review of drought concepts. *Journal of Hydrology*, 391(1): 202-216.

Mu, Q., Heinsch, F.A., Zhao, M. and Running, S.W., 2007. Development of a global evapotranspiration algorithm based on MODIS and global meteorology data. *Remote Sensing of Environment*, 111(4): 519-536.

Myneni, R.B., Ross, J. and Asrar, G., 1989. A review on the theory of photon transport in leaf canopies. *Agricultural and Forest Meteorology*, 45(1-2): 1-153.

Neitsch, S.L., Arnold, J.G., Kiniry, J.R. and Williams, J.R., 2011. Soil and water assessment tool theoretical documentation version 2009, Texas Water Resources Institute.

Nicholson, S. and Farrar, T., 1994. The influence of soil type on the relationships between NDVI, rainfall, and soil moisture in semiarid Botswana. I. NDVI response to rainfall. *Remote Sensing of Environment*, 50(2): 107-120.

Nielsen-Gammon, J., 2011. The 2011 Texas drought: a briefing packet for the Texas Legislature.

Palmer, W.C., 1965. Meteorological drought, 30. US Department of Commerce, Weather Bureau.

Pérez‐Priego, O. et al., 2015. Sun-induced chlorophyll fluorescence and photochemical reflectance index improve remote-sensing gross primary production estimates under varying nutrient availability in a typical Mediterranean savanna ecosystem. *Biogeosciences*, 12(21): 6351-6367.

Piao, S. et al., 2003. Interannual variations of monthly and seasonal normalized difference vegetation index (NDVI) in China from 1982 to 1999. *Journal of Geophysical Research: Atmospheres*, 108(D14).

Porcar-Castell, A. et al., 2014. Linking chlorophyll a fluorescence to photosynthesis for remote sensing applications: mechanisms and challenges. *Journal of Experimental Botany*, 65(15): 4065-4095.

Quiring, S.M. and Ganesh, S., 2010. Evaluating the utility of the Vegetation Condition Index (VCI) for monitoring meteorological drought in Texas. *Agricultural and Forest Meteorology*, 150(3): 330-339.

Rajsekhar, D., Singh, V.P. and Mishra, A.K., 2015a. Multivariate drought index: An information theory based approach for integrated drought assessment. *Journal of Hydrology*, 526: 164-182.

Rhee, J., Im, J. and Carbone, G.J., 2010. Monitoring agricultural drought for arid and humid regions using multi-sensor remote sensing data. *Remote Sensing of Environment*, 114(12): 2875-2887.

Shahid, S., 2010. Rainfall variability and the trends of wet and dry periods in Bangladesh. *International Journal of Climatology*, 30(15): 2299-2313.

Sheffield, J., Wood, E.F. and Roderick, M.L., 2012. Little change in global drought over the past 60 years. *Nature*, 491(7424): 435-438.

Singh, R.P., Roy, S. and Kogan, F., 2003. Vegetation and temperature condition indices from NOAA AVHRR data for drought monitoring over India. *International Journal of Remote Sensing*, 24(22): 4393-4402.

Song, L. et al., 2018b. Satellite sun-induced chlorophyll fluorescence detects early response of winter wheat to heat stress in the Indian Indo-Gangetic Plains. *Global change biology*.

Sun, Y. et al., 2018. Overview of Solar-Induced chlorophyll Fluorescence (SIF) from the Orbiting Carbon Observatory-2: Retrieval, cross-mission comparison, and global monitoring for GPP. *Remote Sensing of Environment*, 209: 808-823.

Sun, Y. et al., 2015. Drought onset mechanisms revealed by satellite solar-induced chlorophyll fluorescence: Insights from two contrasting extreme events. *Journal of Geophysical Research: Biogeosciences*, 120(11): 2427-2440.

Tate, E. and Gustard, A., 2000. Drought definition: a hydrological perspective, Drought and drought mitigation in Europe. Springer, pp. 23-48.

Tucker, C.J. and Choudhury, B.J., 1987. Satellite remote sensing of drought conditions. *Remote Sensing of Environment*, 23(2): 243-251.

Unganai, L.S. and Kogan, F.N., 1998. Drought monitoring and corn yield estimation in Southern Africa from AVHRR data. *Remote Sensing of Environment*, 63(3): 219-232.

Van Loon, A.F. et al., 2016b. Drought in a human-modified world: reframing drought definitions, understanding, and analysis approaches. *Hydrology and Earth System Sciences*, 20(9): 3631.

Vicente-Serrano, S.M., 2007. Evaluating the impact of drought using remote sensing in a Mediterranean, semi-arid region. *Natural Hazards*, 40(1): 173-208.

Vicente-Serrano, S.M., Beguería, S. and López-Moreno, J.I., 2010. A multiscalar drought index sensitive to global warming: the standardized precipitation evapotranspiration index. *Journal of Climate*, 23(7): 1696-1718.

Vicente-Serrano, S.M. et al., 2013. Response of vegetation to drought time-scales across global land biomes. *Proceedings of the National Academy of Sciences*, 110(1): 52-57.

Wang, H. et al., 2018. Response of ecosystem productivity to dry/wet conditions indicated by different drought indices. *Science of The Total Environment*, 612: 347-357.

Wang, H., Rogers, J.C. and Munroe, D.K., 2015. Commonly used drought indices as indicators of soil moisture in China. *Journal of Hydrometeorology*, 16(3): 1397-1408.

Wang, L. et al., 2012b. Dryland ecohydrology and climate change: critical issues and technical advances. *Hydrology and Earth System Sciences*, 16(8): 2585.

Wang, S. et al., 2016. Monitoring and assessing the 2012 drought in the great plains: Analyzing satellite-retrieved solar-induced chlorophyll fluorescence, drought indices, and gross primary production. *Remote Sensing*, 8(2): 61.

Williams, A.P. et al., 2015. Contribution of anthropogenic warming to California drought during 2012–2014. *Geophysical Research Letters*, 42(16): 6819-6828.

Xiao, X. et al., 2004. Satellite-based modeling of gross primary production in an evergreen needleleaf forest. *Remote Sensing of Environment*, 89(4): 519-534.

Yang, X. et al., 2015. Solar-induced chlorophyll fluorescence that correlates with canopy photosynthesis on diurnal and seasonal scales in a temperate deciduous forest. *Geophysical Research Letters*, 42(8): 2977-2987.

Yoshida, Y. et al., 2015. The 2010 Russian drought impact on satellite measurements of solar-induced chlorophyll fluorescence: Insights from modeling and comparisons with parameters derived from satellite reflectances. *Remote Sensing of Environment*, 166: 163-177.

Yu, L., Wen, J., Chang, C.Y., Frankenberg, C. and Sun, Y., 2018. High Resolution Global Contiguous Solar-Induced Chlorophyll Fluorescence (SIF) of Orbiting Carbon Observatory-2 (OCO-2). *Geophysical Research Letters*, 0(ja).

Zhang, L., Jiao, W., Zhang, H., Huang, C. and Tong, Q., 2017. Studying drought phenomena in the Continental United States in 2011 and 2012 using various drought indices. *Remote Sensing of Environment*, 190: 96-106.

Zhang, Y., Song, C., Band, L.E., Sun, G. and Li, J., 2017. Reanalysis of global terrestrial vegetation trends from MODIS products: Browning or greening? *Remote Sensing of Environment*, 191: 145-155.

Zhao, H. et al., 2017. Timescale differences between SC-PDSI and SPEI for drought monitoring in China. *Physics and Chemistry of the Earth, Parts A/B/C*, 102: 48-58.

Zhao, M., Heinsch, F.A., Nemani, R.R. and Running, S.W., 2005. Improvements of the MODIS terrestrial gross and net primary production global data set. *Remote Sensing of Environment*, 95(2): 164-176.

Zhou, L. et al., 2012. Comparison of remotely sensed and meteorological data-derived drought indices in mid-eastern China. *International Journal of Remote Sensing*, 33(6): 1755-1779.

# CHAPTER 6 ACCESSING CHANGES IN WATER CONSTRAINT ON GLOBAL VEGETATION PRODUCTIVITY USING MULTI-SENSOR SATELLITE PRODUCTS

## 6.1 Introduction

Water is fundamental for plant growth, and vegetation response to water availability influences water, carbon, and energy exchanges between land and atmosphere(Ciais et al., 2005b; Huang, Xia, et al., 2018; Novick et al., 2016; Porporato et al., 2002). Vegetation growth is expected to become more water constrained in a warmer climate because warming results in an increase in vapor pressure deficit and possible reductions in soil moisture(Huang, Yu, et al., 2016; Jung et al., 2010; Sherwood et al., 2014; Yuan, Zheng, et al., 2019), while the observed global patterns of greening(Fensholt et al., 2012; Lucht et al., 2002; Zhu et al., 2016) and increasing productivity(Fernández-Martínez et al., 2019; Huang, Xia, et al., 2018) may also enhance vegetation water demand. In addition, higher temperature with more frequent extreme hot days(Dannenberg et al., 2019; Piao et al., 2014), stronger radiation(Wild et al., 2005), and land cover/land use changes(Huang, Xia, et al., 2018) may exacerbate water stress impacts(Beer et al., 2010; Fernández-Martínez et al., 2019). Quantifying vegetation response to water availability at large spatial and temporal scales is challenging, as vegetation growth response to water availability is influenced by many interacting factors, including biome type, hydraulic strategy, water use efficiency, and location(Anderegg et al., 2018; Forzieri et al., 2017; Jiao, Wang and McCabe, 2021; Keenan et al., 2013; Vicente-Serrano et al., 2013). Simultaneously, a short-term decrease in rainfall may have both positive and negative effects on vegetation growth at different

locations. For example, although water deficit negatively impacts many ecosystems, for ecosystems subjected to waterlogging or at high latitudes where temperature is a major limiting factor, short-term precipitation deficiency may result in higher temperatures, leading to enhanced vegetation growth(Chen, Werf, et al., 2013; Kreuzwieser et al., 2014; Lobell et al., 2014; Nemani et al., 2003; Saleska et al., 2007).

Recent studies have documented vegetation response to water availability in terms of the negative impact of drought on vegetation productivity(Buermann et al., 2018b; Ciais et al., 2005b; Zhao et al., 2010), the timescale of vegetation response to drought(Vicente-Serrano et al., 2013), and vegetation resilience and recovery from severe drought(Anderegg et al., 2015; Anderegg et al., 2018). Yet, it remains unclear whether the impact of water availability on vegetation growth is changing in a warming climate. While various water deficit impacts have been documented, to our knowledge, a comprehensive global assessment of changes in long-term vegetation response to water constraints using the full satellite record is still missing. This knowledge gap prevents an adequate understanding of vegetation response to the expected intensification of drought frequency, severity, and duration(Cook et al., 2015; Dai, 2013; Field et al., 2012; Milly et al., 2016; Trenberth et al., 2013; Xu et al., 2019), and change in water availability(Konapala et al., 2020). In addition, recent studies have suggested that the strength of the terrestrial carbon sink might be shifting from an increasing to a decreasing trend(Humphrey et al., 2018; Peñuelas et al., 2017; Yuan, Zheng, et al., 2019), likely as a result of water constraints.

In this study, we evaluated long-term trends of vegetation response to water availability over the last three decades in the extra-tropical Northern Hemisphere using a

robust ensemble of water availability indices and multiple indicators of vegetation growth from 1982 to 2015. We used satellite-derived normalized difference vegetation index (NDVI), enhanced vegetation index (EVI), Vegetation optical depth (VOD), solar-induced chlorophyll fluorescence (SIF), and gross primary productivity (GPP) as proxies of vegetation growth; and self-calibrating Palmer drought severity index (scPDSI) and standardized precipitation evapotranspiration index (SPEI) aggregated over a robust range of time-scales as proxies of water availability. Both SPEI and scPDSI are meteorological water availability indices, and high to low values signify relatively wet to dry conditions in a given area as compared to its long-term average. Therefore a year with low SPEI and scPDSI in a wet area may not necessarily cause vegetation water stress, and may still be wetter than a year with high SPEI and scPDSI in a dry region(Vicente-Serrano et al., 2010). The statistical relationship between water availability indices and vegetation growth has been widely applied to examine the response of vegetation growth to water availability(Doughty et al., 2015; Peters et al., 2018; Schwalm, Anderegg, Michalak, Fisher, Biondi, Koch, Litvak, Ogle, Shaw and Wolf, 2017; Vicente-Serrano et al., 2013).

## 6.2 Data and Methods

### 6.2.1 Satellite observation data

The third-generation biweekly Advanced Very High Resolution Radiometer (AVHRR) NDVI (GIMMS-NDVI3g, available at https://ecocast.arc.nasa.gov/data/pub/gimms/3g.v0) data was used in this study as a proxy for vegetation growth between 1982 and 2015. The study period of 1982-2015 was selected to balance the data availability for vegetation growth and water availability

indicators. For example, the SPEI dataset is currently available only to the year 2015. The GIMMS-NDVI3g data have corrections for sensor degradation, cloud cover, inter-sensor differences, solar zenith angle, viewing angle effects, and volcanic aerosols, making them widely used to study the vegetation dynamics under warming climate(Dannenberg et al., 2019; Huang, Xia, et al., 2018). Ku-band Vegetation optical depth (VOD) was selected from 1988-2015. The maximum value composite method was applied to composite daily VOD into monthly datasets, and the cubic resampling method was used to aggregate $0.05^{o}$ spatial resolution into $0.5^{o}$ to match the spatial resolution from climate datasets. Daily Ku-band VOD data(Moesinger et al., 2020) was obtained from https://zenodo.org/record/2575599 #.XzivuMBKipp. Moderate Resolution Imaging Spectroradiometer (MODIS) based EVI and GPP, as well as SIF data derived from discrete OCO-2 SIF and MODIS observations (GOSIF)(Li and Xiao, 2019), were selected from 2000 to 2015 as complementary proxies for vegetation growth and were used here for evaluating the robustness of the observed trends based on NDVI. GOSIF uses a combination of the Orbiting Carbon Observatory-2 (OCO-2) SIF with MODIS version 6 data, which alleviated the issue of sensor degradation. Monthly GOSIF data were obtained from http://data.globalecology.unh.edu/data/GOSIF/. Version 6 of EVI (MOD13A3) and GPP (MOD17A2H) were aggregated to 0.5°×0.5° to match the resolution of meteorological data. In addition, GPP data from 1982 to 2011 based on MODIS GPP algorithm driven by GIMMS FPAR (fraction vegetation absorbed photosynthetically active radiation) and LAI data(Smith et al., 2016) were used to evaluate the robustness of the observed trends using EVI and GPP and to make up for the absence of MODIS-based vegetation growth data before 2000. The maximum value

composite method and the cubic resampling method were used to composite 8-day and bi-weekly data into monthly with 0.5° spatial resolution for the remote sensing based data to match the spatial and temporal resolution of water availability indices and climate data(Dannenberg et al., 2019). The detailed evaluation of MODIS algorithm based GIMMS-GPP from 1982-2011 could be found in Smith et al.(Smith et al., 2016) .

### 6.2.2 Gridded water availability indices

Standardized Precipitation-Evapotranspiration Index (SPEI) and self-calibrating Palmer Drought Severity Index (scPDSI) are widely used as water availability indices to quantify water deficit onset, duration, magnitude, and spatial extent(Anderegg et al., 2015; Anderegg et al., 2018; Huang, Yu, et al., 2016; Milly et al., 2016). The monthly scPDSI, calculated based on balance model of precipitation, temperature, and potential evapotranspiration (PET)(Abatzoglou et al., 2018; Palmer, 1965) were provided by the Research Data Archive at the National Center for Atmospheric Research (NCAR). The monthly scPDSI was aggregated to 0.5°×0.5° using cubic resampling method. Monthly SPEI was calculated based on historical probability distribution of precipitation minus PET(Vicente-Serrano et al., 2010). Both SPEI and scPDSI used Penman-Monteith method to calculate PET. The main difference between SPEI and scPDSI is that SPEI provides multiple time-scales and scPDSI is with fixed time-scale(Vicente-Serrano et al., 2010). The 0.5° with 1-24 time-scales of SPEI were selected in this study to characterize the cumulative water balance conditions from the previous 1-24 months(Vicente-Serrano et al., 2010). 1-24 month time-scale of SPEIs were obtained from http://digital.csic.es/handle/10261/153475, and scPDSI from 1982 to 2014 are available at https://rda.ucar.edu/datasets/ds299.0/. Aridity index (AI) is defined as the ratio of mean

annual rainfall to mean annual potential evapotranspiration. Aridity index was used identify arid (AI<0.2), semi-arid ($0.2 \leq AI \leq 0.5$), sub-humid ($0.5 \leq AI \leq 0.65$), and humid ($AI \geq 0.65$) regions(Trabucco et al., 2009; Zomer et al., 2008). The spatial AI dataset was obtained from https://cgiarcsi.community/data/global-aridity-and-pet-database/. The 30 arc seconds spatial resolution was aggregated to 0.5°×0.5° using cubic resampling method to match the resolution of water availability indices and meteorological data. In addition to SPEI and scPDSI, Essential Climate Variable (ESA) soil moisture data (version 05.2)(Dorigo et al., 2017; Gruber, Scanlon, Schalie, et al., 2019; Wagner et al., 2012) (www.esa-soilmoisture-cci.org/) was used as an additional water availability indicator to evaluate the water constraint and water surplus trends. The daily ESA soil moisture data was aggregated into monthly using monthly mean values.

### 6.2.3 Forcing datasets

Monthly meteorological (including air temperature, precipitation, incoming shortwave radiation) and atmospheric $CO_2$ data with spatial resolution of 0.5°×0.5° were used to quantify the attributions of the observed relationships between vegetation growth and water availability indices from 1982 to 2015. Monthly air temperature and precipitation data with a spatial resolution of 0.5° × 0.5° were obtained from Climate Research Unit (CRU) at the University of East Anglia (CRU TS 3.23)(Harris et al., 2014). The shortwave radiation data was obtained from the Terrestrial Hydrology Research Group at Princeton University(Sheffield et al., 2006) (http://hydrology.princeton.edu/data/pgf/v2/0.5deg/monthly/).

### 6.3.4 Trend analyses of vegetation and water availability relationships

To examine the general change of vegetation growth responses to water availability, we conducted the analyses of the spatiotemporal relationship between the growing season (April to October) NDVI anomaly and the two water availability indices (SPEI03 and scPDSI) for each grid cell over the Northern Hemisphere from 1982-2015. SPEI03 represents 3-month Standardized Precipitation-Evapotranspiration Index. NDVI anomaly was used to remove the effect of seasonality, and we calculated the NDVI anomaly based on z-score of NDVI using the formula of $A_{j,i} = (NDVI_{j,i} - \overline{NDVI_j})/\sigma$, where $A_{j,i}$ denotes NDVI anomaly for the month j in year i, $\overline{NDVI_j}$ denotes the averaged NDVI of month j over 1982-2015; $\sigma$ stands for the standard deviation of NDVI for month j over 1982–2015. Spearman rank correlation coefficients (r-values) between NDVI anomaly and the two water availability indices ($R_{NDVI\text{-}SPEI}$ and $R_{NDVI\text{-}scPDSI}$) were used to represent the NDVI and SPEI (or scPDSI) relationship. Grid cells with significant positive and negative correlations ($p<0.05$) between vegetation indicators and water availability indices were defined as grid cells associated with water deficit and water surplus, respectively. The ratio between the sum of all the grid cells associated with water deficit and total grid cells was defined as the percentage area associated with water deficit across the Northern Hemisphere each year. The same approach was used to calculate the percentage area associated with water surplus across the Northern Hemisphere each year. Given that the time-scales at which different biome types respond to water availability may differ noticeably(Anderegg et al., 2018), in addition to SPEI03, we further estimated the correlations between NDVI anomaly and SPEI separately for 1 to 24 month time-scales.

To quantify the spatiotemporal dynamics of water deficit and water surplus regions over the last three decades, the trends of correlation coefficients between vegetation growth indicators and water availability indices of 5-year moving window for each grid cell were analyzed using linear and Mann-Kendall trend test (e.g., Figure 6.2a and b). We used 5-year moving window in our trends analysis in this study to smooth out time series fluctuations and highlight trends. Ten-year and 15-year moving window also used in our study to evaluate the robustness of the 5-year moving window trend analysis. A longer the moving window resulted in less total time series points and a reduction in fluctuations from time point to time point, which helped to highlight any potential long-term trend. We focus our presentation of the results on the five-year moving window analysis since it maximized the number of time series points while still consistently highlighting any emergent long-term trends in the data. To analyze the changes in areas associated with water deficit/water surplus across the Northern Hemisphere, the trend of percentage area associated with water deficit/water surplus was analyzed with a 5-year moving window using linear and Mann-Kendall trend analysis (e.g., Figure 6.2c and d). To evaluate the robustness of the relationships between NDVI and the two water availability indices, we used the same method to analyze the relationships between VOD, SIF, EVI, and GPP and the two water availability indices across the Northern Hemisphere (e.g., Figure S6.6). Temporal consistency analysis based on multiple independent satellite observations imply that the observed changes in vegetation water deficit and water surplus responses were not primarily caused by inadequate corrections of sensors for sensor aging and sensor shift(Tian et al., 2016). To make sure that the trends of observed productivity-moisture correlations were not caused by long-term

NVDI trends, we repeated the same analyses of $R_{NDVI\text{-}SPEI03}$ and $R_{NDVI\text{-}scPDSI}$ on detrended NDVI time series, using both linear and nonlinear detrending methods . For the linear detrending method, we first tested the linear trend significance for each pixel from 1982-2015 and then removed the slope of any significant increasing or decreasing trend in each pixel. For non-linear detrend method, we extracted the non-linear trend using interannual moving average method. The non-linear trend was extracted using the decompose function in R. We also find that the drought legacy effect (i.e., reduced vegetation growth and incomplete recovery after extreme drought events)(Frank et al., 2015; Reichstein et al., 2013) is unlikely to play a dominant role in influencing the trend of vegetation response to water availability since we found similar trends in NDVI responses to 1 month SPEI to 24 months SPEI (Figure S6.7). Nevertheless, multiple uncertainties may affect the understanding of the water constraint changes on vegetation in our study. These may include uncertainties of water availability indices at high latitudes, uncertainties of vegetation growth indicators due to snow and/or cloud contamination, and uncertainties due to unaccounted for insect and fire disturbances(Goetz et al., 2005). However, because we found multiple lines of evidence of increasing vegetation water constraint, we do not expect these uncertainties to affect our key findings.

To further test the vegetation water constraint trends in addition to spatiotemporal vegetation-moisture correlations, we examined the temporal trend of NDVI anomalies under drought (SPEI03 < -1.28 and scPDSI < -1). To examine the drought impacts on vegetation while minimize impacts from other confounding factors such as $CO_2$ fertilization and lengthening of the growing season, we used both linear (removing the slope of monthly NDVI for every five years between 1982 and 2015) and nonlinear

(removing the moving average of interannual trend) methods to de-trend NDVI for each grid cell. The de-trended NDVI anomaly was then calculated based on the de-trended z-score of growing-season (April - October) NDVI. We then analyzed the change of de-trended NDVI anomaly under drought conditions. We extracted all the grid cells of de-trended NDVI anomaly that are under drought conditions indicated by 3-month time-scale SPEI (SPEI03) and scPDSI from 1982 - 2015. scPDSI < -1 and SPEI03 < -1.28 were defined as drought conditions(Ciais et al., 2005b).

### 6.3.5 Analysis of vegetation response time to water availability

It has been well documented that climate conditions accumulatively impact vegetation growth and plants have lagged response to climate over a period of time(Tei et al., 2018; Wen et al., 2019; Wu, Zhao, et al., 2015). The concept of drought time-scale of *n* months indicates *n* months of cumulative water balance(McKee et al., 1993; Vicente-Serrano et al., 2010) and significant relationship between NDVI and *n*-month time scale SPEI indicates the existence of a significant relationship between a *n*-month cumulative water balance indicator and vegetation growth(Vicente-Serrano et al., 2013). Accordingly, we defined the minimum SPEI time-scale (in the 1-24 month range) associated with significant positive correlation to NDVI anomaly as the minimum water deficit response time for each grid cell. Similarly, we defined the maximum SPEI time-scale associated with significant negative correlation to NDVI anomaly as the maximum water surplus period for each grid cell. We first extracted the maximum area associated with significant vegetation water deficit by accounting for all the grid cells with significant positive correlation between NDVI anomaly and SPEIs in the subsequent 1- to 24- months. A given grid cell was classified as having vegetation constrained by water scarcity when at

least one of the subsequent 1-24 months exhibited SPEI with a significant positive correlation with NDVI (low SPEI with low NDVI). If in a given grid cell SPEIs had significant positive correlation with NDVI with more than one time lags, the minimum time-lag associated with significant positive correlation was used. Similarly, we extracted the largest areas associated with significant water surplus by accounting for all the grid cells with significant negative correlation between NDVI anomaly and SPEIs in the subsequent 1- to 24- months. A given grid cell was classified as having vegetation affected by water surplus when at least one time-lag exhibited a significant negative correlation between SPEI and subsequent NDVI (low SPEI with high NDVI). If more than one time-lag exhibited a significant negative correlation between SPEIs and NDVI for a given grid cell, the maximum time-lag associated with a significant negative correlation was used. We then analyzed the trends of minimum water deficit response time and maximum water surplus period separately for each grid cell based on a 5-year moving window. The linear trend test was applied for each grid cell over the period of 1982-2015 to examine the significance ($p<0.05$) of trend for vegetation response time to water availability. Since we separately examined the change of water deficit and water surplus regions, a grid with both positive and negative correlation did not affect our analysis.

### 6.3.6 Attribution analysis

The contributions of meteorological factors (mean annual air temperature, precipitation, and shortwave radiation), and atmospheric $CO_2$ to the observed trends of vegetation growth and water availability relationships were assessed using partial regression models. We fitted full models for r-values of the correlations between NDVI

anomaly and water availability indices as a function of mean growing season air temperature, mean growing season precipitation, mean growing season shortwave radiation, and atmospheric $CO_2$ of each five-year moving window for each grid cell. We used the p-value ($p<0.05$) of multivariate regression models to examine whether these factors are statistically contributed to the changes of correlations between NDVI anomaly and water availability indices ($R_{NDVI\text{-}SPEI}$ and $R_{NDVI\text{-}scPDSI}$). To determine the most important contributor of the $R_{NDVI\text{-}SPEI}$ and $R_{NDVI\text{-}scPDSI}$ temporal dynamics, we ranked these factors based on the absolute value of partial correlation coefficients of each factor. This method was applied for every grid cell of the study region to extract the most important contributor of the $R_{NDVI\text{-}SPEI}$ and $R_{NDVI\text{-}scPDSI}$ temporal dynamics based on the spearman partial correlation coefficient. To evaluate the robustness of the attribution analysis based on partial regression models, we also used Lindeman, Merenda and Gold (lmg) relative importance algorithm(Grömping, 2006) to test the relative importance of the meteorological factors and the atmospheric $CO_2$ in explaining the variance of $R_{NDVI\text{-}SPEI}$ and $R_{NDVI\text{-}scPDSI}$. The algorithm was based on variance decomposition for multiple linear regression models; the relative importance of each factor was calculated based on variance of $R_{NDVI\text{-}SPEI}$ and $R_{NDVI\text{-}scPDSI}$ they explained. The relative importance was performed with the 'relaimpo' package (Grömping, 2006) in R. This method was applied to every grid cell of the study region.

**6.4 Results and discussion**

Multiple lines of evidence show a markedly increasing water constraint on extratropical Northern Hemisphere vegetation growth over the last three decades, as evidenced by the expansion of water-deficit regions and the shrinking of water surplus

areas over the last three decades. The spatiotemporal correlations, $R_{NDVI\text{-}SPEI03}$ and $R_{NDVI\text{-}scPDSI}$, indicated that most water deficit areas are located in temperate regions between 30° N and 50° N, while most water surplus regions are located in high latitude boreal regions above 50° N (Figure 6.2a and b). This pattern is consistent with the fact that high-latitude boreal regions are not water limited but energy limited and short-term precipitation deficiency may result in higher solar radiation and temperature (and in some areas less water logging), leading to enhanced vegetation growth(Nemani et al., 2003). We separately analyzed the trends for regions associated with water deficit and water surplus over the 1982–2015 period, and found remarkably divergent trends with a significant expansion of water deficit regions and a contraction of water surplus regions (Figure 6.2c and d). The results were consistent when using either $R_{NDVI\text{-}SPEI03}$ or $R_{NDVI\text{-}scPDSI}$ (Figure 6. 2c and d).

To evaluate the robustness of our analysis, we used different moving windows, tested the impacts of long-term NDVI trends, tested the trends in sub-periods of the growing season, examined the croplands separately, used different vegetation growth indicators, used water availability indicator of different time scales, and used a different water availability indicator (soil moisture)to re-conduct our spatial-temporal analysis. In addition to results based on a 5-year moving window (Figure 6.2), we used 10-year and 15-year moving windows to evaluate the trends. The spatiotemporal trends in $R_{NDVI\text{-}SPEI03}$ and $R_{NDVI\text{-}scPDSI}$ obtained using the 10-year and 15-year moving windows (Figure S6.2) showed great consistency with those from the 5-year moving window analysis (Figure 6.2 a-d). To examine whether the observed trends of productivity-moisture correlations were caused by the long-term NVDI trend, we detrended NVDI using both linear and

nonlinear (moving average) methods and re-conducted our analyses on spatiotemporal trends of $R_{NDVI\text{-}SPEI03}$ and $R_{NDVI\text{-}scPDSI}$. The results (Figure S6.3) showed great consistency with those from non-detrend analysis (Figure 6.2 a-d), indicating that the observed trends of productivity-moisture correlations were not likely caused by the long-term NVDI trend. To examine whether the shrinking of water surplus and the increasing water deficit trends occurred in different sub-periods of the growing season, we examined the spatiotemporal productivity-moisture relationship for three sub-periods: April-June, June-August, and August-October. The temporal trends of significant changes in percentage areas associated with water deficit and water surplus responses for these three sub-periods (Figure S6.4) show that the shrinking of water surplus and expansion of water deficit occurred in most of the sub-periods, except for the shrinking water surplus, which is not significant in the April-June period ($p>0.05$ for Blue line trend in Figure S6.4a and d) than in other sub-periods. It is likely because the increasing snowpack melting exacerbated water surplus in the spring. Interestingly, croplands showed increasing water constraint as well, except for irrigated croplands(Zohaib et al., 2020) (which only account for around 11% of all the grid cells in our study area (Figure S6.5),. In addition to NDVI, we also used the VOD from 1988-2015, MODIS EVI, SIF, and GPP from 2000-2015 and GIMMS3g GPP from 1982-2011(Smith et al., 2016) as vegetation growth indicators. Specifically, we evaluated to what extent the changes in the relationship between vegetation growth and water availability indices (SPEI03 and scPDSI) detected using NDVI were also consistently found with these other productivity indicators (i.e., VOD, SIF, EVI, and GPP). Our results showed comparable patterns of the changing correlations across all combinations of vegetation growth indicators and water

availability indices. The trends of $R_{VOD\text{-}SPEI03}$, $R_{VOD\text{-}scPDSI}$, $R_{SIF\text{-}SPEI03}$, $R_{EVI\text{-}SPEI03}$, $R_{GPP\text{-}SPEI03}$, $R_{SIF\text{-}scPDSI}$, $R_{EVI\text{-}scPDSI}$, and $R_{GPP\text{-}scPDSI}$ were comparable to the patterns of $R_{NDVI\text{-}SPEI03}$ and $R_{NDVI\text{-}scPDSI}$ from the 1988-2015, 2000-2015 and 1982-2011 periods (Figure S6.6). To support the the analysis based on 3-month time-scale of SPEI (SPEI03) as water availability indicator, we re-applied the spatiotemporal vegetation-SPEI correlation based on SPEIs at all time-scales ranging from 1 to 24 months (SPEI01-SPEI24) as water availability indicators. The significant negative and positive trends in the correlation between NDVI anomaly and SPEI were confirmed at all time-scales ranging from 1 to 24 months (Figure S6.7). In addition to SPEI and scPDSI, we also used European Space Agency (ESA) Climate Change Initiative (CCI) program based soil moisture as water availability indicator to evaluate the robustness of spatiotemporal trends of $R_{NDVI\text{-}SPEI03}$ and $R_{NDVI\text{-}scPDSI}$. The spatiotemporal relationship between vegetation growth and soil moisture ($R_{NDVI\text{-}SM}$) showed comparable patterns to the ones found using SPEI and scPDSI as water availability indicators (Figure S6.8).

To further support the increasing water constraint analysis based on spatiotemporal vegetation-moisture correlations, we examined the temporal trend of NDVI anomalies under drought conditions (SPEI03 < -1.28 and scPDSI < -1). We isolated drought impacts from other confounding factors such as the $CO_2$ fertilization and seasonality effect, by: 1) de-trending NDVI and calculating the de-trended NDVI z-score for each grid cell; 2) averaging across all de-trended NDVI z-score pixels experiencing drought conditions (SPEI03 < -1.28, scPDSI < -1) for each year; and 3) testing the interannual trend significance of the drought-related, de-trended NDVI z-score time series (see Methods). Using this method, we found a significant decreasing trend in the

drought-related NDVI z-score time series (i.e., increasing drought impact on vegetation growth) over the last three decades. The decreasing NDVI anomalies under drought (Figure S6.9) indicates an increasing drought impacts on vegetation growth, which further supports our finding that the vegetation water constraint is increasing over the last three decades.

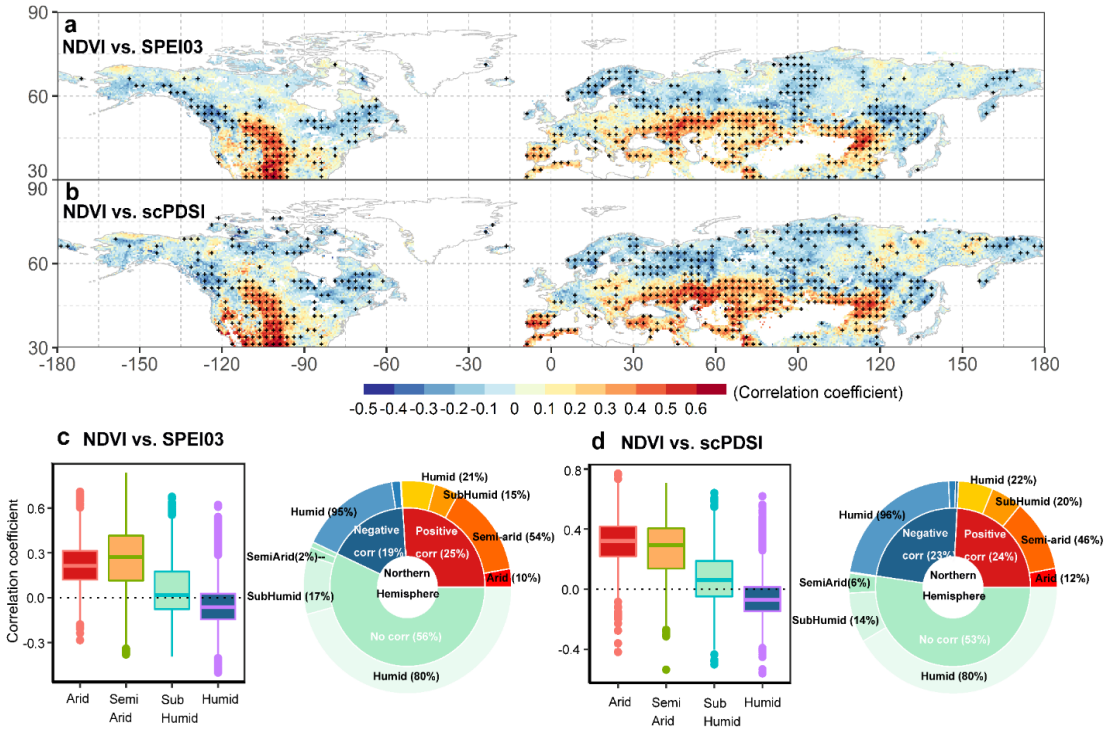


Figure 6.1: Spatial distribution of the correlations between vegetation growth and water availability indices over the last three decades. (a) and (b) show the spatial distribution of correlation coefficients ($R_{NDVI\text{-}SPEI03}$ and $R_{NDVI\text{-}scPDSI}$) between normalized difference vegetation index (NDVI) anomaly and 3-month Standardized Precipitation-Evapotranspiration Index (SPEI03) and Palmer Drought Severity Index (scPDSI) for the entire study period. Black dots indicate significant spearman correlations with $p<0.05$; (c) and (d) are the statistical distributions of $R_{NDVI\text{-}SPEI03}$ and $R_{NDVI\text{-}scPDSI}$ for arid, semi-arid, sub-humid, and humid regions, respectively. The maximum and minimum extents of the

colored boxes indicate the 25$^{th}$ and 75$^{th}$ percentiles and the whiskers represent the 5$^{th}$ and 95$^{th}$ percentiles, respectively.

Second, the mean correlation coefficient (r-value) between NDVI anomaly and SPEI03 across all the grid cells in the Northern Hemisphere has increased steadily over the last three decades, switching from negative to positive for the whole Northern Hemisphere (Figure S6.10). This result indicates that the Northern Hemisphere vegetation growth is becoming increasingly constrained by water deficit, in agreement with our observations that significant positive correlations are typically associated with water deficit while negative correlations are typically observed with water surplus (Figure 6.1). The increase in atmospheric $CO_2$ levels is expected to lead to higher vegetation water use efficiency(Keenan et al., 2013), and increase plant water availability especially in drylands(Abel et al., 2020; Lu, Wang and McCabe, 2016). As such, $CO_2$ increase would induce a more negative correlation between NDVI anomaly and SPEI03 in water deficit regions. However, this study finds a steady increase of r-value between NDVI anomaly and SPEI03 in both water deficit and water surplus regions (Figure S6.11), indicating that $CO_2$ induced water saving is not sufficient to counteract the increasing water constraint.

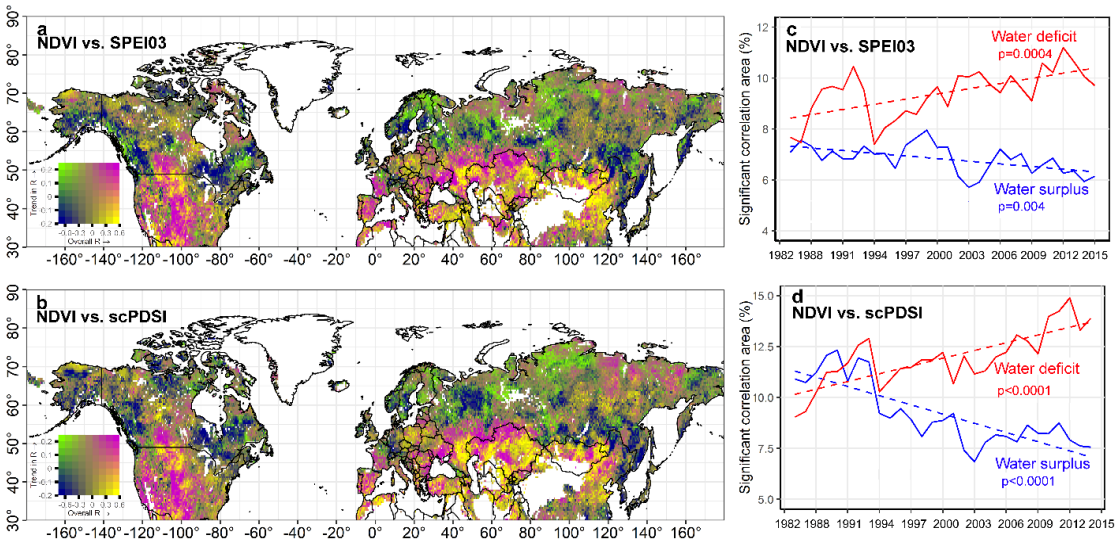


Figure 6.2: Spatiotemporal distribution of the statistically significant correlations between vegetation growth and water availability indices over the last three decades. (a) and (b) show distribution of correlation coefficients ($R_{NDVI\text{-}SPEI03}$ and $R_{NDVI\text{-}scPDSI}$) between normalized difference vegetation index (NDVI) anomaly and 3-month Standardized Precipitation-Evapotranspiration Index (SPEI03) and Palmer Drought Severity Index (scPDSI). The horizontal axis of the color legend is the correlation coefficient between NDVI anomaly and SPEI03 (scPDSI) for the entire study period, the vertical axis of the color legend is the trend of correlation coefficient for the 30 five-year moving windows, no color indicates unvegetated regions. The chartreuse color stands for vegetation water surplus regions where water surplus has been decreasing; navy color indicates vegetation water surplus regions that have been experiencing an increase in water surplus; magenta color is used for water deficit regions that have been seeing an increase in water deficit; and regions colored in yellow are characterized by water deficit and a decrease in water deficit. (c) and (d) show the temporal trends of significant changes in percentage areas associated with water deficit and water surplus responses using five-year moving windows. Blue color stands for the water surplus response and red color for water deficit

response. All the trends of water deficit and water surplus responses are significant in linear trend test and Mann-Kendall trend test ($p < 0.05$). X-axes of (c) and (d) are binned using 5-year moving window to smooth out time series fluctuations and highlight the trends.

Third, a decreasing water deficit response time and shortened water surplus period were observed between the onset of water availability change and their observable impact on vegetation across the Northern Hemisphere. We evaluated the response time and water surplus period based on the statistically significant correlations between NDVI and SPEIs at different time-scales (see Methods). Over the study period, 44% of the Northern Hemisphere regions had NDVI positively correlated to at least one time-scale of SPEIs (Figure 6.3a) and 38% of the Northern Hemisphere regions had NDVI negatively correlated to at least one time-scale of SPEIs ranging from 1 to 24 months (Figure 6.3b). This indicates that 44% of the Northern Hemisphere regions can be considered water deficit region and 38% of the Northern Hemisphere regions can be considered water surplus region for at least one month over the last 30 years. More importantly, our analysis indicates that about 14% of the Northern Hemisphere land area showed a significant decrease in response time, whereas 6% showed a significant increase in response time, resulting in an overall expansion of regions with decreased water deficit response time. In other words, there is an expansion of regions exhibiting a shorter water deficit response time, which corresponds to an increased vegetation susceptibility to stress induced by water scarcity (Figure 6.3c). Similarly, about 6% of the Northern Hemisphere regions showed an increased water surplus period while 15% of the regions showed a decreased water surplus period, resulting in an overall expansion of regions

with decreased water surplus period (i.e., shortened water surplus period) (Figure 6.3d). Based on the previous results, a shorter water surplus duration is expected to favor plant productivity in water surplus regions. The shorter water deficit response time and shortened water surplus period across the Northern Hemisphere are also in support of the notion that vegetation growth in the Northern Hemisphere over the last three decades has become increasingly limited by water scarcity and not by surplus.

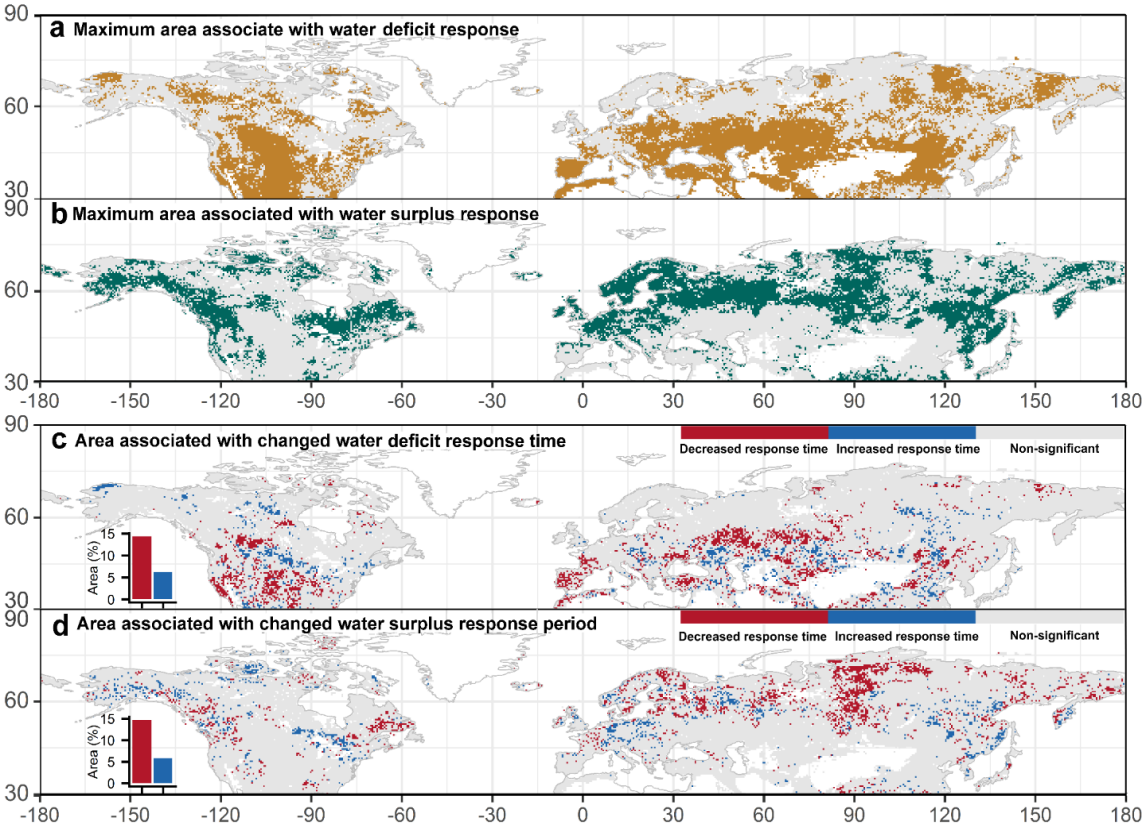


Figure 6.3: Geographical distribution of maximum areas associated with water surplus and water deficit responses as well as the areas associated with changed response times to water surplus and water deficit over the last three decades. (a) presents the maximum area composite of significant positive correlation (water deficit response) between normalized difference vegetation index (NDVI) anomaly and Standardized Precipitation-Evapotranspiration Index (SPEIs) from 1- to 24-month time-scale (gold color); (b) The

maximum area composite of significant negative correlation (water surplus response) between NDVI anomaly and SPEIs from 1- to 24-month time-scale (green color); (c) area associated with change of response time to water deficit; (d) area associated with change of response time to water surplus response. The red and blue bars in (c) and (d) represent the areas of decreased and increased response time, respectively.

We finally evaluated the role of air temperature, precipitation, solar radiation, and atmospheric $CO_2$ in mediating vegetation responses to water availability by carrying out an attribution analysis. We applied a partial correlation algorithm (see methods) to attribute the $R_{NDVI\text{-}SPEI03}$ and $R_{NDVI\text{-}scPDSI}$ to meteorological and atmospheric $CO_2$ drivers (i.e., air temperature, precipitation, solar radiation, and atmospheric $CO_2$). The partial correlation of each factor was calculated for each grid cell (Figure S6.12). The factor associated with the largest absolute value of partial correlation was identified as the dominant factor to the $R_{NDVI\text{-}SPEI03}$ and $R_{NDVI\text{-}scPDSI}$ in that grid cell (Figure 6.4a and b). The area associated with each dominant factor was then calculated for the water deficit and the water surplus regions separately (Figure 6.4a and b). The area fraction associated with each dominant factor was calculated for the water deficit and the water surplus regions, respectively (i.e., the dotted blue and red color regions as identified in Figure 6.1a and b). The partial correlation analysis revealed that $R_{NDVI\text{-}SPEI03}$ and $R_{NDVI\text{-}scPDSI}$ were attributable to precipitation and radiation for a relatively large portion of both the water deficit and water surplus regions (Figure 6.4c and d). Specifically, we found that in water surplus regions (i.e., the dotted blue regions in Figure 6.1a), 29% and 30% of $R_{NDVI\text{-}SPEI03}$ was attributable to precipitation and radiation, respectively (Figure 6. 4c). Similarly, in water deficit regions (i.e., the dotted red color regions in Figure 6.1a), 30%

and 27% of $R_{NDVI\text{-}SPEI03}$ was attributable to precipitation and radiation, respectively (Figure 6.4c). The areas where $R_{NDVI\text{-}scPDSI}$ was explained by precipitation and radiation were consistent with those for $R_{NDVI\text{-}SPEI03}$ (Figure 6.4c and d). It was also found that in water surplus regions 21% and 20% of the $R_{NDVI\text{-}SPEI03}$, and 22% and 22% of the $R_{NDVI\text{-}scPDSI}$ were attributable to temperature and $CO_2$, respectively (Figure 6.4c and d). In water deficit regions, 21% and 21% of $R_{NDVI\text{-}SPEI03}$, and 23% and 21% of $R_{NDVI\text{-}scPDSI}$ were attributable to temperature and $CO_2$, respectively (Figure 6.4c and d). The most likely explanation that the observed productivity-moisture correlations were attributable to a greater extent to precipitation and radiation in both water deficit and water surplus regions is that these two meteorological variables capture water and energy constraints and are closely related at large spatial scales. For example, most of the water deficit regions (e.g., the regions in the south and west of the United States) showed decreasing precipitation and slightly increasing radiation (Figure S6.13a and b); whereas water surplus regions (e.g., southeast United States and multiple regions in Russia) showed increased shortwave radiation and to a lesser extent decreasing precipitation (Figure S6.13a and b). The fact that in some regions temperature is the major attribution factor for the observed correlation patterns is likely due to the increasing frequency in extreme hot days(Piao et al., 2014), which in turn are associated with higher atmospheric water demand(Yuan, Zheng, et al., 2019). In high-latitude water surplus regions, plants affected by cell damage caused by more frequent extreme hot days may consistently experience reduced growth even in drier periods. In water deficit regions higher temperature and solar radiation increase evapotranspiration/potential evapotranspiration making the soils drier, exacerbating vegetation water stress exposure(Oliveira et al., 2011; Wild et al.,

2005). For the regions where $R_{NDVI\text{-}SPEI03}$ and $R_{NDVI\text{-}scPDSI}$ are dominated by $CO_2$, we may be capturing an increase in vegetation water use efficiency under increasing $CO_2$ concentrations(Keenan et al., 2013). To evaluate the robustness of our analysis, we also used a 'relaimpo'(Grömping, 2006) relative importance analysis to quantify the relative contributions of each factor and showed results comparable to those from the partial correlation analysis (Figure S6.14).

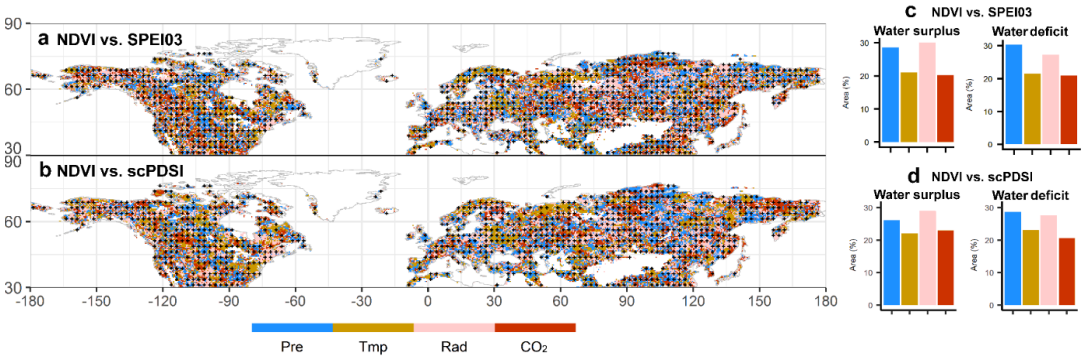


Figure 6.4: Attribution of meteorological factors and atmospheric $CO_2$ to the correlations between normalized difference vegetation index (NDVI) anomaly and water availability indices over the last three decades. (a) and (b) are the spatial distributions of the dominant factor influencing $R_{NDVI\text{-}SPEI03}$ and $R_{NDVI\text{-}scPDSI}$, respectively. The dots show the regions that $R_{NDVI\text{-}SPEI03}$ or $R_{NDVI\text{-}scPDSI}$ variations are significantly explained by precipitation, radiation, temperature and atmospheric $CO_2$. (c) and (d) the percentage areas where the water deficit and water surplus responses can be explained by one of the four dominant factors (i.e., precipitation, temperature, radiation, and $CO_2$). Pre: precipitation; Rad: radiation; Tmp: temperature; $CO_2$: atmospheric $CO_2$.

These results, which appear to be robust with respect to possible trends induced by sensor aging/shift and other sources of uncertainty such as drought legacy effect and

grid cell contaminations (see Methods), provide multiple lines of evidence for an overall increase of water constraints on extratropical Northern Hemisphere vegetation growth over the last 30+ years. With future warming, regions experiencing water constraints will likely increase, resulting in a reduction in carbon uptake across the extratropical Northern Hemisphere, driving a potential amplifying carbon-climate feedback.

**References**


Abatzoglou, J.T., Dobrowski, S.Z., Parks, S.A. and Hegewisch, K.C., 2018. TerraClimate, a high-resolution global dataset of monthly climate and climatic water balance from 1958–2015. *Scientific Data*, 5: 170191.

Abel, C. et al., 2020. The human–environment nexus and vegetation–rainfall sensitivity in tropical drylands. *Nature Sustainability*: 1-8.

Anderegg, W.R. et al., 2018. Hydraulic diversity of forests regulates ecosystem resilience during drought. *Nature*, 561(7724): 538.

Anderegg, W.R. et al., 2015. Pervasive drought legacies in forest ecosystems and their implications for carbon cycle models. *Science*, 349(6247): 528-532.

Beer, C. et al., 2010. Terrestrial gross carbon dioxide uptake: global distribution and covariation with climate. *Science*, 329(5993): 834-838.

Buermann, W. et al., 2018b. Widespread seasonal compensation effects of spring warming on northern plant productivity. *Nature*, 562(7725): 110.

Chen, T., Werf, G., Jeu, R., Wang, G. and Dolman, A., 2013. A global analysis of the impact of drought on net primary productivity. *Hydrology and Earth System Sciences*, 17(10): 3885.

Ciais, P. et al., 2005b. Europe-wide reduction in primary productivity caused by the heat and drought in 2003. *Nature*, 437(7058): 529.

Cook, B.I., Ault, T.R. and Smerdon, J.E., 2015. Unprecedented 21st century drought risk in the American Southwest and Central Plains. *Science Advances*, 1(1): e1400082.

Dai, A., 2013. Increasing drought under global warming in observations and models. *Nature Climate Change*, 3(1): 52.

Dannenberg, M.P., Wise, E.K. and Smith, W.K., 2019. Reduced tree growth in the semiarid United States due to asymmetric responses to intensifying precipitation extremes. *Science Advances*, 5(10): eaaw0667.

Dorigo, W. et al., 2017. ESA CCI Soil Moisture for improved Earth system understanding: State-of-the art and future directions. *Remote Sensing of Environment*, 203: 185-215.

Doughty, C.E. et al., 2015. Drought impact on forest carbon dynamics and fluxes in Amazonia. *Nature*, 519(7541): 78-82.

Fensholt, R. et al., 2012. Greenness in semi-arid areas across the globe 1981–2007—an Earth Observing Satellite based analysis of trends and drivers. *Remote Sensing of Environment*, 121: 144-158.

Fernández-Martínez, M. et al., 2019. Global trends in carbon sinks and their relationships with $CO_2$ and temperature. *Nature climate change*, 9(1): 73.

Field, C.B., Barros, V., Stocker, T.F. and Dahe, Q., 2012. Managing the risks of extreme events and disasters to advance climate change adaptation: special report of the intergovernmental panel on climate change. Cambridge University Press.

Forzieri, G., Alkama, R., Miralles, D.G. and Cescatti, A., 2017. Satellites reveal contrasting responses of regional climate to the widespread greening of Earth. *Science*, 356(6343): 1180-1184.

Frank, D. et al., 2015. Effects of climate extremes on the terrestrial carbon cycle: concepts, processes and potential future impacts. *Global Change Biology*, 21(8): 2861-2880.

Goetz, S.J., Bunn, A.G., Fiske, G.J. and Houghton, R.A., 2005. Satellite-observed photosynthetic trends across boreal North America associated with climate and fire disturbance. *Proceedings of the National Academy of Sciences*, 102(38): 13521-13525.

Grömping, U., 2006. Relative importance for linear regression in R: the package relaimpo. *Journal of statistical software*, 17(1): 1-27.

Gruber, A., Scanlon, T., Schalie, R.v.d., Wagner, W. and Dorigo, W., 2019. Evolution of the ESA CCI Soil Moisture climate data records and their underlying merging methodology. *Earth System Science Data*, 11(2): 717-739.

Harris, I., Jones, P., Osborn, T. and Lister, D., 2014. Updated high-resolution grids of monthly climatic observations–the CRU TS3. 10 Dataset. *International Journal of Climatology*, 34(3): 623-642.

Huang, J., Yu, H., Guan, X., Wang, G. and Guo, R., 2016. Accelerated dryland expansion under climate change. *Nature Climate Change*, 6(2): 166.

Huang, K. et al., 2018. Enhanced peak growth of global vegetation and its key mechanisms. *Nature Ecology & Evolution*, 2(12): 1897.

Humphrey, V. et al., 2018. Sensitivity of atmospheric $CO_2$ growth rate to observed changes in terrestrial water storage. *Nature*, 560(7720): 628-631.

Jiao, W., Wang, L. and McCabe, M.F., 2021. Multi-sensor remote sensing for drought characterization: current status, opportunities and a roadmap for the future. *Remote Sensing of Environment*, 256: 112313.

Jung, M. et al., 2010. Recent decline in the global land evapotranspiration trend due to limited moisture supply. *Nature*, 467(7318): 951.

Keenan, T.F. et al., 2013. Increase in forest water-use efficiency as atmospheric carbon dioxide concentrations rise. *Nature*, 499(7458): 324.

Konapala, G., Mishra, A.K., Wada, Y. and Mann, M.E., 2020. Climate change will affect global water availability through compounding changes in seasonal precipitation and evaporation. *Nature Communications*, 11(1): 1-10.

Kreuzwieser, J. and Rennenberg, H., 2014. Molecular and physiological responses of trees to waterlogging stress. *Plant, Cell & Environment*, 37(10): 2245-2259.

Li, X. and Xiao, J., 2019. A Global, 0.05-Degree Product of Solar-Induced Chlorophyll Fluorescence Derived from OCO-2, MODIS, and Reanalysis Data. *Remote Sensing*, 11(5): 517.

Lobell, D.B. et al., 2014. Greater sensitivity to drought accompanies maize yield increase in the US Midwest. *Science*, 344(6183): 516-519.

Lu, X., Wang, L. and McCabe, M.F., 2016. Elevated CO2 as a driver of global dryland greening. *Scientific Reports*, 6: 20716.

Lucht, W. et al., 2002. Climatic control of the high-latitude vegetation greening trend and Pinatubo effect. *Science*, 296(5573): 1687-1689.

McKee, T.B., Doesken, N.J. and Kleist, J., 1993. The relationship of drought frequency and duration to time scales, Proceedings of the 8th Conference on Applied Climatology. American Meteorological Society Boston, MA, pp. 179-183.

Milly, P.C. and Dunne, K.A., 2016. Potential evapotranspiration and continental drying. *Nature Climate Change*, 6(10): 946.

Moesinger, L. et al., 2020. The global long-term microwave Vegetation Optical Depth Climate Archive (VODCA). *Earth System Science Data*, 12(1): 177-196.

Nemani, R.R. et al., 2003. Climate-driven increases in global terrestrial net primary production from 1982 to 1999. *Science*, 300(5625): 1560-1563.

Novick, K.A. et al., 2016. The increasing importance of atmospheric demand for ecosystem water and carbon fluxes. *Nature Climate Change*, 6(11): 1023-1027.

Oliveira, P.J., Davin, E.L., Levis, S. and Seneviratne, S.I., 2011. Vegetation-mediated impacts of trends in global radiation on land hydrology: a global sensitivity study. *Global Change Biology*, 17(11): 3453-3467.

Palmer, W.C., 1965. Meteorological drought, 30. US Department of Commerce, Weather Bureau.

Peñuelas, J. et al., 2017. Shifting from a fertilization-dominated to a warming-dominated period. *Nature Ecology & Evolution*, 1(10): 1438-1445.

Peters, W. et al., 2018. Increased water-use efficiency and reduced CO 2 uptake by plants during droughts at a continental scale. *Nature Geoscience*, 11(10): 744.

Piao, S. et al., 2014. Evidence for a weakening relationship between interannual temperature variability and northern vegetation activity. *Nature Communications*, 5: 5018.

Porporato, A., D'odorico, P., Laio, F., Ridolfi, L. and Rodriguez-Iturbe, I., 2002. Ecohydrology of water-controlled ecosystems. *Advances in Water Resources*, 25(8-12): 1335-1348.

Reichstein, M. et al., 2013. Climate extremes and the carbon cycle. *Nature*, 500(7462): 287-295.

Saleska, S.R., Didan, K., Huete, A.R. and Da Rocha, H.R., 2007. Amazon forests green-up during 2005 drought. *Science*, 318(5850): 612-612.

Schwalm, C.R. et al., 2017. Global patterns of drought recovery. *Nature*, 548(7666): 202.

Sheffield, J., Goteti, G. and Wood, E.F., 2006. Development of a 50-year high-resolution global dataset of meteorological forcings for land surface modeling. *Journal of Climate*, 19(13): 3088-3111.

Sherwood, S. and Fu, Q., 2014. A drier future? *Science*, 343(6172): 737-739.

Smith, W.K. et al., 2016. Large divergence of satellite and Earth system model estimates of global terrestrial $CO_2$ fertilization. *Nature Climate Change*, 6(3): 306.

Tei, S. and Sugimoto, A., 2018. Time lag and negative responses of forest greenness and tree growth to warming over circumboreal forests. *Global Change Biology*, 24(9): 4225-4237.

Tian, F. et al., 2016. Remote sensing of vegetation dynamics in drylands: Evaluating vegetation optical depth (VOD) using AVHRR NDVI and in situ green biomass data over West African Sahel. *Remote Sensing of Environment*, 177: 265-276.

Trabucco, A. and Zomer, R.J., 2009. Global aridity index (global-aridity) and global potential evapo-transpiration (global-PET) geospatial database. *CGIAR Consortium for Spatial Information*.

Trenberth, K.E. et al., 2013. Global warming and changes in drought. *Nature Climate Change*, 4: 17.

Vicente-Serrano, S.M., Beguería, S. and López-Moreno, J.I., 2010. A multiscalar drought index sensitive to global warming: the standardized precipitation evapotranspiration index. *Journal of Climate*, 23(7): 1696-1718.

Vicente-Serrano, S.M. et al., 2013. Response of vegetation to drought time-scales across global land biomes. *Proceedings of the National Academy of Sciences*, 110(1): 52-57.

Wagner, W. et al., 2012. Fusion of active and passive microwave observations to create an essential climate variable data record on soil moisture. *ISPRS Annals of the Photogrammetry, Remote Sensing and Spatial Information Sciences (ISPRS Annals)*, 7: 315-321.

Wen, Y. et al., 2019. Cumulative effects of climatic factors on terrestrial vegetation growth. *Journal of Geophysical Research: Biogeosciences*, 124(4): 789-806.

Wild, M. et al., 2005. From dimming to brightening: Decadal changes in solar radiation at Earth's surface. *Science*, 308(5723): 847-850.

Wu, D. et al., 2015. Time-lag effects of global vegetation responses to climate change. *Global Change Biology*, 21(9): 3520-3531.

Xu, C. et al., 2019. Increasing impacts of extreme droughts on vegetation productivity under climate change. *Nature Climate Change*, 9(12): 948-953.

Yuan, W. et al., 2019. Increased atmospheric vapor pressure deficit reduces global vegetation growth. *Science Advances*, 5(8): eaax1396.

Zhao, M. and Running, S.W., 2010. Drought-induced reduction in global terrestrial net primary production from 2000 through 2009. *Science*, 329(5994): 940-943.

Zhu, Z. et al., 2016. Greening of the Earth and its drivers. *Nature climate change*, 6(8): 791-795.

Zohaib, M. and Choi, M., 2020. Satellite-based global-scale irrigation water use and its contemporary trends. *Science of The Total Environment*: 136719.

Zomer, R.J., Trabucco, A., Bossio, D.A. and Verchot, L.V., 2008. Climate change mitigation: A spatial analysis of global land suitability for clean development mechanism afforestation and reforestation. *Agriculture, Ecosystems & Environment*, 126(1-2): 67-80.

# CHAPTER 7 QUANTIFYING THE EFFECTS OF DROUGHT ON NEE, GPP, AND ECOSYSTEM RESPIRATION BY CONSIDERING MULTIPLE DROUGHT DIMENSIONS

## 7.1 Introduction

Drought disturbs terrestrial ecosystems in many ways, including alterations to $CO_2$ exchange and the ecosystem carbon balance (Frank et al., 2015). With the projected future increase of drought frequency and intensity, drought events are more likely to have profound impacts and might contribute to irreversible damages of ecosystem function in a warming climate (Anderegg, 2015; Dai, 2011; Dannenberg et al., 2015; Garcia et al., 2014; Hao et al., 2017b; Seddon et al., 2016; Willis et al., 2018; Zhang et al., 2021). Examining how droughts affect the carbon balance is therefore of great importance and requires a thorough understanding of the responses of various ecosystem carbon flux components to drought (Van der Schrier et al., 2006; Zhao et al., 2010). Gross primary production (GPP), net ecosystem production (NEP), and ecosystem respiration ($R_{ECO}$) are key variables for understanding the mechanisms through which climate change alter the carbon balance of an ecosystem (Ciais et al., 2005b; Piao et al., 2008). Drought impacts the carbon balance by causing the rates of ecosystem production and respiration to fluctuate or by disrupting the coupling between them, which makes the sensitivity of GPP, $R_{ECO}$ and NEP to drought a major source of uncertainty in quantifying ecosystem responses to future climate change (Keenan et al., 2010; Meir et al., 2008b; Schwalm et al., 2010; Shi et al., 2014). Severe drought events could result in unprecedented reductions in primary productivity and ecosystem respiration, shifting terrestrial ecosystems more towards a $CO_2$ source rather than a $CO_2$ sink (Baldocchi, 2008; Ciais et

al., 2005b; Dannenberg et al., 2021; Doughty et al., 2015; Hoover et al., 2016; Jiao, Wang, Smith, et al., 2021; Jump et al., 2017).

However, a holistic understanding of ecosystem responses to drought is still lacking and multiple challenges remain. First, ecosystem responses to drought vary largely between humid and arid ecosystems, due to stark differences in the magnitude of key environmental drivers like soil moisture, which can become extremely low in arid biomes, as well as spatial variability in the plant traits that determine drought resistance and resilience (Chaves et al., 2003; Dai, 2011; McDowell et al., 2008; Valipour, 2016; Vicente-Serrano et al., 2020). Compared with drought studies in drylands, drought assessments in humid regions are more limited (Park et al., 2016; Rhee et al., 2010; Sweet et al., 2017). At the same time, drought responses in humid regions are complicated (Vicente-Serrano et al., 2013), in ways that make it difficult to assess the impact of future, hotter drought events (Vicente-Serrano et al., 2020). For example, for some humid regions where temperature is a major limiting factor, short term meteorological drought may result in higher temperatures, leading to enhanced vegetation growth that obscures other aspects of drought limitation (Jiao, Wang, Smith, et al., 2021; Jiao, Wang and McCabe, 2021; Kreuzwieser et al., 2014; Nemani et al., 2003). Second, drought is not only a multiscale (e.g., temporal, spatial) but also a multidimensional phenomenon (McKee et al., 1993). Each dimension (e.g., intensity, time-scale, and timing) could affect ecosystem function through different mechanisms (Gao et al., 2018; Huang, Wang, et al., 2018; Vicente-Serrano et al., 2013). The dimension of drought intensity is often arbitrarily defined based on values of drought indices that quantify statistical anomalies in meteorological variables (Chen, Werf, et al.,

2013; McKee et al., 1993; Paulo et al., 2012). However, the extent to which a decrease in precipitation translates to a moisture deficit that affects plant function will vary in space and time depending on climate regime. For example, an anomalously low precipitation in a wet place, or during a usually wet month, may not necessarily result in a soil water deficit that limits plant function. Thus, it is important to understand how common metrics describing drought intensity actually relate to observed vegetative responses. Next, the dimension of drought time-scale characterizes the cumulative water balance conditions over a specific time period (McKee et al., 1993; Vicente-Serrano et al., 2010). While longer droughts should generally produce more pronounced ecosystem responses, the relationship between drought time-scale and physiological response can differ from one ecosystem to the next (Vicente-Serrano et al., 2013). The dimension of drought timing has also been highlighted as an important factor in tree ring studies (D'Orangeville et al., 2018a; Huang, Wang, et al., 2018) and precipitation manipulation experiments (Lemoine et al., 2018). A drought that occurs during a physiologically important period, for example earlywood growth in trees, will likely be more damaging than a drought occurring during the dormant season. The lagged impact of drought is another important factor, which has been documented in tree rings (Dannenberg et al., 2019; Dannenberg et al., 2020; Kannenberg et al., 2019), eddy covariance data (Knowles et al., 2020), remote sensing data (Berkelhammer et al., 2017), physiological measurements (Earles et al., 2018), and drought monitoring studies (Chang et al., 2018; Li, Wang, et al., 2020; Waseem et al., 2016). Thus, only considering one or two drought dimensions may not objectively reflect the actual drought impacts. Furthermore, the quantifications of drought impacts are even more complicated by the drought responses from different plant biomes.

For example, previous studies in drylands have found that drought is more damaging for grasslands and croplands than forests, where roots can access deeper and more slowly changing pools of water (Anderegg et al., 2012; Vicente-Serrano et al., 2013; Xu et al., 2018). However, in humid regions, soil moisture is less often limiting, and drought responses are often dominated by responses to atmospheric drought (Novick et al. 2016), which are relatively more similar across plant functional types (Denham et al 2021, Grossiord et al. 2020). Thus, in humid regions, the extent to which biomes differ across multiple drought dimensions is not clear.

Despite the rapid development of drought monitoring (Hu, van Dijk, et al., 2020; Jiao, Tian, et al., 2019; Jiao, Wang, et al., 2019), it is difficult to comprehensively quantify drought across all dimensions using a single metric (Jiao, Tian, et al., 2019; Jiao, Wang and McCabe, 2021; Lloyd-Hughes, 2014). The concept of drought time-scale can incorporate multiple drought dimensions, including duration, frequency and intensity. For short time-scale drought indices, each new month has a large impact on the cumulative water balance of the study period, thus it is relatively easy to have the short time-scale drought indices change quickly from wet to dry values to include more drought events (McKee et al., 1993). The relatively quick switch from wet to dry conditions using short-time scale drought indices can reflect droughts of short durations well. For long time-scale drought indices, each new month has relatively small impact on the cumulative values therefore the long time-scale drought indices change slowly and result in fewer droughts of longer duration (McKee et al., 1993). Yet, the time-scale based metrics still cannot reflect other relevant drought information, such as lagged drought impacts and drought timing.

Third, it remains unclear how well popular drought definitions reflect observed changes in plant growth and productivity in humid regions, where even relatively short drought events can starkly reduce the usually high rates of carbon uptake (Roman et al., 2015; Wolf et al., 2016). Numerous drought indices have been developed to quantify drought based on various aspects of observations (e.g., soil moisture, temperature, vapor pressure deficit (VPD), precipitation, and runoff) (Barnes et al., 2016; Green et al., 2019; Novick et al., 2016; Sulman et al., 2016; Zhang, Jiao, et al., 2017; Zhang, Ficklin, et al., 2019) and using different quantification methods (Ruppert et al., 2015; Slette, Post, et al., 2019). Among all these indices, drought indices defined by meteorological variables, such as Standardized Precipitation Evapotranspiration Index (SPEI), are becoming more widely used. However, there are debates about the application of the indices like SPEI, since they may not directly correspond to the plant water stress, especially in humid regions (Slette, Smith, et al., 2019; Zang et al., 2020). In temperate climates, soil moisture tends to be very high during winter and the shoulder seasons (spring and fall, Roman et al. 2015). Thus, even a very anomalous deficit of soil moisture during these periods that drives a low value of SPEI may not actually be limiting to plant growth. It thus remains unclear how useful indices like SPEI are for describing realized drought impacts in humid regions.

Fourth, despite the general negative effects of extreme drought events on ecosystem carbon exchange, GPP, NEP, and $R_{ECO}$ can have unique responses to drought. For example, Shi et al. (2014) indicated differential effects of extreme drought on production and respiration. Hoover et al. (2016) found that $R_{ECO}$ and GPP responded differently to pulse- and press-droughts. Given the emerging interest in modeling

vegetation response to water availability under warming climate (Konapala et al., 2020; Mankin et al., 2019; Xu et al., 2019; Yang et al., 2019), understanding the relative significance of each drought dimension to the dynamics of GPP, NEP, and $R_{ECO}$ will reduce the uncertainty of an accurate prediction of future vegetation-water-carbon interactions (Heimann et al., 2008; Liu, Ballantyne, et al., 2018).

To address these issues, the goal of this research is to provide a comprehensive assessment of the effects of drought on NEP, GPP and $R_{ECO}$ by considering drought intensity, time scale, timing, lagged effect and biome type across humid regions. In our analyses, various drought dimensions were represented using different time scales of SPEI, and ecosystem level GPP, NEP, and $R_{ECO}$ were based on global FLUXNET eddy-covariance observations from various biome types. We aim to first identify the significant drought dimensions that affect GPP, NEP, and $R_{ECO}$ respectively, and then extract the detailed patterns of how GPP, NEP, and $R_{ECO}$ respond to those significant dimensions in humid regions based on different time scales of SPEI.

## 7.2 Materials and methods

### 7.2.1 GPP, NEE and $R_{ECO}$ datasets

In this work, we used monthly GPP, NEE and $R_{ECO}$ as the response variables to drought. We relied on estimates of these fluxes contained in the FLUXNET2015 Tier 1 dataset (Pastorello et al. 2020) derived from a variable USTAR threshold approach (VUT) for data filtering and gap filling, and the so-called "nighttime" method (i.e., extrapolation of night-time values of ecosystem respiration into the daytime based on respiration-temperature relationships) for flux partitioning. Specific FLUXNET2015 variables used in this analysis were GPP_NT_VUT_MEAN, NEE_VUT_MEAN, and

RECO_NT_VUT_MEAN. The sites covered a wide range of biome types in humid regions with aridity index (AI) > 0.65. Z-score was used to quantify the GPP, NEE and $R_{ECO}$ anomalies of a certain month from a site's historical mean condition. Z-score was defined using the equation of $z = \frac{X_i - \mu}{\sigma}$, where $X_i$ is the GPP, NEE and $R_{ECO}$ for the $i$-th month, $\mu$ and $\sigma$ are the mean and standard deviation of GPP, NEE and $R_{ECO}$ observations of the month $i$ from all the observation years. Since all the sites are from Northern Hemisphere, the growing season months from April to October were used in the study. We evaluated a total of 166 global sites in the FLUXNET Tier 1 dataset, and the 32 sites with more than 7-years observation and experienced drought conditions indicated by Stocker et al. (2018) were selected (Figure 7.1; Table S7.1). In total, 2,558 months of GPP, NEE, $R_{ECO}$ data were used. To maintain a consistent sign with GPP, we converted NEE to net ecosystem production (NEP), where a negative NEP indicates a flux of carbon from the biosphere to the atmosphere (and *vice versa*).

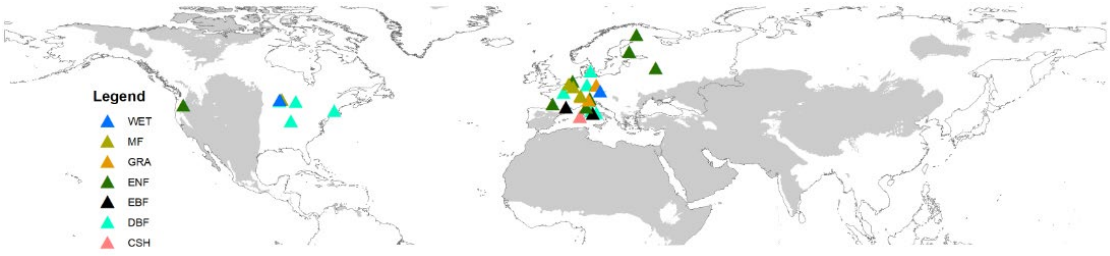


Figure 7.1: Spatial distribution of flux tower sites used in this study (GRA, grasslands; DBF, deciduous broadleaved forest; ENF, evergreen needle leaved forest; EBF, evergreen broadleaved forest; CSH, closed shrubland; WET, wetland; MF, mixed forest). Gray areas in the base map indicate non-humid regions.

### 7.2.2 Drought dimensions

The calculation of SPEIs relies on the probability distributions and length of observations (Stagge et al., 2015; Vicente-Serrano et al., 2010) and most studies suggest calculating monthly SPEI based on time series that are at least 30 years long (Stagge et al., 2015; Tan et al., 2015; Vicente-Serrano et al., 2014). Since the observations of most of the current flux tower sites only cover less than 20 years, we extracted 1-, 3-, 6-, and 9-month time-scales of SPEI for each flux tower sites from gridded SPEI datasets (SPEIbase v.2.6, https://digital.csic.es/handle/10261/202305). SPEIbase v.2.6 was based on the v+ersion 4 of the CRU TS monthly high-resolution gridded multivariate climate dataset which could provide observations back to 1901 (Harris et al., 2020). For the United States and Europe where all of our studied flux towers are located, CRU have extensive observations (Harris et al., 2020) thus make it possible to provide reliable SPEI values for our studied flux tower sites.

The calculation of cumulative drought conditions was based on different time-scales of SPEIs in this study. The arbitrary but typical time-scales of 1, 3, 6, and 9 months SPEIs were used in this study to exemplify cumulative drought conditions ranging from short to long term. Drought intensities were identified based on SPEI values as No drought (SPEI > -1), Moderate drought ( -1.5 < SPEI < -1), Severe drought ( -2 < SPEI < -1.5), and Extreme drought (SPEI < -2) (Wang, Wu, et al., 2014; Wang et al., 2021). Across all the study sites, there are 687 drought months extracted by 1-month SPEI (SPEI-1 < -1), 637 drought months extracted by 3-month SPEI (SPEI-3 < -1), 620 drought months extracted by 6-month SPEI (SPEI-6 < -1), and 614 drought months extracted by 9-month SPEI (SPEI-9 < -1). Drought timing was quantified based on the

calendar timing of a given drought (SPEI < -1) associated with the vegetation growth stages. For each site, we quantified the vegetation growth stages based on mean historical GPP curves (Figure 7.2). To quantify each vegetation growth stage, we first divide GPP curves into two main periods: the 'GPP increasing period' and 'GPP decreasing period' (Figure 7.2). Then we further divided each of these periods based on the percentage of peak GPP (Figure 7.2). We used these phenology stages to quantitatively match the timing of drought occurrence, so site comparisons are more meaningful. The Simultaneous drought condition for each month was identified based on 1-month time-scale of SPEI values. To account for the lagged ecosystem response to changes in water availability and the possible drought legacy effects (Anderegg et al., 2015; Wu, Zhao, et al., 2015), we identified the prior drought condition 1-, 2-, and 3 months before the study period using 1-month time-scale SPEI. We focused on antecedent periods that were 1-, 2-, and 3 months in length because previous work indicates that the vast majority of global ecosystems have a maximum of 3 months lagged response time (Wen et al., 2018; Wen et al., 2019). We termed these antecedent periods Prior_1, Prior_2, Prior_3, respectively.

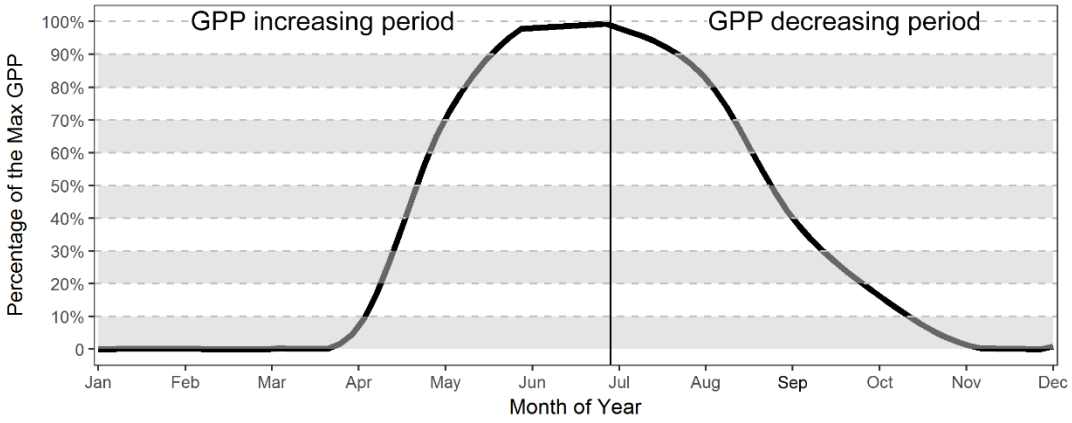


Figure 7.2: The conceptual figure of vegetation growth stages using the percentage of the GPP to the maximum GPP.

### 7.2.3 Statistical analyses

To quantify the effect of drought on GPP, NEP and $R_{ECO}$, we established a series of linear mixed-effect models, investigating the effect of drought intensity, timing and prior drought conditions under different time-scales. Specifically, GPP, NEP and $R_{ECO}$ were used as response variables in different mixed-effect models, and drought intensity, timing, time-scale, and 1-, 2-, 3- month prior drought conditions were explanatory variables. To specify the drought effect on GPP, NEP, and $R_{ECO}$ for different biome types, the biome type was included as the site property variable in the linear mixed model. The model equation takes this form:

$$Y_i = A + \sum_{p=1}^{N_p} B_p Z_{p,i} + B_q W_{q,i} + \epsilon_p + \epsilon_q \quad , \tag{7.1}$$

where A is the overall intercept, Y is the response variable (z-score of GPP, NEP, or $R_{ECO}$, respectively) for site *i*. Z stands for drought dimensions (i.e., drought intensity, timing, and prior drought conditions), p and $B_p$ are the index for each drought dimension and their regression slope for the fixed effects, respectively. $W_q$ indicates biome types

and $B_q$ is the regression slopes for the fixed effects of $W_q$. $\epsilon_p$ and $\epsilon_q$ are random errors associated with Z and W, respectively. Drought timing was categorized as 10% to 100% of peak GPP for GPP decreasing and increasing periods with 10% intervals. Biome types include “grasslands”, “deciduous broadleaved forest”, “evergreen needle leaved forest”, “evergreen broadleaved forest”, “closed shrubland”, “wetland”, and “mixed forest”. In addition, ‘sites’ were incorporated as a random effect term to account for potential site-specific differences. The “prior drought condition” included 1, 2, and 3 months’ mean monthly SPEI-1 values of that month prior to the study period. The linear mixed models, driven by the variables described above, were established under 1-month, 3-month, 6-month, and 9-month time-scale drought conditions indicated by SPEI-1, -3, -6, and -9, respectively, to compare the effect of different drought time-scales on GPP, NEP, and $R_{ECO}$. All the linear mixed-effect models were performed using the nlme-package (Pinheiro, 2010) and lme4 package (Bates et al., 2014) in R 3.4.4 . Followed the protocol for linear mixed model data exploration by Zuur et al. (2010), drought frequency and duration variables were not used in our study to avoid their collinear dependence on drought time-scale. In addition, z-scores of GPP, NEP, and $R_{ECO}$ were used as the response variables to remove the seasonality effects for the normal distributions of GPP, NEP, and $R_{ECO}$ anomalies in the linear mixed models.

## 7.3 Results and Discussion

### 7.3.1 The controlling factors affecting the dynamics of GPP, NEP, and $R_{ECO}$

Drought intensity is not a significant factor in explaining the dynamics of GPP, NEP, and $R_{ECO}$ under 1-month time-scale of drought (Table 7.1, with the effect size of each drought dimensions on GPP, NEP, and $R_{ECO}$ anomalies for 1-, 3-, 6-, and 9-month

drought scenarios shown in Tables S1-S3). Since the 1-month time-scale drought only reflects the drought conditions of the current month, this result indicates that short-term drought does not often induce a productivity decline in humid regions. However, when drought cumulates to longer time-scales (e.g., 6- and 9-month), drought intensity becomes a significant factor impacting the dynamics of GPP, NEP, and $R_{ECO}$ (Table 7.1). Drought timing and prior drought condition were identified as significant factors for both short- and long-term drought. Specifically, GPP and $R_{ECO}$ showed significant sensitivity to drought timing and 1- and 2- month prior drought condition, and drought timing and 1-month prior drought condition, respectively ($p<0.05$ in Table 7.1). NEP showed significant response to the drought timing, identified by 1- and 3-month time-scale of SPEIs ($p<0.05$ in Table 7.1). The overall linear mixed effect model analysis showed that plants generally did not show productivity decline in response to the short-term simultenaous drought conditions (e.g., 1 month time-scale SPEI). However, the ecosystem productivity and respiration showed significant response to long-term cumulative drought, prior drought condition, and drought timing. In other words, when the multidimensionality of drought is considered, the temporally-standardized drought index reflects changes in ecosystem productivity and respiration in response to water stress. Moreover, there was no significant difference in drought response between different biome types. As shown in Figure S7.1, the z-scores of NEP, GPP, and $R_{ECO}$ under long-term droughts (e.g., 6- and 9-month drought) are generally lower than which under short-term drought (e.g., 1- and 3-month drought). However, there is no significant difference among different biome types in response drought ($p>0.05$ for most cases, Figure S7.1). Those patterns are different from the biome type responses in drylands (Xu

et al., 2018). One possible reason is that in humid regions, where soil moisture is often not a limiting factor for plant function (Novick et al. 2016), drought usually does not trigger divergent soil moisture decline that cause significantly different impacts on different biomes.

Table 7.1: Linear mixed model results on the response in GPP, NEP, and $R_{ECO}$ to drought intensity, timing, prior drought condition under 1-, 3-, 6-, and 9-month time-scale drought. Study site was incorporated as a random effect to allow for differences across studies. *indicates statistical significance ($p<0.05$).

| GPP | | | | |
|---|---|---|---|---|
| Variable | 1-month time-scale drought | 3-month time-scale drought | 6-month time-scale drought | 9-month time-scale drought |
| | P-value | P-value | P-value | P-value |
| (Intercept) | 0.008 | 0.2391 | 0.2061 | 0.1245 |
| Intensity | 0.2401 | 0.4931 | <0.001* | <0.001* |
| Timing | 0.002* | 0.0291* | 0.1093 | 0.5947 |
| Prior_1 | <0.001* | 0.0199* | <.0001* | 0.0172* |
| Prior_2 | 0.0264 | 0.1963 | 0.3560 | 0.1965 |
| Prior_3 | 0.2913 | 0.5417 | 0.3600 | 0.1711 |
| Biome Type | 0.553 | 0.0939 | 0.4231 | 0.4219 |

| NEP | | | | |
|---|---|---|---|---|
| Variable | 1-month time-scale drought | 3-month time-scale drought | 6-month time-scale drought | 9-month time-scale drought |
| | P-value | P-value | P-value | P-value |
| (Intercept) | <.0001 | 0.398 | 0.6798 | 0.3849 |
| Intensity | 0.5081 | 0.1345 | 0.0385* | 0.0033* |
| Timing | 0.0325* | 0.035* | 0.4870 | 0.1165 |
| Prior_1 | 0.3059 | 0.1837 | <.0001* | 0.8148 |
| Prior_2 | 0.734 | 0.1594 | 0.5846 | 0.3609 |
| Prior_3 | 0.7343 | 0.365 | 0.2728 | 0.6317 |
| Biome Type | 0.4319 | 0.3618 | 0.7612 | 0.5072 |

| $R_{ECO}$ | | | | |
|---|---|---|---|---|
| Variable | 1-month time-scale drought | 3-month time-scale drought | 6-month time-scale drought | 9-month time-scale drought |
| | P-value | P-value | P-value | P-value |
| (Intercept) | 0.6973 | 0.0049 | 0.1673 | 0.0611 |
| Intensity | 0.9077 | 0.5677 | 0.0371* | 0.0003* |
| Timing | 0.0463* | 0.0455* | 0.0415* | 0.0734 |
| Prior_1 | <0.001* | 0.6611 | 0.0191* | 0.0387* |
| Prior_2 | 0.0346* | 0.8092 | 0.9760 | 0.4962 |

| | | | | |
|---|---|---|---|---|
| Prior_3 | 0.7984 | 0.8102 | 0.7374 | 0.7544 |
| Biome Type | 0.7174 | 0.0751 | 0.2993 | 0.4967 |

### 7.3.2 Decomposed NEP, GPP, and $R_{ECO}$ responses to different drought dimensions

Informed by the significance of the drought factors explaining the dynamics of GPP, NEP, and $R_{ECO}$ in the linear mixed effect models (e.g., Table 7.1), we further examined the specific patterns of how GPP, NEP, and $R_{ECO}$ respond to drought time-scale, intensity, timing and prior drought condition.

#### *7.3.2.1 The response patterns of NEP, GPP, and $R_{ECO}$ to drought time-scales*

Ecosystem production and respiration responded differently to the length of cumulative water deficit. We conducted ANOVA tests to compare the significance of differences for GPP, NEP, and $R_{ECO}$ under different time-scales of drought (Kim, 2014). Our ANOVA results indicate that GPP and NEP consistently declined as the increase of drought time-scale ($p<0.05$) while $R_{ECO}$ did not show significant change. It is also worth noting that under 1-month drought, the median GPP and NEP values were higher than 0, indicating short-term simultaneous meteorological drought generally increases GPP and NEP. One possible explanation for the slight increase of GPP and NEP under simultaneous drought is that the study sites are located in humid regions and plants can access plenty of soil water storage to avoid water stress. In addition, short-term droughts are always accompanied by warm temperature and high solar energy, which are favorable to plant growth to increase photosynthesis in energy limited systems (e.g., humid regions)

(Badeck et al., 2004; Jiao, Chang, et al., 2019; Karnieli et al., 2006). Under longer time-scale droughts, plants succumb to drought stress and reduce photosynthesis, causing GPP and NEP to decrease.

In contrast to the results for GPP and NEP, drought impacts on $R_{ECO}$ were not different for different time-scales. The patterns indicate that $R_{ECO}$ is not sensitive to drought time-scales and the differences in observed NEP response to time scales is mainly caused by GPP decline. It is possible that the relatively low sensitivity of $R_{ECO}$ to drought dimensions may, to an extent, be an artifact of how $R_{ECO}$ is partitioned from the measured net carbon fluxes, which introduces a source of methodological uncertainty (Speckman et al. 2015). The parameters of the temperature-dependent $R_{ECO}$ model used for the nighttime partitioning are updated every two weeks, which should generally allow for the signature of soil moisture deficits to be discerned in the modelled $R_{ECO}$ time series, but cannot capture drought processes occurring over timescales shorter than 14 days, including brief but intense excursions in potential evapotranspiration. Another important consideration is that the response of $R_{ECO}$ to drought often depends on the mineralization of litter and soil C, which are regulated mainly by soil temperature (Shi et al., 2014). Drought time-scale only reflects the cumulative water deficit over a particular period and is not directly related to soil temperature. Nonetheless, the finding that $R_{ECO}$ is less sensitive to drought than GPP has precedent in the literature (Ciais et al., 2005b; Novick et al., 2015; Schwalm et al., 2010; Shi et al., 2014).

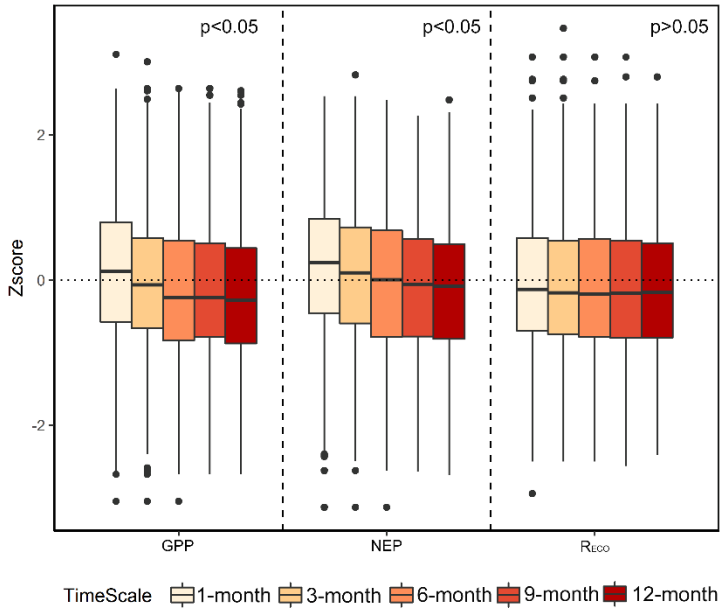


Figure 7.3: Response patterns of NEP, GPP, and $R_{ECO}$ to 1-, 3-, 6-, 9-, and 12-month time-scale of drought (p-value from ANOVA tests were used to test the significance of differences between the groups).

### *7.3.2.2 The response patterns of NEP, GPP, and $R_{ECO}$ to drought intensity and prior drought condition*

Based on the general response patterns of NEP, GPP, and $R_{ECO}$ to drought time-scales, we further decomposed the response patterns of NEP, GPP, and $R_{ECO}$ to drought intensity (Figure 7.4) under various drought time-scales and one-month prior drought condition (Figure 7.5). One-month prior drought impact was selected to indicate the prior drought impact, since the mixed effect model from Table 7.1 indicated one-month prior drought has significant impacts for most cases while 2, and 3 month prior drought generally did not show significant impacts. We found that under the 1- and 3-month time-scales of drought conditions, plants did not show significant decrease of GPP, NEP, and $R_{ECO}$ as the drought intensity increase from no drought to extreme drought ($p > 0.05$,

Figure 7.4a and b). Under 1-month time-scale of drought, GPP actually increased with increasing drought intensity. One possible explanation for the slight increase of GPP and NEP under short-term drought is that the study sites are located in humid regions and plants have access to soil water storage. In addition, short-term droughts are often associated with high solar energy, facilitating vegetation growth in such energy limited ecosystems (Badeck et al., 2004; Jiao, Chang, et al., 2019; Karnieli et al., 2006). When the drought time-scale increased to 6- and 9-month, GPP, NEP, and $R_{ECO}$ showed a significant decline as drought intensity increase (Figure 7.4c and d). We also compared the response patterns of NEP, GPP and $R_{ECO}$ to drought intensities for the current month and one-month prior droughts (Figure 7.5). Neither NEP, GPP, nor $R_{ECO}$ showed significant declines as drought intensity increase under current drought (Figure 7.5), but all three significantly decreased under one-month prior drought. To support the robustness of our analysis, we used TerraClimate based PDSI (Abatzoglou et al., 2018) as the drought indicator to re-conduct the analysis. Our comparison based on TerraClimate based PDSI also indicated that NEP, GPP, and RECO have more significant declines under 1-month prior drought intensities than under simultaneous drought (Figure S7.2). Collectively, our results suggest that in humid regions, ecosystems have significant lagged response to drought (see Figure 7.4, 7.5 and S7.2). One potential cause of the lagged effects is that the drought-driven depletions to soil moisture and soil organic matter were incompletely replenished (Knapp et al., 2008; van der Molen, Dolman, Ciais, Eglin, Gobron, Law, Meir, Peters, Phillips and Reichstein, 2011). Another potential reason is that prior droughts caused vegetation structural changes (e.g., litterfall) and physiological changes (e.g., depletion of carbohydrate reserves and cavitation) requiring

repair/upregulation (Brando et al., 2008; McDowell et al., 2008; van der Molen, Dolman, Ciais, Eglin, Gobron, Law, Meir, Peters, Phillips and Reichstein, 2011). In comparison, the lagged drought impacts are more significant to cause vegetation productivity decline than simultaneous drought impacts. Our study indicates that short-term of meteorological drought indices (e.g., 1-month SPEI) should be used with caution to reflect vegetation drought response in humid regions. However, with the combined use of drought time-scale, intensity, and prior drought conditions, the standardized based meteorological drought indices (e.g., SPEI) are useful indicators to reflect the drought impacts on vegetation carbon uptake in humid regions.

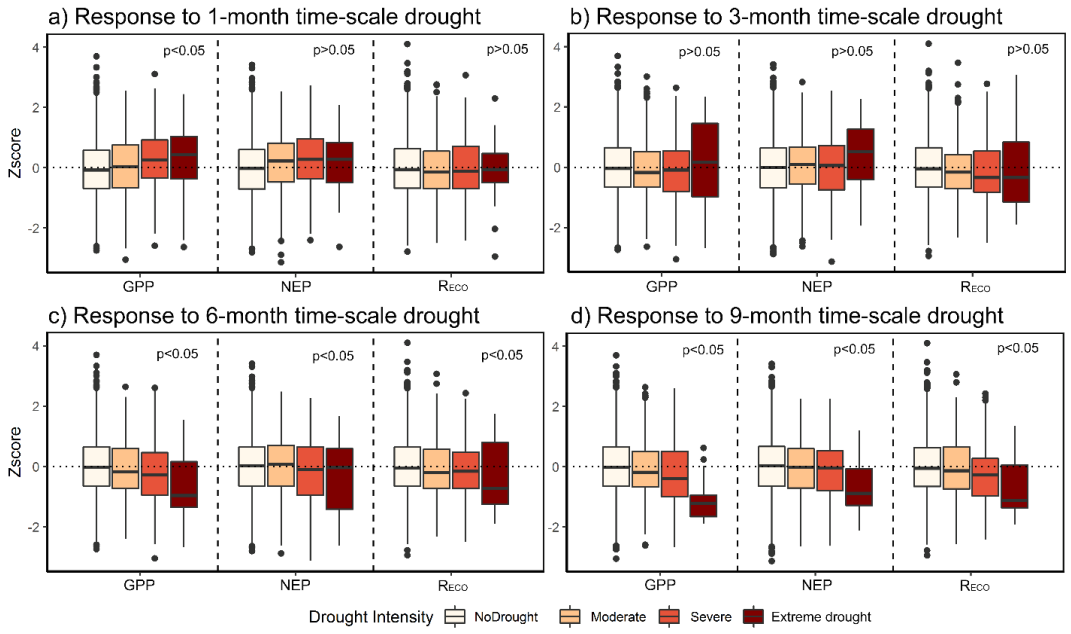


Figure 7.4: Response of NEP, GPP, and $R_{ECO}$ to different drought intensity under 1-, 3-, 6-, and 9-month time-scale of droughts (p-value from ANOVA tests were used to test the significance of differences between the groups).

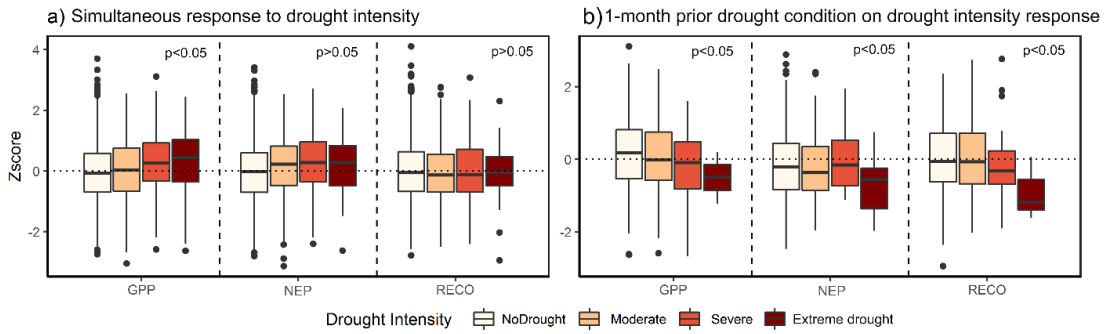


Figure 7.5: The comparison between responses of NEP, GPP, and $R_{ECO}$ to simultaneous and prior drought intensities using one-month time-scale SPEI (p-value from ANOVA tests were used to test the significance of differences between the groups). Y-axis indicated the z-scores of GPP, NEP, and $R_{ECO}$ under different drought intensities of simultaneous (a) and 1-month prior drought (b) conditions.

#### *7.3.2.3 The response patterns of NEP, GPP, and $R_{ECO}$ to drought timing*

We found that under short time-scale drought (e.g., 1- and 3-month), vegetation seems to grow better than normal conditions for most of the GPP increasing stages (Figure 7.6a and b). We also found that the growth stages shortly after the peak stage of the growing season (i.e., the peak growth and 100%-50% of the maximum GPP in decreasing GPP period) were most vulnerable to the negative drought impact than other growth stages. For example, a significant decline in GPP occurred in the growth stages of 100%-50% of the maximum GPP in the decreasing GPP period, under 3-month drought conditions (Figure 7.6b). The z-scores of GPP under drought conditions during the GPP peak period (100% of the maximum GPP period) and 50% - 90% of the maximum GPP during the decreasing period were significantly lower than GPP under drought during other stages (Figure S7.2). For the GPP increasing stages, the GPP values under drought conditions are even higher than GPP under non-drought conditions, while for the growth

stages of 100%-50% of the maximum GPP in the decreasing GPP period, the GPP values under droughts were significantly lower than under non-drought conditions (Figure 7.6). Similar to GPP, NEP and $R_{ECO}$ also showed lower values in those periods than during other stages as the drought time-scale increased from 1 to 9 months. For example, under 1-month drought, $R_{ECO}$ values were lower in the growth stages of 50% and 100% of the maximum GPP in the decreasing GPP period than during other vegetation growth stages (Figure S7.2).

Our analysis highlighted that drought timing is an important factor that should be considered for quantifying the drought impact on GPP, NEP, and $R_{ECO}$ when evaluating the impacts of short-term drought on carbon balance in humid regions. We showed that droughts have the greatest negative effect on carbon uptake when they occur during or slightly after the peak of the growing season. Our finding is consistent with previous tree ring work (D'Orangeville et al., 2018a), precipitation manipulation experiments (Denton et al., 2017; Zeiter et al., 2016), and agricultural meta-analysis (Daryanto et al., 2016; Daryanto et al., 2017) that demonstrate higher sensitivity of plants to mid-season droughts. The impacts of drought timing could be driven by various mechanisms. First, summer droughts could have a more negative impact on vegetation growth due to elevated summer temperatures and vapor pressure deficit (VPD), which can accelerate soil water depletion through enhanced evaporation (De Boeck et al., 2011) and also promote vegetation stress independent of soil water effects (Grossiord et al., 2020; Will et al., 2013). In addition, much tree and crop growth occur during the mid-season period, so droughts that occur at the same time as the most rapid increases in stem and leaf growth will be particularly impactful (Comas et al., 2019; Ji et al., 2003; Wan et al.,

2021). Finally, in humid ecosystems, soil moisture tends to be very high during winter and the shoulder seasons (spring and fall, Roman et al. (2015)). Thus, even a very anomalous deficit of soil moisture during these periods that drives a low value of SPEI may not actually be limiting to plant growth.

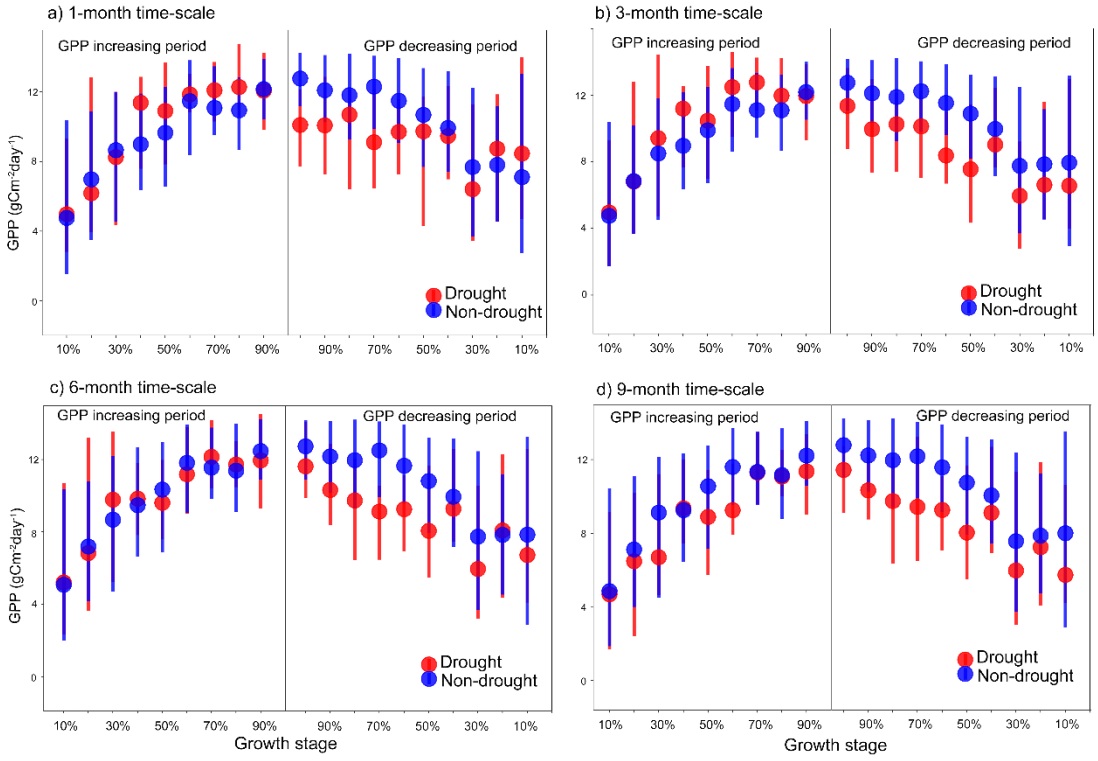


Figure 7.6: GPP distributions under drought (red bars) and non-drought (blue bars) for different vegetation growth stages.

Overall, this analysis provides a comprehensive quantification on the ecosystem carbon flux responses to multiple drought dimensions in humid regions. However, it should be noted that uncertainties may potentially affect the understanding of the ecosystem carbon flux responses to multiple drought dimensions. For example, even with the rapid development of flux tower observations in recent years, most of the flux towers

only cover relatively short observation periods, which are not sufficient to calculate drought indices based on historical occurrence distribution such as SPEI. At the same time, the SPEI values extracted from gridded data may be affected by mismatches between the tower footprint and the footprint of the grid cells.

### 7.4 Conclusions

Despite of the recent rapid advances of drought impact studies, comprehensive evaluations of drought impacts on ecosystem carbon fluxes are still lacking. In this regard, we provided a comprehensive quantification of the impacts of multiple drought dimensions on ecosystem carbon fluxes (NEP, GPP, and $R_{ECO}$) based on the commonly used standardization-based drought index SPEI for humid regions. We found for overall significance, drought timing and prior drought condition are the significant factors affecting NEP, GPP, and $R_{ECO}$ for short-term drought (1- month or 3- month drought). Drought intensity and the one-month prior drought condition are more important than other factors affecting NEP, GPP, and $R_{ECO}$ for the long-term drought (6- month or 9-month drought). For the detailed patterns, we found that $R_{ECO}$ was less sensitive to drought time scale than NEP and GPP. Neither NEP, GPP, and $R_{ECO}$ had significant decrease as the increase of simultaneous drought intensity, but NEP, GPP and $R_{ECO}$ all significantly decreased as drought intensity increased when under one-month prior drought condition. Plants are most vulnerable when both short- and long-term drought occurs during or shortly after the peak growing season . Our results indicated that temporal standardization based meteorological drought indices could be used to reflect plant water stress, but drought timing, antecedent and cumulative drought conditions

need to be considered together. Our study highlights the future prediction of drought impacts on carbon balance should explicitly consider the combined drought impacts from different drought dimensions such as time-scale, intensity, timing, and accumulative impacts.

**References**


Abatzoglou, J.T., Dobrowski, S.Z., Parks, S.A. and Hegewisch, K.C., 2018. TerraClimate, a high-resolution global dataset of monthly climate and climatic water balance from 1958–2015. *Scientific Data*, 5: 170191.

Anderegg, W.R., 2015. Spatial and temporal variation in plant hydraulic traits and their relevance for climate change impacts on vegetation. *New Phytologist*, 205(3): 1008-1014.

Anderegg, W.R., Berry, J.A. and Field, C.B., 2012. Linking definitions, mechanisms, and modeling of drought-induced tree death. *Trends in Plant Science*, 17(12): 693-700.

Anderegg, W.R. et al., 2015. Pervasive drought legacies in forest ecosystems and their implications for carbon cycle models. *Science*, 349(6247): 528-532.

Badeck, F.W. et al., 2004. Responses of spring phenology to climate change. *New Phytologist*, 162(2): 295-309.

Baldocchi, D., 2008. 'Breathing'of the terrestrial biosphere: lessons learned from a global network of carbon dioxide flux measurement systems. *Australian Journal of Botany*, 56(1): 1-26.

Barnes, M.L. et al., 2016. Vegetation productivity responds to sub-annual climate conditions across semiarid biomes. *Ecosphere*, 7(5): e01339.

Bates, D., Mächler, M., Bolker, B. and Walker, S., 2014. Fitting linear mixed-effects models using lme4. *arXiv preprint arXiv:1406.5823*.

Berkelhammer, M., Stefanescu, I., Joiner, J. and Anderson, L., 2017. High sensitivity of gross primary production in the Rocky Mountains to summer rain. *Geophysical Research Letters*, 44(8): 3643-3652.

Brando, P.M. et al., 2008. Drought effects on litterfall, wood production and belowground carbon cycling in an Amazon forest: results of a throughfall reduction experiment. *Philosophical Transactions of the Royal Society B: Biological Sciences*, 363(1498): 1839-1848.

Chang, K.-Y., Xu, L. and Starr, G., 2018. A drought indicator reflecting ecosystem responses to water availability: The normalized ecosystem drought index. *Agricultural and Forest Meteorology*, 250: 102-117.

Chaves, M.M., Maroco, J.P. and Pereira, J.S., 2003. Understanding plant responses to drought—from genes to the whole plant. *Functional Plant Biology*, 30(3): 239-264.

Chen, T., Werf, G., Jeu, R., Wang, G. and Dolman, A., 2013. A global analysis of the impact of drought on net primary productivity. *Hydrology and Earth System Sciences*, 17(10): 3885.

Ciais, P. et al., 2005b. Europe-wide reduction in primary productivity caused by the heat and drought in 2003. *Nature*, 437(7058): 529.

Comas, L.H., Trout, T.J., DeJonge, K.C., Zhang, H. and Gleason, S.M., 2019. Water productivity under strategic growth stage-based deficit irrigation in maize. *Agricultural Water Management*, 212: 433-440.

D'Orangeville, L. et al., 2018a. Drought timing and local climate determine the sensitivity of eastern temperate forests to drought. *Global Change Biology*, 24(6): 2339-2351.

Dai, A., 2011. Drought under global warming: a review. *Wiley Interdisciplinary Reviews: Climate Change*, 2(1): 45-65.

Dannenberg, M.P. et al., 2021. Large-Scale Reductions in Terrestrial Carbon Uptake Following Central Pacific El Niño. *Geophysical Research Letters*, 48(7): e2020GL092367.

Dannenberg, M.P., Song, C., Hwang, T. and Wise, E.K., 2015. Empirical evidence of El Niño–Southern Oscillation influence on land surface phenology and productivity in the western United States. *Remote Sensing of Environment*, 159: 167-180.

Dannenberg, M.P., Song, C., Wise, E.K., Pederson, N. and Bishop, D.A., 2020. Delineating environmental stresses to primary production of US forests from tree rings: Effects of climate seasonality, soil, and topography. *Journal of Geophysical Research: Biogeosciences*, 125(2): e2019JG005499.

Dannenberg, M.P., Wise, E.K. and Smith, W.K., 2019. Reduced tree growth in the semiarid United States due to asymmetric responses to intensifying precipitation extremes. *Science Advances*, 5(10): eaaw0667.

Daryanto, S., Wang, L. and Jacinthe, P.-A., 2016. Global synthesis of drought effects on maize and wheat production. *PloS One*, 11(5): e0156362.

Daryanto, S., Wang, L. and Jacinthe, P.-A., 2017. Global synthesis of drought effects on cereal, legume, tuber and root crops production: A review. *Agricultural Water Management*, 179: 18-33.

De Boeck, H.J., Dreesen, F.E., Janssens, I.A. and Nijs, I., 2011. Whole-system responses of experimental plant communities to climate extremes imposed in different seasons. *New Phytologist*, 189(3): 806-817.

Denton, E.M., Dietrich, J.D., Smith, M.D. and Knapp, A.K., 2017. Drought timing differentially affects above-and belowground productivity in a mesic grassland. *Plant Ecology*, 218(3): 317-328.

Doughty, C.E. et al., 2015. Drought impact on forest carbon dynamics and fluxes in Amazonia. *Nature*, 519(7541): 78-82.

Earles, J.M. et al., 2018. Extreme mid-winter drought weakens tree hydraulic–carbohydrate systems and slows growth. *New Phytologist*, 219(1): 89-97.

Frank, D. et al., 2015. Effects of climate extremes on the terrestrial carbon cycle: concepts, processes and potential future impacts. *Global Change Biology*, 21(8): 2861-2880.

Gao, S. et al., 2018. Dynamic responses of tree-ring growth to multiple dimensions of drought. *Global Change Biology*.

Garcia, R.A., Cabeza, M., Rahbek, C. and Araújo, M.B., 2014. Multiple dimensions of climate change and their implications for biodiversity. *Science*, 344(6183): 1247579.

Green, J.K. et al., 2019. Large influence of soil moisture on long-term terrestrial carbon uptake. *Nature*, 565(7740): 476-479.

Grossiord, C. et al., 2020. Plant responses to rising vapor pressure deficit. *New Phytologist*, 226(6): 1550-1566.

Hao, Z., Yuan, X., Xia, Y., Hao, F. and Singh, V.P., 2017b. An overview of drought monitoring and prediction systems at regional and global scales. *Bulletin of the American Meteorological Society*.

Harris, I., Osborn, T.J., Jones, P. and Lister, D., 2020. Version 4 of the CRU TS monthly high-resolution gridded multivariate climate dataset. *Scientific Data*, 7(1): 1-18.

Heimann, M. and Reichstein, M., 2008. Terrestrial ecosystem carbon dynamics and climate feedbacks. *Nature*, 451(7176): 289-292.

Hoover, D.L. and Rogers, B.M., 2016. Not all droughts are created equal: the impacts of interannual drought pattern and magnitude on grassland carbon cycling. *Global Change Biology*, 22(5): 1809-1820.

Hu, T. et al., 2020. On agricultural drought monitoring in Australia using Himawari-8 geostationary thermal infrared observations. *International Journal of Applied Earth Observation and Geoinformation*, 91: 102153.

Huang, M., Wang, X., Keenan, T.F. and Piao, S., 2018. Drought timing influences the legacy of tree growth recovery. *Global Change Biology*.

Ji, L. and Peters, A.J., 2003. Assessing vegetation response to drought in the northern Great Plains using vegetation and drought indices. *Remote Sensing of Environment*, 87(1): 85-98.

Jiao, W., Chang, Q. and Wang, L., 2019. The Sensitivity of Satellite Solar-Induced Chlorophyll Fluorescence to Meteorological Drought. *Earth's Future*, 7(5): 558-573.

Jiao, W., Tian, C., Chang, Q., Novick, K.A. and Wang, L., 2019. A new multi-sensor integrated index for drought monitoring. *Agricultural and Forest Meteorology*, 268: 74-85.

Jiao, W., Wang, L. and McCabe, M.F., 2021. Multi-sensor remote sensing for drought characterization: current status, opportunities and a roadmap for the future. *Remote Sensing of Environment*, 256: 112313.

Jiao, W., Wang, L., Novick, K.A. and Chang, Q., 2019. A new station-enabled multi-sensor integrated index for drought monitoring. *Journal of Hydrology*, 574: 169-180.

Jiao, W. et al., 2021. Observed increasing water constraint on vegetation growth over the last three decades. *Nature Communications*, 12(1): 1-9.

Jump, A.S. et al., 2017. Structural overshoot of tree growth with climate variability and the global spectrum of drought-induced forest dieback. *Global Change Biology*, 23(9): 3742-3757.

Kannenberg, S.A. et al., 2019. Linking drought legacy effects across scales: From leaves to tree rings to ecosystems. *Global Change Biology*, 25(9): 2978-2992.

Karnieli, A. et al., 2006. Comments on the use of the vegetation health index over Mongolia. *International Journal of Remote Sensing*, 27(10): 2017-2024.

Keenan, T., Sabate, S. and Gracia, C., 2010. The importance of mesophyll conductance in regulating forest ecosystem productivity during drought periods. *Global Change Biology*, 16(3): 1019-1034.

Kim, H.-Y., 2014. Analysis of variance (ANOVA) comparing means of more than two groups. *Restorative Dentistry & Endodontics*, 39(1): 74-77.

Knapp, A.K. et al., 2008. Consequences of more extreme precipitation regimes for terrestrial ecosystems. *Bioscience*, 58(9): 811-821.

Knowles, J.F., Scott, R.L., Minor, R.L. and Barron-Gafford, G.A., 2020. Ecosystem carbon and water cycling from a sky island montane forest. *Agricultural and Forest Meteorology*, 281: 107835.

Konapala, G., Mishra, A.K., Wada, Y. and Mann, M.E., 2020. Climate change will affect global water availability through compounding changes in seasonal precipitation and evaporation. *Nature Communications*, 11(1): 1-10.

Kreuzwieser, J. and Rennenberg, H., 2014. Molecular and physiological responses of trees to waterlogging stress. *Plant, Cell & Environment*, 37(10): 2245-2259.

Lemoine, N.P., Griffin-Nolan, R.J., Lock, A.D. and Knapp, A.K., 2018. Drought timing, not previous drought exposure, determines sensitivity of two shortgrass species to water stress. *Oecologia*, 188(4): 965-975.

Li, J. et al., 2020. Toward monitoring short-term droughts using a novel daily scale, standardized antecedent precipitation evapotranspiration index. *Journal of Hydrometeorology*, 21(5): 891-908.

Liu, Z. et al., 2018. Precipitation thresholds regulate net carbon exchange at the continental scale. *Nature Communications*, 9(1): 1-10.

Lloyd-Hughes, B., 2014. The impracticality of a universal drought definition. *Theoretical and Applied Climatology*, 117(3-4): 607-611.

Mankin, J.S., Seager, R., Smerdon, J.E., Cook, B.I. and Williams, A.P., 2019. Mid-latitude freshwater availability reduced by projected vegetation responses to climate change. *Nature Geoscience*: 1-6.

McDowell, N. et al., 2008. Mechanisms of plant survival and mortality during drought: why do some plants survive while others succumb to drought? *New Phytologist*, 178(4): 719-739.

McKee, T.B., Doesken, N.J. and Kleist, J., 1993. The relationship of drought frequency and duration to time scales, Proceedings of the 8th Conference on Applied Climatology. American Meteorological Society Boston, MA, pp. 179-183.

Meir, P., Metcalfe, D.B., Costa, A. and Fisher, R.A., 2008b. The fate of assimilated carbon during drought: impacts on respiration in Amazon rainforests. *Philosophical Transactions of the Royal Society of London B: Biological Sciences*, 363(1498): 1849-1855.

Nemani, R.R. et al., 2003. Climate-driven increases in global terrestrial net primary production from 1982 to 1999. *Science*, 300(5625): 1560-1563.

Novick, K.A. et al., 2016. The increasing importance of atmospheric demand for ecosystem water and carbon fluxes. *Nature Climate Change*, 6(11): 1023-1027.

Novick, K.A. et al., 2015. On the difference in the net ecosystem exchange of CO 2 between deciduous and evergreen forests in the southeastern United States. *Global Change Biology*, 21(2): 827-842.

Park, S., Im, J., Jang, E. and Rhee, J., 2016. Drought assessment and monitoring through blending of multi-sensor indices using machine learning approaches for different climate regions. *Agricultural and Forest Meteorology*, 216: 157-169.

Paulo, A., Rosa, R. and Pereira, L., 2012. Climate trends and behaviour of drought indices based on precipitation and evapotranspiration in Portugal. *Natural Hazards and Earth System Sciences*, 12(5): 1481-1491.

Piao, S. et al., 2008. Net carbon dioxide losses of northern ecosystems in response to autumn warming. *Nature*, 451(7174): 49.

Pinheiro, P., 2010. Linear and nonlinear mixed effects models. R package version 3.1-97. *http://cran. r-project. org/web/packages/nlme*.

Rhee, J., Im, J. and Carbone, G.J., 2010. Monitoring agricultural drought for arid and humid regions using multi-sensor remote sensing data. *Remote Sensing of Environment*, 114(12): 2875-2887.

Roman, D. et al., 2015. The role of isohydric and anisohydric species in determining ecosystem-scale response to severe drought. *Oecologia*, 179(3): 641-654.

Ruppert, J.C. et al., 2015. Quantifying drylands' drought resistance and recovery: the importance of drought intensity, dominant life history and grazing regime. *Global Change Biology*, 21(3): 1258-1270.

Schwalm, C.R. et al., 2010. Assimilation exceeds respiration sensitivity to drought: A FLUXNET synthesis. *Global Change Biology*, 16(2): 657-670.

Seddon, A.W., Macias-Fauria, M., Long, P.R., Benz, D. and Willis, K.J., 2016. Sensitivity of global terrestrial ecosystems to climate variability. *Nature*, 531(7593): 229.

Shi, Z. et al., 2014. Differential effects of extreme drought on production and respiration: synthesis and modeling analysis. *Biogeosciences*, 11(3): 621-633.

Slette, I.J. et al., 2019. How ecologists define drought, and why we should do better. *Global Change Biology*, 25(10): 3193-3200.

Slette, I.J. et al., 2019. Standardized metrics are key for assessing drought severity. *Global Change Biology*.

Stagge, J.H., Tallaksen, L.M., Gudmundsson, L., Van Loon, A.F. and Stahl, K., 2015. Candidate distributions for climatological drought indices (SPI and SPEI). *International Journal of Climatology*, 35(13): 4027-4040.

Stocker, B.D. et al., 2018. Quantifying soil moisture impacts on light use efficiency across biomes. *New Phytologist*, 218(4): 1430-1449.

Sulman, B.N. et al., 2016. High atmospheric demand for water can limit forest carbon uptake and transpiration as severely as dry soil. *Geophysical Research Letters*, 43(18): 9686-9695.

Sweet, S.K., Wolfe, D.W., DeGaetano, A. and Benner, R., 2017. Anatomy of the 2016 drought in the Northeastern United States: Implications for agriculture and water resources in humid climates. *Agricultural and Forest Meteorology*, 247: 571-581.

Tan, C., Yang, J. and Li, M., 2015. Temporal-spatial variation of drought indicated by SPI and SPEI in Ningxia Hui Autonomous Region, China. *Atmosphere*, 6(10): 1399-1421.

Valipour, M., 2016. Optimization of neural networks for precipitation analysis in a humid region to detect drought and wet year alarms. *Meteorological Applications*, 23(1): 91-100.

van der Molen, M.K. et al., 2011. Drought and ecosystem carbon cycling. *Agricultural and Forest Meteorology*, 151(7): 765-773.

Van der Schrier, G., Briffa, K., Jones, P. and Osborn, T., 2006. Summer moisture variability across Europe. *Journal of Climate*, 19(12): 2818-2834.

Vicente-Serrano, S. and Sergio, M., 2014. The climate data guide: standardized precipitation evapotranspiration index (SPEI). Accedido.

Vicente-Serrano, S.M., Beguería, S. and López-Moreno, J.I., 2010. A multiscalar drought index sensitive to global warming: the standardized precipitation evapotranspiration index. *Journal of Climate*, 23(7): 1696-1718.

Vicente-Serrano, S.M. et al., 2013. Response of vegetation to drought time-scales across global land biomes. *Proceedings of the National Academy of Sciences*, 110(1): 52-57.

Vicente-Serrano, S.M., Quiring, S.M., Peña-Gallardo, M., Yuan, S. and Domínguez-Castro, F., 2020. A review of environmental droughts: Increased risk under global warming? *Earth-Science Reviews*, 201: 102953.

Wan, W. et al., 2021. Drought monitoring of the maize planting areas in Northeast and North China Plain. *Agricultural Water Management*, 245: 106636.

Wang, Q. et al., 2014. Temporal-spatial characteristics of severe drought events and their impact on agriculture on a global scale. *Quaternary International*, 349: 10-21.

Wang, Q. et al., 2021. A multi-scale daily SPEI dataset for drought characterization at observation stations over mainland China from 1961 to 2018. *Earth System Science Data*, 13(2): 331-341.

Waseem, M., Ajmal, M., Lee, J.H. and Kim, T.-W., 2016. Multivariate drought assessment considering the antecedent drought conditions. *Water Resources Management*, 30(12): 4221-4231.

Wen, Y., Liu, X., Pei, F., Li, X. and Du, G., 2018. Non-uniform time-lag effects of terrestrial vegetation responses to asymmetric warming. *Agricultural and forest meteorology*, 252: 130-143.

Wen, Y. et al., 2019. Cumulative effects of climatic factors on terrestrial vegetation growth. *Journal of Geophysical Research: Biogeosciences*, 124(4): 789-806.

Will, R.E., Wilson, S.M., Zou, C.B. and Hennessey, T.C., 2013. Increased vapor pressure deficit due to higher temperature leads to greater transpiration and faster mortality during drought for tree seedlings common to the forest–grassland ecotone. *New Phytologist*, 200(2): 366-374.

Willis, K.J., Jeffers, E.S. and Tovar, C., 2018. What makes a terrestrial ecosystem resilient? *Science*, 359(6379): 988-989.

Wolf, S. et al., 2016. Warm spring reduced carbon cycle impact of the 2012 US summer drought. *Proceedings of the National Academy of Sciences*, 113(21): 5880-5885.

Wu, D. et al., 2015. Time-lag effects of global vegetation responses to climate change. *Global Change Biology*, 21(9): 3520-3531.

Xu, C. et al., 2019. Increasing impacts of extreme droughts on vegetation productivity under climate change. *Nature Climate Change*, 9(12): 948-953.

Xu, H.-j., Wang, X.-p., Zhao, C.-y. and Yang, X.-m., 2018. Diverse responses of vegetation growth to meteorological drought across climate zones and land biomes in northern China from 1981 to 2014. *Agricultural and Forest Meteorology*, 262: 1-13.

Yang, Y., Roderick, M.L., Zhang, S., McVicar, T.R. and Donohue, R.J., 2019. Hydrologic implications of vegetation response to elevated $CO_2$ in climate projections. *Nature Climate Change*, 9(1): 44-48.

Zang, C.S. et al., 2020. Standardized drought indices in ecological research: Why one size does not fit all. *Global Change Biology*, 26(2): 322-324.

Zeiter, M., Schärrer, S., Zweifel, R., Newbery, D.M. and Stampfli, A., 2016. Timing of extreme drought modifies reproductive output in semi-natural grassland. *Journal of Vegetation Science*, 27(2): 238-248.

Zhang, F. et al., 2021. Five decades of observed daily precipitation reveal longer and more variable drought events across much of the western United States. *Geophysical Research Letters*, 48(7): e2020GL092293.

Zhang, L., Jiao, W., Zhang, H., Huang, C. and Tong, Q., 2017. Studying drought phenomena in the Continental United States in 2011 and 2012 using various drought indices. *Remote Sensing of Environment*, 190: 96-106.

Zhang, Q. et al., 2019. Response of ecosystem intrinsic water use efficiency and gross primary productivity to rising vapor pressure deficit. *Environmental Research Letters*, 14(7): 074023.

Zhao, M. and Running, S.W., 2010. Drought-induced reduction in global terrestrial net primary production from 2000 through 2009. *Science*, 329(5994): 940-943.

Zuur, A.F., Ieno, E.N. and Elphick, C.S., 2010. A protocol for data exploration to avoid common statistical problems. *Methods in Ecology and Evolution*, 1(1): 3-14.

# APPENDICES

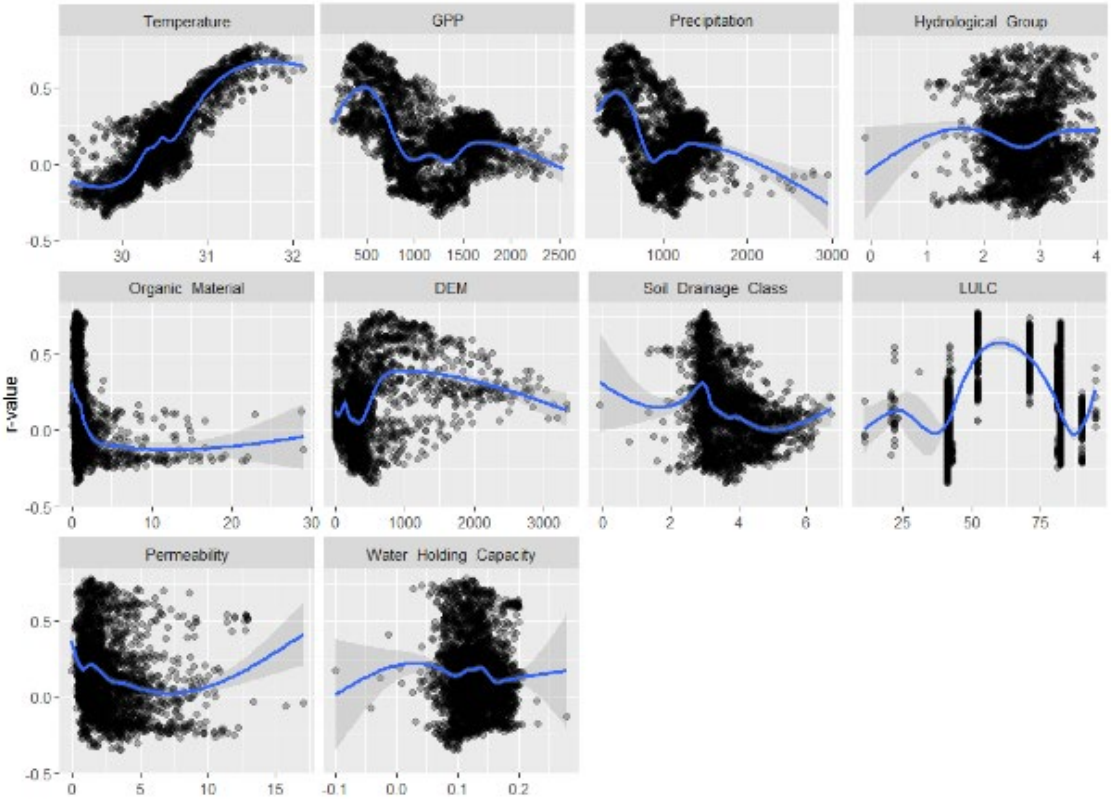


Figure S5.1: The relationships between $R_{SIF\text{-}SPEI05}$ and ten variables.

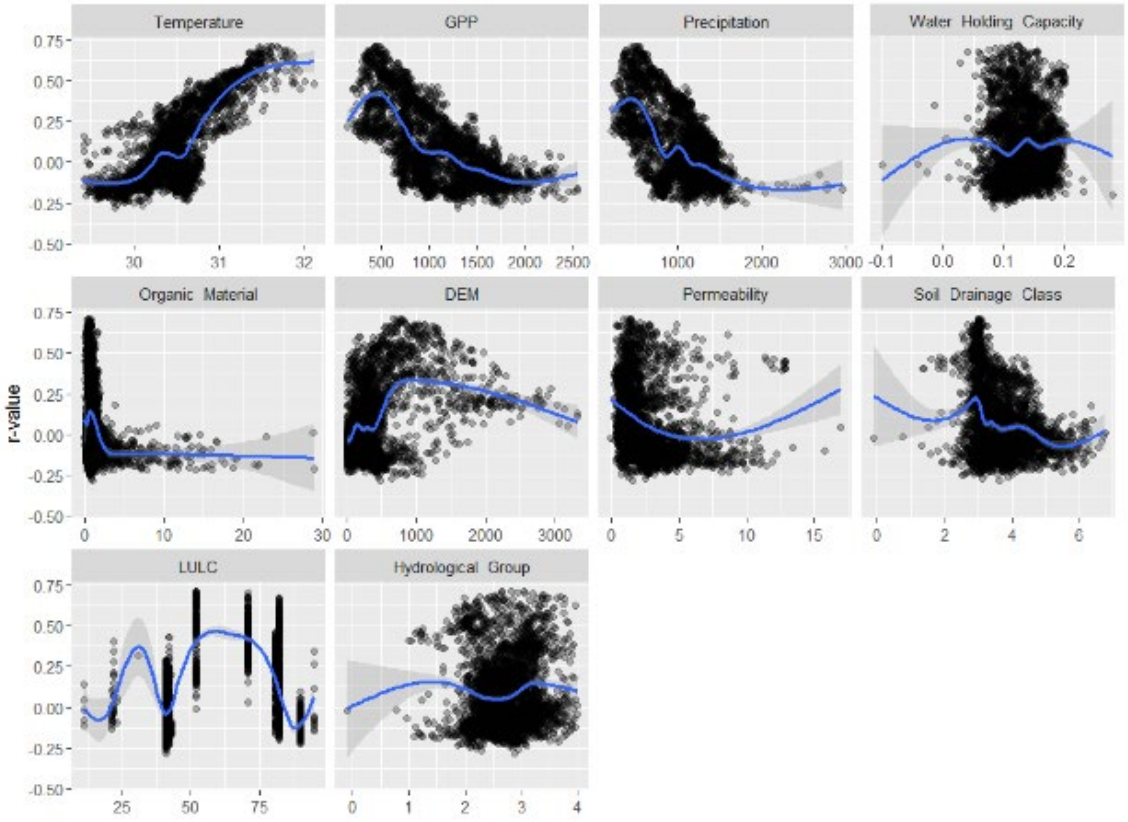


Figure S5.2: The relationships between $R_{SIF^*\text{-}SPEI05}$ and ten variables.

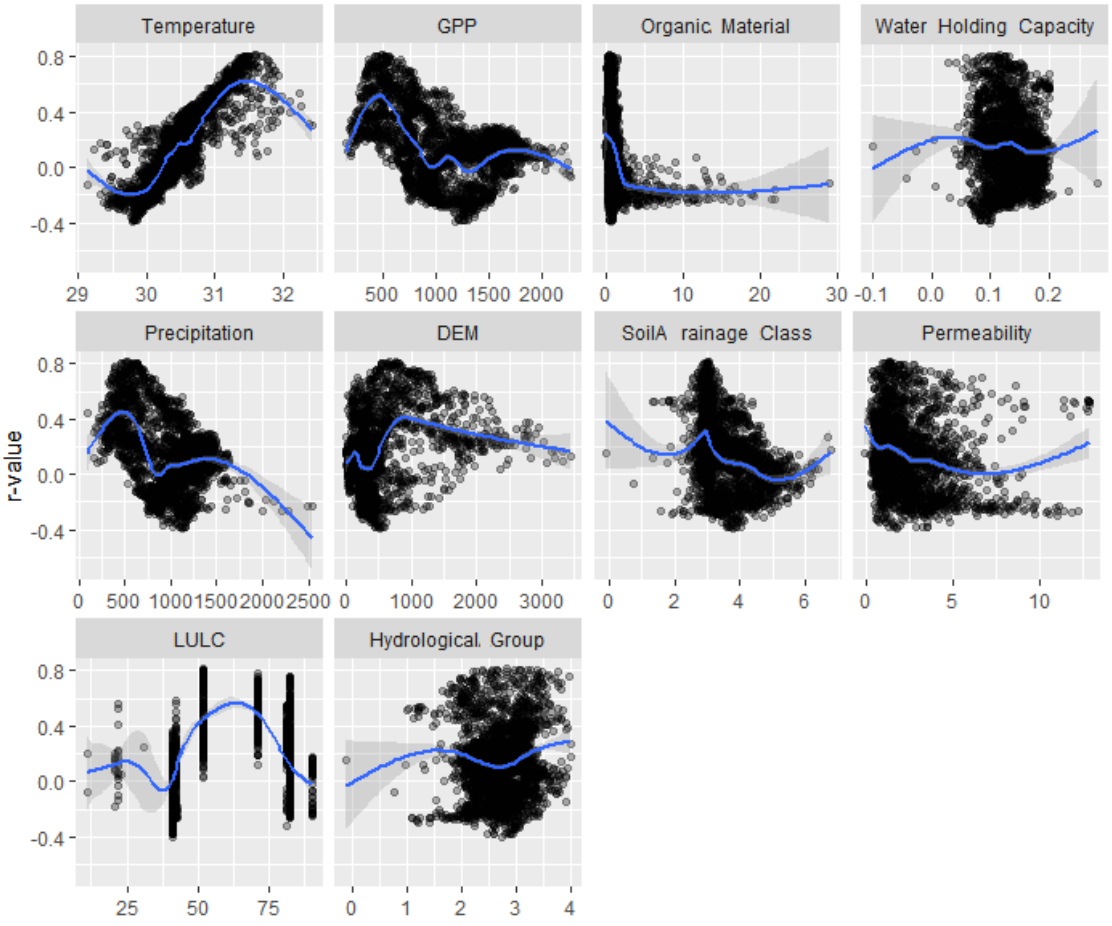


Figure S5.3: The relationships between $R_{SIF^*\text{-}SPI05}$ and ten variables.

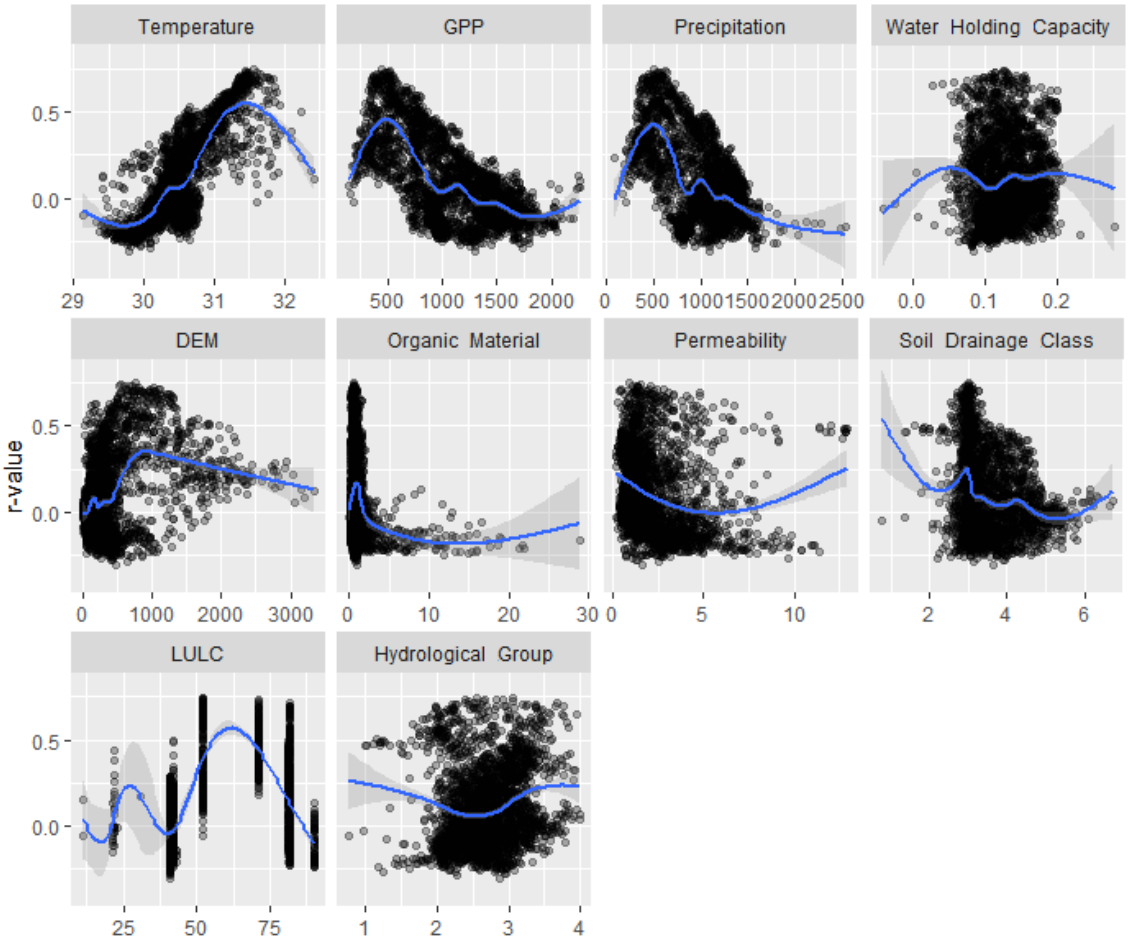


Figure S5.4: The relationships between $R_{SIF\text{-}SPI05}$ and ten variables.

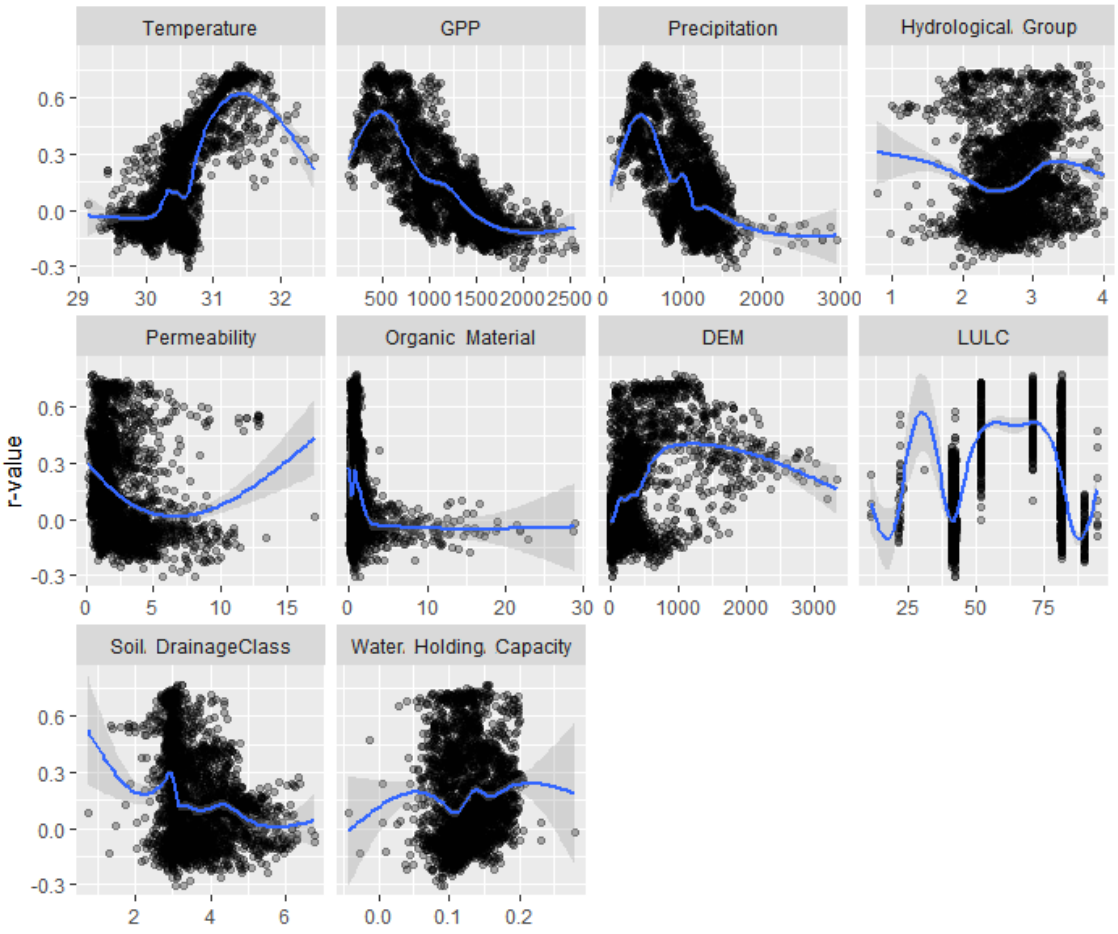


Figure S5.5: The relationships between $R_{SIF\text{-}PDSI}$ and ten variables.

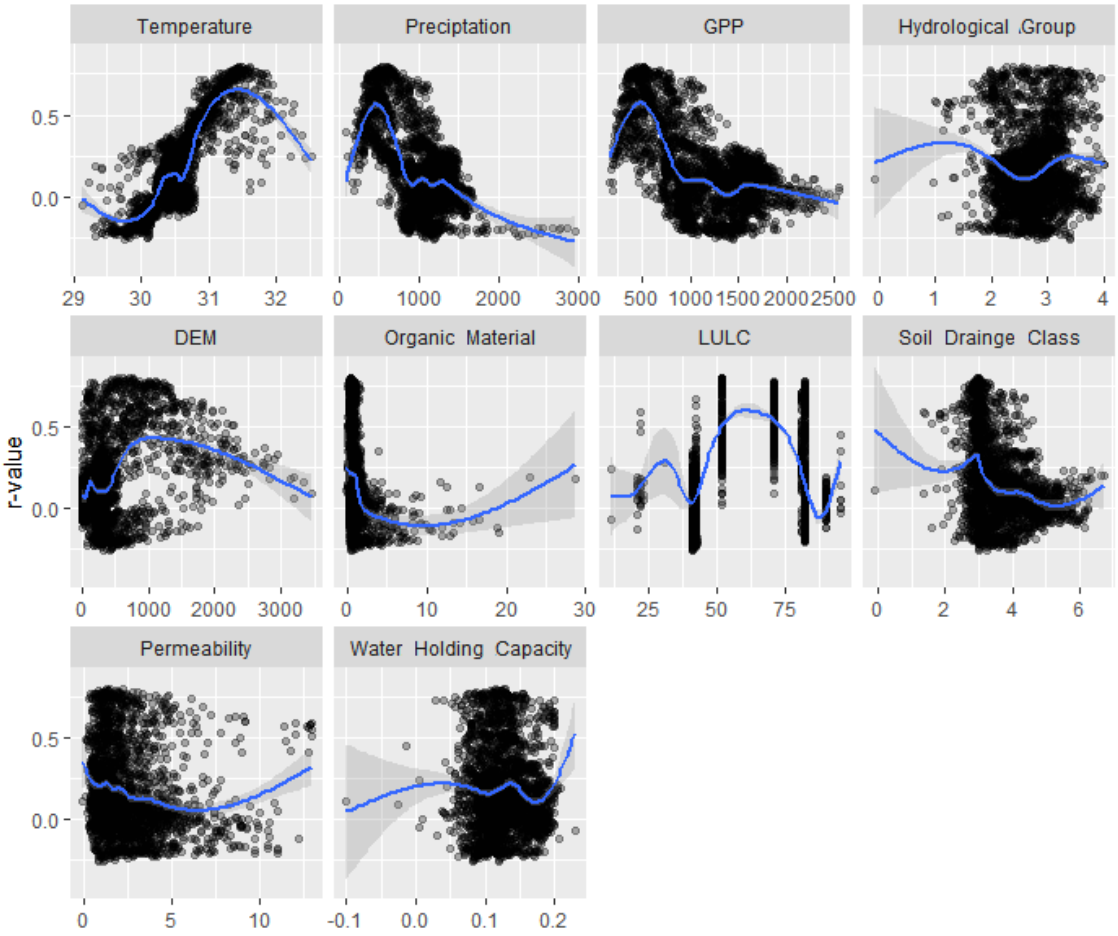


Figure S5.6: The relationships between $R_{SIF^*\text{-}PDSI}$ and ten variables.

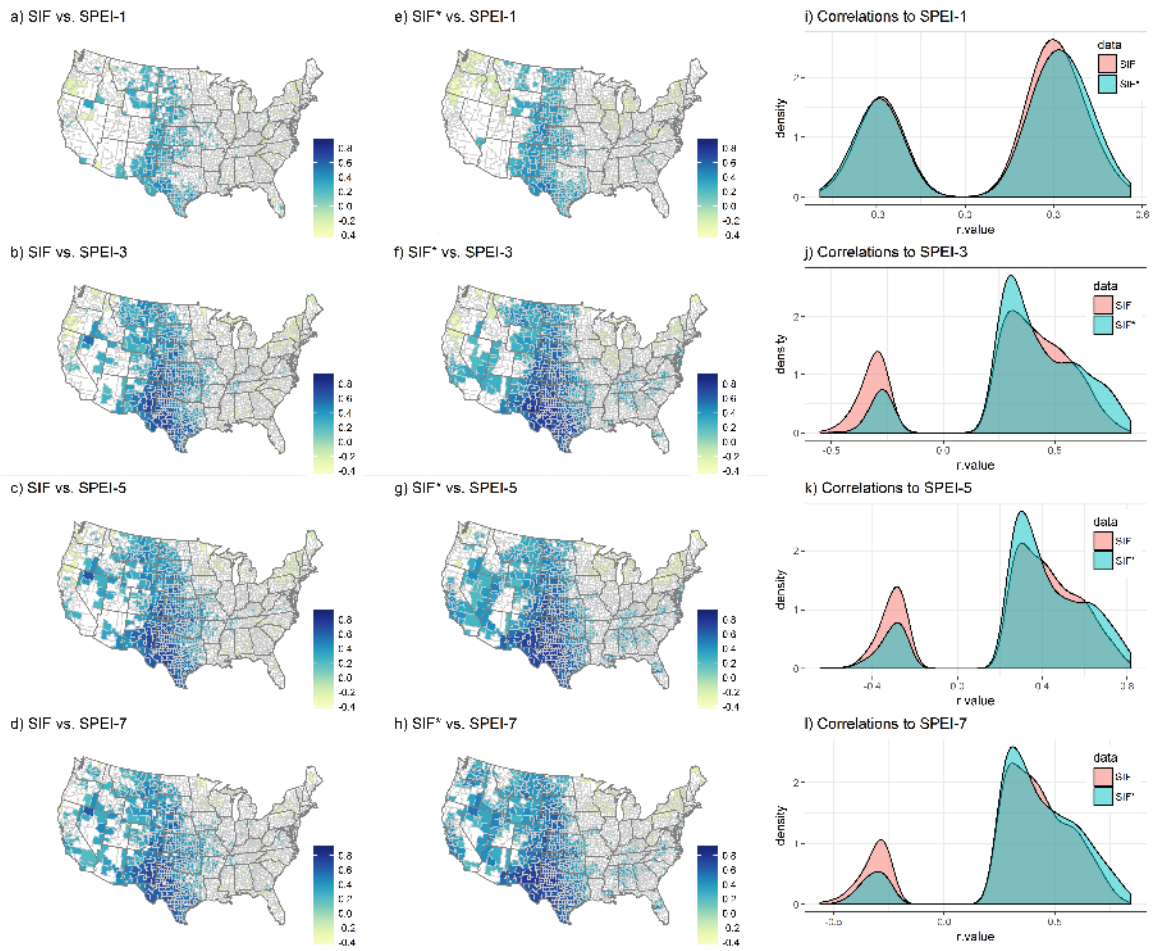


Figure S5.7: The comparison of spatial distribution of correlations between SPEIs and SIF with 0.05 º and 0.5 º spatial resolutions.

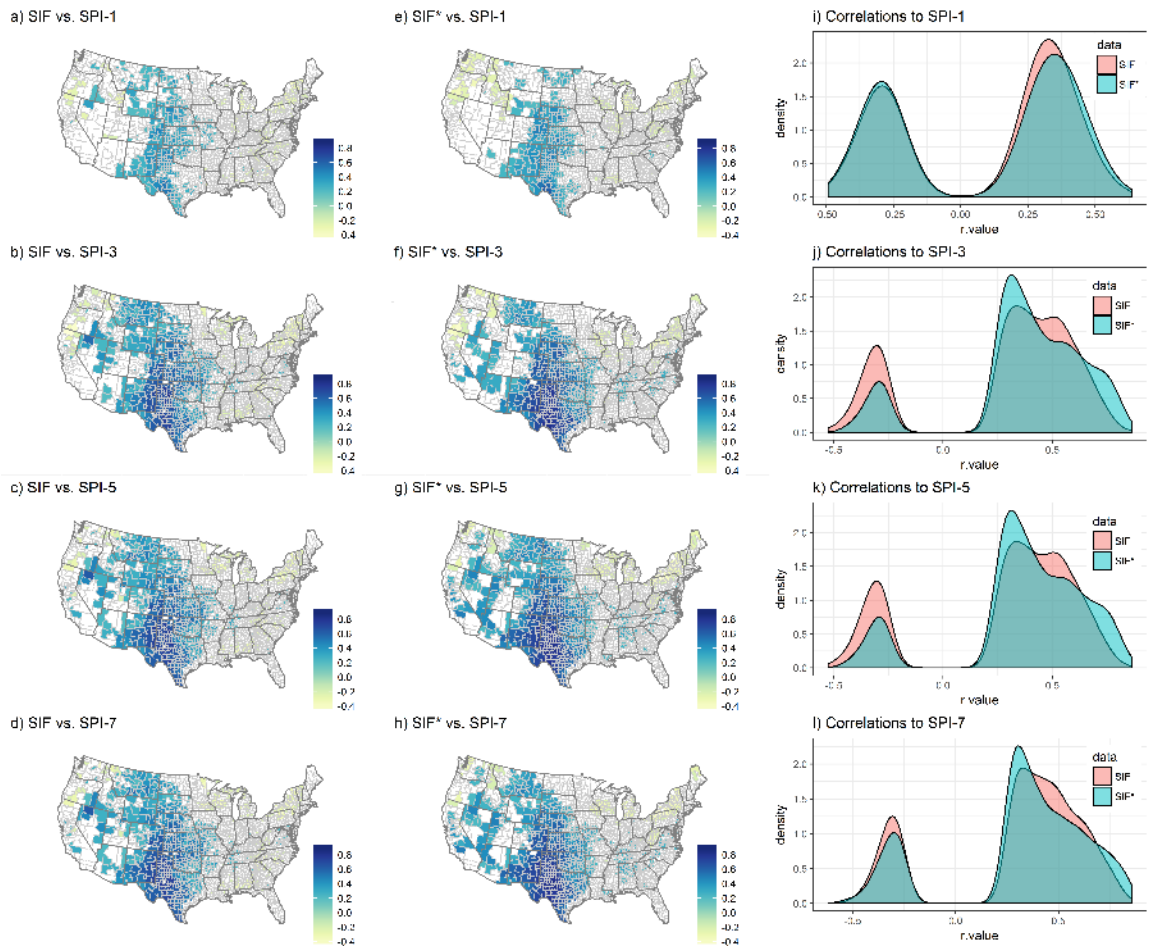


Figure S5.8: The comparison of spatial distribution of correlations between SPIs and SIF with 0.05 $^{o}$ and 0.5 $^{o}$ spatial resolutions.

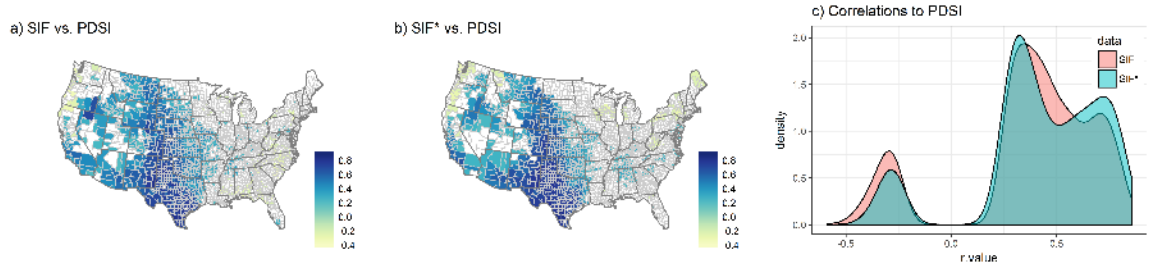


Figure S5.9: The comparison of spatial distribution of correlations between PDSI and SIF with 0.05 $^{o}$ and 0.5 $^{o}$ spatial resolutions.

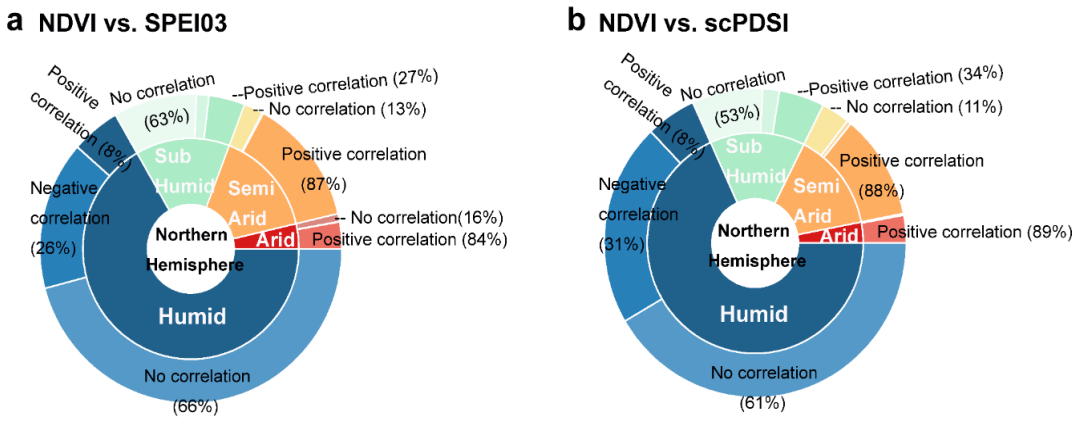


Figure S6.1: The percentage of areas of the significant positive, significant negative, and non-significant correlation coefficients for arid, semi-arid, sub-humid, and humid regions, respectively between normalized difference vegetation index (NDVI) and 3-month Standardized Precipitation-Evapotranspiration Index (SPEI03) (a) and Palmer Drought Severity Index (scPDSI) (b).

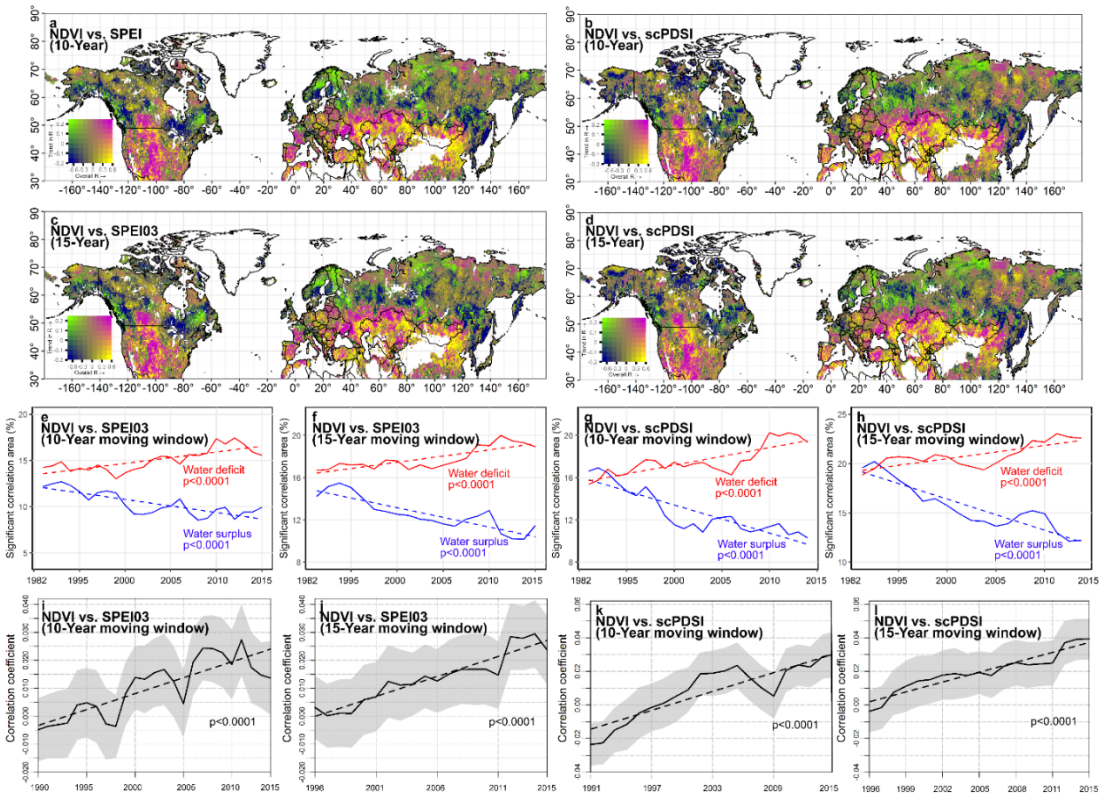


Figure S6.2: Spatiotemporal distribution of the statistically significant correlations between vegetation growth and water availability indices over the last three decades analyzed using 10-year and 15-year moving window. (a) - (d) show distribution of correlation coefficients ($R_{NDVI\text{-}SPEI03}$ and $R_{NDVI\text{-}scPDSI}$) between normalized difference vegetation index (NDVI) anomaly and 3-month Standardized Precipitation-Evapotranspiration Index (SPEI) and Palmer Drought Severity Index (scPDSI) using 10-year moving window and 15-year moving window; (e) - (h) show the temporal trends of significant positive and negative correlation areas using 10-year and 15-year moving windows. Blue color stands for the negative $R_{NDVI\text{-}SPEI03}$ and $R_{NDVI\text{-}scPDSI}$ (water surplus response) and red color for positive $R_{NDVI\text{-}SPEI03}$ and $R_{NDVI\text{-}scPDSI}$ (water deficit response). (i)-(l) show the overall mean $R_{NDVI\text{-}SPEI03}$ and $R_{NDVI\text{-}scPDSI}$ over the study area using 10-

year and 15-year moving windows. All the trends of positive and negative $R_{NDVI\text{-}SPEI03}$ and $R_{NDVI\text{-}scPDSI}$ are significant in linear trend test and Mann-Kendall trend test ($p < 0.05$).

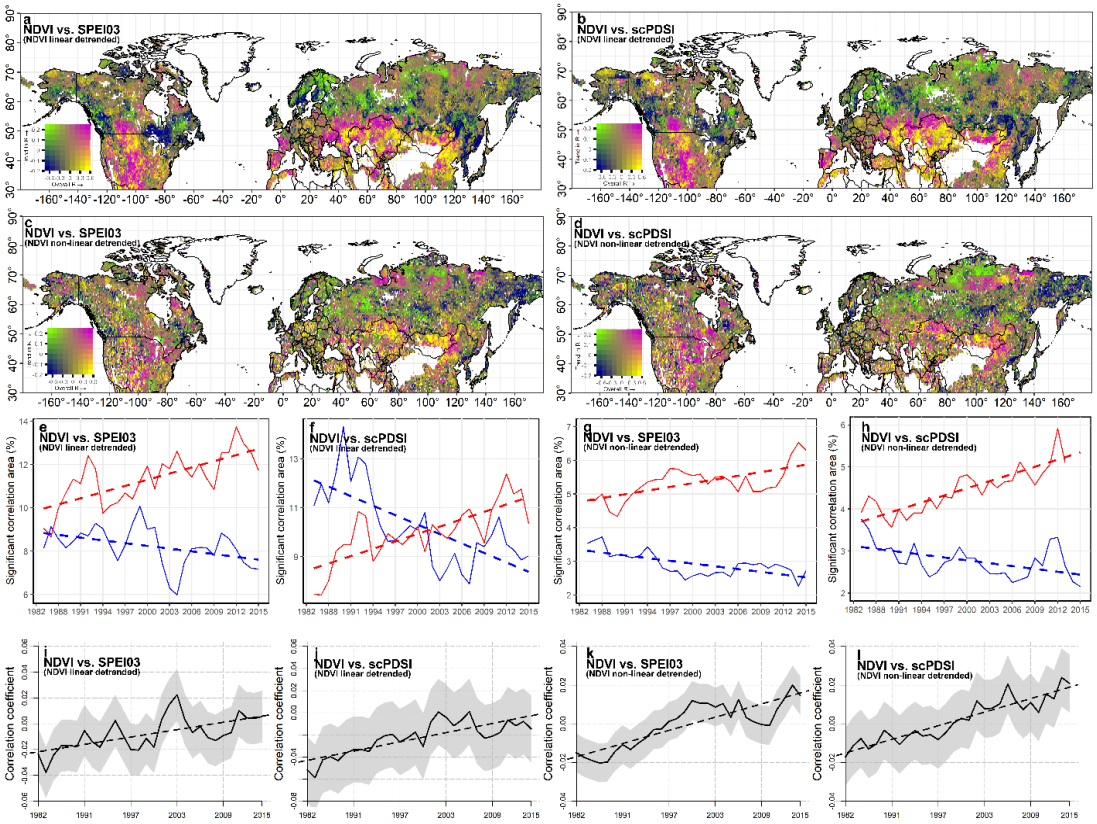


Figure S6.3: Spatiotemporal distribution of the statistically significant correlations between vegetation growth and water availability indices over the last three decades analyzed after NDVI was linearly and nonlinearly detrended. (a) - (d) show distribution of correlation coefficients ($R_{NDVI\text{-}SPEI03}$ and $R_{NDVI\text{-}scPDSI}$) between normalized difference vegetation index (NDVI) anomaly and 3-month Standardized Precipitation-Evapotranspiration Index (SPEI) and Palmer Drought Severity Index (scPDSI) after NDVI was linearly and non-linearly detrended; (e) - (h) show the temporal trends of significant positive and negative correlation areas after NDVI was linearly and nonlinearly detrended. Blue color stands for the negative $R_{NDVI\text{-}SPEI03}$ and $R_{NDVI\text{-}scPDSI}$

(water surplus response) and red color for positive $R_{NDVI\text{-}SPEI03}$ and $R_{NDVI\text{-}scPDSI}$ (water deficit response). (i)-(l) show the overall mean $R_{NDVI\text{-}SPEI03}$ and $R_{NDVI\text{-}scPDSI}$ over the study area after NDVI was linear and nonlinear detrended. All the trends of positive and negative $R_{NDVI\text{-}SPEI03}$ and $R_{NDVI\text{-}scPDSI}$ are significant in linear trend test and Mann-Kendall trend test ($p < 0.05$).

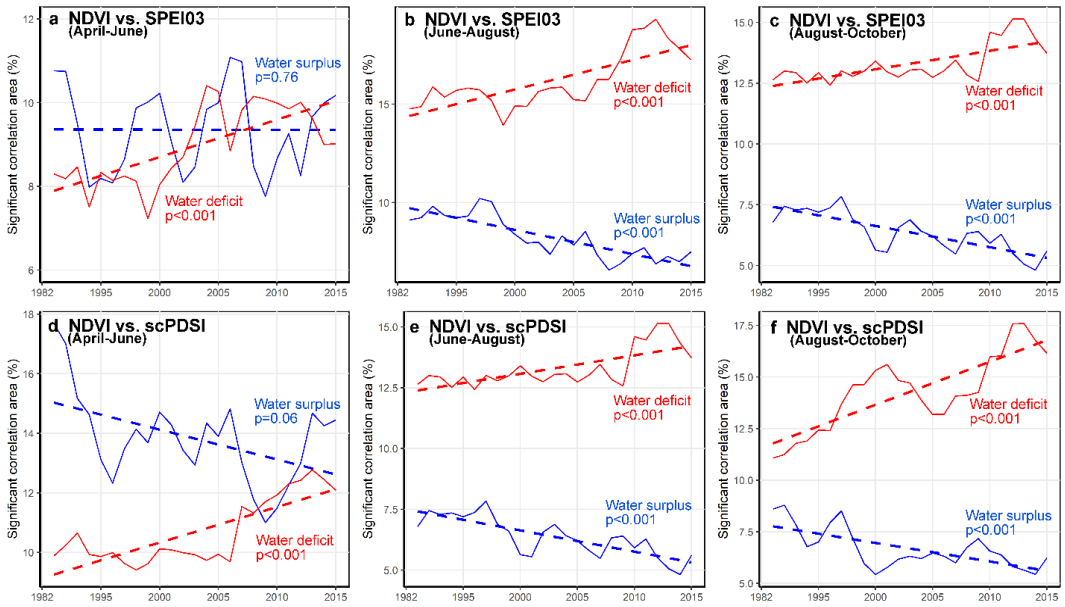


Figure S6.4: Temporal trends of significant changes in percentage areas associated with water deficit and water surplus responses for sub-seasons. (a)-(c) stands for the changes of significant water surplus and water deficit areas evaluated by $R_{NDVI\text{-}SPEI03}$ for April-June (a), June-August (b), and August-October (c); (d)-(e) stands for the the changes of significant water surplus and water deficit areas evaluated by $R_{NDVI\text{-}scPDSI}$ for April-June (d), June-August (e), and August-October (f). Blue color stands for the water surplus response and red color for water deficit response.

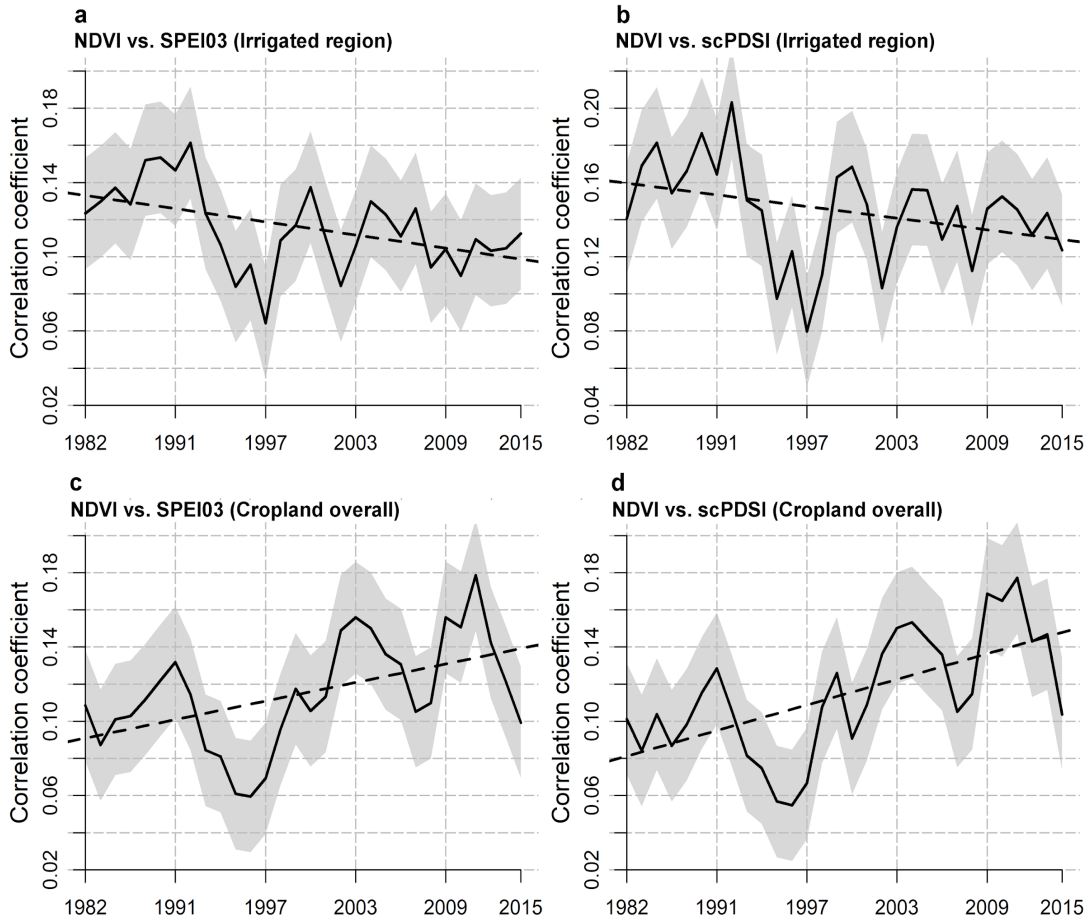


Figure S6.5: The trends of mean correlation coefficients (r-value) between normalized difference vegetation index (NDVI) anomaly and water deficit indices for the irrigated cropland regions over the last three decades. (a) and (b) present r-value between NDVI and 3-month Standardized Precipitation-Evapotranspiration Index (SPEI03) and Palmer Drought Severity Index (scPDSI), respectively of all the grid cells over the irrigated cropland regions for the period of 1982-2015. Black solid lines represent the mean correlation coefficients of all the grid cells and the dashed lines represent a linear trend. The gray areas represent the means ± standard deviation of each correlation efficient. Irrigated area extracted using Global Map of Irrigation Areas from Food and Agriculture

Organization of United Nations (FAO): http://www.fao.org/aquastat/en/geospatial-information/global-maps-irrigated-areas/latest version/. X-axes are binned using 5-year moving window to smooth out time series fluctuations and highlight the trends.

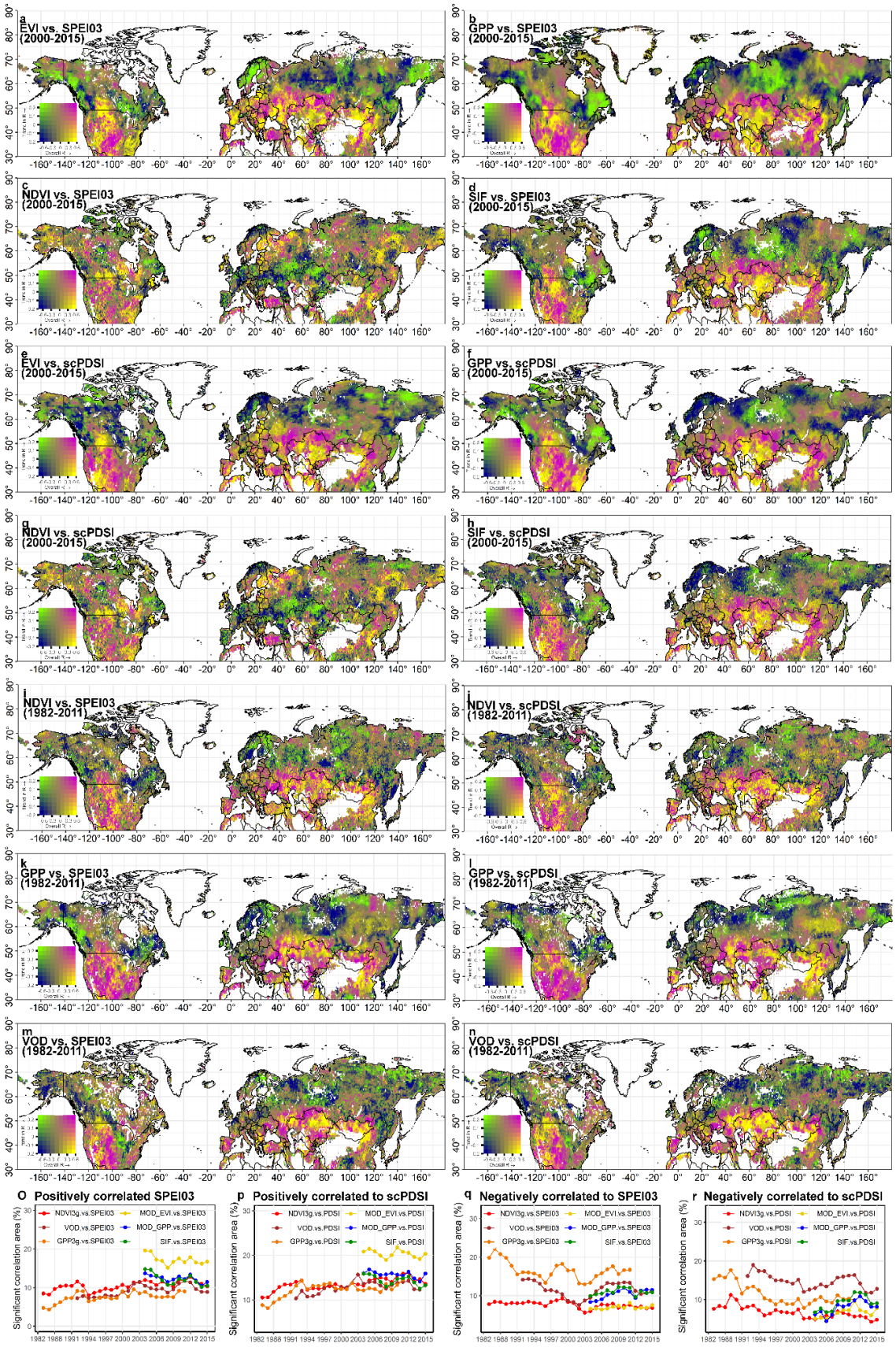
a EVI vs. SPEI03 (2000-2015)
b GPP vs. SPEI03 (2000-2015)
c NDVI vs. SPEI03 (2000-2015)
d SIF vs. SPEI03 (2000-2015)
e EVI vs. scPDSI (2000-2015)
f GPP vs. scPDSI (2000-2015)
g NDVI vs. scPDSI (2000-2015)
h SIF vs. scPDSI (2000-2015)
i NDVI vs. SPEI03 (1982-2011)
j NDVI vs. scPDSI (1982-2011)
k GPP vs. SPEI03 (1982-2011)
l GPP vs. scPDSI (1982-2011)
m VOD vs. SPEI03 (1982-2011)
n VOD vs. scPDSI (1982-2011)
o Positively correlated SPEI03
p Positively correlated to scPDSI
q Negatively correlated to SPEI03
r Negatively correlated to scPDSI
Significant correlation area (%)
NDVI3g.vs.SPEI03
MOD_EVI.vs.SPEI03
VOD.vs.SPEI03
MOD_GPP.vs.SPEI03
GPP3g.vs.SPEI03
SIF.vs.SPEI03
NDVI3g.vs.PDSI
MOD_EVI.vs.PDSI
VOD.vs.PDSI
MOD_GPP.vs.PDSI
GPP3g.vs.PDSI
SIF.vs.PDSI

Figure S6.6: Spatial distribution of the correlation coefficients (r-value) between vegetation growth and water availability indices, and the trend of significant positive and negative correlation areas over the Northern Hemisphere from 2000-2015 and 1982-2011. (a)-(h) present the spatial distribution of correlation coefficient from 2000-2015 between enhanced vegetation index (EVI) and SPEI03 (a); gross primary productivity (GPP) and SPEI03 (b); normalized difference vegetation index (NDVI) and 3-month Standardized Precipitation-Evapotranspiration Index (SPEI03) (c); solar-induced chlorophyll fluorescence (SIF) and 3-month Standardized Precipitation-Evapotranspiration Index (SPEI03) (d). EVI and Palmer Drought Severity Index (scPDSI) (e); GPP and scPDSI (f); NDVI and scPDSI (g); SIF and scPDSI (h). (i)-(l) indicate the spatial distribution of correlation coefficients from 1982-2011 between NDVI and SPEI03 (i); NDVI and scPDSI (j); GPP and SPEI03 (k); GPP and scPDSI (l); Vegetation optical depth (VOD) and SPEI03 (m); VOD and scPDSI (n). (o)-(r) show the trend of significant positive correlation area (o and p) and significant negative correlation area (q and r) between vegetation growth and water availability indices. Red color indicates the relationship between NDVI and drought indices; Brown color shows the relationship between VOD and drought indices; Orange color shows the relationship between GIMMS-GPP and drought indices; Golden color indicates the relationship between EVI and water availability indices; Blue color presents the relationship between MODIS-GPP and availability indices; Green color shows the relationship between GO-SIF and availability indices. X-axes of (o)-(r) are binned using 5-year moving window to smooth out time series fluctuations and highlight the trends.

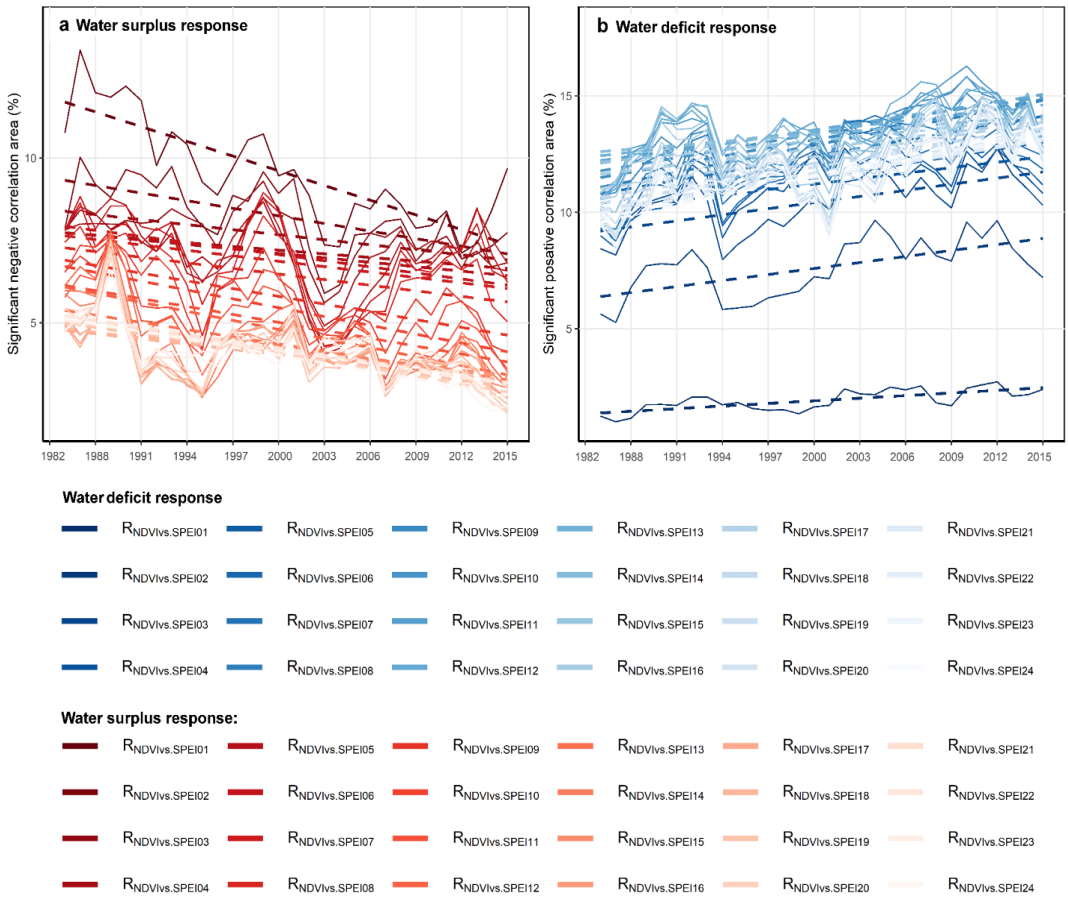


Figure S6.7: Temporal trends of proportion of areas with significant correlations between vegetation growth and availability indices of different time-scales over the last three decades. (a) shows the trend of proportion of areas with significant negative correlations and (b) shows the trend of proportion of areas with significant positive correlations between normalized difference vegetation index (NDVI) and Standardized Precipitation-Evapotranspiration Index (SPEI) for all the time-scales from 1 to 24 months over the Northern Hemisphere over the period of 1982-2015. Red color is ised in the case of negative correlation and blue color is used for positive correlation. Darker color indicates shorter time-scale and lighter color indicates longer time-scale. Dashed lines represent a liner trend. All the trends are statistically significant ($p < 0.05$). X-axes are binned using 5-year moving window to smooth out time series fluctuations and highlight the trends.

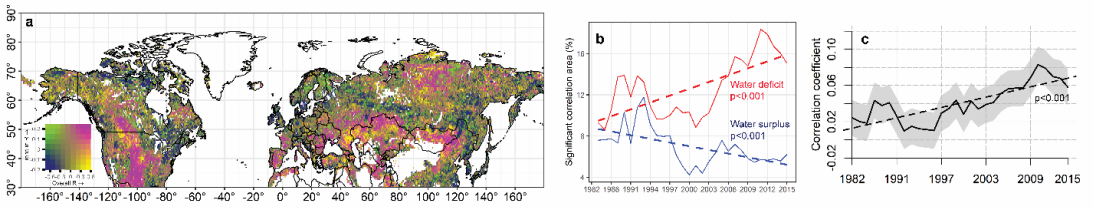


Figure S6.8: Spatiotemporal distribution of the statistically significant correlations between vegetation growth and water availability indices over the last three decades: (a) shows spatial distribution of correlation coefficients ($R_{NDVI\text{-}SM}$) between normalized difference vegetation index (NDVI) anomaly and soil moisture (SM) anomaly. The horizontal axis of the color legend is the correlation coefficient between NDVI anomaly and soil moisture anomaly for the entire study period, the vertical axis of the color legend is the trend of correlation coefficient for the 30 five-year moving windows, no color indicates non-vegetation covered regions; (b) shows the temporal trends of significant changes in percentage areas associated with water deficit and water surplus responses using five-year moving windows. Blue color stands for the water surplus response and red color for water deficit response. (c) shows the overall mean correlation coefficient over the study area. Shaded areas in (c) indicates standard deviation. All the trends of water deficit and water surplus responses are significant in linear trend test and Mann-Kendall trend test ($p < 0.05$).

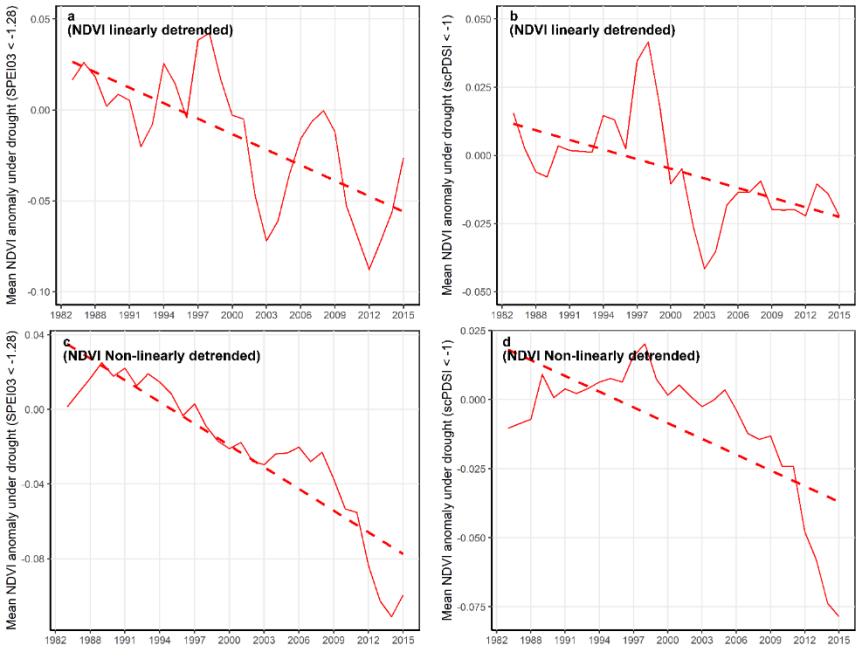


Figure S6.9: Changes in de-trended normalized difference vegetation index (NDVI) anomaly under drought condition over the last three decades. Mean de-trended NDVI (linearly detrended every five years) anomaly under drought conditions indicated by 3-month (a): Standardized Precipitation-Evapotranspiration Index (SPEI03) ) and (b):Palmer Drought Severity Index (scPDSI) over the Northern Hemisphere. (c)-(d) indicate mean de-trended NDVI (nonlinearly detrended based on moving average) anomaly under drought conditions indicated by 3-month (c): Standardized Precipitation-Evapotranspiration Index (SPEI03) ) and (d):Palmer Drought Severity Index (scPDSI) over the Northern Hemisphere. The mean NDVI anomaly was smoothed by a five-year moving window. NDVI anomaly trend was significant in linear trend test and Mann-Kendall trend test ($p < 0.05$). Drought conditions were identified by SPEI03 less than -1.28 and scPDSI less than -1.

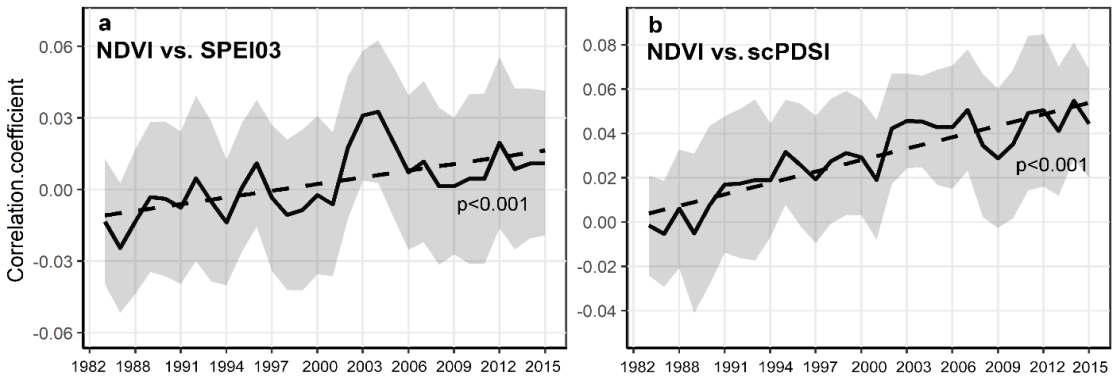


Figure S6.10: The trends of mean correlation coefficients (r-value) between normalized difference vegetation index (NDVI) anomaly and water availability indices over the last three decades. (a) and (b) present r-value between NDVI and 3-month Standardized Precipitation-Evapotranspiration Index (SPEI03) and Palmer Drought Severity Index (scPDSI), respectively of all the vegetated grid cells over the Northern Hemisphere for the period of 1982-2015. Black solid lines represent the mean correlation coefficients of all the grid cells and the dashed lines represent a liner trend. The gray areas represent the means ± standard deviation of each correlation efficient. Both trends are statistically significant ($p < 0.05$). X-axes are binned using 5-year moving window to smooth out time series fluctuations and highlight the trends.

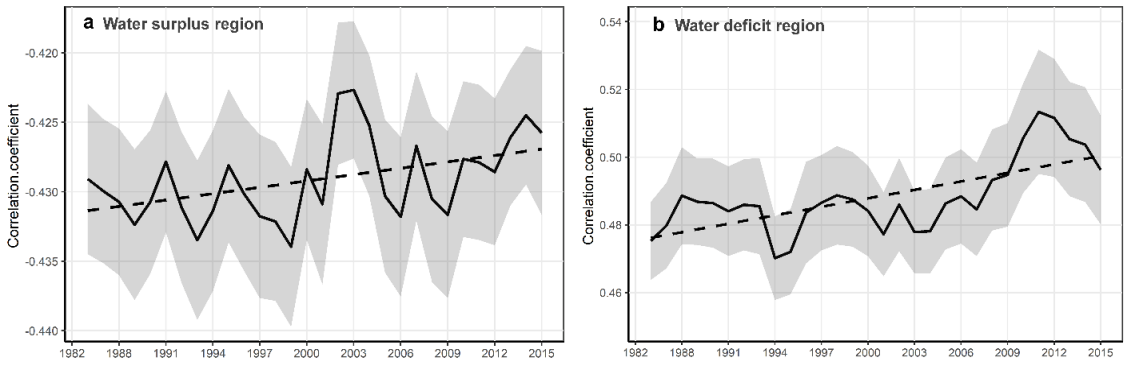


Figure S6.11: The trends of mean correlation coefficients (r-value) of all the grid cells over the Northern Hemisphere for negative (a) and positive (b) correlations between normalized difference vegetation index (NDVI) anomaly and Standardized Precipitation-Evapotranspiration Index (SPEI) over the last three decades. If multiple SPEI time-scales (ranging from 1- to 24-month time-scales) were significantly correlated with NDVI for one grid cell, the minimum negative correlation coefficient for (a) or maximum positive correlation coefficient for (b) was used for this grid cell. The gray areas represent 95% confidence interval of the dashed trend line. X-axes are binned using 5-year moving window to smooth out time series fluctuations and highlight the trends. Both trends are statistically significant ($p < 0.05$).

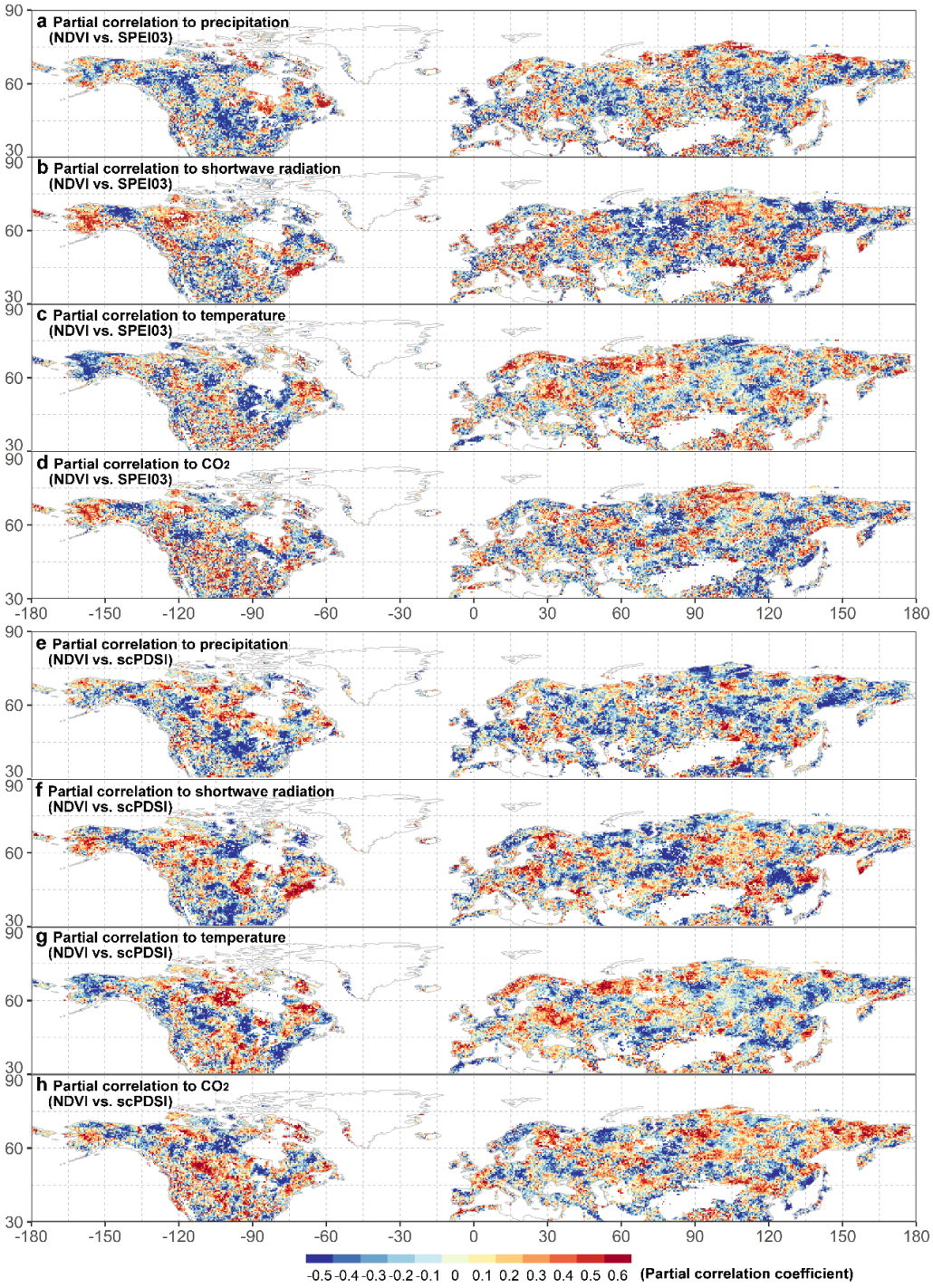


Figure S6.12: Spatial distribution of partial correlation coefficient for the factors of precipitation, shortwave radiation, temperature, and atmosphere $CO_2$ in explaining the dynamics of $R_{NDVI\text{-}SPEI03}$ and $R_{NDVI\text{-}scPDSI}$. (a)-(d) show the spatial distribution of partial correlation coefficient for precipitation (a), shortwave radiation (b), temperature (c), and

atmospheric $CO_2$ (d) in explaining $R_{NDVI\text{-}SPEI03}$; (e)-(h) show the spatial distribution of partial correlation coefficient for precipitation (e), shortwave radiation (f), temperature (g), and atmospheric $CO_2$ (h) in explaining $R_{NDVI\text{-}scPDSI}$.

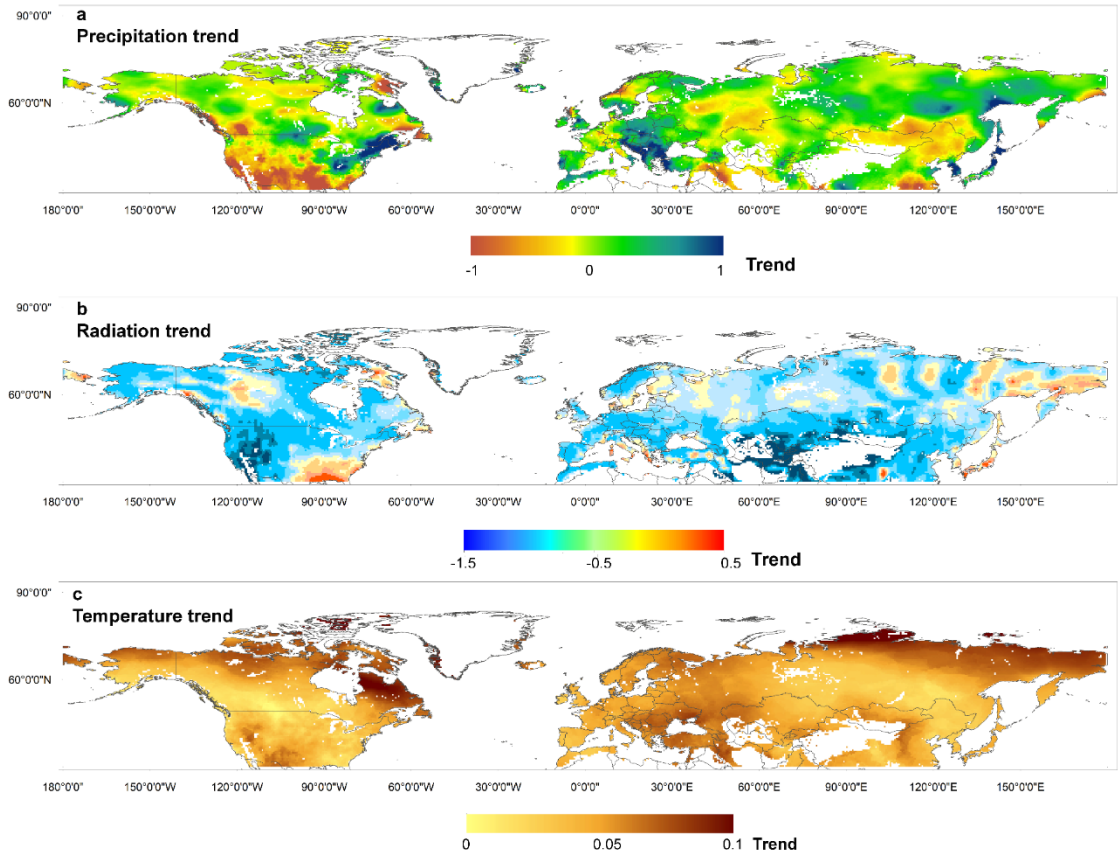


Figure S6.13: Spatial distributions of interannual trends for precipitation (a), shortwave radiation (b), and temperature (c).

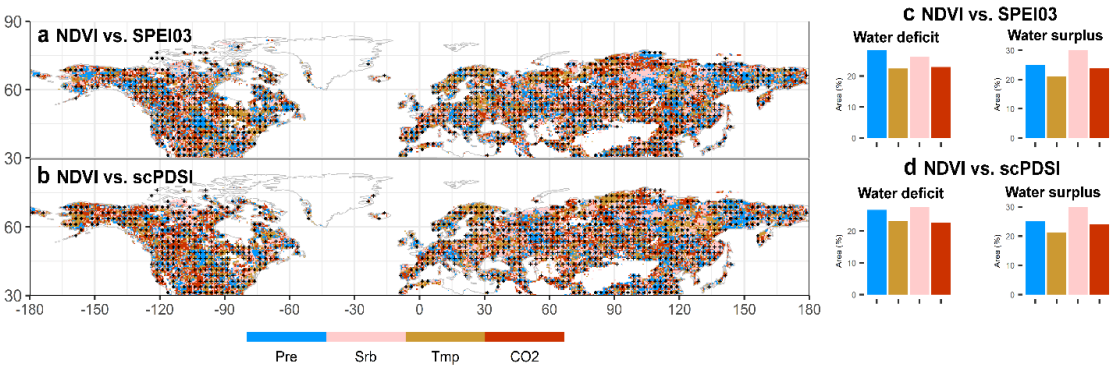


Figure S6.14: Attribution of meteorological factors and atmospheric $CO_2$ to the correlations between normalized difference vegetation index (NDVI) anomaly and water availability indices over the last three decades based on 'relaimpo' relative importance algorithm. (a) and (b) are the spatial distributions of the dominant factor influencing $R_{NDVI\text{-}SPEI03}$ and $R_{NDVI\text{-}scPDSI}$, respectively. The dots show the regions that $R_{NDVI\text{-}SPEI03}$ or $R_{NDVI\text{-}scPDSI}$ variations are significantly explained by precipitation, radiation, temperature and atmospheric $CO_2$. (c) and (d) the percentage areas where the water deficit and water surplus responses can be explained by one of the four dominant factors (i.e., precipitation, temperature, radiation, and $CO_2$). Pre: precipitation; Rad: radiation; Tmp: temperature; $CO_2$: atmospheric $CO_2$.

Table S7.1: Descriptions of the flux tower sites used in this study (GRA, grasslands; DBF, deciduous broadleaved forest; ENF, evergreen needle leaved forest; EBF, evergreen broadleaved forest; CSH, closed shrubland; WET, wetland; MF, mixed forest).

| Site | longitude | latitude | Start year | End year | Vegetation type | Reference (FLUXNET2015 DOI) |
|---|---|---|---|---|---|---|
| BE-Bra | 4.52 | 51.31 | 1996 | 2014 | MF | 10.18140/flx/1440128 |

| | | | | | | |
|---|---|---|---|---|---|---|
| BE-Vie | 5.99 | 50.31 | 1996 | 2014 | MF | 10.18140/flx/1440130 |
| CH-Fru | 8.54 | 47.12 | 2005 | 2014 | GRA | 10.18140/flx/1440133 |
| CH-Lae | 8.37 | 47.48 | 2004 | 2014 | MF | 10.18140/flx/1440134 |
| CZ-wet | 14.77 | 49.02 | 2006 | 2014 | WET | 10.18140/flx/1440145 |
| DE-Gri | 13.51 | 50.95 | 2004 | 2014 | GRA | 10.18140/flx/1440147 |
| DE-Hai | 10.45 | 51.08 | 2000 | 2012 | DBF | 10.18140/flx/1440148 |
| DE-Tha | 13.57 | 50.96 | 1996 | 2014 | ENF | 10.18140/flx/1440152 |
| DK-Sor | 11.64 | 55.49 | 1996 | 2014 | DBF | 10.18140/flx/1440155 |
| FI-Hyy | 24.30 | 61.85 | 1996 | 2014 | ENF | 10.18140/flx/1440158 |
| FI-Sod | 26.64 | 67.36 | 2001 | 2014 | ENF | 10.18140/flx/1440160 |
| FR-Fon | 2.78 | 48.48 | 2005 | 2014 | DBF | 10.18140/flx/1440161 |
| FR-LBr | -0.77 | 44.72 | 1996 | 2008 | ENF | 10.18140/flx/1440163 |
| FR-Pue | 3.60 | 43.74 | 2000 | 2014 | EBF | 10.18140/flx/1440164 |
| IT-Col | 13.59 | 41.85 | 1996 | 2014 | DBF | 10.18140/flx/1440167 |
| IT-Cpz | 12.38 | 41.71 | 1997 | 2009 | EBF | 10.18140/flx/1440168 |
| IT-Lav | 11.28 | 45.96 | 2003 | 2014 | ENF | 10.18140/flx/1440169 |
| IT-MBo | 11.05 | 46.01 | 2003 | 2013 | GRA | 10.18140/flx/1440170 |
| IT-Noe | 8.15 | 40.61 | 2004 | 2014 | CSH | 10.18140/flx/1440171 |
| IT-Ren | 11.43 | 46.59 | 1998 | 2013 | ENF | 10.18140/flx/1440173 |
| IT-Ro1 | 11.93 | 42.41 | 2000 | 2008 | DBF | 10.18140/flx/1440174 |
| IT-SRo | 10.28 | 43.73 | 1999 | 2012 | ENF | 10.18140/flx/1440236 |
| NL-Loo | 5.74 | 52.17 | 1996 | 2013 | ENF | 10.18140/flx/1440178 |
| RU-Fyo | 32.92 | 56.46 | 1998 | 2014 | ENF | 10.18140/flx/1440183 |

| | | | | | | |
|---|---|---|---|---|---|---|
| US-GLE | -106.24 | 41.37 | 2004 | 2014 | ENF | 10.18140/flx/1440069 |
| US-Ha1 | -72.17 | 42.54 | 1991 | 2012 | DBF | 10.18140/flx/1440071 |
| US-Los | -89.98 | 46.08 | 2000 | 2014 | WET | 10.18140/flx/1440076 |
| US-Me2 | -121.56 | 44.45 | 2002 | 2014 | ENF | 10.18140/flx/1440079 |
| US-MMS | -86.41 | 39.32 | 1999 | 2014 | DBF | 10.18140/flx/1440083 |
| US-Syv | -89.35 | 46.24 | 2001 | 2014 | MF | 10.18140/flx/1440091 |
| US-UMB | -84.71 | 45.56 | 2000 | 2014 | DBF | 10.18140/flx/1440093 |
| US-WCr | -90.08 | 45.81 | 1999 | 2014 | DBF | 10.18140/flx/1440095 |

Table S7.2: The effect size (slope) of each drought dimensions on GPP anomaly in the linear mixed effect models under 1-, 3-, 6-, and 9-month drought scenarios.

| GPP | | | | |
|---|---|---|---|---|
| Variable | 1-month drought Effect size (slope) | 3-month drought Effect size (slope) | 6-month drought Effect size (slope) | 9-month drought Effect size (slope) |
| (Intercept) | 0.7031 | -0.5047 | 0.6144 | 1.1130 |
| Intensity(Slight) | 0.0010 | -0.1893 | -0.3376 | -0.5040 |
| Growth(20%_Increase) | 0.0566 | 0.1560 | -0.1531 | -0.1593 |

| | | | | |
|---|---|---|---|---|
| Growth(30%_Increase) | 0.4173 | 0.1546 | -0.0950 | -0.3079 |
| Growth(40%_Increase) | 0.1521 | 0.0995 | 0.2264 | -0.2213 |
| Growth(50%_Increase) | 0.0187 | 0.4105 | 0.2744 | -0.2684 |
| Growth(60%_Increase) | 0.6638 | 0.4577 | 0.3879 | -0.1826 |
| Growth(70%_Increase) | 0.4916 | 0.2929 | 0.1600 | -0.4818 |
| Growth(80%_Increase) | 0.3556 | 0.3475 | -0.2352 | -0.4889 |
| Growth(90%_Increase) | 0.6232 | 0.2730 | -0.0107 | -0.3920 |
| Growth(100%) | -0.6976 | -0.3070 | -0.2556 | -0.2890 |
| Growth(90%_Decrease) | -0.7229 | -0.0531 | -0.2471 | -0.5980 |
| Growth(80%_Decrease) | -1.0015 | -0.2416 | -0.3886 | -0.4115 |
| Growth(70%_Decrease) | -1.0732 | -0.2574 | -0.2713 | -0.1504 |
| Growth(60%_Decrease) | -0.8443 | -0.1660 | -0.1044 | -0.2725 |
| Growth(50%_Decrease) | -1.0675 | -0.0676 | -0.0882 | -0.1182 |
| Growth(40%_Decrease) | -0.7130 | -0.2743 | -0.0997 | -0.4277 |
| Growth(30%_Decrease) | -0.4836 | 0.0338 | -0.2254 | -0.4825 |
| Growth(20%_Decrease) | -0.3134 | 0.3460 | -0.1089 | -0.1325 |
| Growth(10%_Decrease) | -0.1096 | 0.0189 | -0.1610 | 0.1578 |
| Prior_1 | -0.1253 | -0.1622 | -0.1219 | -0.1947 |
| Prior_2 | 0.1031 | -0.0774 | -0.0752 | -0.0174 |
| Prior_3 | -0.0548 | -0.0007 | -0.0601 | -0.1016 |
| Biome(CSH) | 0.0316 | 0.1492 | -0.0567 | -0.0789 |
| Biome(DBF) | 0.1206 | 0.3363 | -0.0975 | 0.0881 |
| Biome(EBF) | 0.0250 | 0.1499 | -0.1014 | -0.0544 |

| | | | | |
|---|---|---|---|---|
| Biome(ENF) | 0.0351 | 0.1782 | -0.0919 | -0.0769 |
| Biome(GRA) | -0.0586 | 0.2442 | -0.0336 | -0.0031 |
| Biome(MF) | 0.3275 | 0.8248 | 0.6083 | 0.5709 |
| Biome(SAV) | 0.7625 | -0.1645 | -0.7433 | 0.5935 |
| Biome(WET) | 0.3528 | 0.8646 | 0.2757 | 0.5251 |
| Biome(WSA) | -0.1283 | 0.0747 | -0.3663 | -0.2780 |

Table S7.3: The effect size (slope) of each drought dimensions on NEE anomaly in the linear mixed effect models under 1-, 3-, 6-, and 9-month drought scenarios.

| NEE | | | | |
|---|---|---|---|---|
| Variable | 1-month drought Effect size (slope) | 3-month drought Effect size (slope) | 6-month drought Effect size (slope) | 9-month drought Effect size (slope) |
| (Intercept) | -0.5412 | 0.8384 | 0.4036 | -0.4177 |
| Intensity(Slight) | 0.1720 | 0.0826 | -0.1260 | -0.2142 |
| Growth(20%_Increase) | 0.7884 | -0.2239 | -0.4633 | -0.1698 |
| Growth(30%_Increase) | 0.6821 | -0.2288 | 0.5561 | -0.1188 |
| Growth(40%_Increase) | 0.3442 | 0.4076 | 0.6646 | 0.0228 |
| Growth(50%_Increase) | 0.0289 | 0.5842 | 0.9342 | -0.2008 |
| Growth(60%_Increase) | 0.5245 | 0.6508 | 1.1620 | 0.1208 |
| Growth(70%_Increase) | 0.5287 | 0.4481 | 0.7671 | -0.0774 |
| Growth(80%_Increase) | 0.3356 | 0.8431 | 0.6928 | 0.1192 |

| | | | | |
|---|---|---|---|---|
| Growth(90%_Increase) | 0.5888 | 0.6862 | 0.7473 | 0.0173 |
| Growth(100%) | 0.7996 | 0.5619 | -0.7954 | -0.0549 |
| Growth(90%_Decrease) | 0.5841 | -0.3601 | -0.7189 | -0.2309 |
| Growth(80%_Decrease) | 0.8071 | -0.0465 | -0.4954 | 0.2238 |
| Growth(70%_Decrease) | 1.1388 | -0.2782 | -0.3440 | 0.1179 |
| Growth(60%_Decrease) | 0.6539 | -0.3328 | -0.8259 | -0.2145 |
| Growth(50%_Decrease) | -0.9086 | -0.4427 | -0.6614 | 0.2758 |
| Growth(40%_Decrease) | 0.6683 | 0.1684 | 0.3778 | -0.0860 |
| Growth(30%_Decrease) | 0.3127 | 0.4793 | 0.6406 | -0.0913 |
| Growth(20%_Decrease) | 0.1598 | 0.4720 | 0.7688 | -0.3681 |
| Growth(10%_Decrease) | 0.2015 | -0.7529 | 0.5589 | -0.1164 |
| Prior_1 | -0.0451 | -0.1446 | -0.1247 | -0.1837 |
| Prior_2 | -0.0224 | -0.1354 | -0.0484 | 0.0564 |
| Prior_3 | 0.0056 | -0.0228 | -0.0409 | -0.0300 |
| Biome(CSH) | -0.2772 | 0.1688 | 0.4946 | 0.2734 |
| Biome(DBF) | -0.1960 | 0.1688 | -0.0581 | -0.0358 |
| Biome(EBF) | -0.1739 | -0.2622 | 0.2697 | 0.2398 |
| Biome(ENF) | -0.1731 | -0.3090 | 0.0432 | -0.0275 |
| Biome(GRA) | 0.0981 | -0.2021 | -0.0942 | -0.2053 |
| Biome(MF) | 0.0095 | -0.7423 | -0.2722 | -0.3141 |
| Biome(SAV) | -0.1664 | 0.0959 | 0.4848 | -0.2101 |
| Biome(WET) | -0.1308 | 0.4924 | 0.2556 | -0.3018 |
| Biome(WSA) | -0.4874 | -0.1057 | 0.2721 | 0.2271 |

Table S7.4: The effect size (slope) of each drought dimensions on $R_{ECO}$ anomaly in the linear mixed effect models under 1-, 3-, 6-, and 9-month drought scenarios.

| $R_{ECO}$ | | | | |
|---|---|---|---|---|
| Variable | 1-month drought Effect size (slope) | 3-month drought Effect size (slope) | 6-month drought Effect size (slope) | 9-month drought Effect size (slope) |
| (Intercept) | 1.3278 | 0.1806 | 1.0058 | 1.5109 |
| Intensity(Slight) | 0.2742 | 0.1965 | -0.2472 | -0.5472 |
| Growth(20%_Increase) | -0.2449 | 0.2114 | -0.3522 | -0.6723 |
| Growth(30%_Increase) | -0.6145 | 0.0557 | -0.3793 | -0.4224 |
| Growth(40%_Increase) | -0.5008 | 0.2322 | -0.4833 | -0.1747 |
| Growth(50%_Increase) | 0.3970 | 0.2961 | -0.1500 | -0.3281 |
| Growth(60%_Increase) | -0.8415 | 0.4749 | -0.0781 | -0.1457 |
| Growth(70%_Increase) | -0.8363 | -0.0845 | -0.2669 | -0.7681 |
| Growth(80%_Increase) | -0.8981 | 0.3692 | -0.7279 | -0.6816 |
| Growth(90%_Increase) | -0.8783 | 0.0802 | -0.4785 | -0.5844 |
| Growth(100%) | -0.7679 | -0.0423 | -0.8336 | -0.7232 |
| Growth(90%_Decrease) | -0.8573 | -0.1816 | -0.7977 | -0.5075 |
| Growth(80%_Decrease) | -1.0047 | -0.1228 | -0.7315 | -0.6111 |
| Growth(70%_Decrease) | -1.2354 | -0.2520 | -0.6967 | -0.1956 |
| Growth(60%_Decrease) | -0.8770 | 0.1936 | -0.5601 | -0.6878 |
| Growth(50%_Decrease) | -1.0311 | -0.0363 | -0.6023 | -0.4465 |

| | | | | |
|---|---|---|---|---|
| Growth(40%_Decrease) | -1.1181 | 0.4220 | -0.5119 | -0.7236 |
| Growth(30%_Decrease) | -1.0015 | -0.1630 | -0.7308 | -0.6004 |
| Growth(20%_Decrease) | -0.5025 | 0.3293 | -0.6082 | -0.5871 |
| Growth(10%_Decrease) | -0.2235 | -0.2860 | -1.0756 | -0.0066 |
| Prior_1 | -0.1350 | -0. 0477 | -0.1107 | -0.1437 |
| Prior_2 | -0.0828 | -0.0773 | -0.0550 | -0.1841 |
| Prior_3 | -0.0035 | -0.0167 | -0.0199 | -0.0946 |
| Biome(CSH) | -0.1771 | 1.0787 | 0.6625 | -0.4349 |
| Biome(DBF) | -0.1079 | 0.1766 | -0.2311 | -0.2258 |
| Biome(EBF) | -0.2388 | 0.1537 | -0.0541 | -0.3381 |
| Biome(ENF) | -0.1973 | 0.1582 | -0.1142 | -0.4836 |
| Biome(GRA) | -0.1939 | 0.1975 | -0.0786 | -0.3123 |
| Biome(MF) | -0.1468 | 0.4605 | -0.1130 | -1.3598 |
| Biome(SAV) | 0.6012 | 0.0722 | -1.0235 | -0.1201 |
| Biome(WET) | -0.0993 | 0.5724 | 0.2793 | -0.5393 |
| Biome(WSA) | -0.5864 | -0.1885 | -0.4216 | -0.7342 |

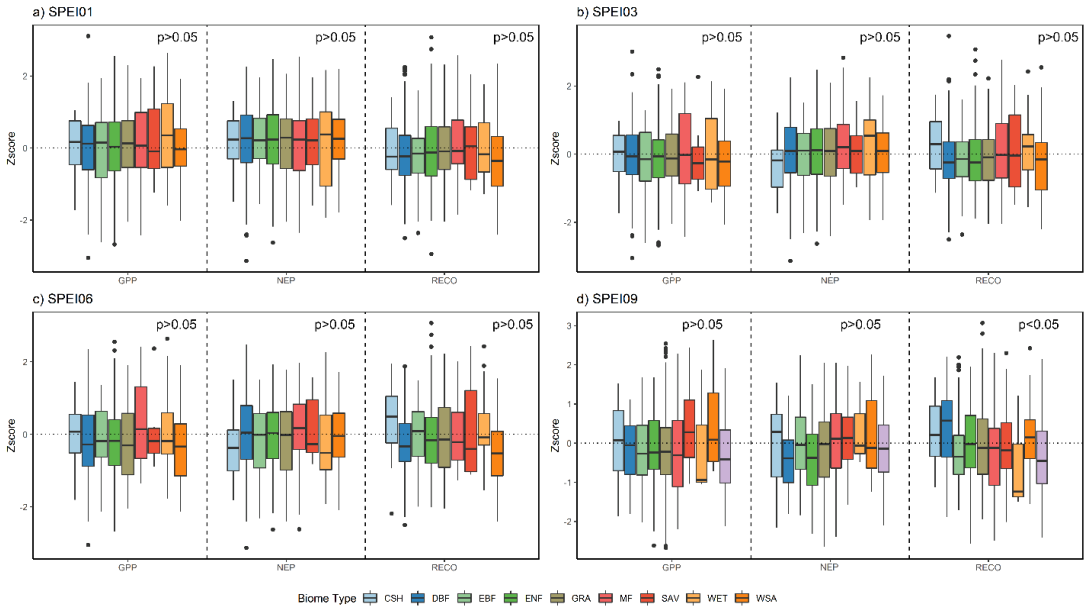


Figure S7.1: Response of NEP, GPP, and $R_{ECO}$ to drought from different biome types under 1-, 3-, 6-, and 9-month time-scale of droughts (p-value from ANOVA tests were used to test the significance of differences between the groups).

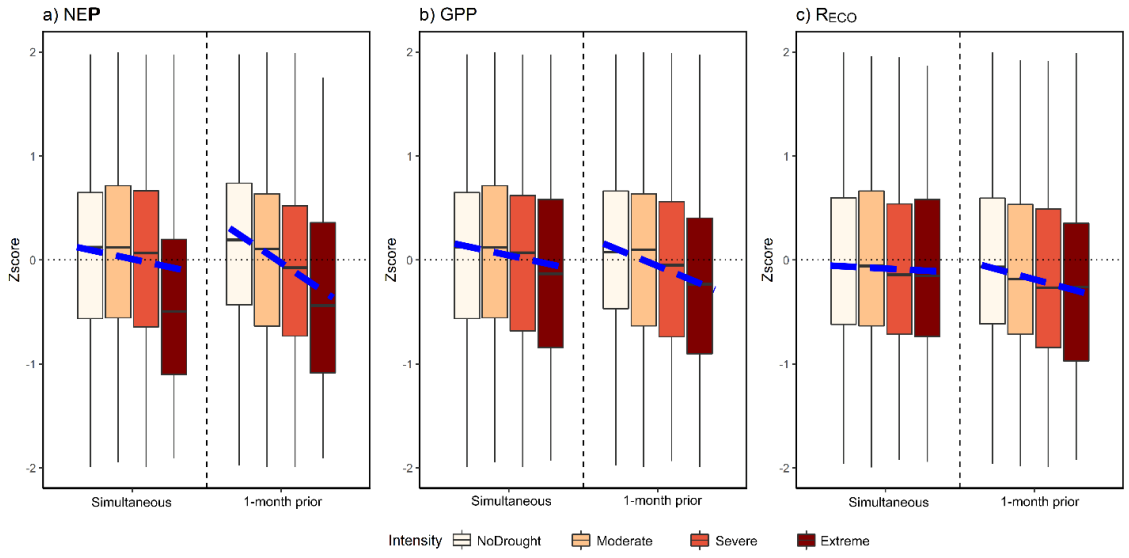

Figure S7.2: The comparison between responses of NEP, GPP, and $R_{ECO}$ to simultaneous and prior drought intensities TerraClimate based PDSI (p-value from ANOVA tests were used to test the significance of differences between the groups). Y-axis indicated the z-scores of GPP, NEP, and $R_{ECO}$ under different drought intensities of simultaneous (a) and 1-month prior drought (b) conditions.

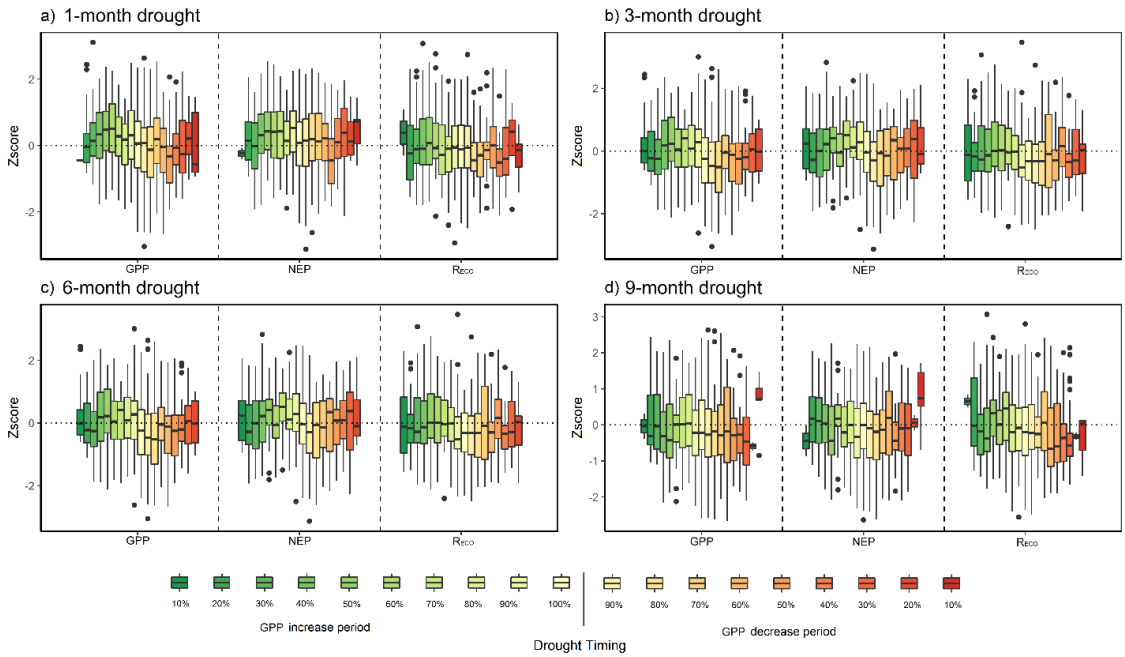


Figure S7.3: Response of NEP, GPP, and $R_{ECO}$ to different drought timing under 1-, 3-, 6-, and 9-month time-scale of droughts (p-value from ANOVA tests were used to test the significance of differences between the groups

# CURRICULUM VITAE

## EDUCATION

Indiana University
Ph.D. in Applied Earth Science
Minor: Statistics
University of Chinese Academy of Sciences
Ph.D. in Geography Information System (GIS)
China University of Mining and Technology
MS. in Geodesy and Surveying Engineering
North China Institute of Science and Technology
BS. in Geodesy and Surveying Engineering

## RESEARCH EXPERIENCE

Indiana University-Purdue University, Indianapolis
Graduate Research Assistant, 09/2017 - 04/2022
University of Chinese Academy of Sciences
Research Assistant, 07/2014 - 06/2017
China University of Mining and Technology
Research Assistant, 07/2011 - 06/2014

## TEACHING EXPERIENCE

2021 Spring
GEOL-G 117-22308 Environmental Geology Laboratory, 13 weeks, Online.
GEOL-G 117-21348 Environmental Geology Laboratory, 13 weeks, Online.

2020 Fall
GEOL-G 117-23944 Environmental Geology Laboratory, 13 weeks, Online.
GEOL-G 117-26702 Environmental Geology Laboratory, 13 weeks, Online.

2019 Fall:
GEOL-G 117-26702 Environmental Geology Laboratory, 13 weeks, In-person.
GEOL-G 117-27070 Environmental Geology Laboratory, 13 weeks, In-person.

2019 Spring:
GEOL-G 117-22150 Environmental Geology Laboratory, 13 weeks, In-person.

2018 Spring:
GEOL-G 117-22989 Environmental Geology Laboratory, 13 weeks, In-person.

## PEER-REVIEWED PUBLICATIONS (ResearchGate, Google Scholar)

**Jiao, W.,** Wang, L., Wang, H., Lanning, M., Chang, Q., & Novick, K. A. (2022). Comprehensive quantification of the responses of ecosystem production and respiration to drought time scale, intensity and timing in humid environments: A

FLUXNET synthesis. *Journal of Geophysical Research: Biogeosciences*, e2021JG006431.

Zhang, Y., Liu, X., **Jiao, W.,** Zhao, L., Zeng, X., Xing, X., ... & Lu, Q. (2022). A new multi-variable integrated framework for identifying flash drought in the Loess Plateau and Qinling Mountains regions of China. *Agricultural Water Management*, *265*, 107544.

Tian, C., Du, K., Wang, L., Zhang, X., Li, F., **Jiao, W.,** Beysens, D., Kaseke, K.F. and Medici, M.G., 2022. Stable isotope variations of dew under three different climates. *Scientific Data*, 9(1), pp.1-7.

Zhao, X., Xia, H., Liu, B., & **Jiao, W.** (2022). Spatiotemporal Comparison of Drought in Shaanxi–Gansu–Ningxia from 2003 to 2020 Using Various Drought Indices in Google Earth Engine. *Remote Sensing*, 14(7), 1570.

**Jiao, W.,** Wang, L., Smith, W., Chang, Q., Wang, H., D'Odorico, P. (2021). Observed increasing water constraint on vegetation growth over the last three decades. *Nature Communications*, 12, 3777.

Zhang, Y., Liu, X., **Jiao, W.,** Zeng, X., Xing, X., Zhang, L., ... & Hong, Y. (2021). Drought monitoring based on a new combined remote sensing index across the transitional area between humid and arid regions in China. *Atmospheric Research*, 105850.

**Jiao, W.,** Wang, L. & McCabe, M. F. (2021). Multi-sensor remote sensing for drought characterization: current status, opportunities and a roadmap for the future. *Remote Sensing of Environment*, 256, 112313.

Chang Q., Xiao X., Wu X., Doughty R., **Jiao, W.,** Qin Y., (2021). Assessing variability of optimum air temperature for photosynthesis across site-years, sites and biomes and their effects on photosynthesis estimation. *Agricultural and Forest Meteorology* 298-299, 108277.

Yuan, Y., Wang, L., Wang, H., Lin, W., Jiao, W., & Du, T. (2021). A Modified Isotope-based Method for Potential High-Frequency Evapotranspiration Partitioning. *Advances in Water Resources*, 104103.

Tian, C., **Jiao, W.,** Beysens, D., Kaseke, K. F., Medici, M. G., Li, F., & Wang, L. (2021). Investigating the role of evaporation in dew formation under different climates using $^{17}$O-excess. *Journal of Hydrology*, 125847.

Qiao, N., Zhang, L., Huang, C., **Jiao, W.,** Maggs-Kölling, G., Marais, E., & Wang, L. (2020). Satellite observed positive impacts of fog on vegetation. *Geophysical Research Letters*, 47.

Chang Q., Xiao X., Wu X., Doughty R., **Jiao, W.,** Bajgain R., Qin Y., Wang J., (2020). Estimating site-specific optimum air temperature and assessing its effect on the photosynthesis of grasslands in mid-to high-latitudes. *Environmental Research Letters*. Mar 6;15(3):034064.

**Jiao, W.,** Tian, C., Chang, Q., Novick, K.A., Wang, L. (2019). A new multi-sensor integrated index for drought monitoring. *Agricultural and Forest Meteorology*, 268: 74-85.

Lei, S., Xu, J., Li, Y., Li, L., Lyu, H., Liu, G., ... & **Jiao, W**. (2019). A semi-analytical algorithm for deriving the particle size distribution slope of turbid inland water based on OLCI data: a case study in Lake Hongze. *Environmental Pollution*, 116288.

**Jiao, W.,** L. Wang, K. A. Novick, Q. Chang, (2019). A new station-enabled multi-sensor integrated index for drought monitoring. *Journal of Hydrology* 574, 169-180.

Tian, C., Wang, L., **Jiao, W.,** Li, F., Tian, F., & Zhao, S. (2019). Triple isotope variations of monthly tap water in China. *Scientific Data*, 7(1), 1-6.

**Jiao, W.,** Q. Chang, L. Wang, (2019). The Sensitivity of Satellite Solar-Induced Chlorophyll Fluorescence to Meteorological Drought. *Earth's Future* 7, 558-573.

Baig, M. H. A., Abid, M., Khan, M. R., **Jiao, W.,** Amin, M., & Adnan, S. (2019). Assessing Meteorological and Agricultural Drought in Chitral Kabul River Basin Using Multiple Drought Indices. *Remote Sensing*, 12(9), 1417.

Wang, L., Kaseke, K. F., Ravi, S., **Jiao, W.,** Mushi, R., Shuuya, T., & Maggs-Kölling, G. (2019). Convergent vegetation fog and dew water use in the Namib Desert. *Ecohydrology,* 12(7), e2130.

Chang, Q., Xiao, X., **Jiao, W.,** Wu, X., Doughty, R., Wang, J., ... & Qin, Y. (2019). Assessing consistency of spring phenology of snow-covered forests as estimated by vegetation indices, gross primary production, and solar-induced chlorophyll fluorescence. *Agricultural and Forest Meteorology*, 275, 305-316.

Tian, C., Wang, L., Tian, F., Zhao, S., & **Jiao, W**. (2019). Spatial and temporal variations of tap water 17O-excess in China. *Geochimica et Cosmochimica Acta,* 260, 1-14.

Kaseke, K. F., Wang, L., Wanke, H., Tian, C., Lanning, M., & **Jiao, W**. (2018). Precipitation origins and key drivers of precipitation isotope ($^{18}O$, $^{2}H$, and $^{17}O$) compositions over Windhoek. *Journal of Geophysical Research: Atmospheres*, 123(14), 7311-7330.

Chang, Q., Zhang, J., **Jiao, W.,** & Yao, F. (2018). A comparative analysis of the NDVIg and NDVI3g in monitoring vegetation phenology changes in the Northern Hemisphere. *Geocarto International*, 33(1), 1-20.

**Zhang, L*., Jiao, W*.,** Zhang, H., Huang, C, Tong, Q (2017). Studying drought phenomena in the Continental United States in 2011 and 2012 using various drought indices. *Remote Sensing of Environment*, 190, 96-106. (**co-first author*)

**Jiao, W.,** Zhang, L., Chang, Q., Fu, D., Cen, Y., & Tong, Q. (2016). Evaluating an enhanced vegetation condition index (VCI) based on VIUPD for drought monitoring in the continental United States. *Remote Sensing*, 8(3), 224.

Chang, Q., Zhang, J., **Jiao, W.,** Yao, F., & Wang, S. (2016). Spatiotemporal dynamics of the climatic impacts on greenup date in the Tibetan Plateau. *Environmental Earth Sciences*, 75(20), 1343.

**Jiao, W.,** Liu, R., Ge., Q., (2013). Assessing urban expansion of Nairobi using Remote sensing images. *Resources Science*, 35, no. 4: 885-891. (In Chinese with English Abstract)

## CONFERENCE PRESENTATIONS

Jiao, W., Wang, L., McCabe, M., (2022) Drought characterization based on multi-sensor remote sensing observations. 102th American Meteorological Society (AMS) (Invited oral).

Jiao, W., (2022) Multi-sensor remote sensing drought characterization, challenges and opportunities. Hydro90. (Invited oral).

Jiao, W., (2021) Observed increasing water constraint on vegetation growth over the last three decades. AGU Fall Meeting 2021, New Orleans, USA (oral)
Jiao, W., (2021) Observed increasing water constraint on vegetation growth over the last three decades. GeoInsider. (Invited oral)
Jiao, W., Wang, L., (2021). Observed increasing water constraint on vegetation growth on Northern Hemisphere over the last 30 years. International Association of Chinese Youth in Water Sciences (CYWater) (oral).
Jiao, W., Wang, L., McCabe, M., (2021). The role of multi-sensor remote sensing for drought characterization: challenges and opportunities. European Geosciences Union (EGU) (oral).
Jiao, W., Wang, L., (2021). Quantifying the responses of ecosystem production and respiration to drought time scale, intensity, timing and lagged response: A FLUXNET synthesis. European Geosciences Union (EGU) (oral).
Jiao, W., Wang, L., Novick, K., Chang, Q., (2019) A new remote sensing framework for drought monitoring. AGU Fall Meeting 2019, San Francisco, USA (oral).
Jiao, W., Wang, L., (2018) Use of Satellite Solar-induced Chlorophyll Fluorescence for Meteorological Drought Assessing: Merits and Limitations. The Geological Society of America (GSA) 2018, Indianapolis, Indiana, USA (oral).
Jiao, W., Wang, L., (2018) Sensitivity of Satellite Solar-induced Chlorophyll Fluorescence to drought monitoring. AGU Fall Meeting 2018, Washington DC, USA (poster).
Jiao, W., Wang, L., (2017) A new multi-sensor index for drought monitoring. AGU Fall Meeting 2017, New Orleans, USA (poster).
Jiao, W., Studying drought phenomena in the Continental United States in 2011 and 2012 using various drought indices (2017). Nagoya University, Japan. (Invited oral)
Jiao, W, December 2017, Drought monitoring using multi-sensor remote sensing data, Chinese Academy of Sciences, China (Invited oral).

## SERVICE

### Journal reviewers (>40 times)

*Agricultural and Forest Meteorology; Environmental Research Letters;*
*Environmental Science and Pollution Research; Frontiers of Earth Sciences ;*
*Geocarto International; Geomatics Natural Hazards and Risk;*
*IEEE Access; International Journal of Applied Earth Observation and Geoinformation;*
*International Journal of Remote Sensing;*
*Journal of Geophysical Research: Biogeosciences ;*
*Journal of Arid Environments; Journal of Arid Land;*
*Land Degradation & Development; New Phytologist;*
*Hydrology and Earth System Sciences; Remote Sensing; Remote Sensing of Environment;*
*Science of The Total Environment; Transactions on Geoscience and Remote Sensing.*

### Invited public talks

Jiao, W., (2021). Multi-sensor remote sensing drought monitoring. Beyond Boundaries - Indiana Academies Symposium.

Jiao, W., Remote sensing for drought monitoring (2018). Summer Teacher Training Program.

## HONORS AND AWARDS

2022 Sherry Queener Graduate Student Excellence, Finalist, Indiana University-Purdue University, Indianapolis;

2022 Chancellor's Scholar Award, Finalist, Indiana University-Purdue University, Indianapolis;

2021-2022 Dr. Arthur Mirsky Geology Fellowship (Science);

2021 Sino-Eco "Best Student Paper" award;

2019 School of Science IUPUI travel grant;

2018 School of Science IUPUI travel grant;

2017 Outstanding graduate student award University of Chinese Academy of Sciences.

## MEMBERSHIPS IN PROFESSIONAL ASSOCIATIONS

Student Member, American Geophysical Union (AGU);

Student Member, American Meteorological Society (AMS);

Student Member, European Geosciences Union (EGU);

Student Member, Geological Society of America (GSA).